State University of Londrina
Department of Electrical Engineering
Doctorate Program in Electrical Engineering

Daniel Strufaldi Batista

Attitude-Independent Magnetometer Calibration including Time-Varying Bias using a Helmholtz Coil powered by a Howland Current Source

Londrina
2023

Daniel Strufaldi Batista

Attitude-Independent Magnetometer Calibration including Time-Varying Bias using a Helmholtz Coil powered by a Howland Current Source

A Thesis submitted to the Electrical Engineering Graduate Program at the State University of Londrina in partial fulfillment of the requirements for the degree of Doctor of Philosophy in Electrical Engineering.

Concentration Area:
Electronic Systems

Advisor:
Prof. Dr. Leonimer Flávio de Melo

Londrina
2023

Batista, Daniel Strufaldi.

Attitude-Independent Magnetometer Calibration including Time-Varying bias using a Helmholtz Coil powered by a Howland Current Source. Londrina, 2023. 238 p.

Advisor: Leonimer Flávio de Melo.

Thesis (Doctor of Philosophy) – State University of Londrina. Department of Electrical Engineering, 2023.

1. Magnetometer Calibration, 2. Hardware-in-the-Loop, 3. Helmholtz Coil, 4. Howland Current Source, 5. Parameter Estimation.

Electrical Engineering Doctorate Program.

Daniel Strufaldi Batista

Attitude-Independent Magnetometer Calibration including Time-Varying Bias using a Helmholtz Coil powered by a Howland Current Source

A Thesis submitted to the Electrical Engineering Graduate Program at the State University of Londrina in partial fulfillment of the requirements for the degree of Doctor of Philosophy in Electrical Engineering.

Advisor:
Prof. Dr. Leonimer Flávio de Melo

Examination Board

Prof. Dr. Leonimer Flávio de Melo
Department of Electrical Engineering
State University of Londrina
Advisor

Prof. Dr. Francisco Granziera Júnior
Department of Electrical Engineering
State University of Londrina
Member

Prof. Dr. Marcelo Carvalho Tosin
Department of Electrical Engineering
State University of Londrina
Member

Prof. Dr. William Reis Silva
Faculty of Gama
University of Brasilia
Member

Prof. Dr. Felipe Oliveira e Silva
Department of Automatics
Federal University of Lavras
Member

Londrina
2023

I dedicate this work to my parents.

In memory of my father.

Acknowledgements

This thesis is in memory and dedicated to my father, who supported me my entire life.

I want to thank my mother for her continuous support during my entire life.

I want to thank my Advisor, Prof. Leonimer, for his trust and support during the thesis.

I want to thank my undergraduate Advisor, Prof. Francisco Granziera, for his support inside the laboratory and his friendship, and Prof. Marcelo Tosin for his support and friendship.

I want to thank all my friends. This journey would have been far more arduous without your support and friendship.

Special thanks to Alexandre, Amanda, Ana Paula, Bruna, Danilo, Edmara, Gabriel, Giovana, Guedes, Guilherme, Lyha, Lucas, Luiz Ricardo, Luiz Guilherme, Malê, Marcos Scaramal, Roberto, and Tamy. I am grateful for having you as friends.

And finally, thank God.

Resumo

As medidas de magnetômetros são uma fonte confiável de informações para diversos sistemas de controle e determinação de atitude. Por exemplo, nanossatélites, veículos aéreos não tripulados, aeronaves e muitos outros sistemas utilizam as leituras de sensores magnéticos. Além disso, o uso de sensores magnéticos de baixo custo aumentou exponencialmente, em missões espaciais e outras aplicações, como consequência do avanço de pequenas espaçonaves e aeronaves nas últimas décadas. Esses sistemas são geralmente construídos em torno de designs menores e de baixo custo e, consequentemente, essas aplicações geralmente dependem de informações fornecidas por sensores MEMS (sistemas microeletromecânicos) de baixo custo. Portanto, a calibração de sensores magnéticos de baixo custo é essencial para garantir a precisão, por exemplo, de sistemas de determinação de atitude que utilizam as informações do campo geomagnético terrestre. No entanto, o avanço das espaçonaves de menor tamanho também adiciona outro problema à calibração dos sensores devido aos sistemas eletrônicos e correntes elétricas presentes ao redor do sensor. Isso pode causar interferências variáveis no tempo nas medições dos sensores, como na forma de *bias*. Nesse sentido, esta tese aborda o problema de calibração de sensores magnéticos de baixo custo considerando interferências variáveis ao longo do tempo. Uma das contribuições desta tese é o estimador utilizado para encontrar os parâmetros de calibração, onde é proposta a aplicação direita de um estimador de mínimos quadrados não lineares para encontrar os parâmetros de calibração do modelo não linear de magnetômetros proposto no algoritmo *Extended Two-Step*. A tese também aborda a expansão deste algoritmo para incluir *bias* variáveis ao longo do tempo. Além disso, esta tese propõe uma metodologia para investigar experimentalmente a calibração dos sensores utilizando um simulador de campos magnéticos. Por conseguinte, outra contribuição desta tese é uma metodologia para usar uma bobina de Helmholtz de três eixos a fim de avaliar a calibração de magnetômetros suscetíveis a interferências variáveis ao longo do tempo. O simulador de campos magnéticos deve gerar estes campos em malha aberta (sem um controlador atuando na malha do campo magnético) para fornecer uma bancada de teste adequada para o problema. Portanto, a tese descreve o simulador, composto pela bobina de Helmholtz, um sistema de simulações Hardware-in-the-Loop (HiL) e uma Fonte de Corrente de Howland (HCS), e demonstra como calibrar este *setup*. O sistema calibrado é usado para gerar campos magnéticos em malha aberta para calibrar magnetômetros sujeitos a interferências variáveis no tempo. Outro tópico desta tese é a fonte de corrente empregada no simulador. Uma fonte de corrente elétrica precisa e estável é essencial para garantir a precisão do campo magnético gerado. Assim, outra contribuição da tese é a análise e os resultados da fonte HCS de alta potência usando amplificadores operacionais de alta potência. A HCS é uma fonte de corrente controlada por tensão linear tipicamente empregada em aplicações de baixa corrente, como as biomédicas, porém apesar do seu amplo uso nessas aplicações e correlatas, a literatura carece de sua análise de erro em condições de corrente mais alta. Dessa forma, este trabalho traz duas contribuições em relação à HCS. Primeiramente, discute como projetar de maneira casada o circuito da HCS de potência em conjunto com o simulador de campos magnéticos. Em segundo lugar, apresenta um estudo detalhado e a análise prática da HCS usando amplificadores de alta potência para aplicações em baixa frequência, com altos requisitos de linearidade e acurácia na corrente elétrica.

Palavras-Chaves: Amplificador Operacional de Potência; Bias Variável no Tempo; Calibração de Magnetômetros; Estimação de Parâmetros; Fonte de Tensão Corrente Controlada por Tensão; Geração de Campo Magnético; *Hardware-in-the-loop*; Helmholtz coil; *Howland Current Source*; Magnetômetros;

Abstract

Magnetometer measurements are a reliable source of information for many attitude determination and control systems. For example, nanosatellites, unmanned aerial vehicles, aircraft, and many applications use magnetic readings in their systems. Moreover, low-cost magnetic sensors have increased exponentially in space missions and other applications owing to the advance of smaller spacecraft and aircraft. Such systems are usually built around low-cost and smaller designs; consequently, these applications commonly depend on the information provided by low-cost MEMS (Micro-Electro-Mechanical Systems) sensors. Therefore, low-cost magnetometer calibration is essential to ensure the accuracy of attitude determination systems that rely on Earth's magnetic field measurements. However, the advance of small spacecraft also adds another concern to the sensor calibration due to electronic systems and electrical currents in a sensor's surroundings, which may cause time-varying interference in its measurements, such as time-varying bias. In this direction, this thesis addresses the problem of low-cost magnetic sensor calibration with time-varying bias. One of the contributions of this thesis is the estimator used to find the calibration parameters, where we propose the straightforward application of a non-linear least squares algorithm to estimate the parameters of the non-linear magnetometer model introduced in the well-known Extended Two-Step calibration algorithm. Besides, we also address how to expand the algorithm to include time-varying bias. In addition to that, this thesis proposes a methodology to investigate the calibration experimentally using a magnetic field simulator. Consequently, another contribution of this thesis is a methodology to use a Helmholtz coil to assess the magnetometer calibration with time-varying bias interference. The magnetic field simulator must generate an open-loop magnetic field (without a controller acting in the magnetic field loop) to accomplish that and provide a test bench for the problem. Therefore, the thesis describes the simulator, composed of the Helmholtz coil, a Hardware-in-the-Loop (HiL) simulation, and a power Howland Current Source (HCS), and how to calibrate the setup. Then, we display how to generate the calibrated open-loop magnetic field, which has a sub-milligauss accuracy, and use it to assess magnetometer calibration with time-varying interference. At last, another topic of this thesis is the electrical current source of the magnetic field simulator, which must have an accurate and stable output to maximize the accuracy and precision of the generated magnetic field. Therefore, this thesis contributes to implementing a thorough theoretical and experimental analysis of the power HCS circuit using high-power operational amplifiers (OpAmps). The HCS is a linear voltage-controlled-current source typically employed in low-current applications such as biomedical ones, but the literature lacks its error analysis in higher current conditions. Therefore, the work has two contributions regarding the HCS. First, we demonstrate how to design and match the power HCS to the requirements and design of a magnetic field simulator. Second, we present a detailed study and practical analysis of the HCS using power OpAmps for direct current applications with requirements of a very accurate and linear output current.

Keywords: Hardware-in-the-loop; Helmholtz cage; Helmholtz coil; Howland current source; Magnetic field simulator; Magnetometer; Magnetometer calibration; Non-linear least squares; Parameter estimation; Power operational amplifier; Sensor calibration; Time-varying bias; Voltage-controlled current source.

List of Figures

List of Tables

List of Acronyms

ADC	Analog to Digital Converter
ADCS	Attitude Determination and Control System
AEB	Brazilian Space Agency (*Agência Espacial Brasileira*)
AHRS	Attitude and Heading Reference System
AWG	American Wire Gauge
BNC	Bayonet Neill–Concelman (BNC Connector)
CAD	Computer Aided Design
CAN	Controller Area Network
CMRR	Common-Mode Rejection Ratio
COTS	Commercial-Off-The-Shelf
DAC	Digital to Analog Converter
DC	Direct Current
ETS	Extended Two-Step algorithm for magnetometer calibration
ETS-A	Analytical solution of the Extended Two-Step
FET	Field-Effect Transistor
HCS	Howland Current Source
HiL	Hardware-in-the-Loop
I2C	Inter-Integrated Circuit
IC	Integrated Circuit
IGRF	International Geomagnetic Reference Field
IMU	Inertial Measurement Unit
LDO	Linear and Low-Dropout regulators
LSB	Least Significant Bit
MARG	Magnetic, Angular Rate and Gravity

MEMS	Micro Electro-Mechanical System
ML	Maximum Likelihood estimator
NLLS	Non-Linear Least Squares calibration algorithm
ODR	Output Data Rate
OpAmp	Operational Amplifier
PCB	Printed Circuit Board
PID	Proportional Integral Derivative control
PSRR	Power Supply Rejection Ratio
ppm	parts per million
PWM	Pulde Width Modulation
RL	Resistor-Inductor circuit
RMS	Root Mean Squared
RMSE	Root Mean Squared Error
RTI	Real-Time Interface library for the dSPACE hardware
SD	Standard Deviation
SMD	Surface Mount Device
SPI	Serial Peripheral Interface
SPICE	Simulation Program with Integrated Circuit Emphasis
SPS	Samples per Second
SUT	System/Sensor Under Test
TAM	Three-Axial Magnetometer
TI	Texas Instruments
TCR	Temperature Coefficient of Resistance
UART	Universal Asynchronous Receiver / Transmitter
UAV	Unmanned Aerial Vehicle
VCCS	Voltage-Controlled Current Source
WMM	World Magnetic Model

List of Symbols

α	Temperature coefficient of resistance (TCR) of a resistor
α_i	*i-th* α intermediate variables used in the initial state estimation of $\mathbf{p}_0$
β_0	intermediate variable used in the initial state estimation of $\mathbf{p}_0$
ε	percentage variation threshold that delimits the NLLS stopping condition
η	Vector representing the Gaussian noise associated to a magnetometer reading
η_x	Gaussian noise associated to a x axis magnetometer reading
η_y	Gaussian noise associated to a y axis magnetometer reading
η_z	Gaussian noise associated to a z axis magnetometer reading
λ	Misalignment angle of the magnetometer sensor model
μ_i	*i-th* μ intermediate variables used in the initial state estimation of $\mathbf{p}_0$
ω	Angular frequency
ϕ	Misalignment angle of the magnetometer sensor model
ρ	Misalignment angle of the magnetometer sensor model
$\sigma_{\mathbf{e}}$	NLLS residual error standard deviation used to compute the NLLS uncertainties
σ_x, σ_y, σ_z	Standard deviation of the Gaussian noise associated with each axis of a magnetic sensor
$\tilde{\xi}$	Intermediate variable used in the initial state estimation solution of $\mathbf{p}_0$
a	x-axis scale factor in the magnetometer sensor model
A_{cm}	Common-mode gain of an OpAmp
A_{d}	Differential gain of an OpAmp
A_o	Finite open-loop gain of an OpAmp
b	y-axis scale factor in the magnetometer sensor model
$\mathbf{b_i}$	*i-th* vector containing the time-varying bias of the magnetometer sensor model
$\mathbf{b}_0$	Chapter 4: Zero-th order (offset) vector of the magnetic field simulator calibration model
$\mathbf{b}_0$	Chapter 5: Bias (offset) vector of the magnetometer sensor model

$\mathbf{B}$	Theoretical programmed magnetic field of the magnetic field simulator HiL setup
$\mathbf{B}_e$ and B_e	Vector or a single value, respectively, of the expected magnetic field magnitude associated to a magnetic sensor measurement(s).
B_x	Chapter 4: Theoretical programmed magnetic field on the x axis of the Helmholtz Coil
B_x	Chapter 5: True orthogonal geomagnetic field in the x axis of the body
B'_x	Intermediate variable used in the initial state estimation of $\mathbf{p}_0$
B_y	Chapter 4: Theoretical programmed magnetic field on the y axis of the Helmholtz Coil
B_y	Chapter 5: True orthogonal geomagnetic field in the y axis of the body
B'_y	Intermediate variable used in the initial state estimation of $\mathbf{p}_0$
B_z	Chapter 4: Theoretical programmed magnetic field on the z axis of the Helmholtz Coil
B_z	Chapter 5: True orthogonal geomagnetic field in the z axis of the body
B'_z	Intermediate variable used in the initial state estimation of $\mathbf{p}_0$
$\hat{\mathbf{B}}$	Fluxgate magnetometer measurements of the magnetic field simulator HiL setup
$\hat{B}_x$	Fluxgate magnetometer measurements on the x axis of the Helmholtz Coil
$\hat{B}_y$	Fluxgate magnetometer measurements on the y axis of the Helmholtz Coil
$\hat{B}_z$	Fluxgate magnetometer measurements on the z axis of the Helmholtz Coil
$\widetilde{\mathbf{B}}$	Magnetometer sensor measurement, mathematically similar to $\widetilde{\mathbf{u}}$
$\widetilde{B}_x$	Magnetometer measurement of the sensor's x-axis sensing element
$\widetilde{B}_y$	Magnetometer measurement of the sensor's y-axis sensing element
$\widetilde{B}_z$	Magnetometer measurement of the sensor's z-axis sensing element
$\widetilde{\mathbf{B}}_\mathbf{0}$	Adjusted (calibrated) magnetic field of the magnetic field simulator HiL setup
$\overline{\mathbf{B}}$	Magnetic field value sent to the HiL simulator setup compensated by the offset
B_{x0}	Zero-th order (offset) parameter on the x axis of the magnetic simulator setup calibration model
B_{y0}	Zero-th order (offset) parameter on the y axis of the magnetic simulator setup calibration model
B_{z0}	Zero-th order (offset) parameter on the z axis of the magnetic simulator setup calibration model
B_{inn}	Magnetic field generated by the three-axial Helmholtz coil's inner pair
B_{mid}	Magnetic field generated by the three-axial Helmholtz coil's middle pair

B_{ext}	Magnetic field generated by the three-axial Helmholtz coil's outer pair
$\left\|\mathbf{B}_{\text{O}}^{\text{total}}\right\|$	Total field intensity generated by a Helmholtz Coil
c	z-axis scale factor in the magnetometer sensor model
$\mathbf{e}$	Residual error representation of the non-linear least squares
$\mathbf{F}$	Fisher information matrix
$\mathbf{H}$	Chapter 4: Batch Linear Least Squares $m \times 9$ matrix with the theoretical values related to the i-*th* order terms
$\mathbf{H}$	Chapters 5/6: Gradient (or Jabocian) matrix of the Non-Linear Least Squares solution
$\mathbf{H}$	Appendix: generic measurement model matrix relating the measured values and the state values vectors in the linear relationship $\mathbf{y} = \mathbf{H}\mathbf{x}$
$\mathbf{H}_{\text{ge}}$, $\mathbf{H}_{\text{ge}'}$	$m \times 6$ and $m \times 7$ matrices used in the batch linear estimation of Gebre-Egziabhe et al.'s algorithm to estimate the initial state of $\mathbf{p}_0$
$\mathbf{H}_{\text{b}}$, $\mathbf{H}_{\text{sf}}$	$m \times 4$ and $m \times 3$ matrices used in the batch liner estimation of the proposed algorithm to calculate the initial state of $\mathbf{p}_0$
i	Electrical current of a Helmholtz Coil winding
i_L	Load's current in the HCS circuit
i_L^i	Load's current in the i-*th* HCS circuit channel
$i_{L\max}$	Maximum output current value of the HCS circuit
i_{inn}	Electrical current of the inner Helmholtz coil pair
i_{mid}	Electrical current of the middle Helmholtz coil pair
i_{ext}	Electrical current of the outer Helmholtz coil pair
$\tilde{I}_i$	Current measurement or signal value of time-varying error source associated to the i-*th* time-varying bias
$I_{\text{b-}}$	Negative input bias current in the non-ideal analysis of the HCS circuit
$I_{\text{b+}}$	Positive input bias current in the non-ideal analysis of the HCS circuit
I_{os}	Input offset current in the non-ideal analysis of the HCS circuit
J	Loss function of the non-linear least squares estimator
$\mathbf{K_1}$	First order 3×3 matrix of the magnetic field simulator calibration model
$\mathbf{K_2}$	Second order 3×3 matrix of the magnetic field simulator calibration model
$\mathbf{K_3}$	Third order 3×3 matrix of the magnetic field simulator calibration model
L	Dimension of the coil side of a square Helmholtz Coil
N	Number of turns in the winding of a Helmholtz Coil
$N_{\text{FGM3D(cycle)}}$	Number of valid measurements taken by the FGM3D sensor during each cycle of the HiL simulation

$N_{\max}$	Maximum number of points that can be generated per second using the magnetic field simulator and the HiL setup
$\mathrm{O_i}$	Intermediate variable in the time-varying sensor model of the i-*th* axis
$\mathbf{p}$	vector containing the magnetometer calibration parameters
$\hat{\mathbf{p}}$	vector containing the estimated magnetometer calibration parameters
$\mathbf{p}_0$	initial state of the calibration parameters
$\hat{\mathbf{p}}_0$	estimated initial state of the calibration parameters
$\mathbf{P}$	Covariance of the estimated states of the non-linear least squares
R	Resistance value
R_{2b}	Sense power resistor of the HCS circuit
R_{adj}	Adjustable resistance value of the FGM3D sensor conditioning circuit
R^i_{adj}	Adjustable resistance value of the i-*th* channel of the HCS
$R^{\mathsf{inn}}_{\mathsf{adj}}$	Adjustable resistance value of the inner channel of the HCS
$R^{\mathsf{mid}}_{\mathsf{adj}}$	Adjustable resistance value of the middle channel of the HCS
$R^{\mathsf{ext}}_{\mathsf{adj}}$	Adjustable resistance value of the outer channel of the HCS
$\mathbf{S}$	Diagonal matrix containing the scale factors parameters in the magnetometer sensor model
$t_{\mathsf{cycle}(\min)}$	Minimum period per cycle to ensure at least one valid measurement of the magnetometer under test
t_{sensor}	Period between measurements of the magnetometer under test
t_{steady}	Steady state period of the magnetic field simulator
$t_{\mathsf{transient}}$	Transient state period of the magnetic field simulator
$\mathbf{T}$	Misalignment matrix of the magnetometer sensor model
$\mathbf{u}$	Earth's magnetic field vector representation in the magnetometer sensor model
$\tilde{\mathbf{u}}$	Sensor measurement vector in the magnetometer sensor model
v^i_{DAC}	Output voltage of the i-*th* DAC channel
v^i_{HCS}	Input voltage of the i-*th* Howland Current Source
$V^{\mathsf{out}}_{\mathsf{FGM3D}}$	Output voltage of the FGM3D fluxgate sensor
v_i	Input voltage of the HCS circuit
v_L	Voltage on the HCS load
v_o	Output voltage of the HCS circuit (voltage on the OpAmp output)
$v_{o\max}$	Maximum output voltage of the HCS circuit (voltage on the OpAmp output)
v_x	OpAmp's non-inverting terminal voltage in the HCS circuit

V_{CMRR}	Common mode rejection ratio equivalent offset voltage in the non-ideal analysis of the HCS circuit
V_{C}	Common mode voltage in the non-ideal analysis of the HCS circuit
V_{D}	Differential voltage in the non-ideal analysis of the HCS circuit
V_{os}	Offset voltage in the non-ideal analysis of the HCS circuit
$V_{\mathsf{OpAmp}}^{\mathsf{out}}$	OpAmp output voltage in the conditioning circuit of the fluxgate sensor
V_{S}	Supply voltage of the HCS circuit and OpAmp
$\hat{\mathbf{X}}$	Matrix with the estimated parameters of the batch linear least squares to calibrate the magnetic field simulator
$\mathbf{x}$	Appendix: generic state vector in the linear relationship $\mathbf{y} = \mathbf{H}\mathbf{x}$
$\mathbf{x}_{\mathrm{ge}}$, $\mathbf{x}_{\mathrm{ge}'}$	Vector with the estimated intermediate variables of the batch linear estimation of Gebre-Egziabhe et al.'s algorithm to estimate the initial state of $\mathbf{p}_0$
$\mathbf{x}_{\mathrm{b}}$, $\mathbf{x}_{\mathrm{sf}}$	Vector with the estimated intermediate variables used in the batch linear estimation of the proposed algorithm to calculate the initial state of $\mathbf{p}_0$
x_0	Offset (bias) element of the magnetometer sensor model in the x axis
x_i	*i-th* time-varying bias parameter of the magnetometer sensor model in the x axis
y_0	Offset (bias) element of the magnetometer sensor model in the y axis
y_i	*i-th* time-varying bias parameter of the magnetometer sensor model in the y axis
$\mathbf{Y}$	Batch least squares $m \times 3$ observation matrix with the non-calibrated fluxgate measurements
$\mathbf{y}$	Appendix: generic measurement vector in the linear relationship $\mathbf{y} = \mathbf{H}\mathbf{x}$
$\mathbf{y}_{\mathrm{ge}}$, $\mathbf{y}_{\mathrm{ge}'}$	$m \times 1$ vectors used in the batch linear estimation of Gebre-Egziabhe et al.'s algorithm to estimate the initial state of $\mathbf{p}_0$
$\mathbf{y}_{\mathrm{b}}$, $\mathbf{y}_{\mathrm{sf}}$	$m \times 1$ vectors used in the batch liner estimation of the proposed algorithm to calculate the initial state of $\mathbf{p}_0$
z_0	Offset (bias) element of the magnetometer sensor model in the z axis
z_i	*i-th* time-varying bias parameter of the magnetometer sensor model in the z axis
Z_L	Load in the Howland Current Source circuit

Contents

1 Introduction

Magnetic sensors are part of a vast number of attitude determination systems. From high-end satellites to low-cost ones or terrestrial applications such as unmanned aerial vehicles, Three-Axis Magnetometers (TAM) are employed in many devices and aerospace missions as part of those systems. Nevertheless, as with most sensors, TAMs are subject to several errors in their measurements, those inherent to the sensor and the ones caused by internal/external disturbances [1, 2]. Therefore, a calibration procedure is essential to guarantee that the device properly operates during its mission.

For obvious reasons, not only do these errors increase in low-cost magnetometers, as they can drift much more during operation [3–5]. Despite that, the use of such low-cost sensors has grown exponentially in space missions over the past few decades, more specifically, due to the increase in small (pico and nano) satellite missions [6]. These satellites are built around a low-cost, small, lightweight, and limited-power budget design. They have, typically, a mass of 0.1 to 1.0 (picosatellites) or 1.0 to 10.0 kg (nanosatellites) and built-in mechanical assemblies varying from 1U to 6U, known as the CubeSats, where 1U represents a standard dimension of 10x10x10 cm.

Most mentioned missions have a limited size, meaning low-cost MEMS magnetic sensors are the only viable option [6–8], and their calibration must be addressed during the mission to minimize errors and to allow for an accurate attitude determination system. Furthermore, if the spacecraft has an active-controlled attitude system, an auto-calibration procedure is essential for optimum results of the ADCS (attitude determination and control system). Several works have addressed theoretical and experimental aspects of magnetic sensor calibration [9], which is one of the subjects in this thesis.

Concerning this topic, this thesis proposes the application of the Non-Linear Least Squares (NLLS) estimator to solve the attitude-independent magnetometer calibration problem based on the well-known sensor model proposed by Foster and Elkaim [2]. Using the NLLS estimator has a few advantages over the Extended Two Step (ETS) solution proposed by Foster and Elkaim, which rewrites the problem using intermediate variables. The thesis contribution section ahead summarizes these advantages. Furthermore, we present a thorough theoretical analysis of the proposed algorithm, simulations, and experimental validation of the solution, which is also compared to the ETS method.

Additionally, due to the nature of small satellites (or UAVs or handheld devices), assembling the TAM isolated from other electronics or employing a boom, for example, is not always feasible. For instance, on high-end missions or satellites, the TAM assembly ensures that any power or electrical current-carrying element will not affect the magnetometer readings. Unfortunately, that is not viable with smaller missions' size, cost, and development time, meaning varying electrical currents (or electronics systems) may induce variable interference

on the magnetic measurements [7, 8, 10–13]. Such interference may cause a time-varying bias error on the sensor measurements, and a calibration procedure with these parameters might be necessary to improve the system's accuracy. Most calibration works consider a time-invariant sensor model [9], such as the ETS solution.

Therefore, we also contribute to the attitude-independent magnetometer calibration with time-varying bias. This thesis depicts how the NLLS algorithm can be expanded to solve the problem and estimate the additional parameters of the time-invariant sensor model plus the time-varying biases. Springmann and Cutler [7] originally proposed the same sensor model in their work, and theoretically, they also use a non-linear least squares estimator to find the parameters. Nevertheless, those authors do not explicitly describe their solution or get into details about it. In this direction, we also show a thorough theoretical analysis of the non-linear least squares method applied in the sensor model with varying bias parameters.

Another issue related to magnetic sensor calibration is how to perform experimental tests to simulate and validate the method with magnetic field values and behavior (interference, for example) similar to that expected during a mission. For instance, rotation tables are unfeasible to test a magnetometer due to their magnetic interference, and developing a manual rotating device is not ideal as it will lack the repeatability of a controlled environment. Besides, in these alternatives, the sensor would be restrained to a constant field value depending on the device's location on Earth. Thus, testing different calibration scenarios is unattainable unless we generate a magnetic field. Consequently, the workaround to assess the magnetometer calibration usually involves using a magnetic field simulator test bench. For example, many aerospace facilities have simulators capable of generating a three-axial magnetic field to test their systems [14–25].

In this direction, the main subject of this thesis is the application of an Earth's magnitude field simulator in the magnetometer calibration study. We present a methodology to use a real-time magnetic field simulator to study existing problems in low-cost magnetometer calibration, such as those found in small satellite missions. We contribute by proposing methods to evaluate the calibration problem, including the time-varying bias interference and conditions identified by a few works related to nanosatellites [7, 8, 11, 13].

The magnetic field simulator, based on a three-axial Helmholtz coil (or Helmholtz cage), was first reported in [26], and an essential part of this thesis is dedicated to improving that simulator's electronics. Therefore, another main topic of study is the contributions regarding the current source of the coil, which is as fundamental as the coil itself in a magnetic field simulator [27]. This work presents a study and experimental results of the design of a power Howland Current Source (HCS) to drive the magnetic field simulator. Despite being widely used in bio-applications [28, 29], there is a lack of results and analysis of the HCS on high-current scenarios, especially an errors analysis and non-linearities in the output current for Direct Current (DC) or low-frequency applications. Therefore, this thesis also reports a new set of analyses and experimental evaluations of a power Howland Current Source.

At last, this thesis proposes and demonstrates a methodology to use the Helmholtz coil to test time-varying bias calibration. Many of Earth's magnetic field simulators described in the literature operate in a closed-loop system configuration to generate a very accurate magnetic field, as the examples in [15, 18, 20, 25]. In such a procedure, a high-end magnetic sensor, with much better specs than the sensor under test, is used as a reference (or ground truth) and compared to the magnetic field setpoint. Hence, the feedback loop

compensates for any error or disturbance caught by the ground truth sensor. However, if the simulator is intended to provide a test bench to evaluate systems susceptible to time-varying interference, the closed-loop system would also compensate for these disturbances (or, at least, partially). That would happen as the volume of the generated magnetic field inside a coil is limited, and the reference sensor and the one under test are relatively close. Hence, it is not viable to analyze time-varying interference using the closed-loop topology to generate the magnetic field.

For this reason, the methodology to use the Helmholtz coil to test time-varying bias calibration requires a magnetic field simulator operating as an open-loop system in terms of the magnetic field readings. Moreover, and more importantly, it is necessary to ensure the accuracy of the generated field to provide a test bench for time-varying interference. Although many works use three-axial coils in an open-loop configuration [14, 17, 21, 24, 25] and mention the need for calibrating the setup [14, 21], only some authors thoroughly address the calibration procedure and show a detailed set of results of their simulators. For instance, such a discussion is seen in [24] and [26]; however, the accuracy reported in these works when operating in an open-loop topology was not satisfactory compared to the requirements set in this thesis of having a sub-milligauss (better than 100 nT) accuracy. Besides, in both works, the authors also focused on the closed-loop solution, which ensured better results. Consequently, we revisit the subject and display in detail the calibration procedure of the magnetic field simulator and an extensive set of results to validate it. Therefore, the calibration and methodology to use the proposed magnetic field simulator to generate an open-loop magnetic field is another topic and contribution of this thesis.

The remainder of this introduction situates the thesis work in the context of the Laboratory of Instrumentation and Embedded Systems research. It also highlights the objectives and contributions of the Doctoral research. Further details on how the thesis improves the current state of the art within each topic is given in their corresponding chapters.

1.1 Research Background, Justification and Objectives

This thesis work is related to a part of the research carried out at the Laboratory of Instrumentation and Embedded Systems within the Electrical Engineering Department of the State University of Londrina. The group has been studying attitude determination using low-cost sensors, magnetometer calibration, and inertial sensor calibration for the last few decades. Part of these works was funded by the Brazilian Space Agency (AEB - *Agência Espacial Brasileira*) through the *Uniespaço* and the *Microgravidade* programs.

One of these projects is an attitude determination system using low-cost sensors, called E-MEMS [30], initially designed to be a payload of a Brazilian microsatellite. However, the E-MEMS concept changed to provide an electronic system that could aid the study of low-cost attitude determination systems in multiple scenarios. That led to a system with the following requirements: I - Provide a stand-alone solution using Magnetic, Angular Rate, and Gravity (MARG) sensors to test and validate embedded attitude determination in a terrestrial environment. II - Allows the testing and calibration of low-cost magnetic and angular rate sensors. III - Have multiple sets of sensors for investigating its impact on attitude determination and deliver redundant data during its missions as a satellite payload. IV - Provide a generic electronic system that could

be used as a payload for other Brazilian vehicles. V - Use multiple sets of sensors arranged in a geometry that allows measuring the vehicle's launch forces without reaching its scale range.

As a result of those research, the laboratory had two relevant results in 2016. First, the E-MEMS participated in the *Rio Verde* operation supported by the *microgravidade* program. It was one of the payloads of the suborbital flight embarked on the German microg-2 microgravity platform, propelled by the Brazilian rocket VSB-30. Second, the laboratory built a Hardware-in-the-Loop (HiL) magnetic field simulator based on a three-axis square Helmholtz coil. The simulator allows for testing magnetic sensor calibration and simulating Earth's magnetic field during dynamic simulations. This second research was funded by the *uniespaço* program.

The system formed by the HiL setup and the Helmholtz coil results were reported in [26]. Those were particularly satisfactory given their relatively low cost and simple design compared to similar ones. Moreover, the design of the Helmholtz coil had a premise of requiring electrical currents smaller than three amperes to achieve the expected maximum magnetic field in each axis. That enabled using a linear symmetric current source based on the Howland Current Source (HCS) [31], built using power operational amplifiers. The Helmholtz coil design with the HCS circuit provided a considerably simple setup without complex electronics, switching elements, or expensive commercial current supplies to power the coil. Also, achieving a simulator with a fast transient state was possible, which is mandatory if a coil is designed to perform dynamic simulations in real time.

Despite those positive results, there were a few limitations in that setup and a superficial analysis regarding its applications, such as the ones related to magnetic sensor calibration. Therefore, this thesis is a direct continuation of [26], aiming to improve the magnetic field simulator results and its elements to allow for a new set of applications using the system. Furthermore, these results seek to aid the development of attitude determination and control systems and small satellite missions.

As introduced before, one of the subjects desired with the simulator use is the calibration analysis of low-cost magnetometers susceptible to time-varying interference. Although a few authors investigated the matter [7, 8, 10–13], they did not present or discuss a methodology to evaluate the interference in a controlled environment. Instead, most identified them and directly applied the algorithms to their in-orbit flight data of nanosatellites or performed tests for a specific mission. This thesis aims for a more general approach and proposes a testing methodology for this calibration using the Helmholtz coil and a HiL setup. Thus, future works can reproduce the methodology to understand the impact of such errors in their satellites, for example.

To use the magnetic field simulator for this purpose, it must generate a magnetic field in an open-loop topology without a feedback compensation loop or controller. Otherwise, since typical Helmholtz coils have a limited volume of generated field uniformity, the magnetic sensor used as the ground truth reference would measure the time-varying bias caused by the electronics, and the controller loop would compensate for the time-varying interference. Therefore, it is crucial to calibrate the simulator to generate a magnetic field as accurately as possible without a closed-loop compensated topology.

Although [26] addresses the open-loop operation of the magnetic field simulator, the results reported in that setup had significant errors when generating an open-loop non-compensated magnetic field. Thus, performing any test or evaluating a magnetometer calibration was impractical in that topology, and the setup

was limited to a closed-loop operation. Therefore, this thesis seeks to improve that setup to achieve both open- and closed-loop operation with a minimum accuracy of one milligauss (< 100 nT), with half this value as the desired one. A significant problem to reach is the current source that drives the Helmholtz coil. As identified in this thesis, the power HCS circuit is susceptible to non-linearities, which can impact the accuracy of the power HCS output current. Therefore, another main topic in this thesis is the study and improvements of the power Howland Current Source circuit and its experimental implementation.

The following subsection summarizes the objectives of the work, which led to the contributions shown in the subsequent section.

1.1.1 Research Objectives

The main objective of this thesis is to improve an existing magnetic field simulator to provide a test bench for low-cost magnetometers. The new setup has to operate by generating magnetic fields in an open-loop non-compensated topology with sufficient accuracy to evaluate those sensors. Another main goal is to develop a Hardware-in-the-Loop (HiL) platform, using the magnetic simulator, to provide a test bench facility to study the magnetometer calibration including the time-varying biases errors.

To reach these objectives, the specific ones are defined:

- Improve the linear voltage-controlled current source (VCCS) based on the Howland Current Source to power the three-axial Helmholtz coil.
- Characterize in detail and evaluates the power HCS sources of errors, including non-linear ones.
- Define and evaluate a calibration procedure for the magnetic field simulator operation generating a non-compensated magnetic field.
- Implement and comprehensively study the non-linear least squares on the attitude-independent magnetometer calibration problem, and expand that solution to include the time-varying bias.
- Demonstrate the use of the simulator to assess the magnetometer calibration problem, including the time-varying interference.

1.2 Summary of the Proposed Contributions and Generated Publications

The proposed contributions of this dissertation are described below. Each chapter has further discussion on their respective contributions. Besides, it is also summarized the scientific publications directly related to the Doctoral work.

1.2.1 Contributions of this Doctoral Work

1. **Magnetic Field simulator for real-time Hardware-in-the-Loop simulation**: this thesis improves the magnetic field simulator reported in [26] to meet the requirements described in the general objectives.

The final setup can operate with a sub-milligauss (<100 nT) accuracy, generating an open-loop or closed-loop magnetic field. Besides, the simulator's plant has a transient period shorter than 10 ms, allowing real-time simulations generating multiple points of magnetic field per second. For instance, when testing a sensor with an output data rate of 40 Hz, assuming the worst-case scenario, the HiL simulation can generate up to 16.66 distinct magnetic field values per second and perform one magnetometer measurement per point. In theory, in the best-case scenario and using a sensor with an output rate higher than 100 Hz, we could generate 33.33 distinct points in a second.

2. **Open-loop magnetic field generation on Helmholtz coil**: the setup has to generate an open-loop magnetic field to comply with the principal objective. To achieve the required sub-milligauss accuracy, we discuss the setup errors, its calibration methodology, and the procedure for the experimental calibration of the system. This thesis provides results to evaluate the capabilities and accuracy of the system during open- and closed-loop operation.

3. **Application of the power Howland Current Source to generate magnetic field**: most magnetic field simulators either do not discuss the current source or use switching inverting topologies or commercially available sources. This thesis, through the publication in Appendix C [32], contributes with a design methodology of a linear, OpAmp-based, voltage-controlled current source to power our tri-axial Helmholtz coil.

4. **Analysis of the Howland Current Source using power amplifiers**: this thesis contributes to the power HCS study by providing a detailed examination of the circuit's source of errors, including non-linear ones. We also discuss the practical constraints and the available components to build a ± 2 A and ± 30 V HCS and elaborate an error budget simulation to evaluate our theoretical error analysis based on power OpAmps specs. By employing strategies to minimize the non-linear errors of the circuit, the final design yielded an accuracy superior to 0.1 % after a first-order calibration.

5. **Attitude-independent magnetometer calibration using the Non-Linear Least Squares**: one of this thesis' novelty is to present the direct application of a non-linear least squares (NLLS) estimator [33] to the well-known sensor model proposed by Foster and Elkaim [2]. Based on the loss function of the NLLS, it is possible to apply the generalization of Newton's root-solving method using the linearized sensor model to find the calibration parameters. Hence, the problem does not need to be rewritten using intermediate variables required by the Extended Two Step (ETS) algorithm of Foster and Elkaim. Furthermore, compared to the ETS solution, the NLLS estimator allows to compute the parameters uncertainties, is suitable for the on-orbit magnetometer calibration since it does not have the constraint that the magnetic field magnitude is constant for all measurements, and it is easy to expand to include other parameters, such as the time-varying bias, is straightforward.

6. **Methodology to evaluate the magnetic sensor calibration subject to time-varying interference**: the thesis reports a methodology to assess the magnetometer calibration, including time-varying bias, using the magnetic field simulator. Our contribution is to propose an experimental Hardware-in-the-Loop (HiL) setup capable of testing, simulating, and evaluating the effect of time-varying sources of magnetic disturbances in a magnetometer's surroundings. Hence, it is possible to simulate the effect of

electrical currents (or electronic circuit interference) and the magnetic field in a controlled environment, reproducing the characteristics of an actual application. Furthermore, the proposed HiL setup can generate and simulate electrical currents while generating the magnetic field. We also thoroughly discuss the NLLS algorithm expanded to solve the sensor model with time-varying biases.

1.2.2 Publications Directly Associated to the Doctoral Work

1. D. S. Batista, F. Granziera Jr., M. C. Tosin, L. F. de Melo. **Three-Axial Helmholtz Coil Design and Validation for Aerospace Applications**. Full paper published in the *IEEE Transactions on Aerospace and Electronic Systems (TAES)* journal, published in February 2018. DOI: 10.1109/TAES.2017.2760560. Copy of the first two pages of the published article [25] presented in Appendix B.

2. D. S. Batista, G. B. da Silva, F. Granziera Jr., M. C. Tosin, D. L. Gazzoni Filho, L. F. de Melo. **Howland Current Source Applied to Magnetic Field Generation in a Tri-Axial Helmholtz Coil**. Full paper published in the *IEEE Access* journal, in September 2019. DOI: 10.1109/ACCESS.2019.2939117. Copy of the published article [32] presented in Appendix C.

3. D. S. Batista, F. Granziera Jr., M. C. Tosin, L. F. de Melo. **Analysis and Practical implementation of a high-power Howland Current Source.** Full paper published in the *Measurement* journal of the International Measurement Confederation, in December 2022. DOI: `10.1016/j.measurement.2022.112404`. Copy of the first two pages of the published article [34] in Appendix D.

4. D. S. Batista, F. Granziera Jr., M. C. Tosin, L. F. de Melo. **Attitude-Independent Magnetometer Calibration using Non-Linear Least Square**. *IEEE Sensors* journal. In Press - Article accepted May 2023. DOI: `10.1109/JSEN.2023.3274495`. Copy of the first two pages of the accepted article [35] presented in Appendix E.

1.3 Text Organization

The remainder of this thesis qualification text is organized as follows.

In Chapter 2, we present the magnetic field simulator setup, which combines a Hardware-in-the-loop simulation and a Three-Axial Helmholtz Coil. The simulator is a direct improvement of [26], and that chapter covers in detail all elements of the system and the description of the auxiliary electronics. The chapter ends by showing test results to validate the simulator and its compliance with the required characteristic. It is worth noting that the contributions related to the design and validation of the Three-Axial Helmholtz coil are seen in [25] and are not replicated in that chapter. Appendix B shows the first pages of the published article.

Chapter 3 shows the contributions associated with the power Howland Current Source (HCS) study. It describes in detail the higher power HCS circuit analysis, its errors and non-linear problems, and the experimental implementation of that circuit for high current situations. This description includes the theoretical analysis and constraints of the HCS, its errors and non-ideal study of the circuit, explains the power HCS requirements, and the available commercial components. Upon this last, that chapter shows an error budget

simulation of the power HCS circuit and evaluates their practical results for several conditions. Chapter 3 results are also partially reported in [34], whose first two pages are seen in Appendix D. At last, contributions to the HCS design to match a magnetic field simulator are seen in the publication in Appendix C and are not replicated in this thesis.

Chapter 4 brings the methodology to generate the calibrated magnetic field using the HiL simulation. It explains the differences between the open- and closed-loop magnetic field generation and the practical calibration procedure to operate the simulator in the former condition. The setup errors, its calibration model, and the parameter estimation are also shown. The chapter includes a set of testing to verify that the setup complies with the accuracy required to provide an adequate test bench to study and assess the calibration of low-cost magnetometers. Results include a thorough validation of the simulator's calibration repeatability and accuracy. At last, we outline the operation of the simulator generating a closed-loop magnetic field, using the closed-loop PID controller proposed in [25], but to the improved simulator.

Chapter 5 discusses the attitude-independent magnetometer calibration problem without the time-varying bias. The first part of that chapter introduces the problem, revisits the state-of-the-art solutions, discusses the magnetometer errors, and situates the NLLS algorithm within the existing literature. Then, it describes the theoretical NLLS solution and reports a large set of simulations to evaluate the algorithm estimation and convergence. It also compares the NLLS algorithm to the analytical solution of the ETS algorithm computed by [36]. At last, the chapter reports the experimental calibration analysis using the magnetic field simulator.

Finally, Chapter 6 exhibits the magnetometer calibration problem, including the time-varying bias, and the methodology to use the magnetic field simulator as a test bench and controlled environment to evaluate the problem experimentally. Initially, that chapter depicts the sensor model and the NLLS solution considering the time-varying bias, followed by the algorithm validation through simulation. Then, it describes the proposed HiL setup and the methodology to employ the magnetic field simulator in the experimental calibration of magnetometers subject to time-varying interference. At last, it shows the experimental results of the time-varying bias calibration using the simulator.

Ultimately, Chapter 7 has final considerations and suggestions for future works.

2 The Magnetic Field Simulator Setup

This chapter presents the magnetic field simulator used in this work, which combines a Hardware-in-the-Loop (HiL) simulation with a three-axial Helmholtz Coil (or Helmholtz Cage) and a Howland Current Source. The setup is an improvement of the one reported in [26], and the Helmholtz coil design and validation are seen in [25]. Appendix B shows the latter, which includes a thorough discussion of the design, requirements, deductions, images, and further details to reproduce the three-axial Helmholtz Coil and the HiL simulation that controls the system. These details are not reproduced here. The Helmholtz coil was designed for real-time HiL simulation of magnetic fields for low-cost magnetometer aerospace applications in a closed-loop topology.

Although the authors in [26] tested the open-loop (non-compensated) use of the simulator, the results had poor accuracy, and they would not be suitable for evaluating the calibration of magnetic sensors. Thus, previous use of the simulator to calibrate or test a sensor was limited to the closed-loop topology, using a high-end commercial fluxgate magnetometer as the ground truth, providing the feedback information for the control loop. This topology requires that the reference sensor and the low-cost sensors under test are placed near each other, and the former compensates for interference caused by the system (sensors) under test. Evaluating magnetometer calibration subject to time-varying interference requires that the setup operates without the closed-loop topology.

The improved simulator can generate compensated (closed-loop) or non-compensated (open-loop) magnetic fields. The former topology allows for the comparison of sensors or evaluation of the calibration depending on the sensor data distribution. The latter allows for a realistic scenario to evaluate a System or Sensor Under Test (SUT) calibration. Time-varying interference caused by the SUT will not be compensated by the reference sensor, allowing for investigating the calibration of systems susceptible to this interference (such as the time-varying bias due to electrical currents and electronics around a magnetometer).

At last, the simulator uses a Hardware-in-the-Loop simulation technique. There are many advantages to using a HiL solution, such as using model-based designs, thus facilitating simulating and testing dynamic systems and models [37,38]. Furthermore, a commercial HiL solution guarantees real-time execution, providing a simple solution to monitor the simulation and enabling real-time parameter changes within the HiL processor.

The remainder of the chapter shows the magnetic field simulator, improved from [26], and discusses its elements in Sections 2.1 to 2.5. Note that the contributions and results related to the power Howland Current Source (the voltage-controlled current source of the simulator) are reported separately in Chapter 3. At last, Section 2.6 assesses the practical validation results of the magnetic field simulator, including its transient response time, maximum magnetic field update rate, the ground truth measurements noise, and the system resolution.

2.1 Overview of the Simulator Setup

The HiL magnetic field simulator setup is based on a dSPACE modular hardware using a DS1006 processor board. The dSPACE solution runs a model-based design developed in Matlab/Simulink using the real-time dSPACE RTI library. The DS1006 real-time embedded execution is monitored using the dedicated software *ControlDesk*. Figure 2.1 shows the simplified block diagram of the setup, which has the following:

1. The three-axial Helmholtz coil [25];
2. The coil's current source solution, a linear Voltage-Controlled Current Source (VCCS) and its interface to the dSPACE Digital-to-Analog Converter (DAC);
3. A fluxgate magnetic sensor that calibrates the system and its auxiliary electronics to interface with the dSPACE Analog-to-Digital Converter (ADC);
4. The main power supply;
5. Any System or Sensor Under Test (SUT), which could be an embedded system with low-cost magnetometers or a commercial AHRS, for example.

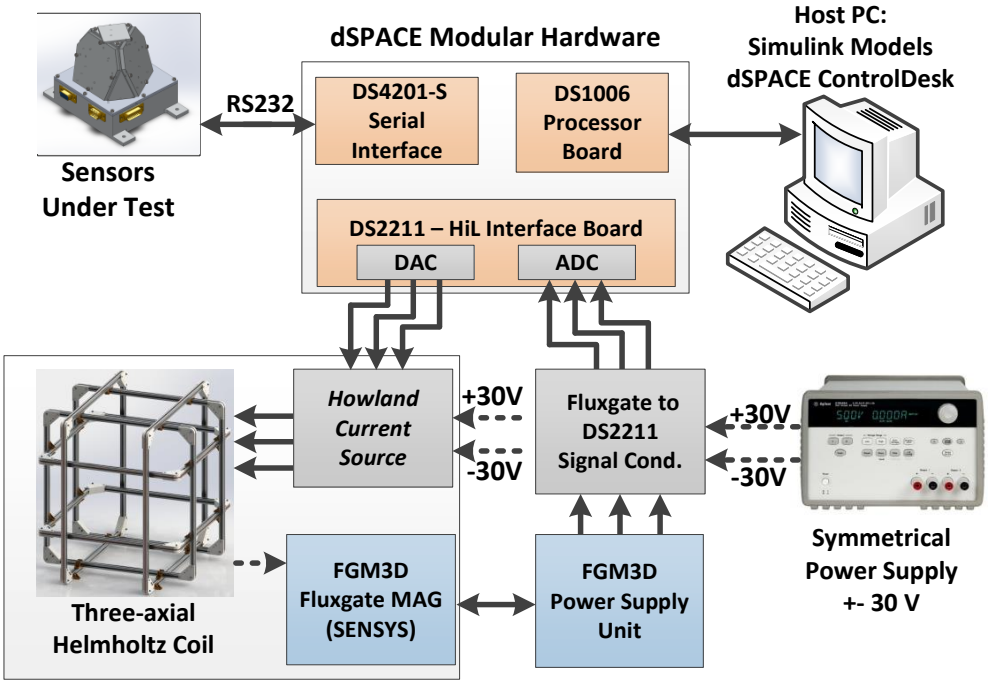

Figure 2.1: Hardware-in-the-loop setup to test magnetic sensors using the three-axial Helmholtz coil and the Howland Current Source.

The dSPACE *ControlDesk* software monitors the HiL simulation variable and controls its parameters. A serial board (DS4201-S) provides the interface to any SUT (magnetic sensor under test) using an RS-232 interface. A HiL DS2211 interface board is responsible for the analog connections. An ADC from that board acquires the measurements of the high-end magnetic fluxgate sensor, and an electronic circuit shapes the sensor's outputs range to one compatible with the DS2211 ADC. At last, the VCCS (three independent channels) drives each Helmholtz coil's pair. The DS2211 DAC controls the input voltage of the VCCS and, consequently, the current flowing in each pair and the generated magnetic field.

The high-end fluxgate magnetometer is an FGM3D from Sensys [39]. The open-loop produced magnetic field is calibrated using the fluxgate readings and the procedure described in Section 4.2. Furthermore, when generating a compensated magnetic field, the HiL setup uses the sensor measurements as feedback to the closed-loop PID discrete controller reported in [25]. In other words, the FGM3D sensor operates as the ground truth of the system.

At last, each VCCS channel is a power Howland Current Source (HCS) circuit, and matching the design of the VCCS to the Helmholtz coil is essential to a magnetic field simulator. This study resulted in the contributions reported [32] and seen in Appendix C. The HCS allows a solution using power operational amplifiers, providing bandwidth and not compromising the setup capability of running real-time simulations. However, the HCS power circuit is susceptible to non-linearities identified in [32], and as the magnetic field is directly proportional to the current, ensuring linearity and accuracy of the HCS is essential to generate a non-compensated open-loop magnetic field. The practical study of the HCS circuit, its errors, and its practical power topology constraints are reported in Chapter 3. The current chapter focuses solely on its design matching the setup's Helmholtz coil.

2.2 The Three-Axial Helmholtz Coil

A square three-axial Helmholtz coil is one of the easiest simulators that can be built among many topologies [40]. In short, a square Helmholtz coil has an ideal ratio (per axis) relating the axis length and the distance between both coils, which maximizes the generated magnetic field uniformity [22]. Assuming that the coil's assembly complies with that proportion and by following Biot-Savart law, the field generated by each pair of such a coil will follow (2.1). Reference [25] provides the full deduction and demonstrates (2.1).

$$\left|\mathbf{B}_{\mathrm{O}}^{\mathsf{total}}\right| = 1.62873 \cdot 10^{-6} \frac{Ni}{L}, \tag{2.1}$$

where the total field intensity, given in Tesla, is directly proportional to the number of turns N, to the current i and inversely proportional to the length L of the coil side.

Defining the coil's size, the number of turns, and the wire gauge depend on the application requirements. Moreover, these parameters are interdependent with the system characteristics, such as the magnetic field uniformity volume, the electrical current value to a necessary maximum field magnitude, the coil's inductance (which dictates the transient time response of the system and, consequently, the maximum simulation frequency), and others. Thus, the project has to address all these constraints with caution. Once again, [25] provides a detailed insight into that matter.

The proposed system goal is to provide a test bench for low-cost magnetic sensors for small satellites and UAVs. It has a 1-meter length on the outer pair and can generate up to 1.5 gauss (or 150 μT) per axis. Figure 2.2 shows the CAD design [41] and the assembled coil [25]. It maintains a theoretical uniformity of 0.02% into an 11×11×11 cm^3 volume around the coil's center. Each pair requires less than 1.5 A to generate that field, avoiding higher current systems to circumvent a complex symmetric switching current source. At last, inductance affects the response time, which must be kept as low as possible to allow a higher simulation spectrum.

The validation and comparison between the theoretical design and built prototype are seen in [25, 26]. Both works also address the uniformity of the coil. Table 2.1 summarizes the electrical parameters of the final assembly and shows the capabilities of each pair calculated using (2.1). At last, we have to define the maximum current (and consequently the voltage) to generate the expected maximum magnetic field value. These constraints are necessary to establish the boundary conditions of the current source, regardless of its topology. Combining the impedance values of the prototype and the desired maximum current value, an electrical current source of ± 2 A with an output voltage range of ± 27 V meets the requirements for all pairs. The following subsection explains how to define a maximum current to a desired magnetic field.

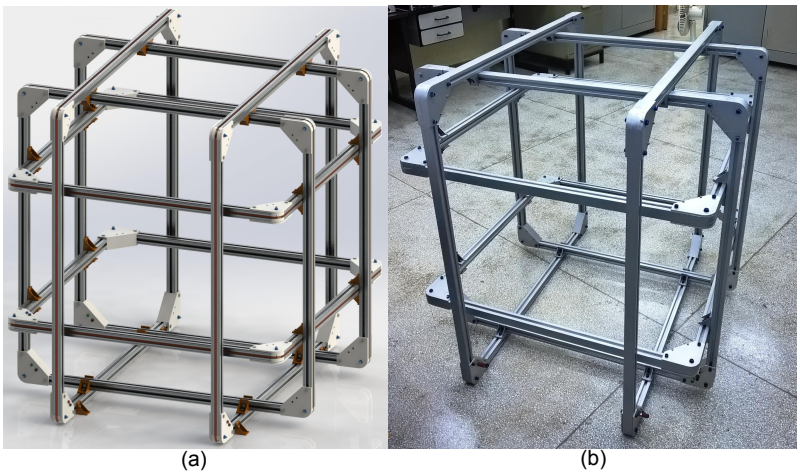

Figure 2.2: Three-axial Helmholtz CAD coil project (a) and final assembly (b). See [25] for further details of the design.

Table 2.1: Electrical parameters of the Helmholtz coil, maximum DC current and generated magnetic field, magnetic field generated per ampere, the measured resistance of each pair to a series connection, necessary voltage per gauss, and approximate inductance.

Coil Pair	*N* (Turns)	*L* (m)	Max. DC Current (A)	Max Field (gauss)	Field per Current (gauss/A)	Series Resistance (Ω)	Coil's voltage per gauss (V_{coil}/gauss)	Approx. Inductance (mH)
Inner (interior)	63	0.88	1.76	2.05	1.116	12.42	13.86	8-18
Middle (central)	72	0.94	1.76	2.15	1.247	14.38	17.94	8-28
External (outer)	73	1.00	1.76	2.09	1.189	15.36	18.26	9-33

2.2.1 The Magnetic Field and Electrical Current Values Requirements per Axis

Although the design allows generating ± 2.0 gauss per axis, this value goes beyond the need of our simulation spectrum and would cause a detriment in the system's resolution. Thus, the final electronic must be tuned to generate a magnetic field in each axis capable of generating the maximum desired field intensity while canceling Earth's magnetic field within the coil (generating a value in the opposite direction in each axis).

The necessary intensity is determined by the sum of the maximum possible value of Earth's magnetic field and the geomagnetic field value where the coil is installed. The first can go up to 0.65 gauss ($65\ \mu$T) depending on the geographic position. The latter is approximately 0.23 gauss ($23\ \mu$T) in Londrina-PR, where the setup

is located. All this information refers to the latest version of the World Magnetic Model [42]. Therefore, each axis must generate at least 0.90 gauss (90 μT) to ensure that the setup can cancel the existing geomagnetic field and simulate the value observed by an object independent of its geographic location and attitude.

Each axis electronics were tuned to generate approximately ± 1 gauss (100 μT), providing a 0.10 gauss tolerance. Using (2.1) and the parameters seen in Table 2.1, it is possible to calculate the generated magnetic field as a function of the electrical current. Equations (2.2)-(2.4) shows this relationship to the inner, middle, and outer pair, respectively, and in gauss.

$$B_{\text{inn}} = 0.0162873 \cdot \frac{63}{0.88} i_{\text{inn}} = 1.166 \cdot i_{\text{inn}} \quad \text{[gauss]} \quad (2.2)$$

$$B_{\text{mid}} = 0.0162873 \cdot \frac{72}{0.94} i_{\text{mid}} = 1.247 \cdot i_{\text{mid}} \quad \text{[gauss]} \quad (2.3)$$

$$B_{\text{ext}} = 0.0162873 \cdot \frac{73}{1.00} i_{\text{ext}} = 1.189 \cdot i_{\text{ext}} \quad \text{[gauss]} \quad (2.4)$$

From (2.2)-(2.4) we can infer that an electrical current of almost ± 1 A is necessary in each pair to generate the desired magnetic field in any direction. The Helmholtz coil design [41] aimed at currents in such ranges, in order to avoid higher current systems requiring, for example, switching topologies. The VCCS design discussed in the next section is tuned to achieve the ± 1 gauss range.

2.3 The Howland Current Source Design

Some contributions of this thesis require the magnetic field simulator to operate while generating an open-loop magnetic field. Therefore, eventual errors caused by the current source are not compensated by a typical closed-loop magnetic field. Hence, it is essential to have a current source as stable and linear as possible. The Howland Current Source (HCS) is a symmetric linear source built using operational amplifiers (OpAmp) and can be controlled by a digital-to-analog converter. However, the power HCS circuit has considerable non-linearities associated with the power OpAmp and the power resistor of the topology (the sensing element of the HCS feedback circuit) [32]. Both are a consequence of thermal drifting in the components, and the circuit design must address these effects to achieve the best performance.

The HCS used in [26] and [25] had typical wire-wound power resistors and the LM675 power OpAmp. That design yielded approximately 0.5% of non-linearities across the ± 1.00 A current range, which was compensated by the closed-loop magnetic field topology [32]. However, that non-linearity translates to a considerable error in the magnetic field generated by an open-loop application. Hence, the HCS had improvements to achieve linearity compatible with the open-loop generation of the magnetic field.

Those studies are reported in Chapter 3. The result of that investigation is a final HCS design that uses an OPA544 power OpAmp and can drive the required electrical current of ± 1.00 A while maintaining a maximum non-linear distortion of around 0.06%. Figure 2.3 shows the schematic of a single channel of the HCS design. The current source has two stages, the first is a conditioning circuit, and the second is the HCS itself. The initial stage uses a precision OPA4227 (or similar) OpAmp to adjust the DAC voltage range (v^i_{DAC}) to the input range necessary for the HCS (v^i_{HCS}). The HCS stage uses the OPA544 power OpAmp to

generate symmetric current value controlled by the v^i_{HCS} voltage.

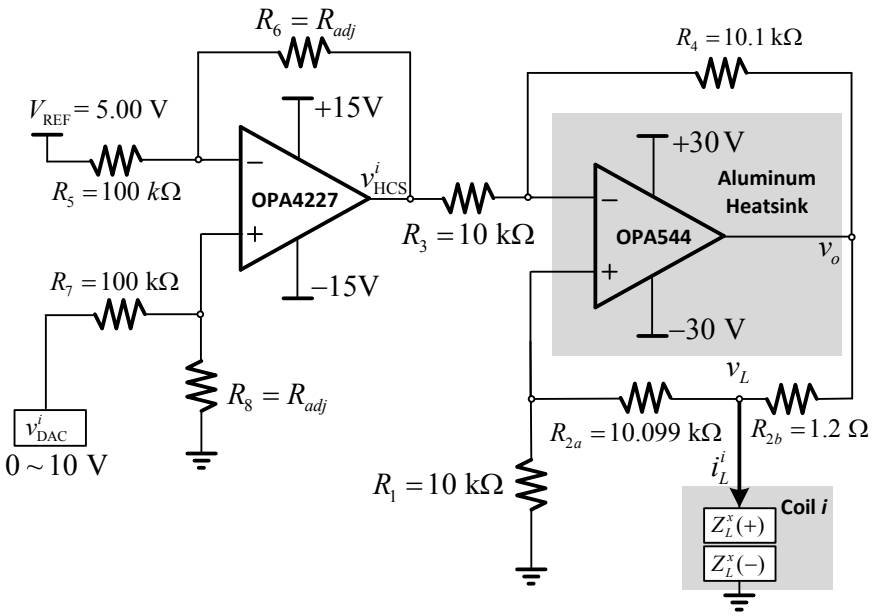

Figure 2.3: Schematic of a single channel of the HCS circuit. R_6 and R_8 values are defined so that the DAC generates ± 1 A of output current.

2.3.1 Defining the HCS Gain and Resistors

The HCS theoretical study and deduction of the ideal output current are found in [28, 32]. In essence, the HCS stage output current is independent of the load (that is, the circuit behaves as a VCCS) if the following relationship is maintained:

$$R_4 R_1 = R_3(R_{2a} + R_{2b}). \tag{2.5}$$

Accounting that (2.5) is satisfied, the output current of the HCS as a function of its input voltage, i.e. the transconductance gain, is given by:

$$i^i_L = -\frac{R_4}{R_3 R_{2b}} v^i_{\mathrm{HCS}}, \tag{2.6}$$

where the superscript i represents the *i-th* coil's pair, given by the inner (inn), middle (mid), or outer (out) pair.

Defining the best compromise values of these resistors is essential to secure the best open-loop results. The OPA544 OpAmp is stable for unitary voltage gain. This value ensures a compromise to reduce the non-linear errors of the power HCS caused by the power OpAmp, and Chapter 3 results assess that. The resistors R_1, R_3, R_{2a} and R_4 in Fig. 2.3 have values in the kilo-ohms range and are selected to generate a voltage gain of 1.01 in the HCS stage circuit. They are subjected to currents in the order of milli-ampere, and heating is not an issue. On the other hand, R_{2b} is around one ohm and has almost the same current i_L as the load, which makes heating expected in this component. Thus, the R_{2b} choice is vital to minimize the HCS errors and is a compromise between a few aspects.

This component must be a power resistor, which can dissipate the heat to the ambient, keeping its temperature within the operating limits. The dissipated power over this resistor may cause significant tem-

perature variations, which will cause proportional resistance variation accordingly to the resistor's temperature coefficient of resistance (TCR). The HCS stability due to R_{2b} temperature is addressed in [32]. Quality commercial power resistors will have their thermal parameters, such as their heat resistance to the air and TCR, characterized within their operating temperature range and made available by their manufacturer. Therefore, this component should have the slightest variation of its resistance possible within the operating temperature range. Additionally, the temperature of this component should be as stable as possible within the operating range of current applied by the HCS's OpAmp.

A higher R_{2b} value reduces the influence of the OpAmp errors (offset voltage, current bias, CMRR, and mismatch effects) in the output current (see [34] or Chapter 3 discussion). Meanwhile, it will increase the resistor heating and may cause the resistance variation discussed in the last paragraph, which affects the output current accuracy. Furthermore, the output current is limited simultaneously by the OpAmp maximum output voltage swing and by the voltage drop in R_{2b}. This discussion is also in [32], and maintaining a lower value resistor allows a larger simulation spectrum. One must note that the load (the coil winding) is inductive, and the impedance rises for higher frequency currents; thus, the resistor choice must consider that. Values around 1 and 1.5 ohm had the best compromise between avoiding excessive resistor heating and reducing the OpAmp non-linear errors.

The final electronics uses a $1.2\ \Omega$/50 W chassis mount resistor. The higher mass and the dissipation frame mounted over the resistor dissipate heat fast, producing a minor temperature variation than lower power-rated resistors. Hence, oversizing the resistor's power rate minimizes any variation due to heating. Typical (50-100 TCR) chassis mount resistors of 50 W, with a TCR of 50 ppm/°C, are relatively easy to obtain and at a moderate cost. Resistors with better TCR specifications, such as foil ones or even higher power ratings, are other possibilities but at a much higher price.

Finally, considering all the resistors values, (2.6) can be rewritten as:

$$i_L^i = -\frac{10.1}{10 \cdot 1.2} v_{\text{HCS}}^i = -0.841666 v_{\text{HCS}}^i, \tag{2.7}$$

which dictates the output current i_L^i as a function of the input voltage of the HCS stage v_{HCS}^i.

2.3.2 Design of the HCS Conditioning Stage

The conditioning stage must be tuned so that the DAC voltage (v_{DAC}^i) range generates the desired magnetic field range of 1 gauss discussed previously. Substituting (2.7) into (2.2)-(2.4), we can find the generated magnetic field, in gauss, given the HCS input voltage v_{HCS}^i. Equations (2.8)-(2.10) shows this relation to each axis.

$$B_{\text{inn}} = 1.166 \cdot i_{\text{inn}} = 0.9814 \cdot v_{\text{HCS}}^{\text{inn}} \tag{2.8}$$

$$B_{\text{mid}} = 1.247 \cdot i_{\text{mid}} = 1.0495 \cdot v_{\text{HCS}}^{\text{mid}} \tag{2.9}$$

$$B_{\text{ext}} = 1.189 \cdot i_{\text{ext}} = 1.0007 \cdot v_{\text{HCS}}^{\text{ext}} \tag{2.10}$$

Using (2.8)-(2.10), we can calculate the v^i_{HCS} voltage range in each axis to generate the ± 1 gauss range. The conversion is straightforward, and the v^i_{HCS} voltage range is approximately ± 1.02 V, ± 0.96 V, and ± 1.00 V to the inner, middle, and outer pair, respectively.

The dSPACE DS2211 DACs have a 0-10 asymmetric voltage excursion. Therefore, the conditioning stages must convert them to the symmetric values above. The OpAmp-based subtractor of Fig. 2.3 is responsible for such. A REF5050 integrated circuit provides the 5.00 voltage reference on the inverting input. Equating the OPA4227 stage of that circuit and assuming that $R_5 = R_7$ and $R_6 = R_8$, we have that:

$$v^i_{\mathrm{HCS}} = \frac{R_6}{R_5} \cdot \left(v^i_{\mathrm{DAC}} - 5.00 \right) = \frac{R^i_{\mathsf{adj}}}{100 \cdot 10^3} \cdot \left(v^i_{\mathrm{DAC}} - 5.00 \right) \tag{2.11}$$

Using (2.11), we can define the value of R^i_{adj} by replacing the v^i_{HCS} and v^i_{DAC} for either voltage extremities values. Equations (2.12)-(2.14) show the final value to each HCS channel. The practical resistor is obtained by using a precision 22 kΩ resistor in parallel with a precision higher one to achieve a value as close as possible to (2.12)-(2.14).

$$R^{\mathsf{inn}}_{\mathsf{adj}} = 100 \cdot 10^3 \cdot \frac{1.02}{5} = 20.4 \text{ k}\Omega \tag{2.12}$$

$$R^{\mathsf{mid}}_{\mathsf{adj}} = 100 \cdot 10^3 \cdot \frac{0.96}{5} = 19.2 \text{ k}\Omega \tag{2.13}$$

$$R^{\mathsf{ext}}_{\mathsf{adj}} = 100 \cdot 10^3 \cdot \frac{1.00}{5} = 20.0 \text{ k}\Omega \tag{2.14}$$

2.3.3 The built HCS Electronics

Figure 2.4 shows the HCS design PCB. Each OPA544 power OpAmp is screwed directly into the aluminum heatsink, and the HCS stage resistors are located below the chassis mount resistor of each pair (R_{2b}). Each of the conditioning stages uses one channel of the OPA4227 OpAmp, which is a quad-channel precision operational amplifier. A single REF5050 integrated circuit (IC) from Texas Instruments regulates the 5.00 V reference voltage to all HCS channels. Two Agilent E3634A precision power supplies provide the ± 30 V input DC voltage, and typical LM317 and LM337 LDO regulators handle the ± 15 V DC voltage that supplies the OPA4227 and the REF5050 ICs. The circuit prototype has two cooling fans to aid in the power dissipation of all OPA544 to minimize non-linear effects due to thermal heating on those components.

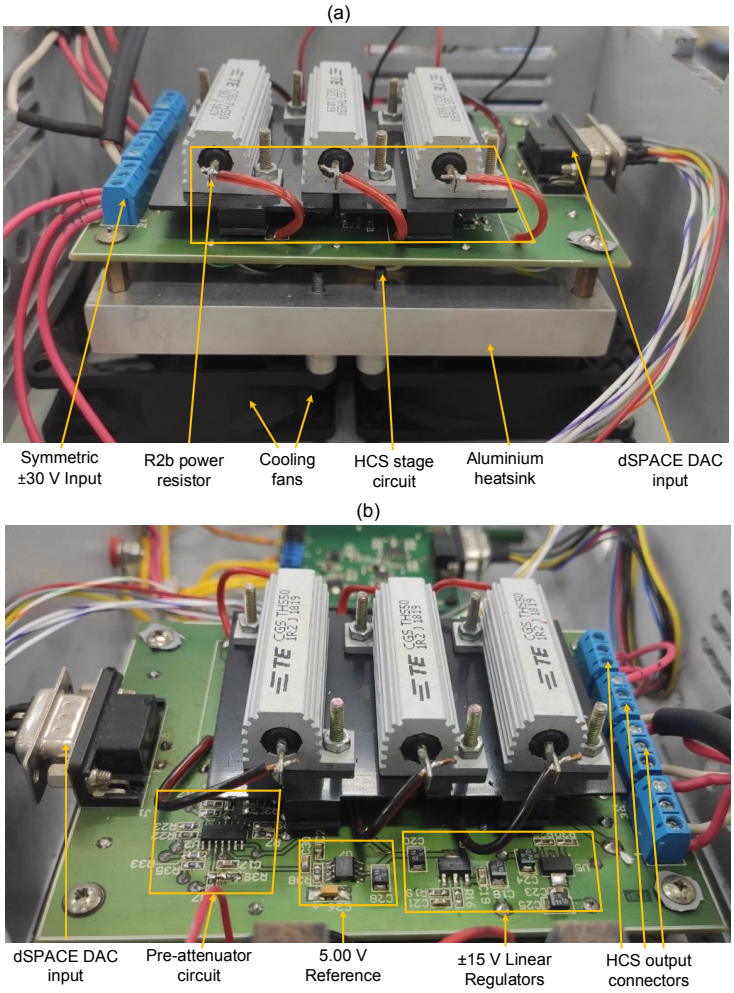

Figure 2.4: Built electronic design of the HCS (three independent channels of the schematic in Fig. 2.3).

2.4 The Fluxgate Sensor and its Acquisition Circuit

The magnetic field simulator has a high-end FGM3D/250 analog fluxgate magnetometer [39] as the reference, or ground truth, sensor. The simulator accuracy and resolution depend on the sensor specifications and its acquisition system, whether operating in an open- or closed-loop topology. The FGM3D's measurements provide the feedback data to the controller loop when generating a closed-loop magnetic field [25] and are used to calibrate the setup when operating in the proposed open-loop topology. The latter is described in Chapter 4.

The FGM3D/250 sensor's main characteristics are full magnetic field scale range of ± 250 μT (± 2.5 gauss); output voltage scale of ± 10 V; a sensitivity of 0.04 V/μT; a minimum guarantee resolution of 150 pT, or 1.5 μG; 2 kHz bandwidth with a noise of 15 pTrms/$\sqrt{\text{Hz}}$ for 0.1 to 10 Hz; and it is powered by a ± 15 V symmetric voltage. In addition, an FGM3D Power Supply Unit accompanies the sensor, which provides the symmetric voltage to power the fluxgate sensor with a simple commercial 12 V DC power supply. Furthermore, this unit has an independent Bayonet Neill Concelman (BNC) connector to each axis output, simplifying the interface with other electronics. The interface to the simulator is discussed next.

Annex I displays the specification sheet of the FGM3D sensor extracted from [39].

2.4.1 The Sensor Signal Conditioning and its Electronic Design

The dSPACE DS2211 ADC has a 0 to 60 V asymmetric voltage input span, while the fluxgate output voltage is ± 10 V for the entire magnetic field range of ± 2.5 gauss. Furthermore, the full range of the FGM3D sensor (± 2.5 gauss) is higher than the maximum value that the setup is tuned to generate (± 1.0 gauss). Therefore, it is necessary to condition the desired sensor output signal range to match the ADC input span.

The fluxgate specified scale range was ± 1.25 Gauss, equivalent to a ± 5 V output. Ideally, this value should be shaped to the DS2211 ADC differential 0 to 60 V input asymmetric span. However, conditioning to such a value would require high-voltage operational amplifiers, which are not easily available and have worse specifications than typical 30-36 V precision OpAmp. The electronic conditioning system uses a precision OPA4227 quad-channel OpAmp to condition each fluxgate output symmetric voltage of ± 5 V to a $0-30$ V differential voltage. Therefore, the value equivalent to a magnetic field of ± 1.25 gauss is acquired by half of the dSPACE ADC span, corresponding to an effective resolution of 13 bits. Figure 2.5 summarizes the electronic circuit of the acquisition system.

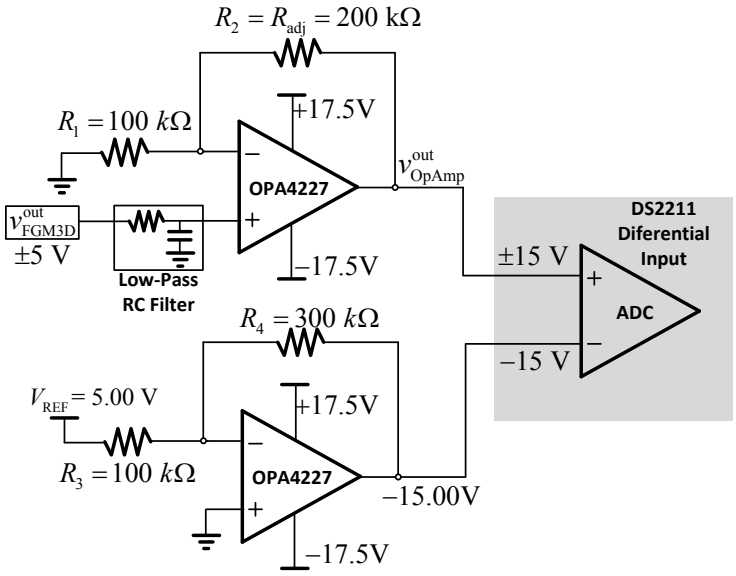

Figure 2.5: Schematic of a single channel of the acquisition and conditioning circuit to match the dSPACE ADC input span to a ± 1.25 gauss scale output of the FGM3D sensor.

Understanding the circuit of Fig. 2.5 is straightforward. Each axis output signal, defined as $V^{\text{out}}_{\text{FGM3D}}$, passes through a low-pass first-order RC filter and receives a gain of 3 in one of the four channels of the OPA4227. Therefore, the OpAmp output voltage ($V^{\text{out}}_{\text{OpAmp}}$) for that axis ranges from ± 15 V to magnetic field values of ± 1.25 gauss. In the remaining OPA4227 channel, a REF5050 IC regulates a 5.00 V reference voltage which receives a gain of -3, resulting in a -15.00 voltage. The positive input of each DS2211 ADC differential channel is connected to the respective conditioned sensor output $V^{\text{out}}_{\text{OpAmp}}$ and the negative input is connected to the -15.00 V signal common to all channels. Thus, the conditioned signal has a $0-30$ differential voltage to a magnetic field of ± 1.25 gauss to each sensing element of the fluxgate sensor. Figure 2.6 shows the electronic circuit prototype, the FMG3D sensor, its power unit, and its connections to the simulator. All the resistors employed in the design are 0.1% tolerance thin film resistors.

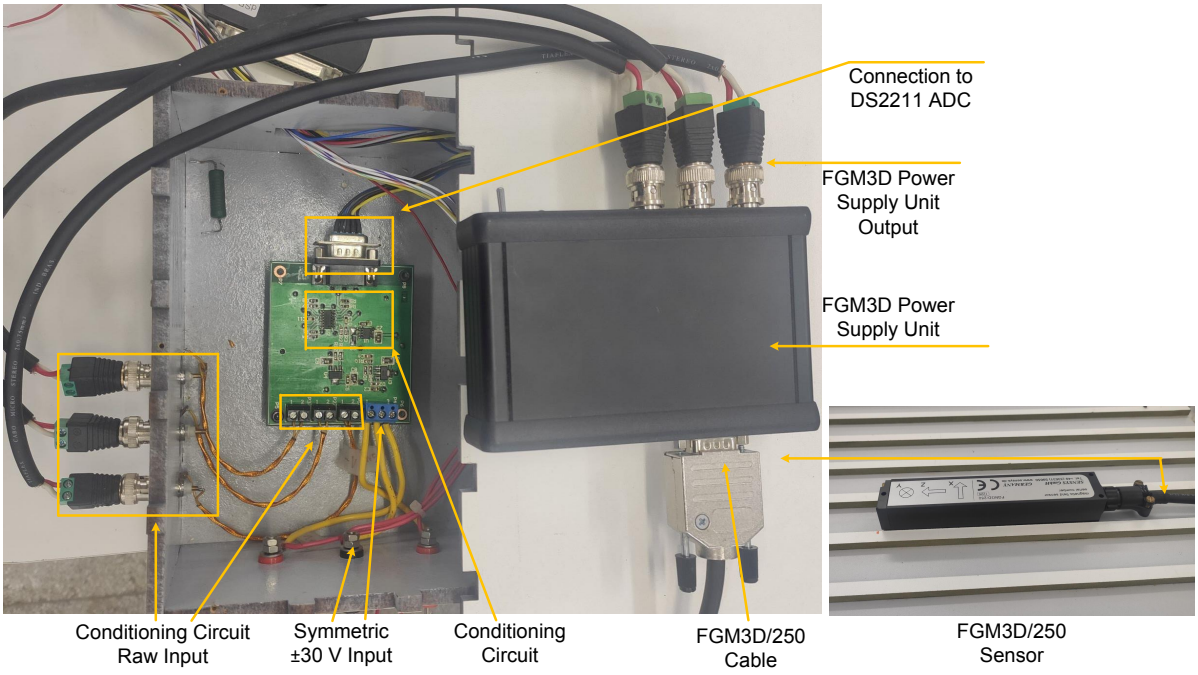

Figure 2.6: The Fluxgate sensor, its power supply unit, and the electronics responsible for the signal conditioning and interface with the DS2211 ADC.

2.4.2 The Fluxgate Sensor Calibration

Any errors associated with the sensor and the acquisition systems are not compensated for either by the setup calibration procedure or the closed-loop topology. Therefore, ensuring the sensor is calibrated is essential during the tests. The FGM3D sensor calibration is evaluated in a free-from-magnetic disturbance environment to guarantee the accuracy of the measurements. The procedure happens in the center of a large open field, ensuring distance from any object that could cause a magnetic disturbance. A non-magnetic structure manually rotates the sensor over all its axes, and a USB-6221 data acquisition system from National Instruments is used for logging the fluxgate measurements.

The parameter estimation follows the procedure described in Chapter 5, including the nine time-invariant parameters and the non-linear least square solution. All data sets collected yielded calibration parameters very close to the ideal one. The fluxgate estimated accuracy of the calibrated data was ± 125 μG better than the raw sensor data. *I.e.*, the uncertainty of the raw measurements is below that value, which is smaller than the system resolution, discussed in Section 2.6.4, and better than a typical low-cost sensor noise and resolution. Therefore, the raw measurements of the FGM3D sensor are considered the ground truth information during the experimental procedures.

2.5 Interface to the Systems and Sensors Under Test

The last element of the setup is the systems (or sensors) under test (SUT). It is possible to interface them to the dSPACE using the serial interfaces available on the HiL DS2211 board and the dedicated serial DS4201-S board. The former has four independent interfaces, two Controller Area Network (CAN) buses, and two

Universal Asynchronous Receiver-Transmitter (UART) channels (RS-232 and RS-422 compatible), and the latter has four RS-232 interfaces available. The SUTs may vary depending on each test and the desired evaluation, and the HiL solution allows for a modular approach, where adding or removing any SUT or magnetometer is relatively straightforward.

The final setup used in this work uses the DS4201-S channels to communicate with the two distinct SUTs. Figure 2.7 shows a diagram of the interfaces and sensors available for the tests. The first SUT is a commercial AHRS Spatial from Advanced Navigation [43] connected directly to a channel of the DS4201-S board. The second is a dedicated embedded system with two low-cost magnetometers, an HMC5883L [44] from Honeywell, and the magnetometer of an ADIS16448 compact precision IMU [45] from Analog Devices. Annex I shows the specification sheets of these and the fluxgate sensors. An STM32F103 microcontroller is responsible for managing the data acquisition of both sensors and passing along the information to the HiL simulation using a second RS-232 interface from the DS4201-S board. It is important to note that all data collected refer to the raw data of each sensor without any filtering or similar data processing.

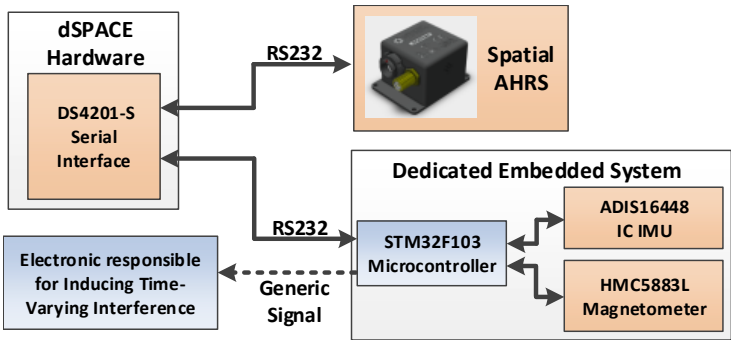

Figure 2.7: Diagram of the available electronics and magnetic sensors under test used during the tests.

Figure 2.8 shows the sensors positioned within the uniformity volume of the Helmholtz coil around the fluxgate sensor. The image was taken during one of the time-varying calibration tests. Additional information on the system under test electronics, and the test methodology, is given in each respective chapter.

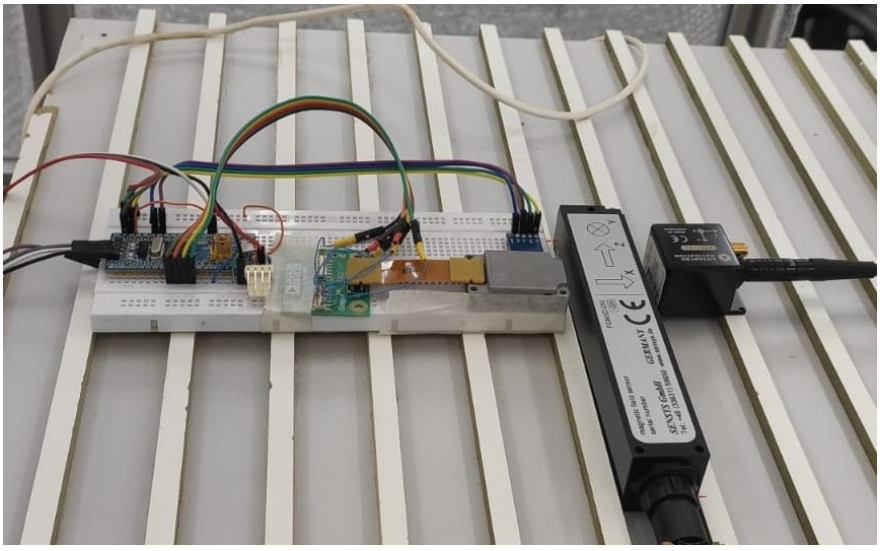

Figure 2.8: Image of the Fluxgate sensor and SUTs during one of the time-varying bias tests.

2.6 The Simulator Practical Capabilities Analysis

The characteristics and validation of the Helmholtz coil are reported in [25]. However, evaluating and characterizing some aspects of the magnetic field simulator plant, composed of the Helmholtz Coil, all the electronics, the fluxgate sensor, and the HiL simulator, is vital. These aspects include the step response of the simulator and its time constant, the resolution and quantization error of the generated magnetic field, and the measurement noise. Subsections 2.6.1 to 2.6.4 depict these characteristics of the built magnetic field simulator.

The plant's step response characteristics, and consequently its time constant, influence the maximum sample rate (number of magnetic field points per second) of the HiL simulation. Commonly, magnetic field simulators consider the operation at their steady state [15, 17–20, 24, 25], independent of simulating an AC magnetic field waveform, for example. In other words, for each point of the simulation, the magnetic field is updated, and the software (in our case, the HiL simulation) has to wait for the plant's transient response before taking (or considering) any magnetometer measurements. Furthermore, that is independent of the system operating in a closed-loop topology or the open-loop non-compensated method. Therefore, the simulator plant time response is vital to determine the sample rate of simulations, and this parameter is even more critical for real-time HiL simulations, such as those proposed here.

The system resolution, quantization error, and noise depend on the ADC and DAC resolution, the current source circuit, the fluxgate sensor, and the acquisition system. Ideally, a magnetic field simulator should have these characteristics at least one order of magnitude better than the SUTs' magnetometer resolution. However, achieving that might not be straightforward and depends directly on many factors, such as the current source, the available ground truth sensor, and others.

2.6.1 The Setup Step Response and Transient Time

Figure 2.9 shows the magnetic field simulator plant. In theory, the time constant of the plant should be independent of the magnetic field step amplitude, and depends on the RL circuit (RL series circuit of the coil), the FGM3D sensor bandwidth, and the low-pass filter on the acquisition circuit of the FGM3D. However, amplifiers are not ideal and magnetic elements may also have magnetic hysteresis. The first is likely to occur on the HCS power OpAmp because the power bandwidth (interrelated to its slew rate) is much lower than its signal bandwidth [46].

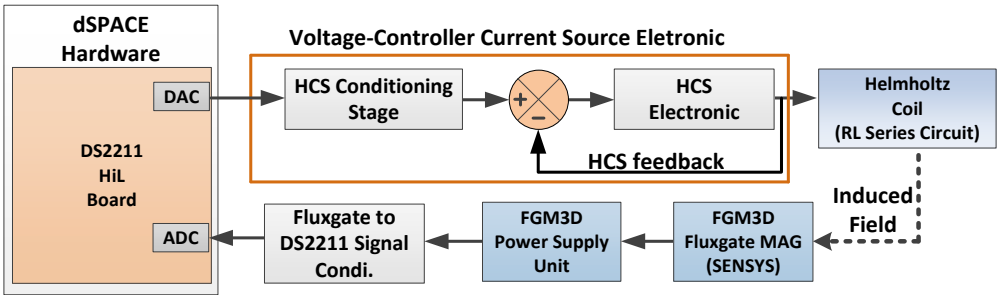

Figure 2.9: Diagram of the hardware elements composing the plant of the magnetic field simulator.

Consequently, as an amplifier slew rate characteristics and eventual magnetic hysteresis may cause the

step response of the plant to depend on the signal amplitude, a practical procedure was performed to assess the time response of the magnetic field simulator plant. The test evaluated the step response for different magnetic field amplitudes, varying from 0.010 gauss (10 mG) to 0.750 gauss (750 mG). Figures 2.10, 2.11, and 2.12 show the step response for the inner, middle, and outer coil, respectively.

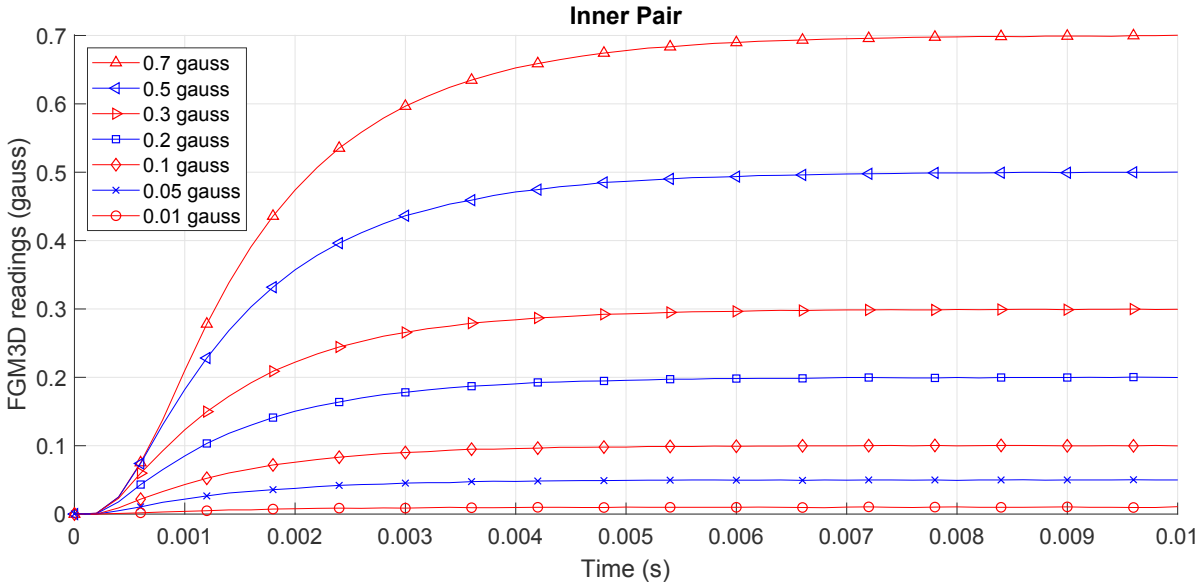

Figure 2.10: Inner pair step response obtained for different magnetic field amplitudes programmed in the HiL simulation.

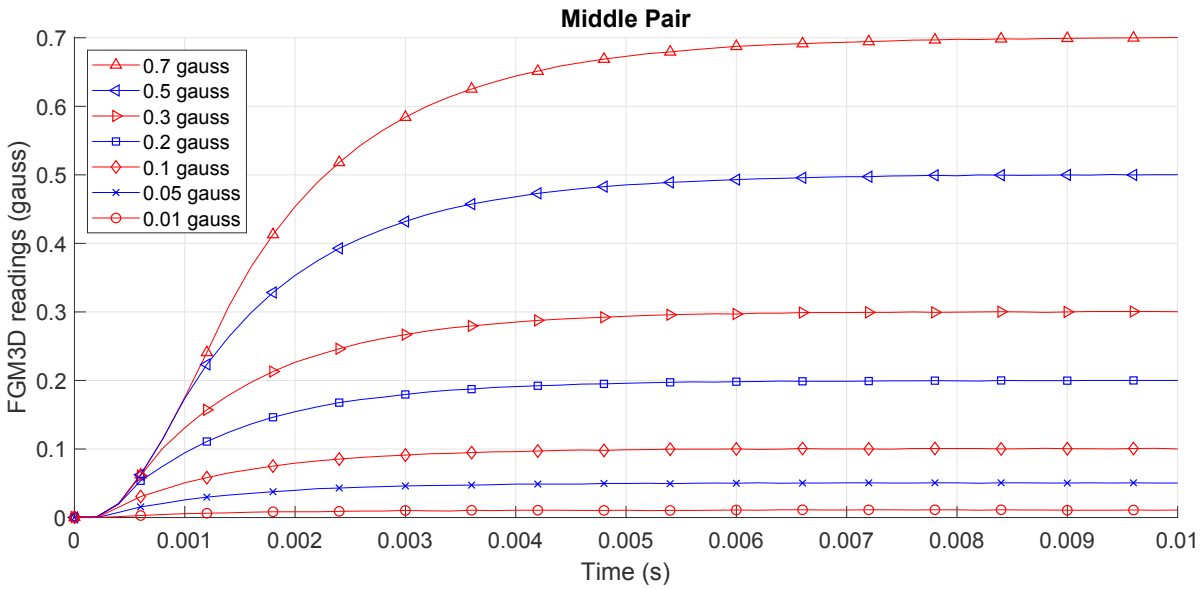

Figure 2.11: Middle pair step response obtained for different magnetic field amplitudes programmed in the HiL simulation.

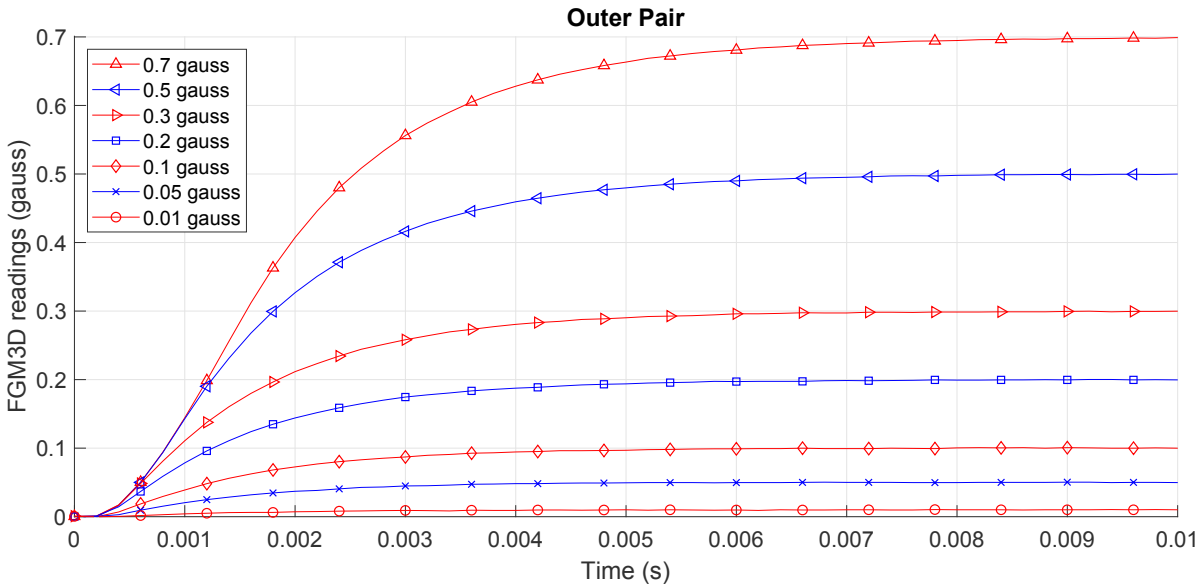

Figure 2.12: Outer pair step response obtained for different magnetic field amplitudes programmed in the HiL simulation.

The first observation from Figs. 2.10, 2.11 and 2.12 is that the inner pair has the fastest response time, and the outer one has the slower, as expected, given their series resistance and inductance values. Nevertheless, an important observation is that the transient time clearly depends on the signal amplitude. The transient response time of each pair, and for different amplitudes, was calculated using criteria of 98.3% of the steady state value. Table 2.2 shows the results for some of the amplitudes evaluated. A formal study, if required, to define the time constant as a function of the signal amplitude is left for future work.

Table 2.2: Approximate transient response time for each Helmholtz in milliseconds and for different amplitude steps. A threshold value of 98.3% of the steady state value was adopted.

Coil	Step Amplitude (Milligauss)									Unit
Pair	10	30	50	80	120	200	300	500	750	
Inner	3.8	4.6	4.8	5.0	5.2	5.4	5.6	5.8	6.2	
Middle	4.0	4.6	4.8	5.0	5.2	5.4	5.6	6.0	6.4	ms
Outer	5.0	5.2	5.2	5.4	5.6	5.8	6.0	6.4	7.0	

If the simulator is going to be used in its steady state, the simulation has to disregard acquisitions taken during the transient state of the magnetic field. It is possible to determine the HiL simulation transient period duration after updating the dSPACE DAC using Table 2.2 data. Although 7 ms complies with the experimental observations, we have established a 10 ms period that the HiL simulation must disregard to comply with the plant's time constant. Note that this thesis does not aim at testing and evaluating a specific SUT; hence, we set a considerable safety margin. Nevertheless, future works can use smaller values to achieve higher rates, if needed, than those reported ahead.

Moreover, the eventual use of the system in a closed-loop topology may have a different transient time depending on the controller, and we must evaluate the setup's time constant when operating in the closed-loop topology. Theoretically, the digital PID controller of [25] improves the transient period. However, the practical implementation is limited by the saturation of the DAC (which restricts the HSC output current range), and

consequently, addressing the closed-loop step response is necessary. Section 4.7 shows the closed-loop step response of the simulator and verifies that despite the saturation issue, the system maintains a transient time inferior to 10 ms. Hence, disregarding this period is suitable for both procedures, and it is possible to adopt the same value for the compensated and non-compensated operation of the simulator.

2.6.2 The Maximum Update Rate of the Simulator

After establishing the transient period of the setup's plant, we must analyze the maximum rates that the HiL simulation can update the magnetic field value and define the procedure to perform the acquisitions of the low-cost sensors under test. The DAC update rate is the number of cycles (the number of different magnetic field points) simulated in a second. Theoretically, the simulator can generate over 140 distinct magnetic field points per second, assuming 7 ms between each one, or 100 points with the safety margin. However, that would not account for the time required to perform the readings of the SUT's magnetometers. Thus, another constraint is that the HiL simulation must disregard the acquisitions of the magnetometers taken during the transient period after it updates the magnetic field values through the DACs. We can accomplish that by:

1. synchronizing the SUT's magnetometers conversion to the HiL simulation, or
2. disregarding the SUT's magnetometers measurements taken during the transient time and ensuring their data conversion was taken after that period.

The first procedure advantage is allowing for a simulation with a higher number of distinct magnetic field points per second compared to the other. For instance, the ADIS16448's magnetometer supports an Output Data Rate (ODR) between 50 and 68.15 Hz using an external synchronization signal; therefore, it would be possible to simulate those number of points per second if the SUT has that sensor and is built with the support to allow an external trigger sent by the HiL simulation hardware. Hypothetically, even higher rates could be achieved depending on the sensor, such as 100 points per second with the current setup.

Yet, the practical implementation of that strategy is limited because it requires a synchronization mechanism to trigger the sensor conversion once the plant's transient period has passed after every DAC update. However, implementing such a mechanism is not straightforward or even possible, depending on the SUT and its magnetometers[1]. Besides, in most situations, the SUTs are independent of the HiL setup, and we seek only to implement the device's communication protocol in the HiL simulation, which allows exchanging data based on its programmed functionalities. Hence, our work employs the second strategy during the tests.

In view of the above, it is evident that the second strategy is more straightforward, and its implementation is possible with any SUT or sensor. Nonetheless, the HiL simulation must guarantee that the data conversion of the sensors under test occurred during the steady state of the generated magnetic field. To ensure that, the simulation has to ignore the measurements taken during the transient time and the first one during the steady state. Disregarding this latter is necessary because, although the HiL simulation receives the data during the steady state, we do not know the precise instant the data conversion occurred within the sensor.

[1] The ADIS16448 sensor is an example that allows triggering the sensor's conversion time to an external signal [45]. However, not only must the sensor have that feature, but the electronic design of the SUT must support that.

Consequently, the magnetic field update rate is limited and depends on the SUT's magnetometers ODR and the plant's transient period. Therefore, to comply with the discussion above, each cycle (magnetic field point) must have a minimum period, $t_{\text{cycle(min)}}$, given by:

$$t_{\text{cycle(min)}} = t_{\text{transient}} + 2 \cdot t_{\text{sensor}}, \tag{2.15}$$

where $t_{\text{transient}}$ is the plant's transient time, and t_{sensor} is the period between each measurement of the sensor. The minimum period of each cycle dictates the maximum number of magnetic field points, $N_{\max}$, the simulator can generate per second when testing a SUT:

$$N_{\max} = \frac{1}{t_{\text{cycle(min)}}}. \tag{2.16}$$

Finally, we analyze the maximum update rate of the simulation when testing the SUT's magnetometer HMC5883L, which has an ODR of 40 Hz, the lowest among the available sensors. Hence, we have a t_{sensor} of 25 ms and a $t_{\text{transient}}$ of 10 ms. Therefore, using (2.16), we can find that each cycle must have 60 ms to ensure at least one valid measurement of the HMC5883L sensor. For a better understanding, Fig. 2.13 summarizes the simplified timing diagram for these conditions, which represents the worst-case scenario when testing a sensor with a throughput of 40 Hz.

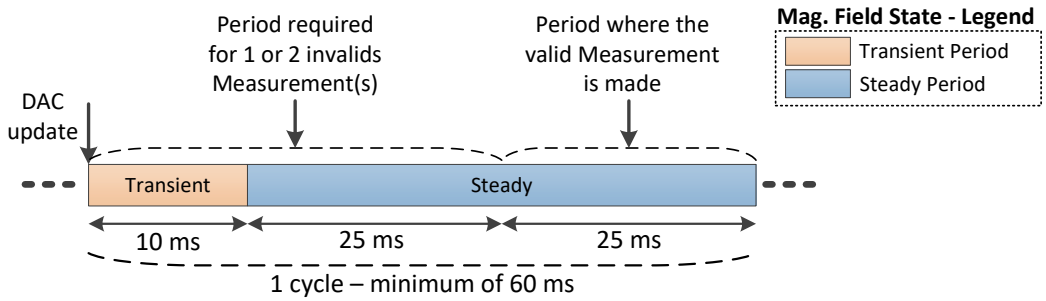

Figure 2.13: Simplified timing diagram (minimum requirements) of the HiL simulation using a sensor with an ODR of 40 Hz.

Therefore, in these conditions, the simulator can generate up to 16.666 distinct magnetic field points in a second (16.666 Hz, or $1/0.060$) while ensuring at least one acquisition of the SUT's magnetometer during each cycle. At last, for the sake of completeness, Table 2.3 shows other minimum values of $t_{\text{cycle(min)}}$ and the maximum number of points possible for different values than an ODR of 40 Hz.

Table 2.3: Maximum number of distinct points the HiL simulation can generate per second according to the sensors under test and the plant's transient time.

Plant's transient and sensor's ODR		**Resulting cycle's characteristics**	
$t_{\text{transient}}$ (ms)	ODR (Hz)	$t_{\text{cycle(min)}}$ (ms)	$N_{\max}$
10	10	0.210	4.76
10	20	0.110	9.09
10	40	0.060	16.66
10	75	0.036	27.77
10	100	0.030	33.33

At last, one should note that we could improve the number of points in Table 2.3 using an additional time stamp between the HiL simulation and the SUT. However, similarly to the first strategy discussed, it would require adding functionalities to the SUT's electronics and software. Therefore, the analysis above represents the worst-case scenario, where it is impossible to determine the magnetic field state during the sensor's conversion of the first data received by the HiL simulation after the plant's transient period.

2.6.3 The HiL Simulation Sample Time and the Fluxgate Sensor Measurement Noise

After determining the maximum number of cycles (number of different magnetic field points), we must specify the HiL simulation fundamental sample time, which defines the fixed-step sample time of the dynamic model solver and the number of acquisitions that the dSPACE ADC performs from the fluxgate sensor. Accordingly, this analysis is essential to evaluate the measurement noise of the FGM3D sensor.

The HiL simulation has a fundamental sample time of 500 μs, and consequently, it has 2000 measurements of the FGM3D per second. Ideally, more samples per second lead to a better outcome, but the model based-design must be executed in real-time in the DS1006 processor board, and there is a practical limit that depends on the complexity of the simulation. Therefore, that number was defined based on the simulations implemented in [26], where we have established that 2000 samples per second (SPS) is a suitable compromise to avoid problems in the real-time execution when simulating a low-Earth orbit and a nanosatellite's dynamic while generating the magnetic field in a closed or open-loop topology.

Since the samples per second are constant, the total number of measurements of the fluxgate sensor in each cycle, given by $N_{\text{FGM3D(cycle)}}$, depends on the number of cycles in a second. Figure 2 shows a simplified timing diagram of the FGM3D measurements during the HiL simulation.

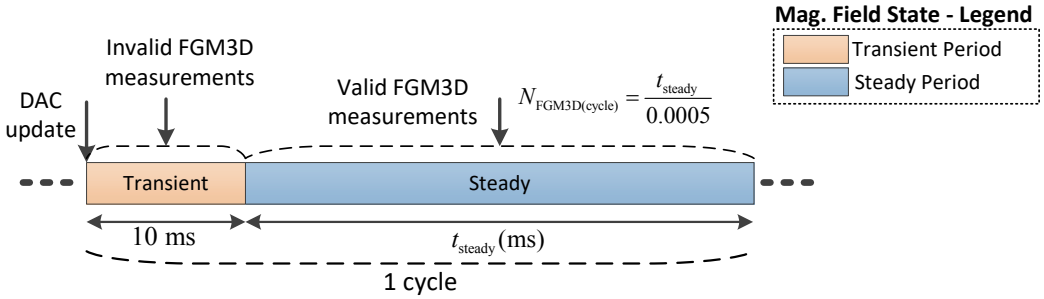

Figure 2.14: Simplified timing diagram of the FGM3D measurements in the HiL simulation.

During the plant's transient time, the HiL simulation disregards all FGM3D readings, and the final reference (ground truth) measurement in each cycle is calculated by taking the average value of all FGM3D readings made during the steady state. Therefore, the noise of the ground truth measurements depends on the number of cycles per second.

Owing to that, we have evaluated the resulting noise for two scenarios. First, we assess a condition with 10 cycles per second, with a steady state period of 90 ms and 180 measurements. In the second, we carry the test with 20 cycles per second, with 80 acquisitions taken during the steady state period of 40 ms. Besides, we recall that the values discussed in Table 2.3 are the maximum number of points in the worst-case scenario.

The experimental test methodology was to set a constant value in each channel DAC that would cancel the Earth's magnetic field within the three-axial Helmholtz coil. In other words, the FGM3D sensor readings would be as close as possible to zero gauss in all axes. Figure 2.15 displays the data collected during 30 seconds of the procedure. For each axis, the plot shows the raw sensor data and the average value calculated every 80 and 180 measurements, equivalent to conditions with 10 and 20 cycles per second, respectively.

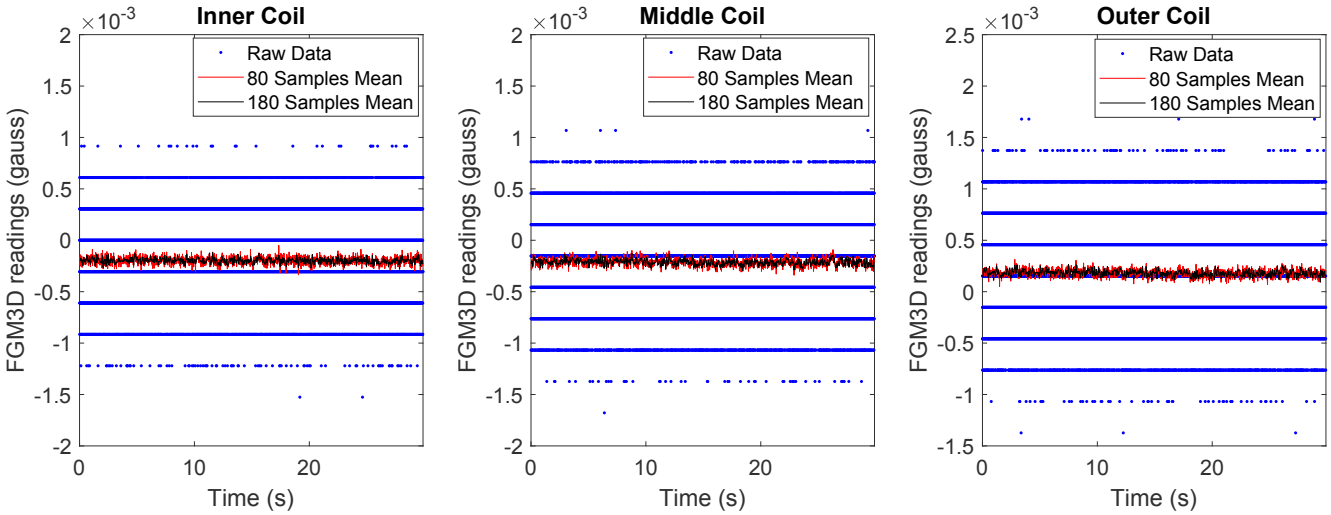

Figure 2.15: Raw FGM3D sensor measurements and average data for 80 and 180 acquisitions to all pairs.

First, each axis subplot in Fig. 2.15 reveals that all axes have a very close behavior. Moreover, it is notable that the raw data acquired by the dSPACE ADC has considerable noise, and the peak-to-peak data has a variation within 9 to 11 least significant bits (LSB), depending on the axis. However, we can see by the visual examination that taking an average of 80 samples reduces the noise to a value smaller than the magnetic field value equivalent to a variation of a 1 LSB step in the acquisition system, and the case with 180 samples further reduces the noise. Table 2.4 shows the standard deviation extracted from the raw and filtered data.

Table 2.4: Standard deviation of the raw and filtered data for the FGM3D sensor for a constant output in all DAC channels. All data are in microgauss (μG).

Coil Pair	Standard Deviation (μG)		
	Raw Data	80 Samples Average	180 Samples Average
Inner	284.2	36.3	25.4
Middle	309.2	36.5	28.3
Outer	344.6	36.7	29.1

When comparing the filtered and the raw data, the numerical data confirm the standard deviation reduction by one order of magnitude. Furthermore, the following subsection verifies that the ADC resolution of the current setup is significantly worse than the standard deviation values of the data filtered by taking the average of 80 or 180 acquisitions of the FGM3D sensor. Thus, the results show that the analog converters available at the dSPACE hardware are a more limiting factor than the noise of the FGM3D filtered data when generating up to 20 cycles per second.

2.6.4 The Simulator Resolution and Quantization Error

The effective resolution of the setup depends on both the magnetic field acquisition and the generation capacities of the built hardware combined with the DS2211 analog interfaces. The former depends on the ADC and the acquisition circuit. The latter is related to the DAC and the HCS design.

The dSPACE DS2211 board has a 14 bits ADC with a 0-60 V range, resulting in a 3.66 mV resolution. Besides, a conditioned sensor voltage of 3.66 mV by the electronics of Section 2.4 is equivalent to 305 μG. Therefore, this is the theoretical resolution of the FGM3D readings, and the quantization error is approximately half of that value. The DS2211 DAC has a 0-10 V output voltage range and 12 bits of resolution, and the current source electronics of Section 2.3 was tuned to generate a magnetic field of ± 1 gauss to the DAC span voltage. This combination results in a resolution of approximately 488 μG in each axis; nonetheless, this value may have slight variations due to a limitation in the precision resistors to comply with (2.12)-(2.14).

Consequently, the acquisition and generation resolution are in the same order of magnitude, and the system resolution and quantization error depend on both and not only on the FMG3D acquisition system. A practical procedure evaluates the actual resolution of the simulator. First, we manually set all DACs so that the FGM3D readings are as close as possible to zero gauss value, and then the HiL simulator increases 1 LSB every 2 seconds only in one axis. Afterward, the system repeats the process for the other two axes.

Figure 2.16 and Table 2.5 show this procedure results. The former shows the graphical result of all axes for a variation of 12 LSB. The latter compares the numerical value of the minimum, maximum, and average step values obtained for 50 steps of 1 LSB.

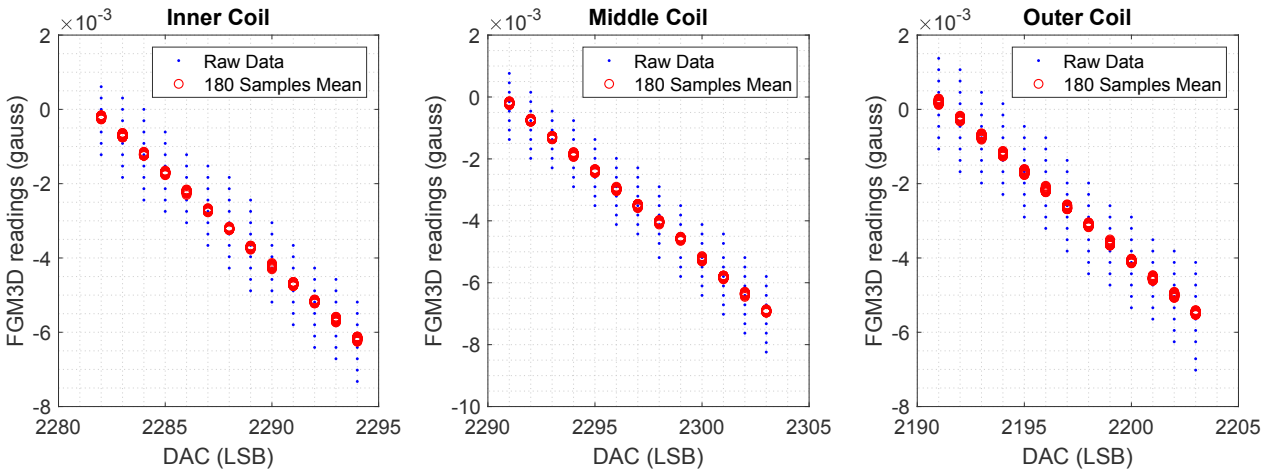

Figure 2.16: FGM3D measurements for all pairs for variations of 1 LSB in the dSPACE DS2211 DAC.

Table 2.5: FGM3D minimum, maximum, and average absolute steps values measured at the FGM3D sensor for variations of 1 LSB in the dSPACE DS2211 DAC. All data are in microgauss (μG).

Coil Pair	Absolute Values (μG) for a variation of 50 LSB in steps of 1 LSB in		
	Minimum	Maximum	Average
Inner	468.2	528.8	495.9
Middle	531.7	642.7	559.9
Outer	450.0	516.6	474.5

Similar to the previous section analysis, Fig. 2.16 confirms that the system noise of the FGM3D averages in a cycle of 180 valid readings (equivalent to 10 cycles per second) is lower than the system resolution. Besides, Table 2.5 data shows that the effective resolution of the system combining the ADC and DAC resolution is around 500 microgauss (μG). However, the values associated with each LSB step are not linear, a consequence of having the acquisition and generation systems resolutions with similar orders of magnitude. Another observation is that the middle pair resolution is slightly worse than the other axes. Achieving an identical resolution for all axes would require precision resistor values to comply with (2.12)-(2.14), and the middle pair was most affected by not having an ideal precision resistor calculated in (2.13).

At last, it is not feasible to separate the resolution of the acquisition and generation systems in the practical test. Thus, it is not possible to rigorously calculate the error of the system, which depends on the generated magnetic field error and the one associated with the FGM3D readings. In practice, assuming the approximately 300 μG acquisition resolution, the quantization error is around 150 μG. However, the actual error is also limited by the generation resolution of approximately 500 μG.

2.7 Conclusions about the Magnetic Field Simulator

The combination of the Helmholtz coil with a linear-based current source and the HiL simulation technique provides vital characteristics to the magnetic field simulator. The setup has a fast transient time, mainly dependent on the coil's inductance and the low-pass filter of the ADC acquisition electronics [25], and controlling the linear VCCS requires no current-control loop or switching sources. Furthermore, the simulator sample time allows for a true real-time HiL simulation, which can simulate dynamics and low Earth orbits for nanosatellites, for example.

The HiL simulation and the SUTs magnetometer are asynchronous, which limits the maximum samples per second. Nonetheless, the values reported in Table 2 exhibit that the HiL simulation can operate in real-time, generating multiple points of magnetic field per second. For instance, a sample range of 4.76 to 16.66 cycles is doable using magnetometers with a 10 and 40 Hz throughput, respectively. Future works can improve, if necessary, the sample time by developing a synchronous mechanism to guarantee that the sensors under test are sampled right after the plant's transient time. That could allow for simulations with up to 100 samples per second in an ideal scenario, a value considerably higher than many magnetic field simulators reported in the literature.

The drawback of the current setup is the dSPACE DS2211 ADC and DAC number of bits, which limit the acquisition resolution of the FGM3D sensor and the resolution of the HCS current source, respectively. The latter ends up limiting the generated magnetic field resolution. Future works can improve the matter using a dedicated analog interface instead of those available at the dSPACE hardware. For the HCS electronics, a possible design is using a 16-bit DAC8565 triple channel with simultaneous sampling or a similar part number. However, for the FGM3D sensor acquisition, a converter with at least 18-bit would be recommended; hence, a design with three ADS8699 or other ADC with similar features would allow simultaneous sampling and an 18-bit solution.

3 The Power Howland Current Source Analysis

This chapter shows the analysis and practical implementations of the Howland Current Source. The development of an accurate and precise VCCS is essential to generate the open-loop (non-compensated) magnetic field required for the magnetometer calibration including time-varying interference. The study shown in this chapter is a continuation of [32] in order to improve that circuit. These results are also reported in [34].

The chapter is organized as follows. The first Section introduce to the high power HCS problem and discuss related works. Section 3.2 shows the theoretical analysis and constraints of the HCS. The errors and non-ideal study of the HCS circuit are shown in Section 3.3. Section 3.4 displays the power HCS requirements, available and possible commercial components, and presents an error budget simulation that evaluates the order of magnitude of all errors discussed in Section 3.3 in the power HCS. At last, Section 3.5 shows the practical circuit, the test methodology, and the experimental results of the HSC implementation.

3.1 Introduction and Review of existing Power HCS Works

The Howland Current Source (HCS) is a grounded-load linear Operational Amplifier (OpAmp) based Voltage-Controlled Current Source (VCCS). The electronic design of an HCS is exceptionally simplistic, requiring a single OpAmp and a bunch of resistors in its improved topology [28, 47]. It can provide a very accurate symmetric output and can be built using a typical precision OpAmp. Therefore, the HCS is a high-performance symmetric VCCS that can provide a much simpler solution than other current sources alternatives [48–50].

The HCS is widely used for biomedical applications, such as neural and electrocutaneous stimulation [51–53] and bio-impedance measurement system [28, 47]. This latter includes electrical impedance tomography [54, 55], impedance cardiograph [56], and others [57, 58]. In such applications, if carefully designed, it is possible to combine the construction simplicity with outstanding output impedance, bandwidth, and stability. Therefore, many authors employ the HCS solution in their biomedical systems. In most of these works, the HCS has to output currents in the micro-amperes or tens of milli-amperes range using low-voltage precision OpAmps.

Although the majority of HCS works are on small current ranges, a few authors have shown the possibility of using the HCS on higher current applications [31, 59–61]. The power HCS solution allows a linear solution to the controlled-current source problem and might have a few advantages over other alternatives. It can easily handle negative and positive currents and zero current transitions (crossover) with low errors. It allows simple electronics and a relatively low-cost design using commercial off-the-shelf components. Compared to switching sources, it has a simple design, has few noise problems, and does not require an external control

loop. However, power OpAmps have poor precision compared to typical precision amplifiers. Despite being a powerful low-cost alternative, there is a gap in the literature regarding a detailed analysis of the errors, accuracy, and, more importantly, the non-linear errors of the power HCS circuit. The latter is critical in the power design and can severely impact the source's accuracy, as reported in [32].

The analysis of the power HCS seen in [31] shows the HCS transconductance gain but limits the error discussion to the problems of resistor mismatch impacting the output impedance, which degrades accuracy. References [59] and [60] follow a similar theoretical examination of the output impedance problems due to mismatch and focus more on detailing their application of the HCS. None of these works quantified their accuracy in their practical implementations. Reference [61] shows a detailed analysis of the HCS stability and output impedance, and its primary goal is the proposal of a design procedure methodology for the power HCS. It uses as an example a VCCS capable of outputting currents up to 1 A and a voltage of ± 10 V. The analysis uses an OPA564, which has a maximum rated current of 1.5 A with a power-supply voltage range of 24 V or $\pm$ 12 V. At last, it reports a maximum relative error of around 5%.

The desired design to drive the magnetic field simulator uses the HCS on a higher current and voltage scenario. Theoretically, the first design reported in [32] can drive currents up to 3 A on a ± 27.5 voltage span using an LM675 OpAmp. A first-order calibration improved that circuit accuracy, but the results showed that the power VCCS built using the LM675 amplifier had considerable non-linearities. A practical procedure proved that the power OpAmp and the HCS power resistor influenced the circuit's linearity, and the output current had $\pm$1% of non-linearities when driving up to $\pm$1.35 A for a Direct Current (DC) or low-frequency ones. This result was adequate to power the magnetic field simulator of a previous work [26] because the setup worked in a closed-loop magnetic field topology, compensating for any non-linearities of the current source. As a result, addressing these non-linear errors was not necessary. The new analyses require the system to generate a non-compensated open-loop magnetic field beside the closed-loop topology. In such circumstances, those HCS errors and that absolute accuracy of 1% translates to a significant inaccuracy in the generated magnetic field. Therefore, an improved design was built and required a thoroughgoing study of the HCS errors. This error analysis and practical investigations are reported here.

This chapter provides insight into the HCS design using power OpAmps and its characterization, including a detailed analysis of the circuit errors. These include the resistor mismatch and variations in the transconductance gain, the R_{2b} resistor influence (see R_{2b} in Fig. 3.1), offset voltage and bias current, and non-linear errors. Although previous works [28, 61] observed part of these errors, the characterization was not in detail or the focus. Another novelty shown is the non-linear effects in the circuit owing to heating effects on the OpAmp drifting and the sense resistor R_{2b}. These errors cause non-linearities in the output current for DC or low-frequency operation, affecting the accuracy and linearity of the circuit. Simulations and practical testing of the VCCS are shown to different amplifiers and distinct circuit conditions to evaluate the mentioned errors. Although the simulations show that heating has a significant impact on the output performance of the power HCS, a SPICE simulation is unlikely to cover and display an exact model of the non-linearities, and practical implementations are necessary to address the power HCS behavior in a particular condition.

To comply with the requirements described in Chapter 2, the proposed VCCS requires driving a maximum current of $\pm$1.35 A (with a theoretical limit of $\pm$2.5 A) at a $\pm$27.5 V voltage span (using a $\pm$30 V supply).

The implementation was evaluated using three power amplifiers, the LM675, the OPA544, and the OPA548, all from Texas Instruments. The study and analysis of the HCS operation, accuracy, and errors around those current and voltage ranges were not found in the literature. Higher voltage and current are possible using other OpAmps options, such as the OPA541 from the same manufacturer or the PA series amplifiers from Apex Microtechnology, but at a considerably higher cost.

The calibrated final HCS design has accuracy and linearities superior to 0.1% when outputting DC currents up to $\pm$2.10 A. Hence, the analysis and implementation prove that a low-cost HCS design, built using commercial off-the-shelf components, can achieve outstanding DC performance, as long as the design adequately addresses the thermal effects and non-linearities of the circuit [32, 34]. Such conditions and needs for a very accurate and precise power VCCS may arise in many other applications, such as component testing, torque control for motors [31], magnetic circuits [32, 59], V-I control for valves [61], and others [60, 62]. Furthermore, it is possible to replicate all the analyses conducted to a VCCS in any other current/voltage range.

3.2 Howland Current Source Theory

Figure 3.1 shows the basic circuit of the improved [28, 63] Howland Current Source (or Pump). The HCS seeks to output a current independent of the load and controlled by the applied input voltage v_i to the OpAmp's negative feedback loop. The first step in that circuit is to establish the necessary conditions to ensure it operates as the intended VCCS regardless of the load [32, 61], seen in Section 3.2.1, which also deduce the equations used in the resistor mismatch error analysis. An important aspect of our analysis is that it considers input voltage only in the inverting loop of the circuit. The HCS has different transconductance gains for the positive and negative feedback and driving only one input while grounding the other may avoid unnecessary distortion [29].

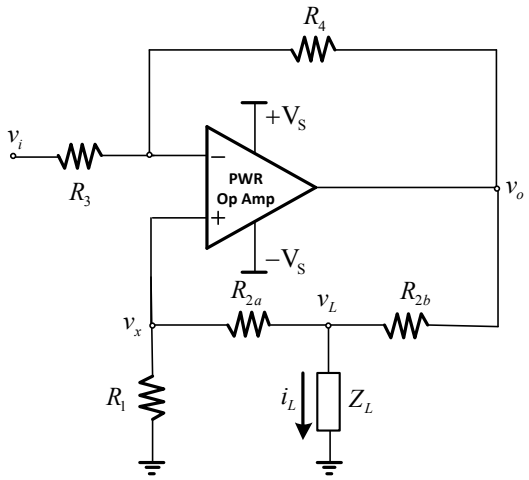

Figure 3.1: Electrical circuit of the improved Howland Current Source [29].

The maximum output current value ($i_{L\max}$) and bandwidth are important circuit design constraints. They depend on the OpAmp maximum output voltage (power OpAmps are not rail-to-rail), the voltage drop at the R_{2b} resistor, and the load's impedance Z_L (for non-resistive ones). Therefore, the maximum output current, the maximum output voltage, Z_L, and R_{2b} are interdependent parameters. Also, the maximum current value will depend on the desired output frequency for inductive or capacitive loads. Section 3.2.2 equates $i_{L\max}$ as

a function of the other parameters and discusses these constraints.

3.2.1 Equating the Load's Current

The load's current deduction can start by equating the negative feedback loop of the HCS circuit seen in Fig. 3.1. Since the currents through R_3 and R_4 are the same, then

$$\frac{v_o - v_x}{R_4} = \frac{v_x - v_i}{R_3}. \tag{3.1}$$

On the positive feedback loop, the current that flows through R_{2a} and R_1 is the same. Thus, it is possible to relate the voltage at the non-inverse input (v_x) and the voltage on the load (v_L), resulting in

$$v_x = v_L \frac{R_1}{R_1 + R_{2a}}. \tag{3.2}$$

Replacing v_x in (3.1) from (3.2) and isolating v_o, we have

$$v_o = v_L \frac{R_1}{(R_1 + R_{2a})} + v_L \frac{R_4 R_1}{R_3(R_1 + R_{2a})} - \frac{R_4}{R_3} v_i. \tag{3.3}$$

Additionally, the positive feedback loop can be equated as

$$i_L = \frac{v_L}{Z_L} = \frac{v_o - v_L}{R_{2b}} - \frac{v_L}{R_1 + R_{2a}}, \tag{3.4}$$

and by combining (3.4) with (3.3) to eliminate v_o and after some algebraic manipulation, i_L is given by

$$i_L = \frac{R_4(R_1 + R_{2a})}{Z_L\Big(R_4 R_1 - R_3(R_{2a} + R_{2b})\Big) - R_3 R_{2b}(R_1 + R_{2a})} v_i. \tag{3.5}$$

Equation (3.5) describes the output current as a function of all the resistor, the input voltage, and the load's impedance. The circuit behave as a VCCS if i_L is independent of Z_L; therefore, the first term in denominator at the right side of (3.5) must vanish, so

$$Z_L\Big(R_4 R_1 - R_3(R_{2a} + R_{2b})\Big) = 0. \tag{3.6}$$

Finally, in order to the circuit of Fig. 3.1 operate as a VCCS it is a necessary condition that the following relationship is maintained

$$R_4 R_1 = R_3(R_{2a} + R_{2b}). \tag{3.7}$$

Accounting that (3.7) is satisfied, (3.5) can be rewritten as (3.8), which describes the ideal output current of the HCS as a function of its input voltage.

$$i_L = -\frac{R_4}{R_3 R_{2b}} v_i \tag{3.8}$$

Equation (3.8) shows the ideal transconductance gain of the HCS. Nevertheless, (3.5) is necessary to evaluate non-linearities in the transconductance gain if the relationship of (3.7) is not perfectly matched. For example, in such a scenario, any load's impedance variations will translate to non-linear effects on the output

current and increase non-linearities caused by any variation of the power resistor R_{2b}.

3.2.2 Maximum Output Current and Frequency

The maximum output current of the HCS depends on the OpAmp maximum output voltage ($v_{o\max}$), the voltage drop across the resistor on the positive feedback loop (R_{2b}), and the maximum desired output frequency (ω), assuming non-resistive loads. To begin the analysis we rewrite (3.4) as a function of v_o, hence

$$v_o = v_L\left(1+\frac{R_{2b}}{Z_L}+\frac{R_{2b}}{R_1+R_{2a}}\right). \tag{3.9}$$

Replacing v_L by the product $i_L Z_L$, isolating the output current i_L, and accounting for the OpAmp maximum output voltage $v_{o\max}$, (3.9) can be rewritten as

$$i_{L\max} = \frac{v_{o\max}}{R_{2b}+Z_L\left(1+\dfrac{R_{2b}}{R_1+R_{2a}}\right)}. \tag{3.10}$$

We can calculate the maximum current value for both a resistive and non-resistive load using (3.10). The former Z_L will be given by a resistive value (R_L), and (3.10) will be given directly by (3.11). The latter leads to a load's impedance that depends on the output frequency, assuming an inductive load given by $Z_L = \sqrt{(R_s)^2+(\omega L_s)^2}$, the maximum current is given by (3.12). A similar expression can be found for a capacitive load and is not demonstrated.

$$i_{L\max}(R_L) = \frac{v_{o\max}}{R_{2b}+R_L\left(1+\dfrac{R_{2b}}{R_1+R_{2a}}\right)} \tag{3.11}$$

$$i_{L\max}(R_s,L_s) = \frac{v_{o\max}}{R_{2b}+\left(\sqrt{R_s^2+\omega^2L_s^2}\right)\left(1+\dfrac{R_{2b}}{R_1+R_{2a}}\right)} \tag{3.12}$$

Assuming the case of a power HCS, the absolute value of R_{2b} is significantly smaller than R_1 and R_{2a}. For example, our power HCS uses $R_{2b} = 1.2\ \Omega$ and other resistors in the kilo-ohms range [32]. Therefore, granting that $R_{2b} \ll (R_1+R_{2a})$, (3.11) and (3.12) can be simplified to (3.13) and (3.14), respectively. These equations relate the maximum HCS output current given the OpAmp voltage swing limits, the feedback resistor R_{2b}, the load's resistance, and to the inductive case, the inductance L_s value and the output current frequency ω.

$$i_{L\max}(R_L) \approx \frac{v_{o\max}}{R_{2b}+R_L} \tag{3.13}$$

$$i_{L\max}(R_s,L_s) \approx \frac{v_{o\max}}{R_{2b}+\left(\sqrt{R_s^2+\omega^2L_s^2}\right)} \tag{3.14}$$

The maximum current value is independent of the frequency for a resistive load, and the maximum frequency will depend only on the circuit bandwidth. However, when driving inductive or capacitive loads, variations in the frequency cause the output voltage v_o to change to maintain the load's current constant. Therefore, despite being evident that with a limited output voltage swing the maximum working current will decrease with frequency, this restraint must be considered both in the HCS and the load design.

3.3 Errors and Non-Ideal Analysis on the HCS Circuit

It is important to distinguish between two kinds of errors: calibratable (non-drifting, including constant and first-order/linear ones) and non-calibratable (higher-order/non-linear and drifting ones). The former is related to static parameters (such as manufacturing tolerances) that do not drift and can be compensated by a calibration procedure. Examples of the former are the common mode rejection ratio (CMRR) since the errors induced by finite CMRR are linear functions of the input voltage and DC errors due to constant offset voltage and current. Examples of the latter are mostly temperature drifts, whether due to ambient temperature fluctuations or power dissipation that varies as a function of input voltage (the most important example is the Howland current source's sense resistor). In addition, OpAmp errors, such as the offset voltage and input bias current, have a constant DC component but also drift on account of changes in the OpAmp temperature. A calibration procedure can compensate for the constant component, but not the ones related to the drifting. The non-linear errors discussed ahead are intrinsic to the circuit, and directly compensating them is not possible. Therefore, identifying and designing the circuit to minimize the non-linear effects is essential to ensure accuracy and linearity.

For instance, the first HCS implementation to drive the simulator showed that both kinds of errors were significant [32]. In that work, the theoretical and calibrated first-order coefficients of the i_L versus v_i had notable differences, *i.e.*, without the calibration procedure, the HCS accuracy is not guaranteed. After calibration, the non-linear errors were evaluated by measuring the difference between the calibrated current curve and the measured current, resulting in approximately 0.8% non-linear errors of the load's current full scale. Furthermore, a practical procedure in that work demonstrated that the errors related to the power OpAmp and the sense resistor (R_{2b}) were in the same order of magnitude. Thus, any possible error caused by both components must be evaluated.

The remainder of the section addresses the possible errors that may happen in the HCS circuit. The last subsection discusses other errors, not critical in our power application where low-frequency accuracy and linearity are the goals. The analysis is valuable independent of the HCS application but is much more critical in a high-current design. Section 3.4 will translate the theoretical analysis to typical power OpAmp data to study the expected errors in the power HCS circuit.

3.3.1 Considered Errors and Analysis Considerations

There are three noteworthy sources of errors in the HCS circuit, and not only do these errors affect the circuit accuracy, but they also might impact the output current linearity. 1 - Those inherent to the OpAmp, which include: offset voltage and its drift with temperature; input bias/offset current and its drift with

temperature; and finite open loop gain. 2 - Errors due to R_{2b} heating, that leads to its resistance variation and non-linear errors as a consequence. 3 - Errors related to (3.7)'s condition not being satisfied, defined as a resistor mismatch. This mismatch results in a Common-Mode Rejection Ratio (CMRR), a static error in the transconductance transfer function, and non-linear errors in cases of the load impedance variation associated with (3.7) not being matched.

Note that we made certain simplifying assumptions while analyzing the circuit, as they introduce negligible errors while significantly reducing the size of these expressions; for instance, except when explicitly analyzing the effect of CMRR, we adopted R_1=R_3 and R_2=R_4. Furthermore, the open loop gain of the OpAmp is assumed infinite, except when analyzing the errors due to finite open loop gain. The sense resistor (R_{2b}) variations due to its temperature variation are not considered, apart from when analyzing the error caused by its own variation. Thus, each error is analyzed independently of the other.

Figure 3.2 shows a reduced model of the non-ideal OpAmp [64, 65] which is considered in the following subsections. All error deductions follow a similar analysis of the output current transfer function seen in Section 3.2.1.

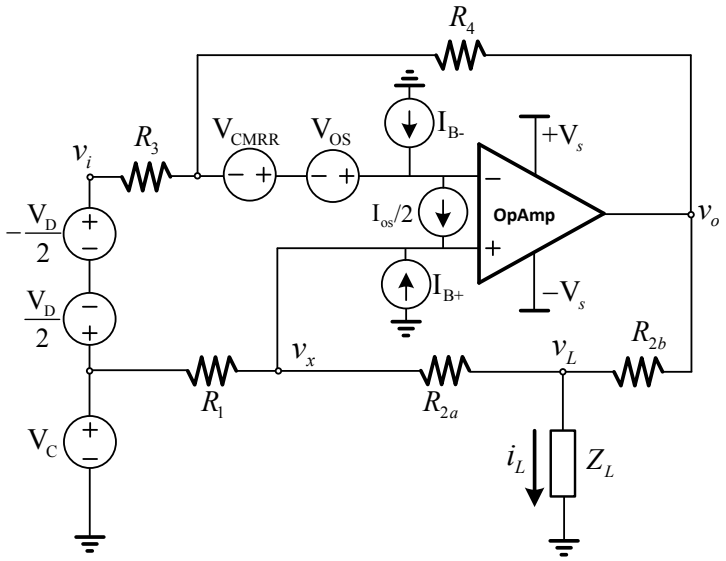

Figure 3.2: Equivalent circuit model used in the non-ideal analysis of the improved HCS circuit.

3.3.2 Offset Voltage and its Drifting

The voltage offset can be represented by a series DC voltage source in series with either of the OpAmp terminals [65]. The transfer function i_L/V_{os} can be found by removing all the other sources in Fig. 3.2. Equating the circuit, and assuming that (3.7) is satisfied, the relation between the load's current and the voltage offset is given by

$$i_L(V_{\text{os}}) = -\frac{1}{R_{2b}}\left(1+\frac{R_4}{R_3}\right)V_{\text{os}}. \tag{3.15}$$

Equation (3.15) shows that the offset voltage error is directly proportional to the R_4/R_3 ratio and inversely to the sense resistor R_{2b}. Assuming the amplifier temperature is steady, its offset voltage is constant, and the resulting output error is constant. Therefore, it is a calibratable error for a constant temperature.

The second problem is the offset voltage drifting, which is related to temperature variation. Typically, manufacturers provide a typical and worst-case drift to a one-degree variation in the OpAmp's temperature and representing the offset variation (ΔV_{os}) as a linear change with the temperature is reasonably accurate [65]. Therefore, it is possible to estimate the worst expected drifting in the load's current due to the amplifier's temperature. Equation (3.16) represents the current's variation due to a temperature variation. The error caused by such a variation is not linearly related to v_i, which makes it non-calibratable.

$$\Delta i_L(\Delta V_{\text{os}}) = -\frac{1}{R_{2b}}\left(1+\frac{R_4}{R_3}\right)\Delta V_{\text{os}}(T_f - T_i). \tag{3.16}$$

3.3.3 Input Bias and Offset Current and their Drifting

The input bias current analysis principle is similar to the offset voltage. We equate i_L as a function of the inverting and non-inverting terminal bias current seen in Fig. 3.2. These currents are given by I_{b-} and I_{b+}, respectively, and assuming (3.7) is matched, the output error contribution of each is given by (3.17) and (3.18).

$$i_L(I_{b-}) = -\frac{R_4}{R_{2b}} I_{b-} \tag{3.17}$$

$$i_L(I_{b+}) = \left(\frac{R_{2a}}{R_{2b}}+1\right) I_{b+} = \left(\frac{R_{2a}+R_{2b}}{R_{2b}}\right) I_{b+} \tag{3.18}$$

Assuming that $R_4 = R_{2b} + R_{2a}$ (which is the case), both currents are directly proportional to R_4 and inversely proportional to the sense resistor R_{2b}. Furthermore, similar values of I_{b+} and I_{b-} result in a load's current with the same magnitude but opposite directions, thus, canceling each other. In other words, the output error due to the input offset current (I_{os}) is

$$i_L(I_{\text{os}}) = \frac{R_4}{R_{2b}}\left(I_{b+} - I_{b-}\right) = \frac{R_4}{R_{2b}} I_{\text{os}}, \tag{3.19}$$

or equating directly as a function of the input offset current $I_{\text{os}}/2$ in Fig. 3.2, leads to

$$i_L(I_{\text{os}}) = \frac{R_4 + (R_{2b}+R_{2a})}{R_{2b}}(I_{\text{os}}/2). \tag{3.20}$$

The error caused by a constant bias offset current is also constant. Thus, it is a calibratable error that causes an offset error. Regarding drifting, the offset bias current (I_{b+} and I_{b-}) also varies depending on the OpAmp's temperature, the power supply voltage, and the common-mode voltage, for example. In the HCS circuit, this problem is minimized because if the drifting in both the positive and negative inputs of the amplifier are equal, it does not impact the load's current.

Nevertheless, the input offset current will likely change as the drifting may have differences between the terminals. Mapping that, however, is difficult since manufacturers do not always provide typical curves of the current offset deviation as temperature and common-mode voltage changes. If an amplifier provides such information, it is possible to evaluate the impact on the current's output. For instance, a temperature variation could be represented by

$$\Delta i_L(\Delta I_{\text{os}}) = \frac{R_4}{R_{2b}}\Big(I_{\text{os}}(T_2) - I_{\text{os}}(T_1)\Big), \tag{3.21}$$

where T_2 and T_1 are the temperatures, and I_{os} defined as a function of the temperature. Similarly to the offset voltage, the error caused by the offset current is not linearly related to the input voltage; therefore, it is a non-calibratable error.

3.3.4 Finite Open-Loop Gain

The deduction in Section 3.2.1 considered the ideal infinite open-loop gain for the circuit. Assuming a finite gain (A_o), (3.7)'s condition, and equating the load's current similarly, it will be given by

$$i_L = -\frac{R_4}{\frac{R_{2b}(R_3+R_4)}{A_o} + R_{2b}R_3} v_i. \tag{3.22}$$

For DC signals or low frequency, typical values of open-loop gain are above 90 dB for power OpAmps and higher for precision amplifiers. Thus, the finite gain causes a small error in the transconductance gain, which is linear and calibratable.

The manner is more critical for high-frequency use of the HCS circuit or ones with variable frequency. In such a scenario, the open-loop gain can degrade significantly, impacting the transconductance gain or causing it to vary depending on the frequency. This latter could result in a non-linear error. However, for the power HCS at low-frequency signals, and considering that our applications focus on accuracy, A_o is not a significant concern compared to other errors.

3.3.5 Common-Mode Rejection Ratio (CMRR) due to Resistor Mismatch

An amplifier CMRR is the ratio of the differential gain (A_{d}) and the common-mode gain (A_{cm}) of the amplifier [66]. In practice, CMRR is typically measured by changing the common-mode voltage V_{cm} and observing the change in output. This measured change can be referred to the input and considered as an offset voltage V_{CMRR} at the amplifier's inputs [65]. In other words, the CMRR error can be expressed in terms of the change in the input offset voltage with respect to changes in the input common-mode voltage [64, 65], such as the model of Fig. 3.2, and related by:

$$\text{CMRR} = \left(\frac{A_{\text{d}}}{A_{\text{cm}}}\right) = \left(\frac{\Delta V_{\text{cm}}}{\Delta V_{\text{CMRR}}}\right) \tag{3.23}$$

There are two sources of common-mode error in the HCS circuitry. The first is intrinsic to the amplifier (CMRR_{OA}) and the second (CMRR_{R}) is caused if the positive and negative feedback gain are not matched, i.e., (3.7) is not satisfied. The CMRR_{R} appears as a consequence of the resistor mismatch and the problem is similar to a differential amplifier [66]. Equating i_L/V_{D} and i_L/V_{C} in Fig. 3.2, and taking the relation between them leads to

$$\text{CMRR}_{\text{R}} = \frac{[R_3(R_{2a}+R_{2b}) + R_4R_1 + 2R_4R_{2a}]/2}{R_3(R_{2a}+R_{2b}) - R_1R_4}, \tag{3.24}$$

where the denominator $(R_3(R_{2a}+R_{2b}) - R_1R_4)$ represents the absolute resistor mismatch value. Alternatively, (3.24) can be simplified to (3.25), which also represents the CMRR_{R} considering that V_{D} is applied

only at the inverting input of the amplifier with the non-inverting input grounded.

$$\text{CMRR}_\text{R} \approx \frac{R_1 R_4 + R_{2a} R_4}{R_3(R_{2a} + R_{2b}) - R_1 R_4}. \tag{3.25}$$

A higher feedback gain (R_4/R_3 or R_2/R_1) results in a better common mode rejection to a similar resistor mismatch. For example, using 1% tolerance resistors and assuming a total mismatch with the same value results in approximately 46 and 60 dB of CMRR_R for a feedback gain of 1 and 10, respectively. Employing 0.1% resistors and considering the same mismatch value, the CMRR_R increases to 66 and 80, respectively, for the same feedback gains.

Power amplifiers have typical values of CMRR above 90 dB. Hence, unless precision resistors such as 0.01% tolerance are used, it is possible to see that the resistor mismatch tends to be more critical than the OpAmp CMRR for low-frequency signals [66]. An amplifier's CMRR might degrade considerably for higher frequencies, requiring both CMRRs to be addressed together, which is not the scenario for the proposed use of the HCS. Works [66] and [67] provide the combined CMRR analysis for differential amplifiers, which can be replicated in the HCS circuit.

At last, it is important to note that for a constant mismatch, and low-frequency signals where the OpAmp CMRR will not deviate, the total error caused by the common-mode voltage is a linear function of the input voltage [68]. Therefore, it is a first-order and calibratable error.

3.3.6 Transconductance Gain Deviation due to R_{2b} drifting

Equation (3.8) shows that the HCS transconductance gain depends on the power resistor R_{2b}. This resistor is subject to almost the same current i_L as the load, and in a power HCS, the magnitude of R_{2b} is in the ohms range, which makes heating expected in this component. If the R_{2b} resistance varies owing to a temperature rise, the transconductance will drift during operation resulting in a non-linear error. Thus, the design must address the effects of its resistance deviation due to thermal drift.

A resistor's resistance variation with its temperature is given by

$$\Delta R_i = (\alpha R_i \Delta T).10^{-6}, \tag{3.26}$$

where ΔT (°C) is the temperature variation in an interval $(T_f - T_i)$, α is the resistor's Temperature Coefficient of Resistance (TCR), given in parts-per-million per degree (ppm/°C), R_i is the resistor value at T_i, and ΔR (Ω) is the resistance variation due to the temperature variation ΔT.

Combining (3.26) and (3.8), taking the partial derivative, and assuming that temperature variations of R_3 and R_4 compensate each other, results in (3.27). This equation, deduced in [32], describes the relationship between the relative rate of change of the current load as a function of the resistor's TCR and the relative rate of change of the input voltage.

$$\frac{\Delta i_L}{i_L} = -\frac{\Delta R_{2b}}{R_{2b}} + \frac{\Delta v_i}{v_i} \tag{3.27}$$

The output current changes ideally should depend only on variations of the controlled voltage v_i, but

(3.27) shows it will also vary proportionally to ΔR_{2b}, and (3.26) dictates that. For instance, using a typical wirewound power resistor with a TCR of 100 ppm [69], and considering its temperature rises 50 °C above ambient temperature (which is reasonable for a power resistor), its resistance may vary 5000 ppm. That is equivalent to 0.5% of the resistor's absolute value, thus, causing a non-linear error of 0.5%, which is unrelated to v_i and is not mappable.

The resistor temperature during operation will depend on several factors, such as the output current curve and frequency. The problem is that the output current and the resistor temperature relationship are non-linear. Therefore, the resulting error due to R_{2b} is non-linear. Section 3.4 shows further discussion for the output error to a percentage variation of R_{2b} and shows examples of the resulting error in milli-amperes assuming distinct resistor's TCR.

3.3.7 Transconductance Static Gain Error due to Resistor Mismatch and Drifting associated with Z_L Variation

The last addressed problem is the resistor mismatch errors if (3.7)'s condition is not satisfied. Rewriting (3.5) as (3.28) shows that the transconductance gain will have a constant error in the presence of a resistor mismatch, which is dependent on the values of R_1, R_{2a}, Z_L, and the resistor mismatch value given by $R_4R_1 - R_3(R_{2a} + R_{2b})$.

$$i_L = \frac{R_4}{Z_L\left(\dfrac{R_4R_1 - R_3(R_{2a} + R_{2b})}{R_1 + R_{2a}}\right) - R_3R_{2b}} v_i \tag{3.28}$$

The denominator term multiplying Z_L in (3.28) is constant and results in a static and first-order error for a fixed load value. However, a non-linear transconductance drift will occur if Z_L changes during operation. This effect can be associated with the heating on the load or applications with varying loads, and (3.28) can be used to estimate the transconductance gain deviation depending on the scenario. A calibration can compensate for the static transconductance error but not for its drifting.

For example, assuming a 0.1% mismatch, with $10\ k\Omega$ resistors, a R_{2b} resistor of $1\ \Omega$, and a constant 10 ohms load, the transconductance transfer function will have a 0.5% first order error. Now, for every 20% variation of the load's resistance (2 ohms) during operation, the transconductance will have an additional 0.1% non-linear error, which translates to a 1 mA error to each ampere generated. Non-constant loads applications [32, 51] could lead to higher errors compromising accuracy and the VCCS linearity.

3.3.8 Other errors and the HCS stability

The circuit stability, the output impedance, PSRR (Power Supply Rejection Ratio), and further open-loop gain analysis might be required depending on the application. In our DC and low-frequency (< 100 Hz) high-current application focused on accuracy and precision, such problems are not a primary concern as the ones discussed. The practical implementation of [32] had no stability problems with the circuit. We also note that many power applications will have an inductive load, which limits the output frequency or makes it impossible to use the HCS circuit due to the OpAmp limited voltage swing (Section 3.2.2 discussion).

On the contrary, applications requiring high-frequency output currents require further analysis. Typical biomedical circuits are the case [28,29,47,70–72], and other power HCS authors [31,61] have addressed those errors. Thus, we do not replicate the stability and the output impedance analysis here. Instead, we redirect the reader to those works.

In addition, it is unfeasible to work with the proposed power HCS circuit in frequencies similar to those of biomedical applications and even the ones reported in [61]. High-power amplifiers have a limited power bandwidth in the required current and voltage range. For example, typical ± 3 A / ± 30 V will have a power bandwidth inferior to 70 kHz. However, many non-linearities and distortions related to PSSR, open-loop gain, slew-rate limitation, and CMRR might be increased for a narrower frequency range, such as 1-10 kHz. Therefore, expecting the same accuracy reported in this work for higher frequencies is unfeasible, and other topologies are likely necessary.

For instance, the power HCS of [61] uses an OPA564, a 1.5 A / 24 V amplifier, which has considerably better specifications and power bandwidth than a 3 A / 60 V (or ± 3 A / ± 30) OpAmp. Nevertheless, for authors seeking such a linear and accurate power HCS for higher frequencies, it would be necessary to combine our low-frequency accuracy/linearity analysis with the frequency study (stability and output impedance) seen in authors such as [61]. Additionally, the works of [28,29,47] could provide the theoretical background in the stability and the output impedance matters.

3.4 The Power HCS Requirements, Available Commercial Component Selection and Error Budget Simulation

The electronics design requires three independent VCCS channels to drive each pair of the magnetic field simulator, whose impedance is in the 10-$15\ \Omega$ range. Although the electronics described in Chapter 2 were tuned to generate an electrical current of ± 1.0 A, the HCS design must output ± 1.5 A as the maximum range. The typical output frequency ranges from DC currents up to 20 Hz, but the design should account for a maximum of 50 Hz.

Furthermore, the analysis in [32] shows a possible value range for R_{2b} to the application, which should stay below 2.5 ohms. Defining the R_{2b} range is a compromise between the required output current, the maximum output voltage swing, and the load's resistance or impedance. Higher values limit the output current and frequency values for a specific amplifier voltage swing, and (3.10) dictates these constraints. The proposed HCS requires an OpAmp with ± 30 V supply to comply with the load's characteristics, the specified maximum current and frequency, and the sense resistor threshold.

3.4.1 Possible Commercial Component and their Specifications

Component selection is essential to guarantee the HCS output accuracy and linearity. Although selecting precision components is of the utmost importance to reach the required specifications, the choice should stick to Commercial off-the-Shelf (COTS) components and avoid extremely high-cost parts, such as hundred dollars amplifiers and resistors.

3.4.1.1 Power Operational Amplifier

There are few COTS options for power OpAmps that combine a minimum output current of 2 A and a supply voltage of ± 30 V. Texas Instruments (TI) and Apex Microtechnology have parts complying with that, which are not easily found in many manufactures. The former has options like the LM675, the OPA544, the OPA548, and higher-rated options like the OPA541 and OPA549. The latter has the PA amplifier series, such as the PA09 and the PA10. However, the PA series amplifiers are much more expensive than the LM675 or OPA series from TI.

Table 3.1 summarizes the most important specifications of the LM675, the OPA544, and the PA09. The other options are similar to another one and are omitted. For example, the OPA548 has similar specs to the LM675, with a better CMRR and open-loop gain, and the PA10 is slightly worse than the PA09.

Except for the input bias/offset current, which is significantly higher on the LM675 OpAmp than the others, the remainder of the parameters is in the same order of magnitude. The OPA544 is the best cost-benefit solution overall, and the LM675 is the cheapest option. The error simulation budget in the following subsection uses the OPA544 and LM675 specifications as a baseline. Finally, due to the cost, the practical circuit testing reported later uses the LM675, the OPA544, and the OPA548 OpAmps.

Table 3.1: Specifications of the power operational amplifiers considered in the implementation of the proposed topology [73–75].

Error / Specification	Unit	LM675 [73]		OPA544 [74]		PA09 [75]	
		Typical	Worst-Case	Typical	Worst-Case	Typical	Worst-Case
Offset voltage	mV	± 1	± 10	± 1	± 5	± 0.5	± 3
Offset voltage drift	μV/°C	± 25	NS	± 10	NS	± 10	± 30
Input bias current	pA	± 200000	± 2000000	± 15	± 100	± 5	± 100
Input offset current	pA	± 5000	± 50000	± 10	± 100	± 2.5	± 50
Offset current drift over 25-100 °C	pA	NS		± 100*		NS	
$CMRR_{OA}$	dB	90	70	106	90	104	NS
Open loop gain	dB	90	70	103	90	98	80
PSRR	dB	90	70	100*		98*	
Gain-bandwidth product	MHz	5.5		1.4		150	

NS stands for an information not specified by the manufacturer.
An asterisk (*) indicates data extracted from the typical curves.

3.4.1.2 R_{2b} Sense Resistor

The sense resistor stability is critical and results in substantial non-linearities. Therefore, it is required to either use a very precise resistor or to oversize the resistor power rating to minimize temperature variation. Possible choices of R_{2b} use the results reported in [32] as a background, which identified many non-linearities caused by a 1 Ω / 10 W, despite having to dissipate a maximum power around 2 W.

Z-foil ultra-high precision resistors would be recommended to avoid these linearities and for less cost-sensitive precision requirements, such as the Vishay Precision Group VPR221SZ with a specified temperature

drift of $0.05-0.2$ ppm/°C. Since the magnetic field simulator requires three independent HCS channels, those types of resistors would impact the cost significantly.

For sub-ohms range resistors ($10-200$ mΩ), there are many options with ± 25 ppm/°C with power ratings around 5 W. However, for higher R_{2b} values, around the $1-2$ ohms range, there are limited options with a similar TCR and avoiding extremely high-cost and previsions parts. Therefore, a possible workaround to the $1-2$ ohms range is to use typical 50-100 W chassis mount power resistors with a TCR of 50 ppm. Oversizing its rating reduces its temperature variation, minimizing the non-linearities reported in [32], and may help avoid using higher-cost Z-foil precision resistors.

3.4.1.3 Remaining Resistors

The CMRR and transconductance gain are strongly sensitive to resistor matching. Despite that, the first-order calibration procedure can compensate for the CMRR errors, and ideally, the main interest is to reduce temperature drift between the resistor. A possibility to mitigate this issue is to use a precision-matched resistor array, such as the LT5400 from Analog Devices, formerly Linear Technology. They have a $\pm 0.025\%$ matching ratio and a manufacturer-specific "matching for CMRR" specification of $\pm 0.015\%$ (which translates into approximately 71 dB of CMRR for an HCS gain of 1), as well as ± 0.2 ppm/°C typical temperature drift.

Nevertheless, such arrays are much more expensive than typical $0.05-0.1\%$ resistors and have limited values combination (and a non-conventional footprint). Therefore, for practical testing, our work employs typical $0.05-0.1\%$ tolerance thin film resistors, specifically the ERA A type series from Panasonic Industry with a ± 10 ppm/°C temperature coefficient.

3.4.2 Error Budget Simulation

The error budget simulation is calculated using the OpAmp data specified at Table 3.1, the resistors discussed in the previous subsection, and all the errors deduced in Section 3.3. Furthermore, all errors were simulated and validated using the LTspice software and the model of Fig. 3.2.

The budget seeks to understand the impact of changing the OpAmp, varying the feedback gain, the R_{2b} value, and the absolute value of the resistors in the circuit. The goal is to understand the impact of those parameters in the order of magnitude of the load's current error. Four different conditions summarize the results. They provide enough information to understand the impact of each circuit parameter on the load's error and its order of magnitude.

The first case (circuit conditions used as a baseline) is the practical circuit of [32]. That circuit had an LM675 amplifier, a feedback gain of approximately 10 (to guarantee the LM675 stability), using the following resistors: R_1=R_3=1 $k\Omega$, R_2=R_4=10 $k\Omega$, and the sense resistor R_{2b} in the 1-1.2 ohm range. The second case uses the OPA544 instead of the LM675, with identical resistors as the previous one. The third reduces the feedback gain to 1 using the OPA544 by increasing the resistors R_2 and R_4 to 10 $k\Omega$. The last case uses similar conditions to the third but reduces R_{2b} to 0.1 Ω instead of 1 Ω.

Table 3.2 shows the error budget for the four considered scenarios. For each error and scenario, we consider

typical and worst-case errors. Those related to the OpAmp are given in Table 3.1. To the resistor CMRR and the mismatch effect, we consider a mismatch of 0.1% and 0.4% as typical and worst-case, respectively. At last, the error due to R_{2b} drift is shown depending on the percentage variation of its absolute value. Thus, Table 3.3 shows additional analysis to the R_{2b} error, displaying the error according the resistor TCR and different values of temperature variation.

Table 3.2: Error budget simulation for the HCS circuit considering four different scenarios.

Error Source Description[1]		Effect on the Load's [3]	Circuit Conditions for R_{2b} and Feedback Gain Values							
			LM675 - Case 1		OPA544 - Case 2		OPA544 - Case 3		OPA544 - Case 4	
			G=10, R_{2b}=1		G=10, R_{2b}=1		G=1, R_{2b}=1		G=1, R_{2b}=0.1	
			Typical	Worst-case	Typical	Worst-case	Typical	Worst-case	Typical	Worst-case
Offset voltage	Static (C)	mA	± 11	± 110	± 11	± 55	± 2	± 10	± 20	± 100
	Drift (NC)	mA/10°C	± 2.75	-	± 1.1	-	± 0.2	-	± 2.0	-
Offset Current	Static (C)	μA	± 500	± 5000	0.1	1	0.1	1	1	10
	Drift (NC) 50-100°C	μA/50°C	± 5000	-	1	-	1	-	10	-
A_0	Static (C)	mA/A	-0.35	-3.5	-0.08	-0.35	-0.015	-0.065	-0.015	-0.065
CMRR$_R$[2]	Static (C)	ΔmA/V_{CM}	± 1	± 4	± 1	± 4	± 1	± 4	± 10	± 40
R_{2b}	Drift (NC)	ΔmA/(ΔR_{2b}%)	± 9.9	-	± 9.9	-	± 9.9	-	± 9.9	-
Mismatch[2] and Z_L (Z_L=10Ω)	Static (C)	mA/A	± 9	± 36	± 9	± 36	± 5.5	± 22	± 46	± 164
	Drift (NC)	ΔmA/(ΔZ_L%)	± 0.085	± 0.34	± 0.085	± 0.34	± 0.05	± 0.20	± 0.45	± 1.4

[1] Static (C) refers to constant or first-order calibratable errors, and Drift (NC) stands to non-linear non-calibratable effects.

[2] The analysis of errors associated to the resistor mismatch and the CMRR$_R$ we consider 0.1% and 0.4% mismatch as typical and worst-case, respectively.

[3] Constant errors are indicated as mA or μA and the remainder of the errors are indicated in a the respective current unit per source of error. For example, mA/A indicates the load's error in mA per each ampere.

Table 3.3: Error Budget to R_{2b} temperature variation to different values of TCR.

Current Error (mA)				
TCR \ ΔT	10°C	25°C	50°C	75°C
0.2 ppm/°C	± 0.002	± 0.005	± 0.010	± 0.015
1 ppm/°C	± 0.010	± 0.025	± 0.050	± 0.075
25 ppm/°C	± 0.249	± 0.624	± 1.248	± 1.871
50 ppm/°C	± 0.499	± 1.248	± 2.494	± 3.735
100 ppm/°C	± 0.999	± 2.494	± 4.975	± 7.444

Note that the error signal depends on the output current direction, and both positive and negative errors are expected independent if the resistor has negative or positive TCR.

The error discussion is broken down into general considerations, the constant and first-order errors analysis, and non-linear errors.

3.4.2.1 General Errors Considerations

The first two cases of Table 3.2 allow assessing and comparing the LM675 and OPA544 expected errors in a similar circuit condition. The OPA544 has slightly better results with significant improvement in the errors due to the offset current. In the LM675, offset current causes errors in the same order of magnitude as the others,

while in the OPA544, it is almost negligible compared to the others. That is the advantage of amplifiers with Field-Effect Transistors (FET) inputs, such as the OPA544 and the PA09, compared to the LM675 and OPA548 amplifiers. Therefore, one must consider the effects of the offset current when using those or similar components.

The second and third cases assess the effect of the feedback gain in the circuit. Table 3.2 shows that reducing the feedback gain from 10 to 1 minimizes most errors effect, such as the offset voltage and current, the open-loop gain, and the mismatch-related errors (not the CMRR one). The CMRR error effect is similar to a given common mode voltage, however, smaller gains result in a higher dynamic voltage change in V_{cm} (see Fig. 3.1). Thus, that's the only negative effect of reducing the feedback gain, which, in theory, is a calibratable error.

The last observation is that the reduction of the sense resistor R_{2b} in the fourth case increases most errors. Despite minimizing the error due to R_{2b} self-heating, reducing R_{2b} value may compromise accuracy. Table 3.3 also shows that unless low TCR (< 1 ppm/°C) resistors are employed, they can result in significant errors unless a higher temperature variation is avoided. Therefore, using a higher sense resistor value would be beneficial, as long as the resulting TCR error is minimized, either using a low TCR resistor or guaranteeing the resistor's power dissipation effectiveness.

3.4.2.2 Constant and First-order Errors Considerations

All errors indicated by Static (C) in Table 3.2 are, in theory, calibratable. The static offset voltage and current result in a DC error in the output current, and the remaining ones are linear functions of the input voltage (V_{cm} has a linear relation with the input voltage).

It is notable that those errors are considerably high and have a significant percentage value of the maximum current. Even in the best overall scenario, the third case, it is unlikely that the HCS circuit will have a trustable initial accuracy without a calibration procedure. Offset voltage and the resistor mismatch can seriously impact the transconductance gain, which may lead to significant practical errors if one considers the ideal condition given by (3.8), as observed in [32]. Therefore, the error analysis shows the importance of performing a first-order calibration on the HCS circuit, especially if accuracy is necessary.

3.4.2.3 Non-linear Errors Considerations

Lastly, we address the non-linear errors in Table 3.2, indicated by drifting and non-calibratable (NC) effects. Those are the offset voltage drift and offset current drift, the power resistor temperature variation, and the load's impedance variation associated with the positive and negative feedback gain mismatch.

Offset voltage drift has a considerable effect in all cases independent of the OpAmp, and reducing the feedback gain is the alternative to minimize its effect. Offset current drifting is not a concern to FET input amplifiers but the LM675 cases show that it can impact the circuit linearity for non-FET amplifiers.

Table 3.2 shows that percentage variations of the power resistor R_{2b} have a huge impact on linearity, and Table 3.3 translates that to different resistor's TCR to given temperature variation. Using precise foil resistors

with a TCR smaller than 1 ppm/°C will reduce the non-linearities to dozens of micro-amperes. Employing typical resistors with TCRs of 50 or 100 ppm/°C may lead to non-linearities in the milli-amperes range if its temperature rises even 10 degrees. Therefore, oversizing its power ratings and providing a forced manner to dissipate heat would be an alternative to reduce non-linear effects.

Ultimately we have non-linear effects consequently to the load's impedance variation. Avoiding heat or load variation might be unfeasible, depending on the application. Thus, the alternative in such conditions is to use ultra-precise resistors or arrays, as mentioned before.

3.5 The Practical Test Circuit, Methodology and Results

The same HiL setup described in Chapter 2 allows testing of the circuit. The dSPACE DS2211 board Digital-to-Analog Converter (DAC) controls the input voltage of the HCS channel. That circuit, reproduced again in Fig. 3.3 to facilitate the analysis, is used to evaluate the power HCS accuracy and linearity.

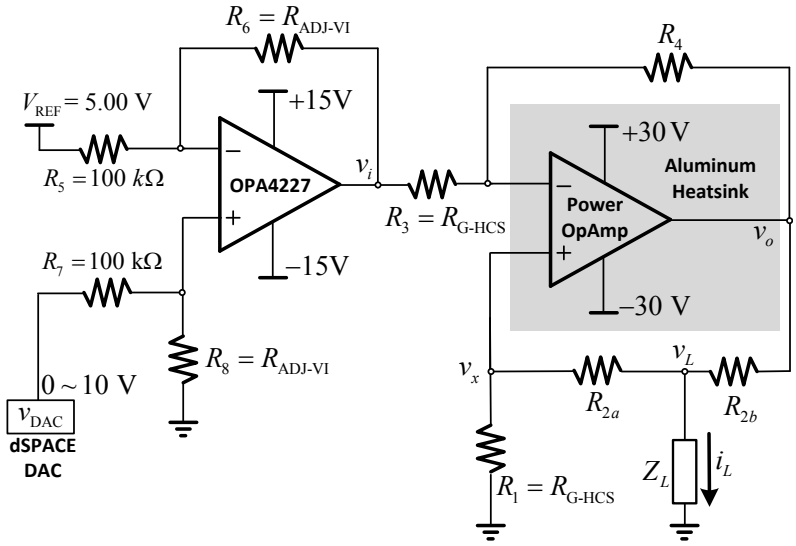

Figure 3.3: Schematic of the HCS test circuit. The resistors R_3 and R_4 adjust the HCS feedback gain, and subsequently, R_6 and R_8 are adjusted depending on the maximum desired output current value.

As explained in the previous chapter, the circuit has two stages: the conditioning differential amplifier circuit, which shapes the input 0-10 V signal into a symmetric signal v_i suitable for the following block, the Howland current source itself. The HCS feedback gain is defined by R_1–R_4. The pre-attenuator stage gain is adjusted by R_6 and R_8 resistors, which depend on the feedback gain of the HCS and the desired output current. Combining the differential amplifier equation with (3.8) and assuming perfect resistor matching in both stages, the theoretical (ideal) load's current as a function of v_{DAC} is given by:

$$i_L(v_{\text{DAC}}) = -\frac{R_4}{R_3 R_{2b}} \frac{R_6}{R_5} (v_{\text{DAC}} - 5), \tag{3.29}$$

which is the equation used to evaluate the non-calibrated errors of the HCS circuit.

Note that there are some requirements when matching the resistors. For example, we first define R_{2b} and R_4 values in each case. Consequently, to match the condition of (3.7), $R_{2a} = R_4 - R_{2b}$. In the circuit

implementation, R_{2a} value is obtained using series and parallel precision resistors. See [32] for additional information.

3.5.1 Test Methodology

The test methodology to assess the accuracy and linearity of the HCS is similar to those used in [32] and later replicated in the analysis of [34]. The test simulates a DC sweep, linearly varying the HCS input voltage at constant steps and a very low frequency. To summarize, the dSPACE HiL DAC is configured to generate several voltage cycles per test. Each cycle starts at 5 V (relative to an output current of zero amperes). Next, the voltage is increased linearly up to 10 V, producing the maximum negative current. Then the voltage is linearly decreased to 0 V, which produces the maximum positive voltage. Finally, the voltage is linearly swung back to 5V, ending the cycle. Each voltage step stands for 16 LSB of the DAC, making a total of 512 points per cycle. The voltage is kept constant for a few seconds between steps. The DAC input voltage and the VCCS output current are measured and acquired by a precision multimeter.

Subsection 3.5.2 reports the initial assessment of the linearity, calibration, and repeatability of the HCS used in the first implementation of the magnetic field simulator [25, 26]. That circuit had an LM675 OpAmp, feedback gain of approximately 10 in the HCS stage, and a typical 10 W wirewound resistor of 1.2 Ω, similar to the first case simulated in the Error Budget Simulation of the previous section. In that test, we repeat 18 cycles, and the circuit is kept constant for 2 seconds at each point, resulting in a procedure with an elapsed time of 05:08:28 h. That test sought to evaluate the circuit's non-linearities and repeatability over several hours.

Each cycle data is used to calculate a first and third-order polynomial fit of the data, which allows for assessing the circuit's linearity and repeatability. We also evaluate the non-linear errors of the output by analyzing the first-order calibrated transconductance equation versus the measured data. Reference [32], seen in Appendix C, presents an extended set of results of that initial validation. In Subsection 3.5.2, we show the most relevant test to understand the non-linearities observed in the first HCS implementation and the first-order polynomial fit consistent during a procedure with extended period of time.

The remainder of the Subsections, 3.5.3 to 3.5.6, show the tests, based on the cases described in the Error Budget Simulation, performed to establish an improved version of the HCS. These tests led to the final design described in Section 2.3 and used throughout the thesis. These results are partially seen in [34], whose initial pages are shown in Appendix D. We evaluate the non-calibrated output current and its error for each test, which generates the first-order polynomial fit. The first-order parameters are used to generate the calibrated output current and its error. In each test, we repeat two voltage cycles, and the voltage is kept constant for 5 seconds per point; hence, each cycle has 2560 seconds. Except for the test reported in Section 3.5.6, which compares different output current swings, the differential amplifier stage resistors were tuned so that the HCS would generate a maximum output current swing of approximately ± 1.35 A.

In Section 3.5.3, we repeat the conditions of the previous circuit (LM675 OpAmp, HCS feedback gain around 10, and the 1.2 Ω/10 W R_{2b} resistor) to compare the results for three different OpAmps: the LM675, the OPA544, and the OPA548. Next, the circuit with the OPA544 OpAmp is used to evaluate the outcome

for distinct R_{2b} resistors and different gains in the HCS feedback. Those results are reported in Sections 3.5.4 and 3.5.5, respectively. Combining these previous results, Section 3.5.6 assesses the circuit linearity for the best HCS condition for different maximum currents.

3.5.2 First HCS Linearity and Calibration Test Results

The initial HCS design had a feedback gain of approximately 10, using $R_4 = 10.1$ kΩ, $R_3 = 1$ kΩ, and $R_{2b} = 1.2$ Ω resistors. The conditioning state resistors value were $R_5 = 100$ kΩ and $R_6 = 3.3$ kΩ. Therefore, the theoretical equation was given by

$$i_{L_{\text{ideal}}} = -0.27775 \cdot v_{\text{DAC}} + 1.38875. \tag{3.30}$$

As explained in the previous subsection, the HiL setup generated 18 cycles of 512 points each, during approximately 5 hours, to assess the HCS linearity. Table 3.4 shows each cycle's coefficient of the data's first-order and third-order polynomial fit, the average value, and the standard deviation.

Table 3.4: First-order and third-order polynomial fit coefficients of $i_L \times v_{\text{DAC}}^i$ for all 18 cycles completed in the test.

Cycle	First Order Fit Coefficients		Third Order Fit Coefficients			
	Coef. A	Coef. B	Coef. A	Coef. B	Coef. C	Coef. D
1	1.341292	−0.272393	1.333576	−0.266970	−7.74E-04	2.57E-05
2	1.341250	−0.272378	1.333518	−0.266900	−7.92E-04	2.70E-05
3	1.340846	−0.272336	1.333580	−0.267250	−6.92E-04	2.02E-05
4	1.341317	−0.272397	1.333600	−0.266929	−7.85E-04	2.63E-05
5	1.341242	−0.272389	1.333445	−0.266872	−7.91E-04	2.64E-05
6	1.341285	−0.272394	1.333521	−0.266948	−7.72E-04	2.52E-05
7	1.341286	−0.272393	1.333599	−0.266953	−7.80E-04	2.61E-05
8	1.341338	−0.272393	1.333666	−0.266959	−7.80E-04	2.62E-05
9	1.341258	−0.272391	1.333587	−0.267008	−7.63E-04	2.49E-05
10	1.341283	−0.272394	1.333465	−0.266888	−7.87E-04	2.62E-05
11	1.341218	−0.272384	1.333576	−0.266998	−7.67E-04	2.52E-05
12	1.341181	−0.272394	1.333472	−0.266928	−7.86E-04	2.65E-05
13	1.341254	−0.272406	1.333491	−0.266900	−7.93E-04	2.68E-05
14	1.341336	−0.272405	1.333536	−0.266866	−7.98E-04	2.70E-05
15	1.341354	−0.272372	1.333638	−0.266921	−7.79E-04	2.59E-05
16	1.341390	−0.272362	1.333662	−0.266917	−7.78E-04	2.59E-05
17	1.341363	−0.272344	1.333690	−0.266934	−7.71E-04	2.54E-05
18	1.341283	−0.272340	1.333521	−0.266866	−7.79E-04	2.56E-05
average	1.341251	−0.272380	1.333562	−0.266953	−7.74E-04	2.56E-05
std. dev.	±0.0001175	±0.0000218	±0.0000724	±0.0000867	±0.23E-04	±0.15E-05

Table 3.4 allows us to draw a few conclusions about the initial HCS design used in [26] and [25]. First, comparing the same coefficients during each cycle confirms the circuit's repeatability during the five hours test. The repeatability is supported by the standard deviation of all parameters on a much smaller order of magnitude than the coefficients A and B. Furthermore, considering all measurements, we can find the calibrated equation of the transconductance gain. Hence, the calibrated function of the output current is given by the average first-order coefficients, which results in the following:

$$i_{L_{\text{calibrated}}} = -0.272380 \cdot v_{\text{DAC}} + 1.341251. \tag{3.31}$$

Although (3.30) and (3.31) are close, the slope coefficient difference is approximately 2% and the other almost 3.5%. This difference indicates that the non-calibrated output accuracy is not guaranteed. The next subsection compares the same circuit for multiple OpAmps and shows the uncalibrated graphical error. For that reason, this analysis is left for that section.

At last, we address the non-linearities of the results. The coefficients of the third-order polynomial fit in Table 3.4 confirms that the output current has a linear tendency. The higher-order terms, C and D, are on a much smaller magnitude than the first order coefficient A. Nevertheless, the source has some non-linearities that must be evaluated. Figure 3.4 shows all measurements points and the first-order fit function given by (3.31). Three areas are highlighted in that graph, and they clear indicates that the measured data error varies during the interval. The non-linear error, calculated using the difference of the measured data to the calibrated curve of (3.31), is depicted in Fig. 3.5 for a better analysis.

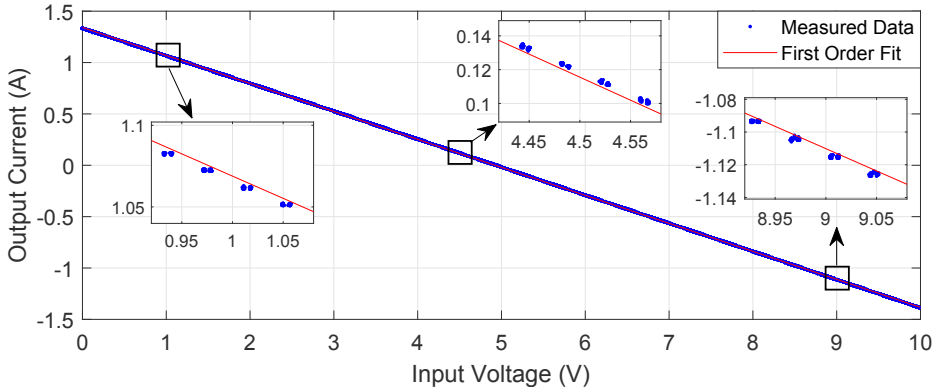

Figure 3.4: Plot of the HCS output current versus input voltage (v_{DAC}) for all measurements and the first-order polynomial fit curve.

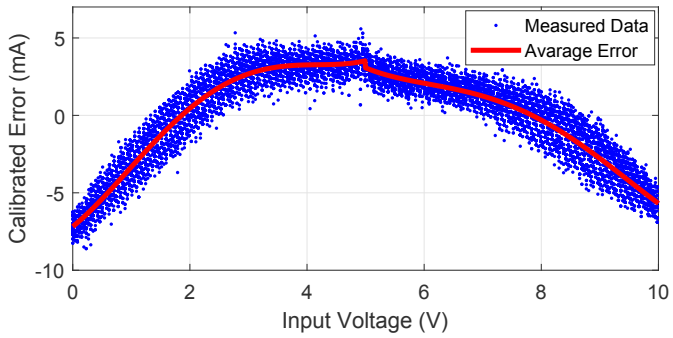

Figure 3.5: Calibrated results for the first test: the difference between the first-order calibrated transconductance equation for all 18 cycles measurements and the average error for each v_{DAC} value.

The absolute non-linear error of Fig. 3.5 varies from approximately -7.5 mA up to 4 mA. Therefore, the calibrated output has an error with a peak-to-peak value of 11.5 mA. Assuming the maximum current was approximately ± 1.35 A, the maximum percentage error is $100 \cdot (0.0115/2.60 \approx 0.43)\%$. Another mention is that the error is not symmetric for positive and negative currents. We remind that an input voltage from $0-5$ V generates a positive output current and a negative value from $5-10$ V.

Depending on the application, this error is a minor concern. For example, when using the magnetic field simulator in a closed-loop topology, they are compensated by the controller [25]. Also, the source linearity is excellent considering the cost-effective solution using the LM675, which is the cheapest power OpAmp available

in the required voltage/current range. However, depending on the application, these non-linearities above 10 mA would decrease the accuracy, which is the case to generate an open-loop magnetic field. Therefore, the following sections show the practical evaluation of the circuit to minimize the non-linearities in the output current.

3.5.3 LM675, OPA544 and OPA548 Comparison Results

Owing to the description in the methodology, the HCS of the previous section was tested using the LM675, the OPA544, and the OPA548 OpAmps. Figure 3.6 displays the uncalibrated and calibrated results of the OpAmp comparison test, and Table 3.5 shows the numerical analysis. The uncalibrated results are obtained by subtracting the measurements from the expected current from the ideal transconductance equation. The calibrated result displays the difference between the measurements and the calibrated transconductance equation calculated using the coefficients of the first-order fit.

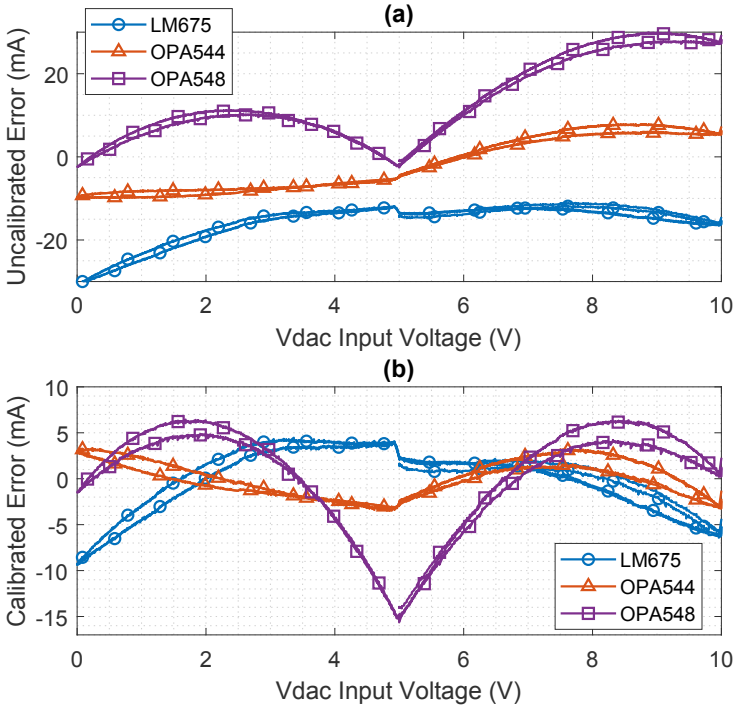

Figure 3.6: Uncalibrated (a) and calibrated (b) results for the test comparing the errors for three distinct power OpAmps. Test conditions: feedback gain of 10 for the HCS stage and the $1.2\Omega/10$W wirewound R_{2b} resistor.

Table 3.5: Numerical error results of the OpAmp test comparison seen in Fig. 3.6.

Test Condition		**Current Error (mA)**				
OpAmp (Current)	Type	Min.	Max.	Pk-pk	Avg.	RMSE
LM675	Uncalb.	-30.9	-11.1	19.8	-15.8	16.5
(± 1.38 A)	Calib.	-9.4	4.5	13.9	8.5	3.4
OPA544	Uncalb.	-9.9	7.9	17.8	-1.7	6.5
(± 1.38 A)	Calib.	-3.5	3.3	6.8	-0.0	1.9
OPA548	Uncalb.	-2.6	29.9	32.5	13.1	16.4
(± 1.37 A)	Calib.	-15.6	6.5	22.1	9.1	5.7

Both the graphical and the numerical results demonstrate that the practical uncalibrated current diverges

significantly from the expected theoretical one calculated by (3.8). To confirm that, equations (3.32)-(3.34) show the calibrated transconductance equation for the LM675[1], the OPA544, and the OPA458, respectively. The coefficients have non-negligible differences from the ideal curve, shown in (3.30).

$$i_{L_{\text{LM675-calibrated}}} = -0.276607 \cdot v_{\text{DAC}} + 1.367217 \tag{3.32}$$

$$i_{L_{\text{OPA544-calibrated}}} = -0.275623 \cdot v_{\text{DAC}} + 1.376102 \tag{3.33}$$

$$i_{L_{\text{OPA548-calibrated}}} = -0.274956 \cdot v_{\text{DAC}} + 1.387840 \tag{3.34}$$

These deviations in the calibrated curve of the first-order coefficient of the curve i_L versus the input voltage confirm that the initial accuracy is not guaranteed, and the practical implementations transconductance gain may have significant errors from the theoretical one of (3.8).

This result reinforces the theoretical error budget analysis in Table 3.2, and the uncalibrated and calibrated errors for the LM675 and the OPA544 are compatible with the order of magnitude of the error budget simulation. Table 3.5 also displays that the error is reduced considerably after the first-order calibration procedure. The reduction of the peak-to-peak error for all amplifiers shows that uncalibrated current had first-order errors that were compensated by the calibration. Accordingly, Fig. 3.6(b) shows the non-linear errors existing in the HCS circuit, which are asymmetric for the negative and positive output currents (input voltages below 5V generate positive currents, and above that threshold, negative values).

At last, it is notable that the OPA544 has superior results compared to the others. The non-linear error magnitude is smaller than the other amplifiers, and the Root-Mean-Squared Error (RMSE) data of the calibrated output current collaborate with the graphical results of Fig. 3.6. Hence, the OPA544 is used in the remainder of the tests to evaluate the other conditions.

3.5.4 R_{2b} Resistor Comparison Results

The test to compare resistors with distinct resistance and power rated values uses three R_{2b} part-numbers. The first is the typical 10 W wirewound used in the previous tests and the second is a 50 W chassis mount resistors P/N THS501R2J from TE Connectivity, both with $1.2\ \Omega$ and 50 ppm/°C. And the last is a $0.1\ \Omega/7$ W and 20 ppm/°C SMD resistor from Rohm Semiconductor, P/N GMR100HTCFAR100. The test was performed using the OPA544 amplifier and a feedback gain of approximately 10, similarly to previous analysis.

For the first two resistors, the circuit is identical to that reported in the previous sections. For the $0.1\ \Omega/7$ W, the value of the R_6 resistor of the practical circuit of Fig. 3.3 is increased by 12 times, compensating that the R_{2b} value is decreased by the same ratio. Hence, the theoretical transconductance remains the same for all cases.

Figure 3.7 shows the non-linear calibrated errors for all resistors. Note that the results for $1.2\ \Omega$ resistors are duplicated and shown in a different y scale for better visualization. Table 3.6 displays the numerical analysis of the test. Note that we omit the uncalibrated errors for simplification since the uncalibrated lack of

[1] This test took part using a different LM675. Hence, the coefficients for the LM675 OpAmp in this section are expected to deviate from the one shown in Section 3.5.2.

accuracy has already been established in the previous results.

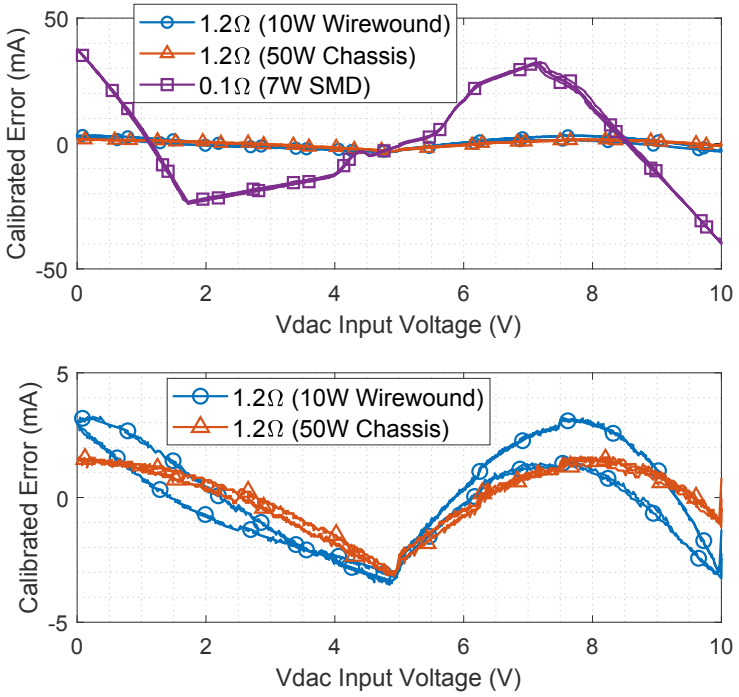

Figure 3.7: Calibrated results for the test comparing the errors for three distinct sense resistors (R_{2b}). Test conditions: feedback gain of 10 using the OPA544 OpAmp.

Table 3.6: Numerical error results of the R_{2b} test comparison seen in Fig. 3.7.

Test Condition		**Current Error (mA)**				
R_{2b}	i_L (A)	Min.	Max.	Pk-pk	Avg.	RMSE
$1.2\ \Omega$ / 10 W Wirewound	± 1.38	-3.5	3.4	6.9	-0.001	1.9
$1.2\ \Omega$ / 50 W Chassis Mount	± 1.33	-3.2	1.8	5.0	-0.002	1.3
$0.1\ \Omega$ / 7 W SMD	± 1.17	-40	38	78	-4.5	19.3

The first observation from the results is that using a smaller R_{2b} value increases non-linearities by ten times compared to the other cases with the $1.2\ \Omega$ resistor. Furthermore, the maximum current swing was reduced to ± 1.18 A, indicating that the practical transconductance gain diverged significantly from (3.29). We can verify that by inspecting the calibrated output current obtained using the first-order coefficients using the measurements, given by:

$$i_{L_{0.1\ \Omega/7\ \mathrm{W}}} = -0.226259 \cdot v_{\mathrm{DAC}} + 1.141432. \tag{3.35}$$

Since the conditioning stage resistors were adjusted to compensate for the smaller value of R_{2b}, the theoretical output current equation is the same given by (3.30), repeated below to facilitate the analysis:

$$i_{L_{\mathrm{ideal}}} = -0.27775 \cdot v_{\mathrm{DAC}} + 1.38875, \tag{3.36}$$

which confirms that the errors have increased considerably with the reduction of the R_{2b} resistor.

Such a result is compatible with the error budget simulation analysis made in Section 3.4.2. Furthermore, comparing the third and fourth cases simulated in Table 3.2 indicates that reducing the R_{2b} value by ten times

could increase both calibrated and non-calibrated errors by the same amount. Hence, the test confirms that decreasing the resistor may significantly impact the circuit's accuracy and linearity.

Finally, comparing the results of the wirewound and the chassis mount resistor shows the effect of the R_{2b} temperature variation in the circuit non-linearities. The chassis resistor reduces the peak-to-peak and RMSE error by approximately 30%. These results reveal that despite dissipating a maximum of 2.2 W, oversizing R_{2b} to a 50 W instead of a 10 W is necessary to minimize the non-linear effects due to temperature variation of R_{2b}. Further improvements would require using ultra-precise foil resistors, which are not shown here due to their increased cost.

3.5.5 Feedback Gain Comparison Results

The circuit with the OPA544 and the $1.2\ \Omega$ / 50 W chassis mount resistor is used in the test to assess the effect of different feedback gain in the HCS circuit linearity. To sum up, we used the conditioning stage circuit to compensate for the HCS feedback gain reduction to maintain the output equation as closed as possible from the original. For example, to reduce the gain from 10 to 1 (G=1), R_3 and R_1 are increased to 10.1 kΩ to match R_2 and R_4, and R_6 and R_8 are increased to 33 kΩ. A similar change is made for every gain tested.

This test objective is to evaluate the non-linearities of the circuit. Consequently, only the calibrated results are shown, i.e., the measurement differences for the calibrated transconductance equation. Fig. 3.8 displays the calibrated errors for four values of gains, G=0.5, G=1, G=5, and G=10. Table 3.7 shows the numerical analysis of the data[2].

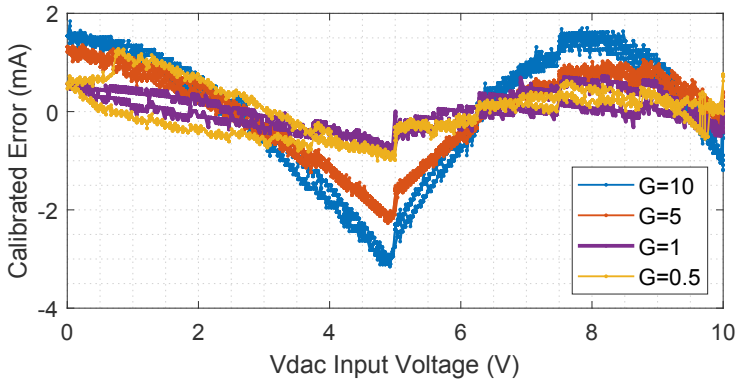

Figure 3.8: Calibrated results for the test comparing the errors for different values of the HCS feedback gain. Test conditions: OPA544 using the 1.2 Ω / 50 W chassis mount resistor.

Table 3.7: Numerical error results of the HCS feedback gain test comparison seen in Fig. 3.8.

Test Condition		**Current Error (mA)**				
Gain (G)	i_L (A)	Min.	Max.	Pk-pk	Avg.	RMSE
10	± 1.33	-3.15	1.84	4.99	-0.002	1.29
5	± 1.29	-2.27	1.45	3.72	-0.002	0.89
1	± 1.34	-0.88	0.72	1.60	-0.000	0.35
0.5	± 1.35	-1.00	1.27	2.27	-0.001	0.47

[2]The data used to assess the condition G=10 differs from that reported in [34]. In that work, the analysis considered a test that resulted in a smaller maximum current output swing, a consequence of the conditioning stage resistors. In this thesis, we use the previous section's result for G=10. Hence, Fig. 3.8 and Table 3.7 have different results compared to that work for G=10. Nevertheless, the analysis and conclusions are not impacted.

The calibrated results show the reduction of non-linear effects when decreasing the feedback gain from 10 to 5 and from 5 to 1. The first reduces the peak-to-peak and RMSE error by 25% and 32%, respectively, and the latter further reduces them by 50% and 60%, respectively. Such a result is befitting with the error budget simulation analysis shown in Section 3.4.2.

Although further reductions of the gain below the unit value have improved the negative current semi-cycle (input voltages above 5 V), they ended up deteriorating the linearity to positive output currents, as seen in Fig. 3.8 for G=0.5 and input voltages between 0-5 V. Addressing that, however, is left for future analysis. In addition, the work of [26] has shown that reducing the feedback gain may lead to stability issues and oscillations in the errors, and these issues occur mainly for positive output currents.

Therefore, the HCS circuit with unitary feedback gain has yielded the best outcome in terms of linearities and accuracy.

3.5.6 Best Circuit Results for Different Currents Values

The last test addresses the circuit linearity and accuracy to the best conditions obtained for different maximum load currents. The HCS circuit uses the 50 W chassis mount and $1.2\ \Omega$ R_{2b} resistor, $R_4 = 10.1$ kΩ, $R_3 = R_1 = 10$ kΩ. The differential amplifier stage was tuned to generate approximately ± 1.0 A, ± 1.5 A, and ± 2.1 A, respectively. In that stage, R_5 and R_7 values are kept at 100 kΩ, and R_6 and R_8 were adjusted to generate the three distinct current values.

Figure 3.9 shows the calibrated results obtained for all three values of the output current swing tested. Table 3.8 displays the numerical data analysis of the calibrated results.

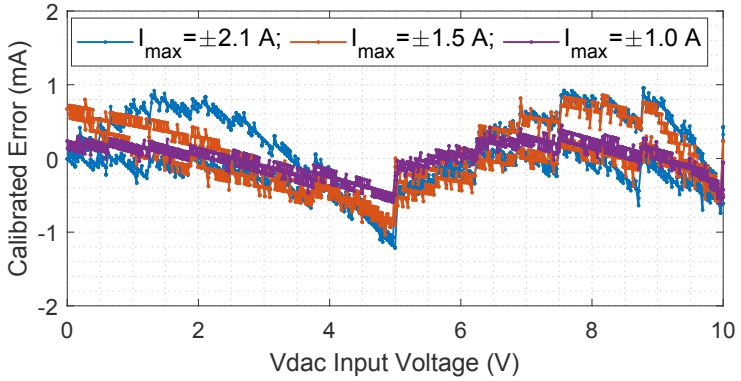

Figure 3.9: Calibrated results for the best HCS circuit tested for different maximum values of the load's current. Test condition: OPA544, $1.2\ \Omega$ chassis mount resistor, and unit HCS feedback gain.

Table 3.8: Numerical error results of the HCS test best circuit combination for different maximum currents seen in Fig. 3.9.

Test Condition	**Current Error (mA)**				
i_L (A)	Min.	Max.	Pk-pk	Error (%)	RMSE
± 0.98	-0.62	0.45	1.07	0.054	0.21
± 1.50	-1.04	0.86	1.90	0.063	0.41
± 2.12	-1.21	0.95	2.16	0.050	0.46

The final HCS design has errors in the ± 1 mA range, and all cases had an error smaller than 0.1% of

the load's current total swing. At last, increasing the maximum current increases the graphical non-linearities seen in Fig. 3.9, but they do not vary in terms of the percentage of the load's current. Nevertheless, the RMSE error is significantly smaller when driving smaller values, proving that accuracy is better for a ± 1 A output and tends to deteriorate for higher values.

3.6 HCS Results Discussion and Conclusions

The final circuit results with linearity and accuracy better than 0.1% of the total output current swing are outstanding considering the simplicity of the HCS design and that the proposed design avoids ultra-precise and high-cost components. Hence, the linear VCCS based on the Howland topology is simple to be built and can achieve excellent results. Practical results have collaborated with the theoretical analysis and the error budget simulation for typical commercial components. Besides, the data and tested cases display the importance of avoiding thermal variations in the power resistor and OpAmp.

Furthermore, the R_{2b} resistor is essential in the design. Smaller values increase the amplifier's errors, but higher values may cause errors due to heating on the resistor and limit the maximum load's current. Therefore, selecting the best sense resistor is a compromise, and oversizing its power ratings or using low TCR (< 1 ppm/°C) is necessary to avoid non-linear errors.

Addressing the non-linear errors due to resistor mismatch associated with Z_L variations was not observable in our practical testing. More specific testing with a known mismatch and a load more susceptible to impedance variations would be necessary. This investigation is left for future works, but our analysis and the error budget simulation in the previous section characterize the expected error to provide a base value.

The HCS circuit is one of the most simple VCCS topologies, requiring a single amplifier and passive components, and designing a high-power HCS is no different. The drawback of the power circuit is its initial accuracy (differences in the theoretical transconductance transfer function versus the practical one) and its sensitivity to thermal effects on the power OpAmp and the sense resistors, which leads to non-linearities in the load's current.

A calibration procedure is essential to guarantee the HCS circuit performance in accuracy-critical applications. The long-term testing with 18 repeated cycles has verified the circuit repeatability, demonstrating that the calibration mitigates linear and first-order errors. Furthermore, the results proved that a low-cost HCS solution using commercially available off-the-shelf components might achieve accuracy and linearity better than 0.1% using the OPA544 amplifier and avoiding heating in the power resistor R_{2b}.

Future works, or future improvements of the magnetic field simulator, can examine the HCS circuit with better specifications parts (such as amplifiers from Apex Microtechnology, a foil sense resistor, and resistors arrays) and for higher-current and voltage scenarios. Nevertheless, the circuit performance is limited by the thermal effects of the power amplifier and sense resistor. Another possibility is to investigate a power composite amplifier HCS [62, 76], which could, in theory, improve accuracy and linearity.

4 Methodology to Generate the Magnetic Field and the Setup Calibration

This chapter presents the procedure for calibrating the magnetic field simulator and generating the open-loop magnetic field. The open-loop accuracy is essential for the time-varying interference calibration analysis with the proposed methodology using the simulator. Therefore, this chapter discusses the setup calibration model, the practical approach for the open-loop use of the Helmholtz coil, and the investigation of the open-loop magnetic field results. The latter includes tests of the simulator setup capability, accuracy, and repeatability. Besides, the chapter shows the operation of the simulator in a closed-loop topology and its results using the fluxgate sensor as the reference (ground truth). Although the closed-loop does not allow for some of the contributions, it provides a more accurate and straightforward solution to use the simulator for cases where the non-compensated open-loop technique is not mandatory.

The work of [26] reports previous open-loop calibration results using the same electronics as [25]. Those results had poor open-loop accuracy, and the setup could not provide a platform for the magnetometer analysis subject to time-varying interference. Consequently, the electronic systems improvements reported in the previous chapters were paramount. The remainder of the chapter is organized as follows. Section 4.1 briefly introduces the open-loop and closed-loop operation of a magnetic field simulator. Section 4.2 shows the theoretical setup calibration model, and Section 4.3 the practical procedure that yielded the best results during the work. The information seen in those sections focuses on the relevant information required for using the methodology independent of the magnetic field simulator. The results and repeatability investigation are seen in Sections 4.4 and 4.5. A comparison between calibration models and further discussion on the practical procedure are seen in Section 4.6. Analysis and results in this section are relevant for future use of our magnetic field simulator but not crucial for reproducing the methodology. At last, Section 4.7 reports the closed-loop results of the improved simulator using the approach and controller design described in [25].

4.1 Overview of the Simulator Operation generating Open-Loop or Closed-Loop Magnetic Field

Magnetic field simulators have been used to evaluate magnetometer calibration, simulate Earth's magnetic field, and test attitude determination and control systems in many works [14–21, 24, 26]. The most straightforward way to use such a system is in a closed-loop magnetic field using a reference sensor as ground truth, as done in [15, 18, 20, 25]. Figure 4.1 illustrates a generic diagram of the closed-loop use of a magnetic field simulator. The feedback signal of the controller is the measurements of a reference sensor, whose data is used as the ground truth magnetic field, and the controller is responsible for managing the current sources.

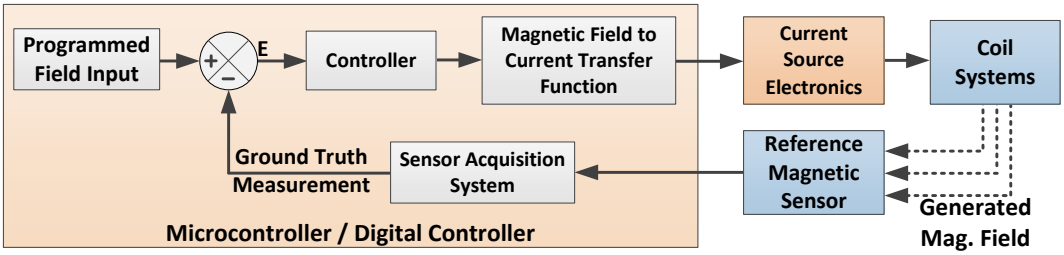

Figure 4.1: Generic diagram of a closed-loop compensated operation of a magnetic field simulator. The reference sensor and the magnetometers under test are placed within the coil's uniformity volume.

In the closed-loop operation, the reference sensor and the magnetometer (or the system under test) are placed within the coil's uniformity region. Thus, the SUT magnetometer is subject to the *true* field of the reference sensor. However, if the SUT's electronics generate time-varying interference or an additional electronic seeks to simulate these errors, they are measured by the reference sensor; consequently, the controller loop will compensate them. Time-varying bias calibration, for example, is not possible using this method.

The simulator must generate the magnetic field without the controller loop to provide an adequate test bench in conditions depending on the analysis desired, such as the time-varying bias problem. Figure 4.2 shows a generic diagram of a simulator generating the non-compensated magnetic field. It is important to note that the current source may have a controller or a feedback system. The problem in such an operation is to guarantee the accuracy of the generated magnetic field.

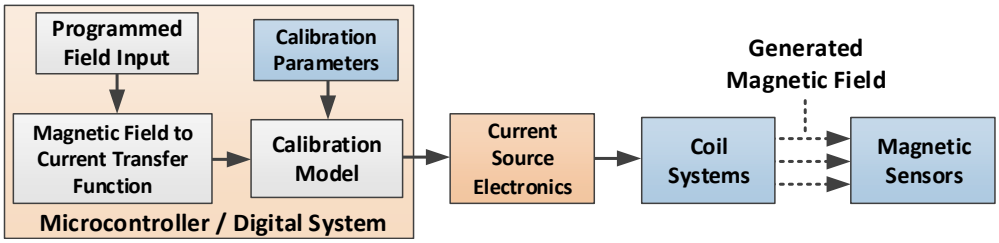

Figure 4.2: Generic diagram of an open-loop operation of a magnetic field simulator.

While many studies utilize three-axial coils in an open-loop configuration [14,17,21,24,25] and acknowledge the need for calibration [14, 21], only a few authors extensively address the calibration procedure and provide detailed simulator results. For example, [24] and [26] delve into such discussions. However, the accuracy reported in these works was far from the sub-milligauss accuracy sought here when operating in the open-loop topology.

The magnetic field simulator has various error sources, both linear and non-linear, originating from the coil system and electronics, as discussed in the following section. Besides, the issue is more pronounced in low-cost magnetic field simulators, which in many cases, like ours, are located outside a purpose-built facility free from magnetic disturbances. Thus, achieving reasonable accuracy requires calibration.

4.2 The Theoretical Calibration Model of the Magnetic Field Simulator

The magnetic field simulator setup is subject to many errors: scale factor errors from each pair assembly; misalignment between each Helmholtz coil pair; offsets and scale factor errors caused by the HCS circuit;

non-linearities due to the power OpAmp and power resistor in each HCS channel; errors on account of cross heating between each axis electronics; Earth's magnetic field component observed inside the coil; possible non-linearities due to magnetic hysteresis; among others. The calibration model seeks to compensate for all those disturbances.

Determining a calibration model depends on the magnetic field simulator. Therefore, each different simulator (the combination of the coil and its electronics/current source) might require a distinct model from the one suggested below. For example, Oliveira [24] used a second-order model, but its results showed that only the first-order terms had significant values. However, the setup of our original simulator described in [25] greatly benefited when adding a third-order calibration parameter, significantly improving the generated field accuracy, as shown in the results reported in [26].

Models will not be compared in detail here, as each experimentalist must test their systems to find the one that best minimizes the errors. In our case, the HCS has non-linear results, which explains the advantage of using high-order calibration parameters. Section 4.6.2 shows the practical results comparison of a first-, second-, and third-order calibration model to our setup. The proposed third-order model results are within the system's effective resolution and accuracy. Thus, the theoretical comparison of higher-order models shows no benefit in further expansion than the third-order one. Therefore, the model used herein is given by:

$$\begin{bmatrix} \hat{B}_x \\ \hat{B}_y \\ \hat{B}_z \end{bmatrix} = \mathbf{K_3} \begin{bmatrix} B_x^3 \\ B_y^3 \\ B_z^3 \end{bmatrix} + \mathbf{K_2} \begin{bmatrix} B_x^2 \\ B_y^2 \\ B_z^2 \end{bmatrix} + \mathbf{K_1} \begin{bmatrix} B_x \\ B_y \\ B_z \end{bmatrix} + \begin{bmatrix} B_{x0} \\ B_{y0} \\ B_{z0} \end{bmatrix}, \tag{4.1}$$

where $\hat{B}_x$, $\hat{B}_y$, and $\hat{B}_z$ (or $\hat{\mathbf{B}}$ vector) are the fluxgate readings in each axis; B_x, B_y, and B_z (or $\mathbf{B}$ vector) are the theoretical (expected) magnetic field; $\mathbf{K_1}$, $\mathbf{K_2}$, and $\mathbf{K_3}$ are 3×3 matrices, respectively with the first-, second-, and third-order calibration parameters; and b_{x0}, b_{y0}, and b_{z0} (or $\mathbf{b}_0$ vector) are the zeroth order (offsets) parameters.

In (4.1), the zero-th order parameters will compensate for the earth's magnetic field components within the coil and eventual offsets caused by the electronics in the HCS drive. The diagonal of the first-order term $\mathbf{K_1}$ will compensate for scale factors errors of both the coils and the current source electronics, whereas the adjacent terms will primarily compensate for misalignment between pairs. At last, the higher-order parameters correct the non-linear errors.

4.3 Practical Calibration Procedure and Parameters Estimation

Having set the model, we must decide on the practical procedure and estimation process to estimate the calibration parameters. There are two viable strategies:

1. Generate the magnetic field using the theoretical data without any compensation. Use the fluxgate measurements and the theoretical values to estimate the calibration parameters (matrices and offset) at once. Finally, generate the open-loop calibrated field;

2. Start by estimating the offset parameters independently. Generate the magnetic field using the theoretical

data compensated by the offset. Use the fluxgate measurements and the offset compensated data to estimate all matrices parameters. Finally, generate the open-loop calibrated field.

Although the first strategy seems more suitable from a theoretical point of view, the second strategy has shown better practical results, and it's the one reported. Furthermore, it is a similar procedure used in [24,26]. The comparison between both approaches and the hypothesis for such a result is seen in the complementary analysis in Section 4.6.1 and is not relevant for reproducing the calibration approach.

The selected method handles the offset in an independent calibration procedure. After the simulation estimates the offset values, it will permanently compensate the subsequent simulations, whether those are simulations to calibrate the coil (estimating the matrices parameters) or running the calibrated simulation to evaluate the open-loop magnetic field generation. This method is more straightforward to cancel Earth's magnetic field component and make up for eventual electronics offset.

Figure 4.3 summarizes the procedure to calibrate the system and generate the open-loop magnetic field. It has the offset estimation procedure independent of the rest of the simulation. Once the offset is estimated, it either operates in the calibration mode or in the calibrated magnetic field generation mode.

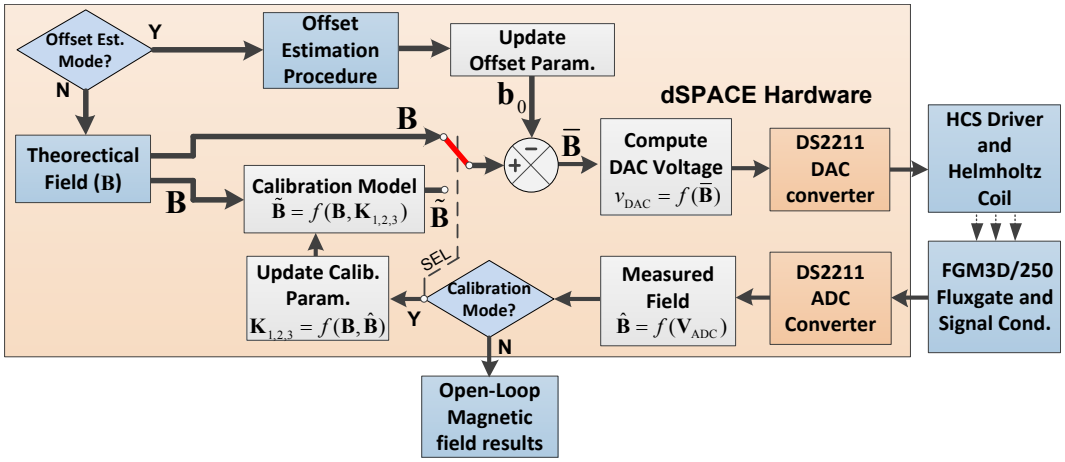

Figure 4.3: Diagram of the procedure to determine the calibration parameters of the magnetic field simulator.

If the HiL simulation is set to the offset estimation mode, it estimates (or updates) the offset parameters based on a practical approach without any mathematical modeling. This procedure starts by setting all theoretical fields to zero (B_x=B_y=B_z=0) and updating the offsets parameters ($\mathbf{b}_0$) with the fluxgate readings ($\hat{\mathbf{B}}$). After that, the simulation recursively adjusts each axis offset (b_{x0}, b_{y0}, and b_{z0}) until the residual fluxgate readings ($\hat{B}_x$, $\hat{B}_y$, $\hat{B}_z$) are all lower than half of the system's resolution value to all axes. Note that the offset parameter is not compensated for scale factors or nonlinearity between axes. Thus, the recursion is essential to ensure that the estimated values are correct.

Now that the system compensates for the offset independently, determining the remainder of the parameters can not follow (4.1) directly. The practical problem is reduced to (4.2).

$$\begin{bmatrix} \hat{B}_x \\ \hat{B}_y \\ \hat{B}_z \end{bmatrix} = \mathbf{K_3} \begin{bmatrix} B_x^3 \\ B_y^3 \\ B_z^3 \end{bmatrix} + \mathbf{K_2} \begin{bmatrix} B_x^2 \\ B_y^2 \\ B_z^2 \end{bmatrix} + \mathbf{K_1} \begin{bmatrix} B_x \\ B_y \\ B_z \end{bmatrix} \tag{4.2}$$

During the calibration procedure (matrices estimation), the simulation will feed the theoretical field value ($\mathbf{B}$) without compensations. The offset value ($\mathbf{b}_0$) will be subtracted from the theoretical one, resulting in the actual commanded field to the HiL simulation, given by $\overline{\mathbf{B}}$. Once all points have been simulated, the matrices ($\mathbf{K_1}$, $\mathbf{K_2}$, and $\mathbf{K_3}$) are estimated using a batch least squares estimator formulated with the fluxgate measurements and the theoretical values. Section 4.3.1 discusses the parameter estimation.

After the calibration procedure, the system generates the open-loop calibrated magnetic field. To achieve that, the HiL simulation switches the calibration mode to the open-loop magnetic field generation mode seen in Fig. 4.3. Therefore, the adjusted magnetic field, given by $\tilde{\mathbf{B}}$, is calculated as a function of the theoretical field value and the calibration parameters. The offset value is now subtracted from $\tilde{\mathbf{B}}$, resulting in the commanded magnetic field, given again by $\overline{\mathbf{B}}$. At last, the fluxgate measurements ($\hat{\mathbf{B}}$) represent the final calibrated magnetic field and can be used to evaluate the calibration results. The simulator calculates the adjusted magnetic field ($\tilde{\mathbf{B}}$) using the mathematical procedure seen in Section 4.3.2.

4.3.1 Matrices Parameter Estimation

The batch least squares estimator [33] is used to estimate all matrices parameters. Given m measurements taken during the simulation, we have that:

$$\hat{\mathbf{X}} = (\mathbf{H}^\mathsf{T}\mathbf{H})^{-1}\mathbf{H}^\mathsf{T}\mathbf{Y}, \tag{4.3}$$

where $\mathbf{Y}$ is a $m \times 3$ matrix with the uncalibrated fluxgate measurements, given by (4.4). $\mathbf{H}$ is a $m \times 9$ matrix containing each order term of (4.2) calculated with the theoretical field $\mathbf{B}$. Equation (4.5) shows $\mathbf{H}$. And $\hat{\mathbf{X}}$ is a 3×9 matrix with the 27 estimated parameters.

$$\mathbf{Y} = \begin{bmatrix} \hat{B}_{x1} & \hat{B}_{y1} & \hat{B}_{z1} \\ \hat{B}_{x2} & \hat{B}_{y2} & \hat{B}_{z2} \\ \vdots & \vdots & \vdots \\ \hat{B}_{xm} & \hat{B}_{ym} & \hat{B}_{zm} \end{bmatrix} \tag{4.4}$$

$$\mathbf{H} = \begin{bmatrix} B_{x1}^3 & B_{y1}^3 & B_{z1}^3 & B_{x1}^2 & B_{y1}^2 & B_{z1}^2 & B_{x1} & B_{y1} & B_{z1} \\ B_{x2}^3 & B_{y2}^3 & B_{z2}^3 & B_{x2}^2 & B_{y2}^2 & B_{z2}^2 & B_{x2} & B_{y2} & B_{z2} \\ \vdots & \vdots & \vdots & \vdots & \vdots & \vdots & \vdots & \vdots & \vdots \\ B_{xm}^3 & B_{ym}^3 & B_{zm}^3 & B_{xm}^2 & B_{ym}^2 & B_{zm}^2 & B_{xm} & B_{ym} & B_{zm} \end{bmatrix} \tag{4.5}$$

4.3.2 Determining the Adjusted Magnetic Field

As the practical procedure deals with the offset separately, it also does not influence the computation of the adjusted magnetic field ($\tilde{\mathbf{B}}$). Now, we seek to determine $\tilde{\mathbf{B}}$ which will generate the compensated magnetic

field so that the fluxgate readings ($\hat{\mathbf{B}}$) follows the expected theoretical field ($\mathbf{B}$). Therefore, this could be calculated by inverting (4.2) assuming that the theoretical field values are replaced by $\tilde{\mathbf{B}}$ and that $\hat{\mathbf{B}} = \mathbf{B}$; however, (4.2) is non-invertible, and the solution is to apply the recursive method found in Oliveira [24]. To calculate $\tilde{\mathbf{B}}$, we begin by rewriting (4.2) as:

$$\mathbf{B} = g\left(\tilde{\mathbf{B}}\right) + \mathbf{K}_1\tilde{\mathbf{B}}, \tag{4.6}$$

where $g(\tilde{\mathbf{B}})$ is given by the high order terms of (4.2), and $\mathbf{B}$ is the theoretical value that is expected to be measured in the calibrated system. The method iteratively finds $\tilde{\mathbf{B}}$ using the linear term of (4.6) as a starting point:

$$\tilde{\mathbf{B}}_\mathbf{0} = \mathbf{K}_1^{-1}\mathbf{B}, \tag{4.7}$$

and the following iterative values of $\tilde{\mathbf{B}}_\mathbf{i}$ will be given by

$$\tilde{\mathbf{B}}_\mathbf{i} = \mathbf{K}_1^{-1}\left(\mathbf{B} - g(\tilde{\mathbf{B}}_{i-1})\right), \tag{4.8}$$

until the iterative process meets a stopping criterion, which compares if the previous and the actual iteration adjusted value is below a certain threshold. In all cases, three iterations were sufficient to reach the criterion. The HiL simulator calculates the adjusted magnetic field $\tilde{\mathbf{B}}_\mathbf{i}$ in real-time to every point simulated, using the theoretical field and the calibration parameters.

4.4 Open-Loop Magnetic Field Generation Results

This section shows the open-loop results for the system. The open-loop magnetic field results were similar for various theoretical magnetic field inputs, and the overall system performance and accuracy were the same in all tested cases. Therefore, this section summarizes the results using two distinct waveforms displayed in Subsection 4.4.1. Then, Subsection 4.4.2 shows the uncalibrated and calibrated results.

Section 4.5 further comments about the calibration parameters and the system repeatability. That section includes the analysis of the calibration behavior versus different generated magnetic field inputs and the parameter stability to a similar waveform for tests taken hours apart from each other.

4.4.1 The Theoretical Magnetic Field Input

The examples chosen to summarize the open-loop results and capability of the system simulate an object rotating around its axes subjected to a constant magnetic field of 500 mG. Figures 4.4(a) and 4.4(b) show the magnetic field value of all axes versus the time. Figures 4.5(a) and 4.5(b) display the respective 3D sphere representation of the magnetic field of each input, that is, the vector components of the magnetic field plotted in three dimensions, which we will also refer to as the *attitude sphere*.

Those particular cases were selected because they provide adequate coverage of the *attitude sphere* [7] surface to demonstrate the magnetometer calibration in Chapters 5 and 6. Both inputs seen in Fig. 4.4 describe a similar rotation, but in the second example, the x and y axes are rotated compared to the first. This difference is relevant to compare the calibration parameter's interdependence to a given magnetic field

input. This particular discussion follows in Section 4.5.

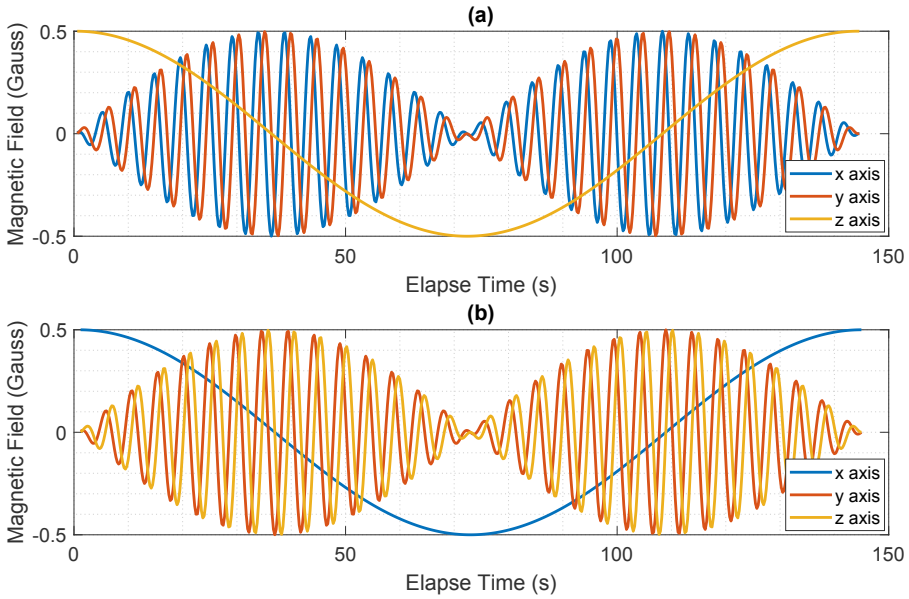

Figure 4.4: Plot of the axis components of the theoretical programmed magnetic field used as an example with a constant magnitude value of 500 milligauss. (a) First example. (b) Second example.

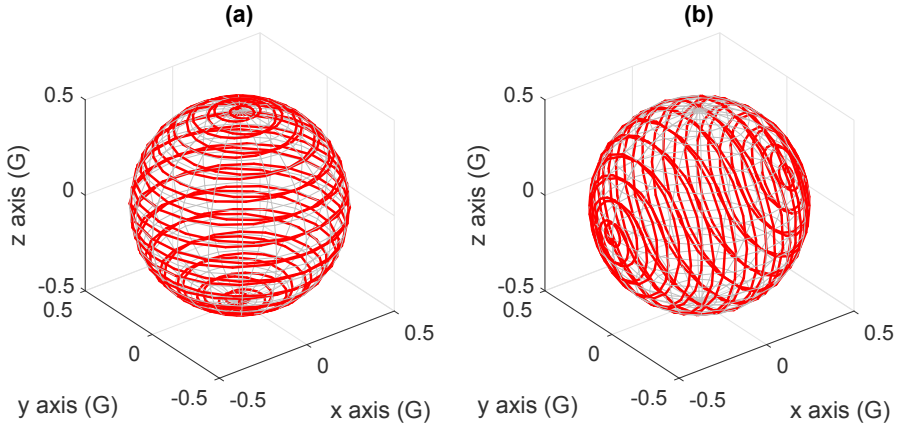

Figure 4.5: Three dimensions plot of the magnetic field vector components. (a) Fig. 4.4(a) waveform. (b) Fig. 4.4(b) waveform.

4.4.2 Uncalibrated and Calibrated Results

The test follows the procedure discussed in Section 4.3 for both magnetic field waveforms seen in Fig. 4.4. The simulation starts with the iterative calibration of the offset values for all axes and then proceeds to generate the theoretical data. Figure 4.6 displays the uncalibrated results for both inputs, *i.e.*, the fluxgate measurements minus the expected values. These results show that all axes have an error in the same order of magnitude for both magnetic field inputs. The uncalibrated results yield errors ranging from 10 to 50 milligauss in all axes. The visual analysis of the data displays that the z axis has the worst accuracy, with errors reaching 10% of the generated signal amplitude (± 500 mG). However, as examined in Section 4.6, most of the error magnitude is associated with the first-order behavior of the setup, *i.e.*, each axis scale factor, and the misalignment parameters. A numerical analysis of the uncalibrated errors is not relevant here, as the graphical data shows that it is not possible to ensure the system's accuracy without a calibration procedure.

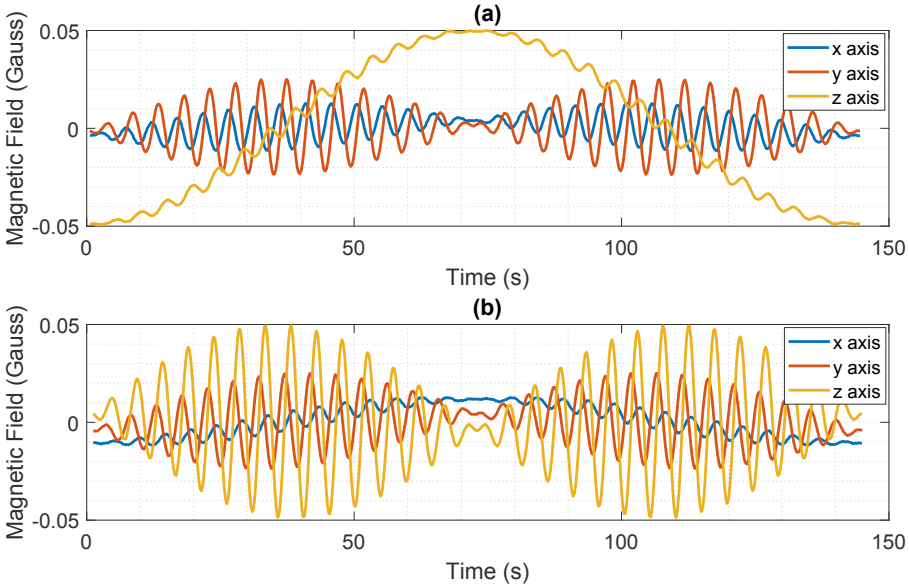

Figure 4.6: Open-loop uncalibrated magnetic field error results. (a) Waveform of Fig. 4.4(a). (b) Waveform of Fig. 4.4(b).

In the sequence, the fluxgate measurements of the uncalibrated systems are used to estimate the remainder of the calibration parameters. Table 4.1 shows the calculated values for both waveforms. By inspecting them, it is notable that both $\mathbf{K_1}$ matrices have very similar values, and differences among the elements of $\mathbf{K_1}$ between the tests are in one order of magnitude smaller than the actual value. However, the matrices $\mathbf{K_2}$ and $\mathbf{K_3}$ have a more pronounced difference in both the main diagonal and some of the adjacent terms when comparing the parameters estimated for each magnetic field input. For instance, the more evident disparity is the diagonal terms of $\mathbf{K_3}$.

Table 4.1: Calibration parameters obtained for both magnetic field inputs of the open-loop tests.

Parameter	**Test: Waveform 1 - Fig. 4.6(a)**	**Test: Waveform 2 - Fig. 4.6(b).**
$\mathbf{b_0}$ (mG)	$\begin{bmatrix} 113.54 & 115.53 & 69.29 \end{bmatrix}$	$\begin{bmatrix} 113.54 & 115.53 & 69.29 \end{bmatrix}$
$\mathbf{K_1}$	$\begin{bmatrix} 0.976823 & 0.005941 & -0.007586 \\ -0.008640 & 0.951028 & -0.002273 \\ 0.008640 & 0.001439 & 0.900857 \end{bmatrix}$	$\begin{bmatrix} 0.977070 & 0.005813 & -0.007611 \\ -0.008506 & 0.951012 & -0.002288 \\ 0.008756 & 0.001368 & 0.900443 \end{bmatrix}$
$\mathbf{K_2}$	$\begin{bmatrix} 0.002862 & 0.000617 & 0.000897 \\ -0.000359 & 0.002986 & 0.000346 \\ 0.000345 & 0.000306 & 0.001743 \end{bmatrix}$	$\begin{bmatrix} 0.002357 & 0.000822 & 0.000902 \\ 0.000438 & 0.003114 & -0.000130 \\ 0.000371 & -0.000007 & 0.002115 \end{bmatrix}$
$\mathbf{K_3}$	$\begin{bmatrix} 0.003483 & 0.000179 & -0.000070 \\ 0.000074 & 0.003929 & -0.000912 \\ 0.000093 & 0.000578 & 0.002449 \end{bmatrix}$	$\begin{bmatrix} 0.002508 & 0.000135 & -0.000026 \\ 0.000066 & 0.002732 & -0.000189 \\ -0.000575 & 0.000232 & 0.004879 \end{bmatrix}$

The contrast in the calibration parameters for each magnetic field waveform leads to the hypothesis that optimum results require a calibration procedure separately for each specific input. Consequently, a generic calibration would result in non-optimum open-loop accuracy outcomes. This hypothesis is also plausible since the power OpAmp's thermal drift and the HCS circuit's power resistor may have different effects on the output linearity depending on the waveform. Thus, Section 4.5 further discusses the calibration parameters versus

the magnetic field input and the repeatability of the parameters for multiple tests of the same waveform for a more conclusive analysis.

Finally, using the calibration parameters, the HiL simulation repeats the process and generates the magnetic field using the adjusted value calculated by the third-order calibration model. The fluxgate measurements are used to evaluate the calibrated errors, which are seen in Fig. 4.7 for each waveform. In both cases, the graphical analysis shows that the difference between the measured and the expected value ranges from approximately ± 500 μG for all axes. Table 4.2 exhibits the numerical data analysis of the calibrated error.

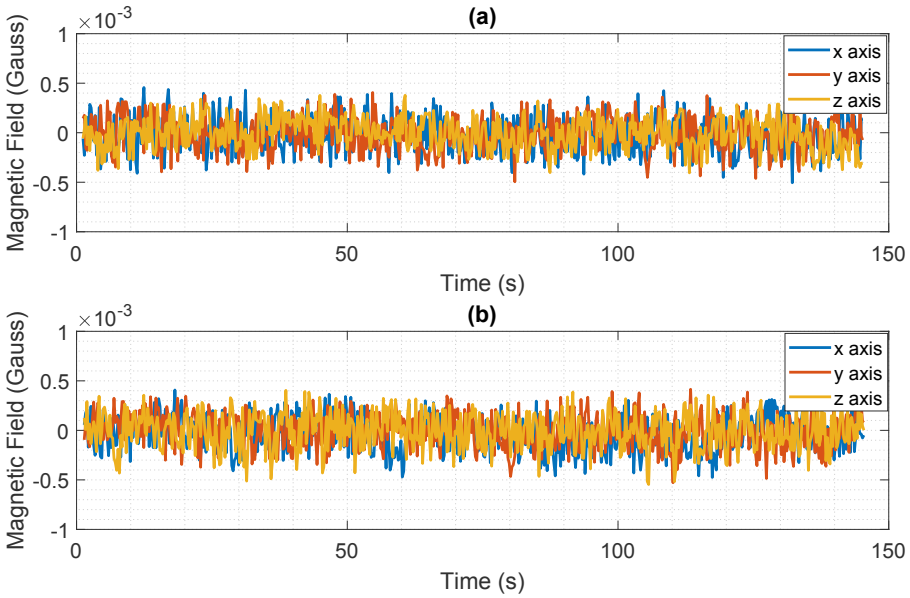

Figure 4.7: Open-loop calibrated magnetic field error results for the third-order model. (a) Waveform of Fig. 4.4(a). (b) Waveform of Fig. 4.4(b).

Table 4.2: Numerical analysis of the open-loop calibrated error results.

Test	Axis	Mean Error (μG)	RMS Error (μG)	Error Min. (μG)	Error Max. (μG)	Peak-to-peak Error (μG)
Fig. 4.7(a)	**x**	-18.94	185.91	-504.97	456.24	961.21
	y	-10.05	177.99	-495.39	405.64	901.03
	z	-6.01	161.17	-405.29	377.99	783.28
Fig. 4.7(b)	**x**	-33.44	184.62	-475.12	407.39	882.51
	y	-5.83	176.52	-528.53	414.67	943.20
	z	-4.19	184.35	-546.49	403.70	950.19

The numerical analysis shows that the RMS error values are between 160 to 200 μG in all axes, while the peak-to-peak ranges from 780 to 960 μG. Recapitulating the results of Section 2.6.4, the magnetic field simulator has a quantization error of approximately 150 μG in the fluxgate acquisition with a resolution around 150 μG in the generated field. Hence, the open-loop calibrated error is in a similar order of magnitude as the system resolution.

Compared to those values, the open-loop RMS error is lower than the magnetic field acquisition resolution, which is around 305 μG. Furthermore, the peak-to-peak error in all axes to both tests is smaller than 2 LSB of the approximately 500 μG resolution to the magnetic field generation. Therefore, the calibration method

reduces the error to the same magnitude as the resolution of the system, and better results would require upgrading the analog converters available at the setup. These results reiterate the analysis of Chapter 2, which pointed out that data converters (DAC and ADC) of the dSPACE are a drawback of the current setup.

4.5 Calibration Parameters versus the Magnetic Field Input and the Repeatability of the Setup

Two tests perform further analysis on the calibration behavior of the magnetic field simulator. The first aims to compare the open-loop results of a specific magnetic field input using calibration parameters obtained from another. The second evaluates the calibration parameters' stability and deviation using data collected over several hours for similar waveforms.

Equivalent to the previous section, this analysis had equivalent results and conclusions regardless of different magnetic field inputs. Therefore, it also summarizes the results using the magnetic field inputs already seen in Fig. 4.4.

4.5.1 Calibrated Results for a Specific Input using Calibration Parameters Estimated for Different Inputs

The experiment uses both magnetic field inputs of Fig. 4.4. These inputs will be referred to as the first and second magnetic field inputs or Waveform 01 and Waveform 02, respectively, to facilitate the reader's comprehension. The HiL simulation starts by generating both inputs without any calibration. Hence, two sets of calibration parameters are estimated, one for Waveform 01 and another for Waveform 02. Next, the setup generates the first magnetic field input using the third-order calibration model for each set of parameters. Figure 4.8 shows the calibrated error for this procedure. At last, the simulator generates the second magnetic field input using both sets of parameters. The results of calibrated error of this test can be seen in Fig. 4.9.

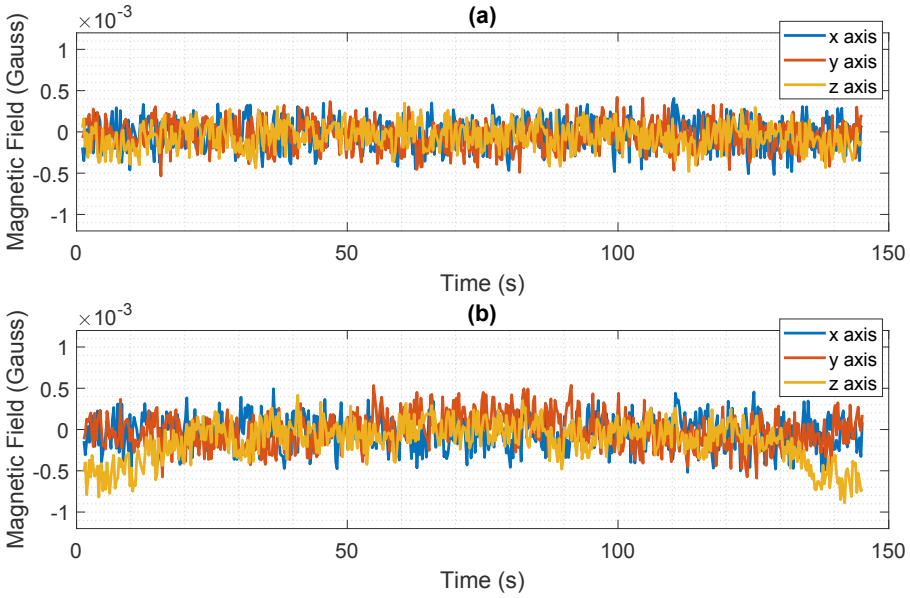

Figure 4.8: Calibrated error results for the magnetic field input of Waveform 01. (a) Using the set of parameters obtained from Waveform 01. (b) Using the set of parameters obtained from Waveform 02.

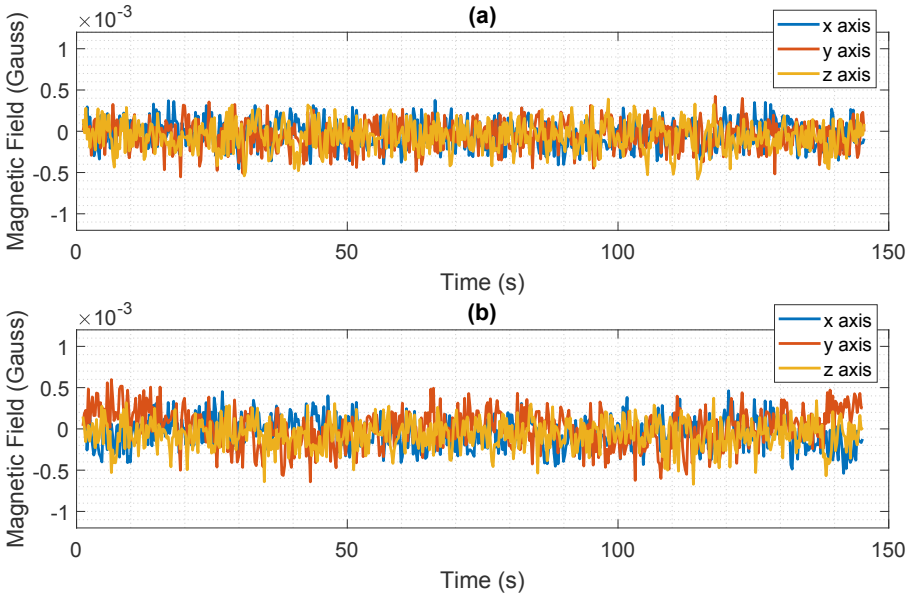

Figure 4.9: Calibrated error results for the magnetic field input of Waveform 02. (a) Using the set of parameters obtained from Waveform 02. (b) Using the set of parameters obtained from Waveform 01.

The results of Figs. 4.8(a) and 4.9(a) are similar to those reported in the previous section. However, the error outcome of Fig. 4.8(b) demonstrates that the calibrated output accuracy degraded compared to Fig. 4.8(a). Hence, using the calibration parameters estimated using Waveform 02 did not produce an optimal result when generating the calibrated magnetic field input of Waveform 01. Analogously, the same happened when using the calibration parameters set of Waveform 01 to generate the field of Waveform 02, which is confirmed by comparing Figs. 4.9(a) and 4.9(b). The numerical data analysis of the calibrated error is reported in Tables 4.3 and 4.4, respectively, for the results of Figs. 4.8 and 4.9.

Table 4.3: Numerical analysis of the data in Fig. 4.8 obtained for Waveform 01.

Test Result	Axis	Mean Error (μG)	RMS Error (μG)	Error Min. (μG)	Error Max. (μG)	Peak-to-peak Error (μG)
Fig. 4.8(a)	**x**	-26.80	189.05	-516.24	406.22	922.46
	y	-49.71	184.85	-533.78	418.43	952.21
	z	-56.60	168.74	-479.45	349.64	829.09
Fig. 4.8(b)	**x**	-38.42	203.84	-518.18	493.29	1011.47
	y	-12.27	210.58	-589.73	535.61	1125.34
	z	-137.77	278.56	-890.01	416.70	1306.71

Table 4.4: Numerical analysis of the data in Fig. 4.9 obtained for Waveform 02.

Test Result	Axis	Mean Error (μG)	RMS Error (μG)	Error Min. (μG)	Error Max. (μG)	Peak-to-peak Error (μG)
Fig. 4.9(a)	**x**	-33.64	172.42	-455.90	374.16	830.06
	y	-50.46	178.93	-553.20	423.77	976.97
	z	-63.19	187.82	-579.64	389.19	968.83
Fig. 4.9(b)	**x**	-52.37	192.88	-538.29	461.73	1000.02
	y	9.33	228.63	-641.41	597.64	1239.05
	z	-68.16	189.49	-670.62	372.40	1043.02

The data of Tables 4.3 and 4.4 verifies that the open-loop calibrated results degrade when using a

different waveform from that used to estimate the parameters. For the first waveform, the z axis accuracy has a significant impact when using the set for parameters of the other waveform. The RMSE increases from 168.74 μG to 278 μG in that axis. In the other axes, the accuracy is also impacted but by a smaller margin compared to that. The peak-to-peak error outcome is also worse for all axes. For the second magnetic field input, the y axis is the one that has the worst impact by using the set of parameters obtained from the other waveform. Nevertheless, it is evident that the RMSE and peak-to-peak error accuracy diminishes compared to the ideal case, which is to generate the magnetic field input using the calibration parameters from the same waveform.

Despite that, the open-loop results are still reasonable for the non-optimum outcome if we compare the error values with the resolution of the setup. Once more, the setup's ADC resolution is approximately 300 μG, and the magnetic field generation resolution is around 500 μ G. Therefore, the error of Figs. 4.8(b) and 4.9(b) are in the same order of magnitude. The RMSE is maintained within 1 LSB of the ADC resolution, similar to the optimal scenario error of Figs. 4.8(a) and 4.9(a).

Nevertheless, it is evident that the simulator must be calibrated to each magnetic field waveform to generate an optimal open-loop magnetic field. Still, even the non-optimum scenario yields a good calibration compared to the resolution of the system, confirming that the actual state of the simulator setup has the ADC and DAC resolution as the main drawback. Consequently, improving them is mandatory for further investigation of the calibration and evaluating the possibility of enhancing the open-loop results.

4.5.2 Calibration Parameters Repeatability Analysis over Time and for Different Inputs

The test objective is to assess the stability of the calibration parameters and their standard deviation for repeated tests over time for the same magnetic field input. Furthermore, it seeks to understand the outcome of the parameters for different waveforms and compares their stability for these distinct inputs. The test uses both magnetic field inputs of Fig. 4.4 and a third one seen in Fig. 4.10 to perform that analysis. The waveform of Fig. 4.10 is similar to both seen in Fig. 4.4 but with a shifted rotation among the axes.

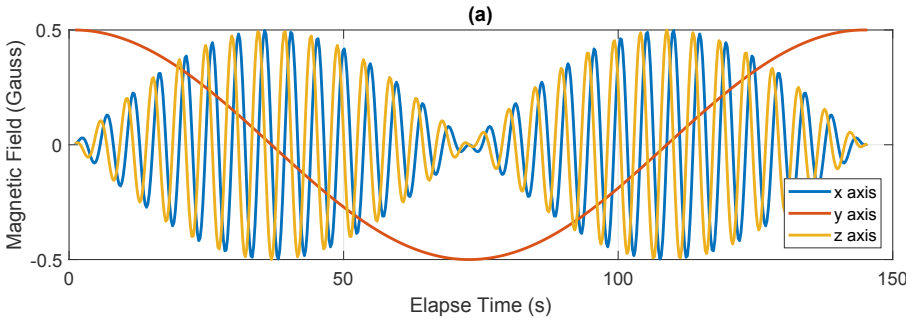

Figure 4.10: Axis components of the additional magnetic field input used in the repeatability test.

The test methodology is straightforward. After performing the offset calibration procedure, the system generates the three magnetic field waveforms with a couple of minutes between one another. Next, the system is kept on for around an hour before generating the same inputs again. The simulator repeats this interleaved sequence n times. All the tests run the uncalibrated model as the goal is to use them to estimate the calibration

parameters. The steps below enumerate the methodology:

1. Calibrate the offset parameters;
2. Generate the uncalibrated magnetic field of Figs. 4.4(a) (Waveform 01);
3. Wait a couple of minutes and generate the uncalibrated magnetic field of Fig. 4.4(b) (Waveform 02);
4. Wait a couple of minutes and generate the uncalibrated magnetic field of Fig. 4.10 (Waveform 03);
5. Wait approximately an hour;
6. Repeat steps 2 to 5 for n times;

The procedure had ten repetitions ($n = 10$). Table 4.5 shows the results, which include the average value of the calibration parameters estimated for each waveform and the standard deviation of each parameter.

Table 4.5: Mean value and standard deviation of the parameters obtained when repeating ($n = 10$) the magnetic field inputs of Figs. 4.4(a), 4.4(b), and 4.10.

Parameter	Waveform	Mean Value	Standard Deviation
$\mathbf{K_1}$	**Fig. 4.4(a)**	$\begin{bmatrix} 0.976721 & 0.005932 & -0.007568 \\ -0.008647 & 0.951008 & -0.002271 \\ 0.008643 & 0.001424 & 0.900885 \end{bmatrix}$	$\begin{bmatrix} 0.000062 & 0.000008 & 0.000008 \\ 0.000010 & 0.000099 & 0.000010 \\ 0.000012 & 0.000010 & 0.000049 \end{bmatrix}$
	Fig. 4.4(b)	$\begin{bmatrix} 0.976862 & 0.005801 & -0.007603 \\ -0.008470 & 0.951048 & -0.002214 \\ 0.008774 & 0.001337 & 0.900484 \end{bmatrix}$	$\begin{bmatrix} 0.000050 & 0.000006 & 0.000006 \\ 0.000011 & 0.000038 & 0.000009 \\ 0.000014 & 0.000007 & 0.000024 \end{bmatrix}$
	Fig. 4.10	$\begin{bmatrix} 0.976669 & 0.005766 & -0.007730 \\ -0.008449 & 0.951672 & -0.002430 \\ 0.008733 & 0.001440 & 0.900577 \end{bmatrix}$	$\begin{bmatrix} 0.000032 & 0.000022 & 0.000004 \\ 0.000007 & 0.000026 & 0.000007 \\ 0.000004 & 0.000023 & 0.000027 \end{bmatrix}$
$\mathbf{K_2}$	**Fig. 4.4(a)**	$\begin{bmatrix} 0.002906 & 0.000644 & 0.001000 \\ -0.000377 & 0.002953 & 0.000326 \\ 0.000257 & 0.000227 & 0.001663 \end{bmatrix}$	$\begin{bmatrix} 0.000047 & 0.000036 & 0.000031 \\ 0.000009 & 0.000010 & 0.000008 \\ 0.000032 & 0.000031 & 0.000024 \end{bmatrix}$
	Fig. 4.4(b)	$\begin{bmatrix} 0.002607 & 0.001114 & 0.001173 \\ 0.000239 & 0.003131 & -0.000309 \\ 0.000199 & -0.000168 & 0.001955 \end{bmatrix}$	$\begin{bmatrix} 0.000034 & 0.000055 & 0.000042 \\ 0.000033 & 0.000025 & 0.000021 \\ 0.000011 & 0.000026 & 0.000019 \end{bmatrix}$
	Fig. 4.10	$\begin{bmatrix} 0.003061 & 0.001115 & 0.000669 \\ 0.000246 & 0.002394 & 0.000314 \\ -0.000107 & 0.000168 & 0.002016 \end{bmatrix}$	$\begin{bmatrix} 0.000099 & 0.000083 & 0.000101 \\ 0.000013 & 0.000011 & 0.000015 \\ 0.000024 & 0.000025 & 0.000026 \end{bmatrix}$
$\mathbf{K_3}$	**Fig. 4.4(a)**	$\begin{bmatrix} 0.003531 & 0.000143 & -0.000072 \\ 0.000197 & 0.003984 & -0.000865 \\ 0.000019 & 0.000616 & 0.002192 \end{bmatrix}$	$\begin{bmatrix} 0.000065 & 0.000031 & 0.000095 \\ 0.000012 & 0.000032 & 0.000065 \\ 0.000050 & 0.000045 & 0.000102 \end{bmatrix}$
	Fig. 4.4(b)	$\begin{bmatrix} 0.002473 & 0.000039 & 0.000081 \\ -0.000010 & 0.002158 & -0.000208 \\ -0.000742 & 0.000097 & 0.005033 \end{bmatrix}$	$\begin{bmatrix} 0.000097 & 0.000040 & 0.000054 \\ 0.000042 & 0.000029 & 0.000046 \\ 0.000055 & 0.000030 & 0.000088 \end{bmatrix}$
	Fig. 4.10	$\begin{bmatrix} 0.004047 & 0.000212 & 0.000024 \\ -0.000184 & 0.000775 & 0.000028 \\ -0.000067 & -0.000108 & 0.003707 \end{bmatrix}$	$\begin{bmatrix} 0.000052 & 0.000078 & 0.000025 \\ 0.000050 & 0.000070 & 0.000026 \\ 0.000032 & 0.000069 & 0.000044 \end{bmatrix}$

Table 4.5 allows the evaluation of two critical system characteristics. First, the standard deviation of each parameter is compared to their actual estimated values, which provides a metric for the simulator's

repeatability over time for the same input. In addition, it is possible to compare similar parameters for each waveform. Hence, it can provide information on the causes of the previous section's results.

The examination of Table 4.5 depicts that the standard deviation of the majority of the elements for all three waveforms has values on a smaller order of magnitude than the actual estimated mean value. However, a few exceptions are seen in a few adjacent parameters of $\mathbf{K_2}$ and $\mathbf{K_3}$ matrices. In these elements, the estimated mean value is on a smaller order of magnitude, whereas the standard deviation is in the same magnitude as the other parameters. Thus, it shows that these specific parameters do not significantly impact the setup, and the uncertainties on the estimation are similar to others with a significant value. Therefore, the most important conclusion about the standard deviation data is that its analysis shows that the system calibration is stable and has repeatability over time to a given magnetic field input.

Although the system is stable for a specific waveform input, examining all the matrices' elements for each waveform shows some variations depending on the magnetic field. Furthermore, the differences between some parameters are in a higher order of magnitude than the uncertainties of the standard deviation data. Consequently, it demonstrates that the variations of the parameters result from the magnetic field input and not due to calibration uncertainties.

Such a contrast in the estimated parameters for each waveform is more pronounced on the diagonal elements of $\mathbf{K_2}$ and $\mathbf{K_3}$ matrices. For instance, taking a 3σ uncertainty of the standard deviation for the latter matrix leads to smaller values than the differences in the diagonal elements. Nonetheless, this is also true for the first-order matrix. Hence, it confirms the hypothesis from Table 4.1 analysis of Section 4.4, which indicated that each input could lead to slightly different calibration matrices. Another observation is that these differences in the elements of the higher-order calibration matrices support the assumption that each magnetic field input effects have its own impact on the non-linear effects of the generated magnetic field.

Lastly, we emphasize that a generic calibration of the magnetic field simulator is not ideal due to the parameter variation observed and would lead to non-optimum results. Thus, as aforementioned, the best outcome in terms of accuracy is only achievable if the calibration parameters are estimated using the same waveform that will be employed later in testing any magnetometer or SUT. Nevertheless, the resolution of the analog data converters available at the dSPACE hardware is a substantial limiting factor in the current simulator stage, and a more conclusive investigation would require a system with better converters. Therefore, if the setup undergoes future improvement, repeating these testing could provide a better insight into the open-loop calibration to different magnetic field inputs.

4.6 Complementary Analysis of the Simulator Calibration

This section shows complementary testing and analysis of the open-loop use of the magnetic field simulator. A first experimental procedure compares both methods to compensate for the offset, discussed in Section 4.3, by assessing the generated field accuracy in each case. Therefore, it demonstrates why we choose the manual technique to estimate the bias instead of simultaneously calculating the offset and the matrices parameters. The second test evaluates the results of the calibrated magnetic field using different calibration order models.

4.6.1 Comparison of the Practical Procedures for the Calibration

Section 4.2 has described the two different procedures to calibrate and use the magnetic field simulator, which are:

1. Generate the magnetic field using the theoretical data without any compensation. Use the fluxgate measurements and the theoretical values to estimate the calibration parameters (matrices and offset) at once. Finally, generate the open-loop calibrated field;
2. Start by estimating the offset parameters independently. Generate the magnetic field using the theoretical data compensated by the offset. Use the fluxgate measurements and the offset compensated data to estimate all matrices parameters. Finally, generate the open-loop calibrated field.

Oppositely to the second procedure used throughout this thesis, the first method does not use the manual compensation of the offset. Hence, the uncalibrated theoretical field value is fed to the simulation without the offset correction. The difference between the fluxgate measurements and the expected values is used to simultaneously estimate all matrices of the calibration model (Section 4.2) and the offset parameters.

The parameter estimation process in this methodology is equivalent to that reported in Section 4.3 but using the full model presented in Section 4.2. However, the batch least squares method is unsuitable for estimating the calibration parameters with the additional offset terms. That is a consequence of (4.3) becoming non-invertible if the matrix $\mathbf{H}$, defined in (4.5), has an additional column with the offset values. The alternative is to estimate the matrices and the offset independently in a recursive manner. Doing so makes it possible to use the batch estimator described in Section 4.3 to independently compute the offsets and matrices and use the previous results in a recursive procedure. This solution is not detailed here.

4.6.1.1 Test Methodology

The practical test methodology is also similar to that in Section 4.4 and follows the steps below:

1. Generate the uncalibrated magnetic field of Fig. 4.4(a) using Procedure 1;
2. Estimate the calibration parameters using the previous item results;
3. Generate the calibrated magnetic field using the third-order correction model;
4. Repeat items 1 to 3 using Procedure 2 (with the manual offset model);
5. Repeat items 1-4 for n times.

The test was repeated five times ($n = 5$) for each procedure in an alternate manner. Although we evaluate different magnetic field inputs, the results had the repeatability as those reported in Section 4.5. Consequently, we summarize the results to a single waveform, specifically the one seen in Fig. 4.4(a).

4.6.1.2 Test Results

We start the analysis by depicting the uncalibrated error results for both procedures. Figure 4.11 shows the uncalibrated error obtained in each methodology for the first repetition out of the five. We should note to the reader that visually, the uncalibrated error plot is identical for every repetition; hence, we suppress additional uncalibrated graphics. The alternative procedure result, which estimates the offset simultaneously to the matrices, is seen in Fig. 4.11(a), and Fig. 4.11(b) shows the results to the manual offset strategy. In the former, it is evident that axes errors are not centered around the y axis, whereas in the latter, they are.

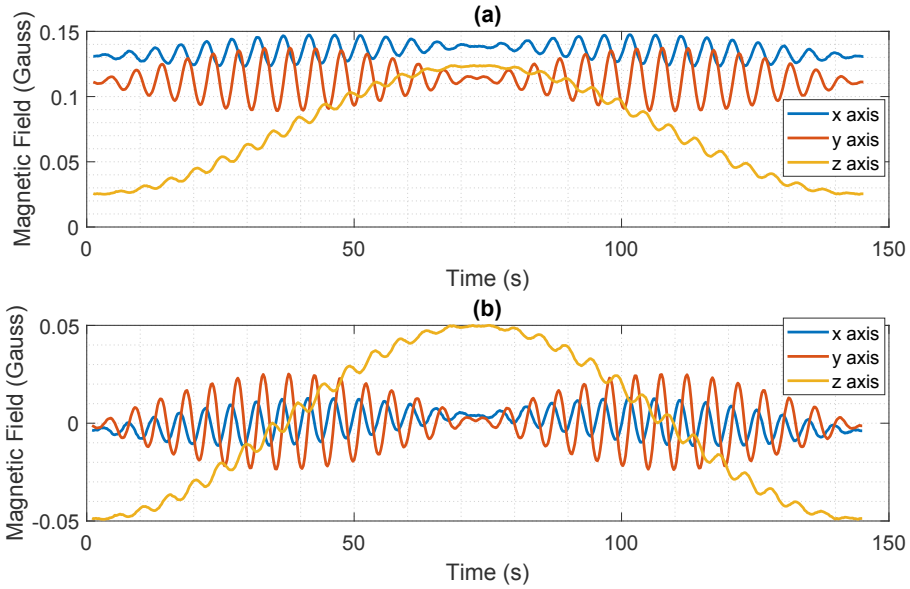

Figure 4.11: Open-loop uncalibrated magnetic field results for the comparison of the practical calibration procedures. (a) Procedure 1 - Alternative procedure. (b) Procedure 2.

Finally, Table 4.6 exhibits the numerical analysis of the error, displaying the average mean error and its standard deviation, the average RMSE and its standard deviation, and the average peak-to-peak error and its standard deviation, obtained using all five repetitions results.

Table 4.6: Mean and standard deviation uncalibrated error analysis for the five tests repeated for each calibration procedures. All units are in milligauss.

Test Type	Axis	Mean Error (mG)	RMS Error (mG)	Peak-to-Peak Error (mG)
Without Manual Offset Compensation (Alternative Procedure)	**x**	134.96 ± 0.009	135.11 ± 0.009	24.24 ± 0.11
	y	112.77 ± 0.006	113.42 ± 0.006	48.42 ± 0.08
	z	74.27 ± 0.018	82.06 ± 0.016	98.85 ± 0.09
With Manual Offset Compensation (Section 4.1 Methodology)	**x**	0.30 ± 0.007	6.48 ± 0.003	24.53 ± 0.12
	y	0.26 ± 0.002	12.34 ± 0.002	48.96 ± 0.10
	z	0.20 ± 0.016	35.00 ± 0.007	99.20 ± 0.15

Since the second procedure compensates the offset independently, the average mean value of the uncalibrated error is close to zero. The measured values, around hundreds of microgauss (0.2 to 0.3 mG), is below the setup's effective resolution and show that the offset is compensated, as expected. On the contrary, the alternative methodology has significant offset values, as they are only estimated afterward, simultaneously

with the remainder of the parameters. Hence, the average component of the first procedure error is the offset value of the setup. Lastly, we observe that the peak-to-peak error is very similar regardless of the procedure among all axes, verifying that the differences in both methodologies are the constant component of the offset.

For each procedure and all five repetitions, we calculate the calibrated error. The results for the first and the last repetitions are seen in Figs. 4.12 and 4.13. Due to the similarity of the remaining three trials with the ones reported, we omit their graphical results.

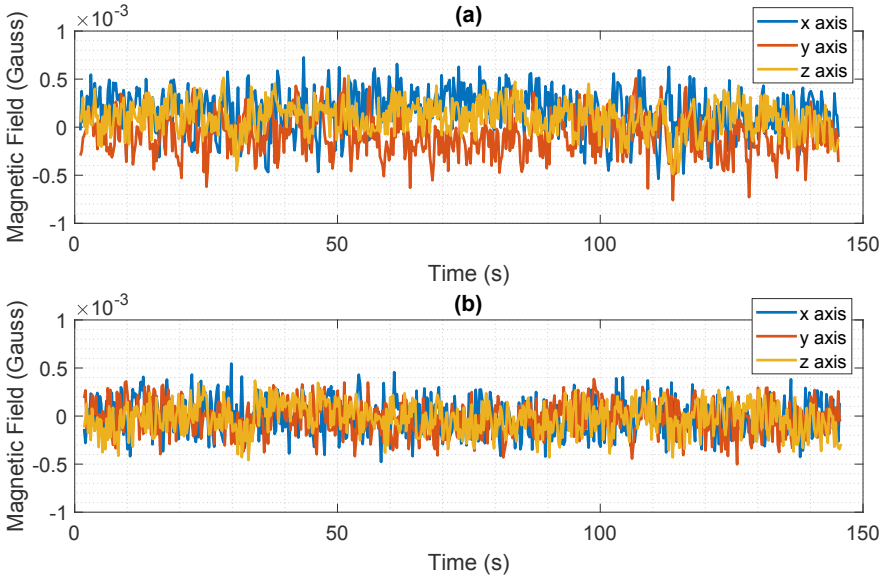

Figure 4.12: First repetition results of the open-loop calibrated magnetic field obtained for the input of Fig. 4.4(a). (a) Procedure 1 - Alternative procedure. (b) Procedure 2.

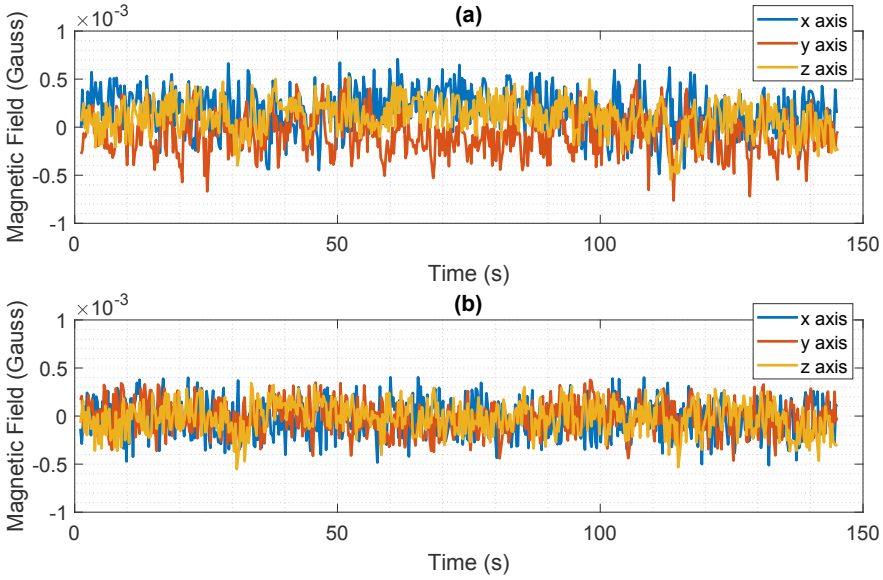

Figure 4.13: Fifth repetition results of the open-loop calibrated magnetic field obtained for the input of Fig. 4.4(a). (a) Procedure 1 - Alternative procedure. (b) Procedure 2.

The open-loop error to the test with the manual offset compensation, seen in Figs. 4.12(b) and 4.13(b), are similar to those in Section 4.4. The error seen in Figs. 4.12(a) and 4.13(a) are for the alternative procedure without the manual compensation; graphically, they are almost identical. Both results reinforce, once more,

the system repeatability and how the open-loop error is similar for repeated tests.

Although both procedures have errors in the same order of magnitude, it is clear that the approach without manual offset compensation has a worse result. To corroborate that, the numerical data analysis for all five repetitions follows in Table 4.7, which includes the average value of the mean error and its standard deviation, the average RMSE error and its standard deviation, and the peak-to-peak error and its standard deviation calculated using the data collected for all five repetitions in each approach.

Table 4.7: Mean and standard deviation calibrated error analysis for the five tests repeated for each calibration procedures. All units are in microgauss.

Test Type	Axis	Mean Error (μG)	RMS Error (μG)	Peak-to-Peak Error (μG)
Without Manual Offset Compensation (Alternative Procedure)	**x**	-161.01 $\pm$ 4.63	278.22 $\pm$ 3.08	1228.60 $\pm$ 47.33
	y	-74.38 $\pm$ 3.92	228.38 $\pm$ 2.99	1267.62 $\pm$ 31.25
	z	95.81 $\pm$ 1.51	202.55 $\pm$ 2.85	1043.53 $\pm$ 27.84
With Manual Offset Compensation (Section 3.1 Methodology)	**x**	-20.82 $\pm$ 5.52	189.68 $\pm$ 2.27	968.80 $\pm$ 38.19
	y	-18.06 $\pm$ 3.36	177.42 $\pm$ 1.01	863.46 $\pm$ 25.05
	z	-22.08 $\pm$ 1.78	166.68 $\pm$ 0.77	860.74 $\pm$ 36.22

Table 4.7 results establish that the manual offset compensation yields better results. The average value, the RMSE, and the peak-to-peak error are consistently better independently of the axis. Furthermore, the standard deviation calculated for the five repetitions is considerably smaller than the differences between both procedures. For instance, the average RMSE differences are 88.54 μG, 50.96 μG, and 35.87 μ, respectively, for the x, y, and z-axis, whereas the standard deviation is below 3 μG for all axes. Hence, it supports the conclusion that the manual technique to compensate for the offset has a better outcome in terms of accuracy. Consequently, this method was detailed in Section 4.2 and employed in all the other testing reported in this thesis where the open-loop use of the magnetic field simulator is required.

Even though we do not further investigate the reason behind that behavior, the hypothesis is that the non-linear errors of the power Howland Current Source electronics have a distinct impact on both procedures. For instance, the uncalibrated and calibrated waveforms have approximately the same average value when using the manual offset compensation procedure, confirmed by the mean error in Table 4.6. On the contrary, if the offset is compensated only on the calibrated waveform, the uncalibrated and calibrated magnetic fields operate in a distinct mean value. Again, the uncalibrated results of the alternative procedure in Table 4.6 confirm that. This average magnetic field value on the waveform translates to an output current in the HCS circuit. This current, in turn, causes heating in the power OpAmp of the HCS and its power resistor. Therefore, the point of operation of the HCS is more consistent with the manual offset procedure, and the calibration parameters are more accurate to compensate for the non-linear errors in such a scenario.

4.6.2 Comparison of the Calibration Model for Different Orders

Reference [26] reports a thorough study on the calibration order model impact in our magnetic field simulator using the previous electronics. Despite having the same HiL simulation to operate the coil, that previous setup had the non-improved version of the power HCS using the LM675 OpAmp. For that simulator electronics

version, the experimental results in [26] demonstrated that a third-order calibration model would improve the open-loop errors compared to first- and second-order ones. In addition, it also experimented with higher-order models without further gains in the calibration.

This work repeated the comparison between the first, second, and third-order models to evaluate the open-loop results of the improved setup discussed in Chapter 2. Also, it is noteworthy that the model seen in [26] had an extra second-order matrix than the one reported in Section 4.2. Consequently, that work model had 36 parameters (four 3×3 matrices), whereas our current model has 27 (three 3×3 matrices). Even with the previous electronics and the simulator setup, these additional terms had estimates one order of magnitude smaller than the others, barely benefiting the calibration (if benefiting at all). Hence, the third-order calibration model of this thesis is simplified compared to [26] without those nine parameters.

4.6.2.1 Test Methodology

We use the manual offset compensation procedure to compare the first, second, and third-order models. The lower-order models are not explicitly shown as they are analogous to the third-order model. For instance, the second-order model does not have the parameters of the $\mathbf{K}_3$ matrix, and the first-order model only contains the nine terms of the $\mathbf{K}_1$ matrix. Again, they are detailed in [26]. Nevertheless, for each model, the estimation process and obtaining the adjusted magnetic field is equivalent to the one reported.

Both magnetic field inputs of Fig. 4.4 were used during the test, which follows the steps below:

1. Generate the uncalibrated magnetic field of Fig. 4.4(a);
2. Uses the previous open-loop results to estimate the calibration parameters for all models;
3. Generate the first-order calibrated magnetic field;
4. Repeat the previous for the second-order model;
5. Repeat item 3 for the third-order model;
6. Repeat items 1-5 to the magnetic field waveform of Fig. 4.4(b);
7. Repeat items 1-6 for n times.

Results are almost identical for every repetition due to the repeatability of the setup already established in previous sections. Consequently, we summarize the results of a single experiment. Furthermore, only the calibrated results are discussed.

4.6.2.2 Test Results

The calibrated results for each model are displayed in Figs. 4.14 and 4.15. The first shows the calibrated error for the magnetic field input of Fig. 4.4(a), and the latter for the waveform of Fig. 4.4(b). The inspection of both figures provides similar conclusions. It is visible that the third-order calibration yields slightly superior results than the second-order and considerably better ones than the first-order model. Hence, the graphical results confirm the calibration improvements using non-linear terms.

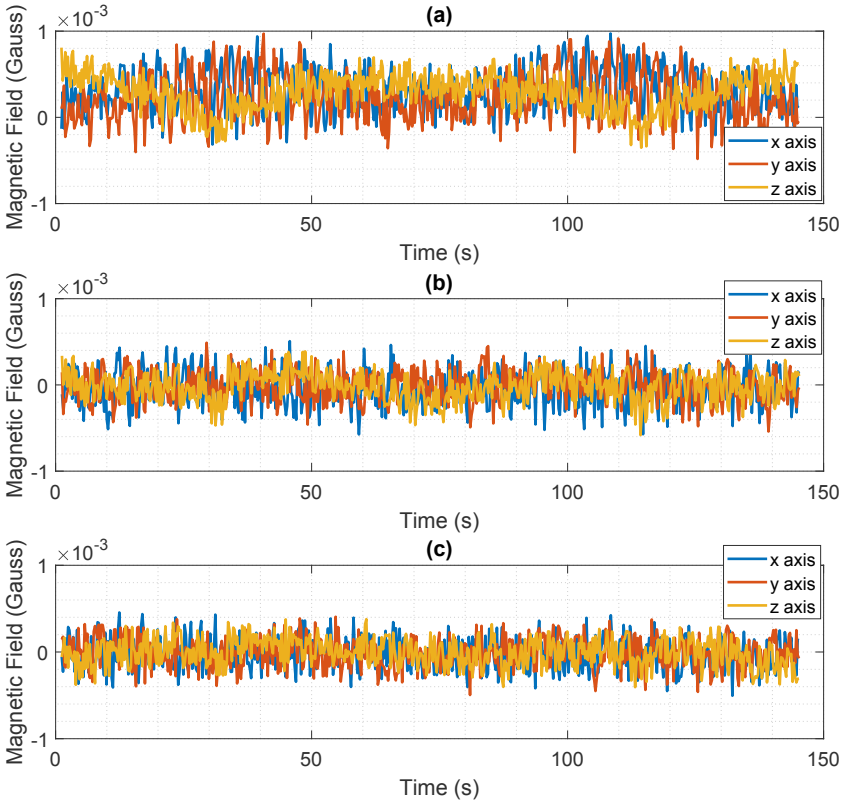

Figure 4.14: Open-loop calibrated magnetic field results obtained for the input of Fig. 4.4(a). (a) First-order model. (b) Second-order model. (c) Third-order model.

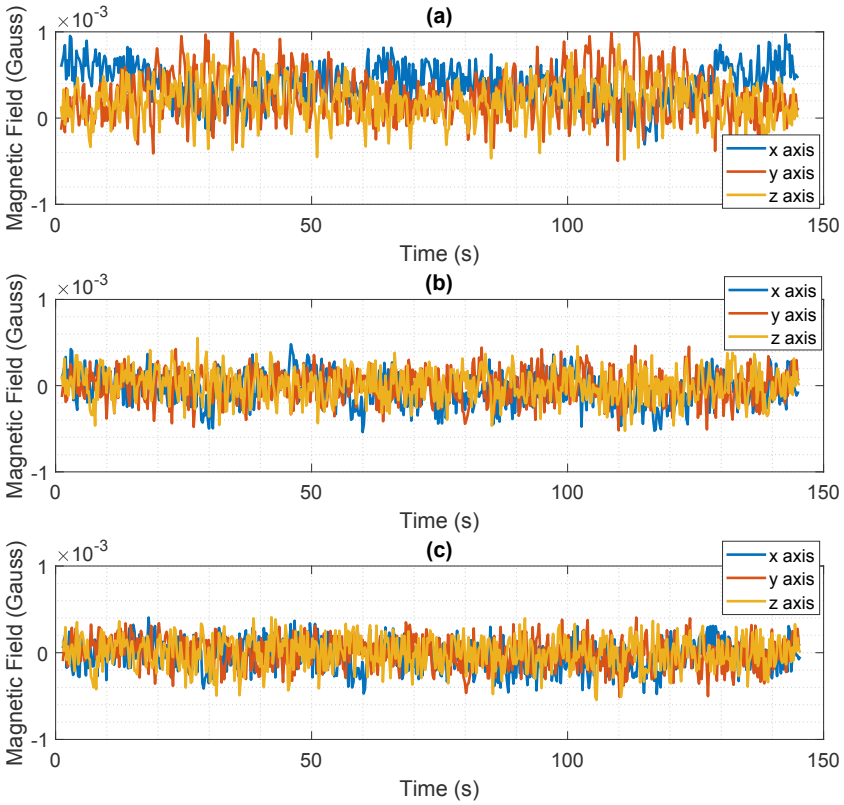

Figure 4.15: Open-loop calibrated magnetic field results obtained for the input of Fig. 4.4(b). (a) First-order model. (b) Second-order model. (c) Third-order model.

Tables 4.8 and 4.9 provide a numerical comparison to the results of Figs. 4.14 and 4.15, respectively. They show the average, the RMSE, the minimum and maximum value, and the peak-to-peak value of the error to each axis and all calibration orders. The data corroborate that the first-order calibration is considerably less effective than the higher ones. Although both higher-order models show similar order of magnitude errors, the third-order calibration improves the setup accuracy. Hence, all tests have employed that particular model.

Table 4.8: Numerical analysis of the open-loop calibration for the results seen in Fig. 4.14.

Calibration Model	Axis	Mean Error (μG)	RMS Error (μG)	Error Min. (μG)	Error Max. (μG)	Peak-to-Peak Error (μG)
First-Order	x	315.67	397.27	-315.11	972.24	1287.45
	y	227.76	360.13	-482.46	970.38	1452.84
	z	288.72	361.26	-352.60	808.17	1160.87
Second-Order	x	-39.26	213.73	-574.54	507.40	1082.04
	y	-9.82	182.90	-540.53	488.93	1029.56
	z	-18.29	170.96	-582.18	389.14	971.32
Third-Order	x	-18.94	185.89	-504.58	455.70	960.28
	y	-10.05	177.96	-496.03	406.23	902.26
	z	-6.05	161.24	-405.86	378.65	784.51

Table 4.9: Numerical analysis of the open-loop calibration for the results seen in Fig. 4.15.

Calibration Model	Axis	Mean Error (μG)	RMS Error (μG)	Error Min. (μG)	Error Max. (μG)	Peak-to-Peak Error (μG)
First-Order	x	389.54	450.50	-305.85	996.71	1272.66
	y	264.36	385.06	-497.10	1098.20	1595.30
	z	206.04	313.73	-479.93	897.99	1377.92
Second-Order	x	-38.13	200.78	-539.75	480.18	1019.93
	y	-7.17	185.34	-517.70	462.45	980.15
	z	-2.33	187.33	-523.42	552.50	1075.92
Third-Order	x	-34.07	184.90	-476.29	405.94	882.23
	y	-5.62	176.73	-509.31	405.99	915.30
	z	-3.66	184.56	-545.02	408.52	953.54

4.7 Closed-Loop Magnetic Field Generation using the Simulator

The works of [26] and [25] describe the closed-loop operation of the magnetic field simulator in detail. Therefore, a thorough discussion about the controller topology, how to design it based on our setup's plant, and others information are found in those works. This thesis reports the results of the closed-loop magnetic field generation to the improved simulator setup, with the new Howland Current Source and the enhanced accuracy.

The diagram of Fig. 4.16 summarizes the operation of the HiL simulation with the magnetic field simulator. The HiL simulation uses a digital PID controller, which was tuned using the MIGO technique (M-Constrained Integral Gain Optimization) and MATLAB's SISO Design tool. The operation of the controller is simple, and the error signal is obtained by the difference between the desired magnetic field value and the one observed by the acquisition system of the FGM3D sensor.

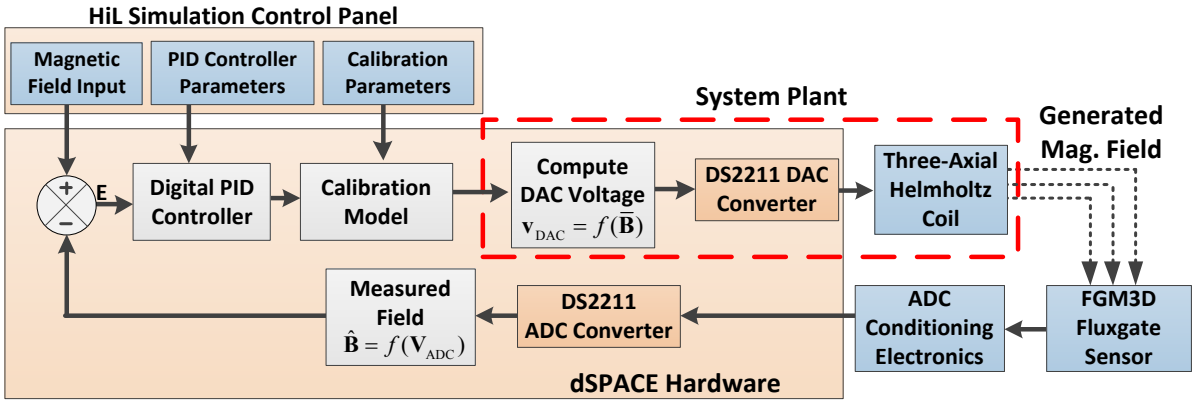

Figure 4.16: Diagram of the closed-loop operation of the magnetic field simulator.

The sample time of the simulator follows the same concept discussed in Section 2.6. The digital PID controller runs at 2 kHz, and the HiL simulation can generate up to 16.66 distinct magnetic field values when testing sensors with a data throughput of 40 Hz. Similarly to the open-loop operation, we could increase that number in the closed-loop topology, but it would require a synchronization method with the SUTs magnetometers. The following subsections show the closed-loop step response and the magnetic field results of the simulator.

4.7.1 Closed-Loop Step Response of the Simulator

The HiL simulator was programmed to generate a step response of different amplitudes to evaluate the controller response and transient time. Figure 4.17 shows the fluxgate sensor measurements to step response for amplitudes of 0.10, 0.25, and 0.50 gauss for all pairs.

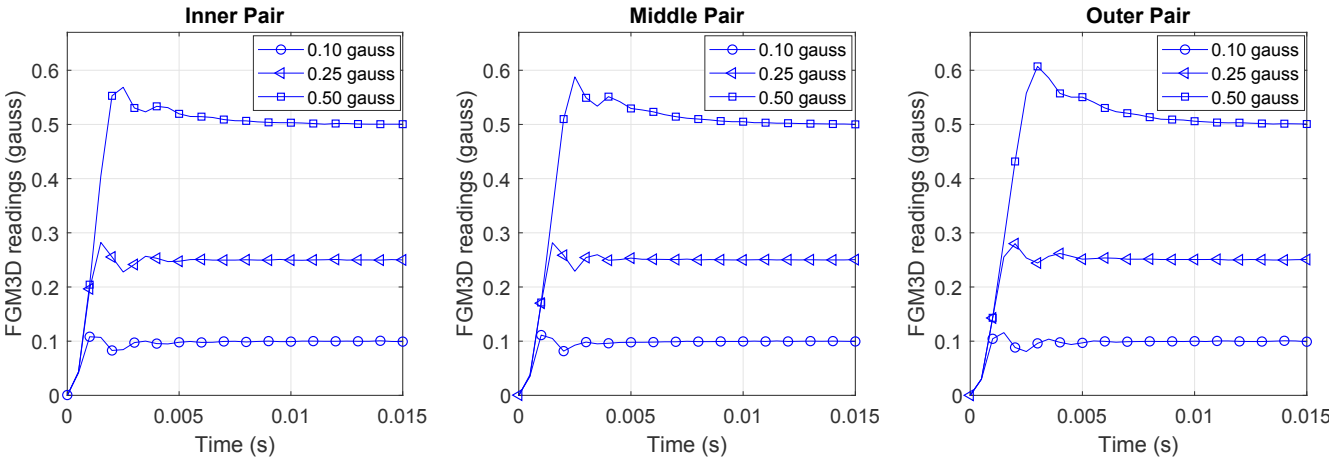

Figure 4.17: Closed-loop step response obtained in each axis of the magnetic field simulator for three different amplitudes.

Figure 4.17 results show that the order of magnitude of the closed-loop transient time is similar to the open-loop reported in Section 2.6.1. The controller slightly improves the transient time for amplitudes up to 0.25 gauss but has the opposite effect for values higher than 0.50 gauss. This fact was observed in [25] and is a limitation of the simulator setup, which reaches the DAC saturation value for abrupt changes in the

magnetic field input. Consequently, the controller takes longer to achieve the steady state.

Nevertheless, such abrupt changes (> 0.25 gauss) in the magnetic field input do not configure the typical use of the simulator. For instance, dynamic simulations ranging from 4 to 20 points per second will likely have smaller steps than that between the simulation cycles. Therefore, adopting a transient time of 10 ms for the closed-loop operation is conceivable, similar to the value of the open-loop simulations. Hence, the simulator disregards any magnetometer measurement during a 10 ms period after an update in the DAC. Such a condition leads to a sample time with those exact requirements discussed in Sections 2.6.2 and 2.6.3.

Therefore, the maximum number of points simulated in the closed-loop operation must also comply with the discussion in those sections. For instance, as we adopt the same transient time of 10 ms, we would be limited to a maximum of 16.66 cycles per second using a sensor under test with an output data rate of 40 Hz. And for sensors with different throughputs, the maximum value would follow Table 2.3.

4.7.2 Closed-Loop Magnetic Field Results

The magnetic field inputs of Fig. 4.4 (Waveforms 01 and 02) are used to evaluate the closed-loop results. Figure 4.18 shows the FGM3D measurements minus the theoretical setpoint value. Also, we must note that the experimental investigation of the data withdraws all measures taken during the transient time of the simulator. Table 4.10 shows the numerical analysis extracted from the data of Fig. 4.18.

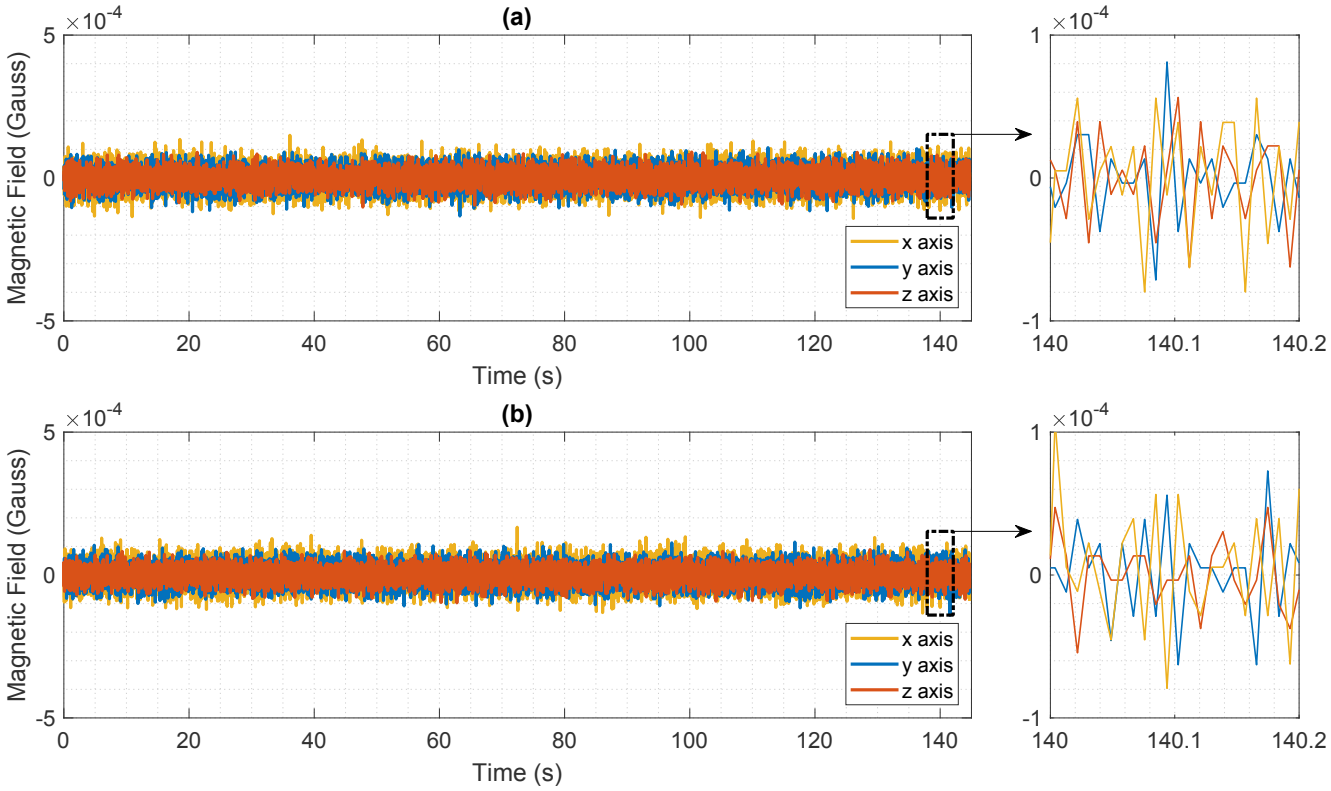

Figure 4.18: Magnetic field error for the closed-loop operation. (a) Result for the magnetic field input of Fig. 4.4(a) waveform. (b) Result for the magnetic field input of Fig. 4.4(b) waveform.

Table 4.10: Closed-loop error data analysis for the results seen in Figs. 4.18(a) and 4.18(b).

Waveform Test	Axis	Mean Error (μG)	RMS Error (μG)	Error Min. (μG)	Error Max. (μG)	Peak-to-peak Error (μG)
Fig. 4.18(a)	**x**	0.03	35.8	-132.9	124.2	257.1
	y	0.01	27.9	-114.6	108.2	222.8
	z	-0.03	44.0	-141.4	149.3	290.7
Fig. 4.18(b)	**x**	0.05	36.0	-140.9	131.8	272.7
	y	-0.04	27.7	-97.3	92.6	189.9
	z	0.01	44.1	-133.1	167.1	300.2

Results show that the output error depends on the controller capability and not on the input waveform, which is expected by a system operating in a closed-loop topology. Furthermore, the RMSE errors in all axes are within the simulator's resolution, proving the controller is correctly compensating for the deviation of the output and the setpoint value. At last, the results reported above were consistent with every input tested; therefore, this section summarized them with these two waveforms similar to those used in the open-loop analysis.

The updated HiL simulator has considerably better closed-loop results than those reported in [25] because of the improved HCS and the system's resolution. These results reiterate the digital controller effectiveness proposed in that work.

The closed-loop operation of the simulator is an option for cases where the open-loop non-compensated generated magnetic field is not mandatory. For instance, it is suitable for comparing different magnetometer calibration algorithms or evaluating the calibration outcome to a specific dataset. In addition, it allows a more straightforward use without requiring calibration for each magnetic field input.

4.8 Conclusion of the Chapter

The results reported show that the improved magnetic field simulator can operate by generating an open-loop (non-compensated) or closed-loop (compensated) magnetic field. Although the latter provides a more straightforward and accurate solution to generate any desired magnetic field, it is only suitable for some situations.

For instance, testing a magnetometer subject to a time-varying interference or evaluating if a SUT produces any interference to a magnetometer is unfeasible, or at best not ideal, with the closed-loop topology. In addition, in smaller magnetic field simulators, such as ours, retaining a sensor to provide the feedback measurement can be a disadvantage, as these simulators may have a limited uniformity volume of the generated magnetic field. Therefore, the calibration methodology presented is vital in those circumstances.

Also, smaller magnetic field simulators and nanosatellites (or UAVs, among others) testing facilities might not have a completely dedicated area for the simulator. Consequently, they are subject to interference from surrounding elements, such as electronics or ferromagnetic materials, or even the structural part of the building. Once more, that is the case with our setup, and each experimentalist would have to evaluate their system. In these conditions, it is also imperative to establish a methodological calibration procedure for using the

simulator without a closed-loop topology.

The proposed setup calibration procedure works, and the simulator can generate an open-loop magnetic field with an accuracy superior to 1 milligauss. In addition, the final open-loop error observed is in the same order of magnitude as the actual resolution of the system. Consequently, further investigation and possible improvements of the calibration procedure are not attainable with the current DAC and ADC used to control the HCS and to acquire the fluxgate readings, respectively. Hence, future works should pursue manners to improve the system resolution and then repeat the chapter's tests and methodological analysis. That would allow for better insights into the system's accuracy without the current restraints caused by its resolution.

Despite the resolution limitation, the open-loop calibration works well and has sufficient accuracy to test low-cost magnetic sensors. For reference, the low-cost magnetometer used in Chapters 5 and 6 analyses has a noise with 1.5 milligauss of standard deviation, supported by the test reported in Appendix A.1. Another important conclusion is that the excitation field used to find the estimated parameters for the open-loop field correction should be the same base field used for the sensor's calibration for optimum results. Different magnetic field inputs lead to slightly different calibration parameters, mainly the second and third-order elements. Nevertheless, the system has long-term stability to a specific waveform calibration. Results have shown that tests conducted ten hours apart led to almost identical calibration and open-loop results.

At last, the simulator has the scope to perform real-time simulations in a range of 4-20 samples, depending on the sensor under test, per second while generating an open-loop magnetic field with a sub-milligauss precision. Thus, despite requiring a new calibration for different waveforms, the setup is capable, for example, of generating in real-time the magnetic field experienced by a nanosatellite in a low Earth orbit while simulating its dynamics. It also shows the system's capability to perform analysis of low-cost magnetometer calibrations, which can include time-varying interference investigations.

5 The Attitude-Independent Magnetometer Calibration using the Non-Linear Least Square Solution

A great deal of attitude determination systems rely on information provided by magnetic sensors. Therefore, three-axis attitude-independent magnetometer calibration is critical to achieving the best outcome in these systems' performance in spacecraft, aircraft, UAVs, and other applications. This thesis solely assesses the attitude-independent calibration problem, and all forward mentions of calibration implicate and are related to these methods. Most calibration works consider only time-invariant errors in their model, such as [2, 77–79]. Nevertheless, a few authors [7, 8, 10, 11, 13] have shown how CubeSats and similar spacecraft may benefit from including time-varying bias in the sensor model. This chapter discusses the former, whereas the latter is investigated in Chapter 6.

The current chapter addresses the theoretical problem of the time-invariant three-axial magnetometer calibration and the proposed formulation to estimate the parameters using a Non-Linear Least Squares (NLLS) algorithm. We show that it is possible to use the NLLS solution directly using the well-known non-linear sensor model proposed by Foster and Elkaim [2] in the Extended Two-Step (ETS) algorithm. Theoretically, the attitude-independent calibration work of Springmann and Cutler [7], which includes time-varying bias parameters, uses a similar minimization technique to estimate the parameters. However, the authors do not explicitly show their solution (that work focuses on the on-orbit nanosatellite calibration, including varying bias interference, not on the estimator itself) and indicate that the algorithm convergence does not depend on the initial parameters. On the contrary, the convergence of the non-linear least squares formulation, applied in the sensor model presented in the ETS algorithm [2], depends on the parameters' starting point. We also display evidence of this issue and that, in general, convergence is ensured if a reasonable estimate of scale factors and offsets is provided; consequently, the NLLS requires an initial guess algorithm or a previous estimation of the parameters. In this direction, we also present a simplified new formulation to compute the offsets and scale factors and other possible algorithms to provide an initial estimate of them.

There are a few noteworthy advantages of using the direct NLLS estimator to the non-linear sensor model of the ETS solution. First, it allows computing the calibration parameters uncertainties using the Cramér-Rao Inequality lower bounds [33], which is essential for evaluating the calibration quality. Secondly, it does not require the assumption that all magnetometer measurements have a constant magnetic field magnitude, which may be required for on-orbit magnetometer calibration, where the magnetic field varies with the spacecraft's position. Besides, it is a more straightforward and easier-to-implement solution than others, such as those seen in [78, 80, 81], and does not require computing the Hessian matrix, as required by a few algorithms. At

last, expanding it to include other calibration parameters, such as time-varying bias [7], is straightforward.

The NLLS algorithm and the proposed one to estimate scale factors and bias are validated through simulation and experimental data using the magnetic field simulator. In addition to that, we compare our algorithm to the analytical solution of the extended two-step (ETS-A) of [2], which was recently computed and shown by Menezes Filho et al. [36]. The latter provides a step-by-step solution of the ETS-A algorithm, which allows the exact reproduction. Furthermore, the authors also compare the ETS-A to other methods [77,78,80–82], providing a small survey among their contributions and also to other works observations [83, 84]. As a result, it is possible to compare the proposed algorithm and the ETS-A implementation and infer our algorithm performance compared to these other results.

The remainder of the chapter is organized as follows. Section 5.1 introduces the problem, reviews the state-of-the-art solutions, and situates our algorithm within the existing literature. Section 5.2 discusses the magnetometer errors and shows the time-invariant sensor model, and Section 5.3 depicts the proposed non-linear least squares solution to estimate the parameters. Section 5.4 exhibits possible algorithms to estimate the initial scale factor and bias used to ensure the NLLS algorithm convergence. Section 5.5 shows the NLLS algorithm validation through simulations. Lastly, Section 5.6 demonstrates the experimental calibration of low-cost magnetic sensors using the magnetic field simulator.

5.1 The Calibration Problem and Existing Solutions

The calibration problem can be divided into two steps: the sensor error model and the solution to estimate the model's parameters. Several sources of errors can corrupt a magnetometer measurement, which can be constant (time-invariant) and time-varying ones [7]. Furthermore, they are either inherent to the sensor or due to surrounding elements, such as ferromagnetic materials and electronic systems. Section 5.2 discusses the errors.

Several attitude-independent methods consider a sensor model with nine-time invariant parameters, including scale factors, bias, and nonorthogonality. References [2,77–79,85] are examples of that. Applying such a model seeks to correct hard, and soft iron errors, scale factors, null shift errors, and nonorthogonality [7]. Our work considers this model for the time-invariant analysis and in cases where mapping varying currents (or interferences) is not feasible. The inclusion of the time-varying parameters in the sensor model is seen in [7, 10], for instance. The first adds varying parameters to compensate for magnetorquer coupling effects. The latter adds one bias parameter on each axis for every known (and observable) variable electrical current surrounding the sensor. The time-varying sensor model is discussed in Chapter 6.

Numerous algorithms exist to estimate the time-invariant parameters, which can be batch, real-time, and artificial intelligence-based. The first approach for the attitude-independent problem resulted in the batch calibration algorithm, known as TWOSTEP, proposed by Alonso and Shuster in references [86] and [77]. The first performed the bias calibration, and the other included scale factors and misalignment between the sensor's axes. The TWOSTEP algorithm is a two-step procedure based on the negative-log-likelihood loss function. The first step provides an initial offset parameter estimation using a centering approximation, followed by a Gauss-Newton iterative method to evaluate the parameters.

Another algorithm, which relies on the premise that the magnetic field magnitude is constant during the calibration process, was suggested by Gebre-Egziabher et al. [1, 87] to calibrate scale factors and offsets. Foster and Elkaim [2] proposed an extension of that work to include misalignment angles. This well-known solution, Extended Two-Step (ETS), rewrites the problem into auxiliary variables and applies a batch least squares next. It is essential to observe that although both the ETS and the TWOSTEP methods compensate for scale factors, bias, and misalignment, the sensor model is equivalent but not identical.

Many solutions came afterward, with some of them being derived from those above. Notable mentions are: the real-time extended and the unscented Kalman filter implementation of [85] based on the solution of Alonso and Shuster; the Maximum Likelihood (ML) Estimator of [78] based on the ETS formulation and the optimal ML of [81]; the total least-squares solutions of [79, 80], where the former follows the ETS model and the latter the TWOSTEP idea; artificial intelligence or adaptive algorithms [88–91]. Recently, some authors compared a few of these solutions [9, 36, 84].

We also note that many other attitude-independent formulations came to include additional parameters [7, 82, 92–94]. For instance, these include the calibration of the magnetometer to a vehicle's, or another sensor's frame, unified calibration with inertial sensors, and applications with time-varying bias. However, except for the time-varying bias study reported in Chapter 6, these go beyond the scope and contributions of our algorithm.

All the above solutions are attitude-independent and use the same principle: the magnetic field components are unknown as the sensor information is used to estimate attitude, and the algorithm depends either on the knowledge of the expected magnitude of the geomagnetic field or on the premise that every measurement has a constant magnitude value. Typically, the magnitude value is obtained by a geomagnetic field model, such as the International Geomagnetic Reference Field (IGRF) [95] or the World Magnetic Model (WMM) [42], using the geographical location of the sensor. The problem cost function is based on the principle of minimizing the difference between the expected magnitude (B_e) and the measured magnitude ($\widetilde{B}_e$), $\min(B_e - \widetilde{B}_e)$, or $\min(B_e^2 - \widetilde{B}_e^2)$, where $\widetilde{B}_e$ depends on each axis measurements, $\widetilde{B}_x$, $\widetilde{B}_y$, and $\widetilde{B}_z$.

One of this thesis' novelty is to present the direct application of a Non-Linear Least Squares (NLLS) estimator [33] to the ETS sensor model proposed by Foster and Elkaim [2]. Based on the loss function of the NLLS, it is possible to apply the generalization of Newton's root-solving method using the linearized problem model to find the calibration parameters. Hence, the problem does not need to be rewritten using intermediate variables required by the ETS algorithm. Despite a few differences in the formulation, our method can be seen as an expansion of the works of [1] and [96], where the authors applied a similar concept to calibrate scale factors and offsets, respectively, for three-axial magnetometers and accelerometers. At last, an NLLS solution was proposed previously by [97]; nonetheless, that work followed the sensor model and formulation of Alonso and Shuter [77]. Therefore, our NLLS solution has a different formulation.

5.2 The Three-Axial Magnetometer Errors and the Sensor Model

Errors are either inherent to the sensor or a consequence of elements in its surrounding. Therefore, we must separate these errors to understand the time-invariant sensor model and conditions to compensate for time-

varying interference. The source of errors are well-known in the literature and include hard and soft iron effect, sensor bias (or zero bias / null shift), scale factors, non-orthogonality, sensor noise, and non-linearity errors. See references [1, 2, 7, 36] for further discussion. A brief description of each follows below.

Hard Iron distortions are created by objects that produce a magnetic field, resulting in a permanent bias in the local magnetic field. In other words, it is a bias produced by unwanted magnetic fields near the magnetometer, typically due to ferromagnetic (hard iron) materials. These materials perturb the magnetic field at the sensor's location, resulting in an offset between the ambient and measured magnetic fields. Hard iron errors are independent of the ambient magnetic field vector and are parametrized as a bias (offset) in each magnetometer sensing element. To sum up, hard iron errors represent magnetic field sources, which add (or subtract) to the Earth's magnetic field.

Soft Iron effects generate a magnetic field that depends on the externally applied field. In other words, they are errors caused by materials that distort and stretch the local magnetic field. Soft iron errors represent the magnitude and direction change experienced by the Earth's magnetic field due to near ferromagnetic objects. Supposing a linear response between the external field and the resulting field induced by a soft iron material (non-hysteretic response, which most authors assume [2, 7]), these errors are represented by a combination of a scale factor and misalignment error.

Null shift or zero bias is an error inherent to the sensor which results in a constant offset that adds (or subtracts) a fixed value to the output value of the sensor. A bias component parameterizes it in each axis and, mathematically, is similar to the hard iron effect.

Scale factor errors are inherent to the sensor and result in a deviation of the sensor scale sensitivity. This error is parameterized by a scale factor term in each axis and treated independently. Furthermore, we must note that, mathematically, part of the soft iron is also represented by a scale factor on each axis. Therefore, the scale factor parameter combines the errors caused by soft materials and those inherent to the sensor.

Non-orthogonality error is the inherent deviation of the sensitivity axis from the orthogonal sensor axes. Usually, the model assumes a plane as the reference, and the measurements are correct for this frame. The parameterization is done through misalignment error parameters and is mathematically similar to the soft iron effect. Calibration of the sensor frame to the body frame requires additional information and is usually neglected, especially for low-cost sensor applications.

Non-linearity errors inherent to the device are a deviation between the sensor's input and output linear relationship. The non-linear behavior is assumed to be negligible by most authors [2, 7] and is not included in the sensor model. This assumption is valid because even low-cost magnetometers have deviations smaller than 0.2% to the full scale of the output range[1].

Sensor noise is the stochastic (uncertainties) component observed in the sensor output. As with most sensors, we assume a Gaussian distribution with zero means, which is true for most cases. However, only experimental data can confirm the noise distribution in each case.

[1] Examples are the low-cost HMC5883L magnetometer from Honeywell and the ADIS16448 IMU. Both magnetic sensors have a worst-case linearity of 0.1% for the full scale (see Annex I).

The time-invariant model [1, 2, 77–79, 85] assumes that the nine-parameters model compensates for all previous errors, which is true in an ideal scenario. For example, a ferromagnetic material and a sensor mounted in the same frame as the body will cause a constant and invariant error, as explicitly discussed in [2]. On the other hand, if an object approaches the sensor or rotates with respect to the sensor frame, it will result in a varying (temporary or not) and non-constant error. Even errors inherent to the sensor may drift over a long time, which is why on-orbit or in-use calibration of the magnetometers is necessary.

That said, we can further separate the errors in inherent to the sensor and internal or external disturbances. *Internal disturbances* are errors caused by elements around the sensor (ferromagnetic materials, other electronics systems, structures) that are rigidly mounted on a platform with respect to the magnetometer and the platform itself. In other words, they are fixed in the same frame as the sensor and at a relatively fixed position, which is often the case in spacecraft. On the contrary, *external disturbances* include objects producing a magnetic field in the surrounding environment that are not fixed with respect to the magnetometer. Consequently, elements in the surrounding environment that are not rigidly attached to the sensor and disturb the geomagnetic field are sources of external magnetic disturbances. Again, such disturbances are not usually the case in spacecraft, for obvious reasons, but are more likely to occur on terrestrial attitude determination systems, for example, on a handheld device or a UAV.

5.2.1 The Time-Invariant Sensor Model

A comprehensive understanding of the model is found in [2] and [78]. It is not viable to define a practical model to account for all the previous errors separately. Physically, separating hard iron from zero bias and separating the effects of soft iron from scale factors and non-orthogonality is unfeasible. Thus, the sensor model is reduced to nine parameters, including offset and scale factor in each axis and three misalignment angles. The sensor measurement $\tilde{\mathbf{u}}$ and Earth's magnetic field $\mathbf{u}$ can be related as:

$$\tilde{\mathbf{u}} = \mathbf{STu} + \mathbf{b_0} + \eta, \tag{5.1}$$

where $\mathbf{S}$ is a 3×3 diagonal matrix containing the scale factors, $\mathbf{T}$ is a 3×3 matrix with the misalignment terms, $\mathbf{b_0}$ is the offsets parameters 3×1 vector, and η the 3×1 vector with the noise associated to each axis. Rewriting (5.1) to show the parameters as a function of the measurements and Earth's magnetic field in each axis, we have the model given by:

$$\begin{bmatrix} \widetilde{B}_x \\ \widetilde{B}_y \\ \widetilde{B}_z \end{bmatrix} = \begin{bmatrix} a & 0 & 0 \\ 0 & b & 0 \\ 0 & 0 & c \end{bmatrix} \begin{bmatrix} 1 & 0 & 0 \\ \sin(\rho) & \cos(\rho) & 0 \\ \sin(\phi)\cos(\lambda) & \sin(\lambda) & \cos(\phi)\cos(\lambda) \end{bmatrix} \begin{bmatrix} B_x \\ B_y \\ B_z \end{bmatrix} + \begin{bmatrix} x_0 \\ y_0 \\ z_0 \end{bmatrix} + \begin{bmatrix} \eta_x \\ \eta_y \\ \eta_z \end{bmatrix}, \tag{5.2}$$

where $\widetilde{B}_{\mathrm{x}}$, $\widetilde{B}_{\mathrm{y}}$, and $\widetilde{B}_{\mathrm{z}}$ denote the observed components of the vector over the sensor axes; B_x, B_y, and B_z are the true (unknown) orthogonal geomagnetic field; the errors, which we seek to estimate, are given by the scale factors of each axis (a, b and c), the offset values (x_0, y_0, and z_0), and the misalignment angles from the sensor axes with respect to the true magnetic field orthogonal trihedron ρ, λ, and ϕ. Regarding the misalignment angles, the model assumes that $\widetilde{B}_x$ and B_x are coincident and $\widetilde{B}_y$ is contained within the x-y plan from the orthogonal trihedron. This results in a misalignment angle between $\widetilde{B}_y$ and B_y, given by ρ, and a misalignment

between $\widetilde{B}_z$ and B_z, which is characterized by two angles that measure the misalignment between $\widetilde{B}_z$ and the x-z plan, and the misalignment between $\widetilde{B}_z$ and the y-z plan, given by λ and ϕ, respectively. For further clarification, once more we redirect the reader to [2, 7].

Alternatively, each axis measurement can be represented individually by (5.3)-(5.5), respectively, for the x, y, and z axes. This representation might be easier to understand and provides a better manner to find the Jacobian and other elements required for the parameter estimation discussed in the next section.

$$\widetilde{B}_{\mathrm{x}} = aB_{\mathrm{x}} + x_0 + \eta_{\mathrm{x}} \tag{5.3}$$

$$\widetilde{B}_{\mathrm{y}} = b\Big(B_{\mathrm{x}}\sin(\rho) + B_{\mathrm{y}}\cos(\rho)\Big) + y_0 + \eta_{\mathrm{y}} \tag{5.4}$$

$$\widetilde{B}_{\mathrm{z}} = c\Big(B_{\mathrm{x}}\sin(\phi)\cos(\lambda) + B_{\mathrm{y}}\sin(\lambda) + B_{\mathrm{z}}\cos(\phi)\cos(\lambda)\Big) + z_0 + \eta_{\mathrm{z}} \tag{5.5}$$

5.3 The proposed Non-Linear Least Squares Algorithm

The Non-Linear Least Squares (NLLS) [33] is a method that seeks to iteratively minimize the loss function (J) given by:

$$J = \frac{1}{2}\mathbf{e}^{\mathsf{T}}\mathbf{e} = \frac{1}{2}\Big[\tilde{\mathbf{y}} - \hat{\mathbf{y}}\Big]^{\mathsf{T}}\Big[\tilde{\mathbf{y}} - \hat{\mathbf{y}}\Big] = \frac{1}{2}\Big[\tilde{\mathbf{y}} - \mathbf{f}(\hat{\mathbf{x}})\Big]^{\mathsf{T}}\Big[\tilde{\mathbf{y}} - \mathbf{f}(\hat{\mathbf{x}})\Big], \tag{5.6}$$

where $\mathbf{e}$, in the typical formulation of the NLLS [33], is the residual error of the measured values $\tilde{\mathbf{y}}$ and the estimated values $\hat{\mathbf{y}}$. This last, in turn, is a function of the values of the estimated parameters $\hat{\mathbf{x}}$, given by $\hat{\mathbf{y}} = f(\hat{\mathbf{x}})$.

5.3.1 The NLLS Formulation adapted on the Attitude-Independent Calibration

The calibration problem is attitude-independent, meaning it is impossible to relate the sensor measurement and an expected value. The formulation requires knowledge of the expected magnetic field magnitude, B_e, associated with each measure. The squared magnitude (B_e^2) is given by the sum of all vector components ($B_x^2 + B_y^2 + B_z^2$), following the relationship:

$$B_e^2 = B_x^2 + B_y^2 + B_z^2 = f(\widetilde{\mathbf{B}}, \mathbf{p}), \tag{5.7}$$

where the true unknown components of the magnetic field B_x, B_y, and B_z are functions of the sensor measurement ($\widetilde{\mathbf{B}}$) and the parameters ($\mathbf{p}$), which is a 9×1 vector. The resulting model of the problem, $f(\tilde{\mathbf{B}}, \mathbf{p})$, is found by isolating B_x, B_y, and B_z in (5.3)-(5.5) and replacing into (5.7). That yields (5.8).

$$\begin{aligned} f\left(\tilde{\mathbf{B}}, \mathbf{p}\right) = B_x^2 + B_y^2 + B_z^2 = \left(\frac{\widetilde{B}_{\mathrm{x}} - x_0}{a}\right)^2 + \left(\frac{a(\widetilde{B}_{\mathrm{y}} - y_0) - b\sin(\rho)(\widetilde{B}_{\mathrm{x}} - x_0)}{ab\cos(\rho)}\right)^2 + \\ \left(\frac{ab\cos(\rho)\left(\widetilde{B}_{\mathrm{z}} - z_0\right) - ac\sin(\lambda)\left(\widetilde{B}_{\mathrm{y}} - y_0\right) + bc\Big(\sin(\lambda)\sin(\rho) - \cos(\rho)\sin(\phi)\cos(\lambda)\Big)\left(\widetilde{B}_{\mathrm{x}} - x_0\right)}{abc\cos(\rho)\cos(\phi)\cos(\lambda)}\right)^2 \end{aligned} \tag{5.8}$$

Relating this formulation to the NLLS, the algorithm seeks to minimize the loss function, given by the difference between the square geomagnetic field module (B_e^2) and the vector components calculated by (5.8).

Finally, the attitude-independent calibration loss function will be given by:

$$J = \frac{1}{2}\left[\mathbf{B}_e^2 - \mathbf{f}(\tilde{\mathbf{B}}, \mathbf{p})\right]^{\mathsf{T}}\left[\mathbf{B}_e^2 - \mathbf{f}(\tilde{\mathbf{B}}, \mathbf{p})\right], \tag{5.9}$$

where, assuming m measurements, $\mathbf{B}_e^2$ is an $m \times 1$ vector with the expected magnetic field magnitude associated to each measurement, and $\mathbf{f}(\tilde{\mathbf{B}}, \mathbf{p})$ a $m \times 1$ vector calculated for all measurements using (5.8). Note that $\mathbf{B}_e$ can be a vector with constant values or a different value associated to each measurement.

The algorithm description and theory demonstration are found in [33]. It iteratively minimizes (5.9) by updating the calibration parameters using the residual error linearly approximated by the gradient matrix of the sensor model. Therefore, in each iteration, the algorithm updates the calibration parameters following (5.10), where the parameter increment term is calculated via the NLLS solution given by (5.11).

$$\hat{\mathbf{p}}^{+} = \hat{\mathbf{p}}^{-} + \Delta\mathbf{p}, \tag{5.10}$$

where $\hat{\mathbf{p}}^{+}$ and $\hat{\mathbf{p}}^{-}$ are, respectively, the updated and the previous iteration 9×1 vector containing the calibration parameters, and $\Delta\mathbf{p}$ is a 9×1 vector containing the parameters increment, calculated by:

$$\Delta\mathbf{p} = \left(\mathbf{H}^{\mathsf{T}}\mathbf{H}\right)^{-1}\mathbf{H}^{\mathsf{T}}\mathbf{e}, \tag{5.11}$$

where $\mathbf{H}$ is the gradient, or Jacobian, matrix and $\mathbf{e}$ is the residual error in each iteration. In the attitude-independent problem formulation, the former is given by (5.12) and the latter by (5.13). The residual error $\mathbf{e}$ is an $m \times 1$ vector containing the difference of each squared expected magnitude and the model, given by (5.8), evaluated for each measurement at the last estimated set of parameters $\hat{\mathbf{p}}$. $\mathbf{H}$ is the $m \times 9$ Jacobian matrix calculated from each measurement and from $\hat{\mathbf{p}}$.

$$\mathbf{H} = \left.\frac{\partial \mathbf{f}(\widetilde{\mathbf{B}}, \mathbf{p})}{\partial \mathbf{p}}\right|_{\hat{\mathbf{p}}} \tag{5.12}$$

$$\mathbf{e} = \mathbf{B}_e^2 - \mathbf{f}(\widetilde{\mathbf{B}}, \hat{\mathbf{p}}) \tag{5.13}$$

The NLLS algorithm uses the previous set of parameters $\hat{\mathbf{p}}$ (or the initial estimate $\hat{\mathbf{p}}_0$ for the first iteration, which is discussed in Section 5.3.4) to calculate the residual error ($\mathbf{e}$) and the loss function, using (5.13) and (5.6), respectively. It then checks if the stop criteria have been reached, and, if not, it computes the full matrix $\mathbf{H}$ using (5.12), the parameter increment vector through (5.11), and updates the calibration parameters using (5.10).

The algorithm repeats the last paragraph process until it reaches either a stop criteria or a maximum number of iterations. Next, it computes the uncertainties of the estimated parameters using a similar concept to the Gramér-Rao Inequality [33], which provides the lower bounds for the variance of an unbiased estimator. The stopping criteria and the uncertainties computation are discussed in Sections 5.3.2 and 5.3.3, respectively.

Figure 5.1 comprehensively illustrates the NLLS algorithm flowchart.

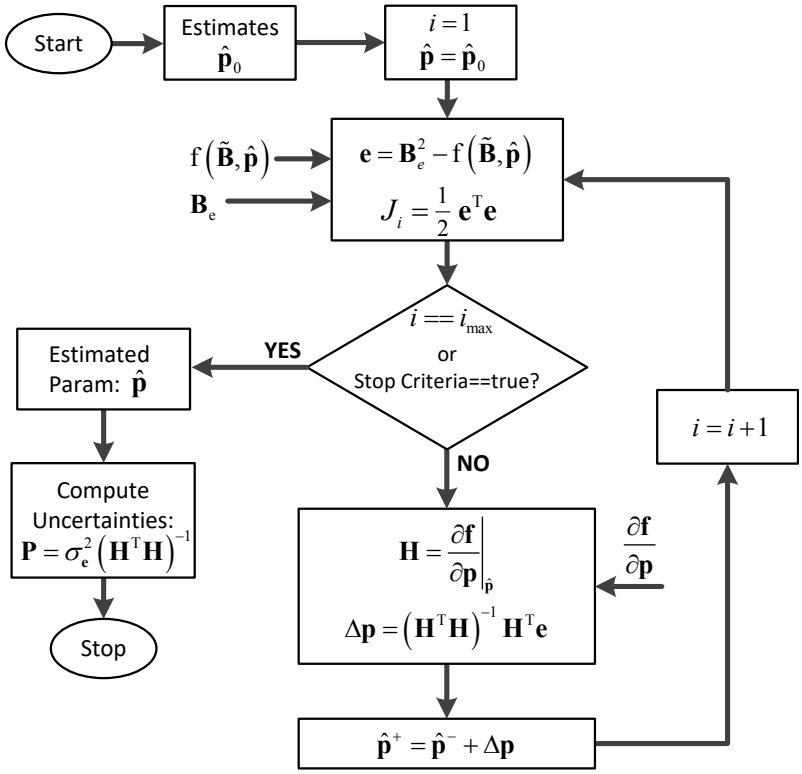

Figure 5.1: Flowchart of the proposed NLLS calibration algorithm.

5.3.2 The NLLS Stopping Criteria

The stopping condition criteria checks the decrease of the loss function J compared to the previous iteration beyond the third loop. Therefore, if (5.14) condition is valid and if $i \geq 3$ the algorithm ends the loop.

$$\delta J(\%) \equiv 100 \times \frac{|J_i - J_{i-1}|}{J_i} < \varepsilon, \tag{5.14}$$

where ε represents the percentage variation threshold that delimits the stopping condition. The Monte Carlo analysis in Section 5.5 has additional discussion; however, typical observations have shown that values between 0.05% and 0.2% are sufficient to ensure an accurate estimation.

Running at least three iterations avoids (5.14) misleading to a true false stopping in the second loop. Depending on the initial starting vector of the parameters and the input data, the first two iterations may have extremely close values of J, even though the algorithm has yet to achieve convergence. These rare but existing cases were found in some of the Monte Carlo simulations reported in Section 5.7, which addresses the algorithm's convergence and makes further comments on the number of iterations.

5.3.3 The Fisher information Matrix and Lower-bound Estimated Covariance

After reaching the stop criteria, the algorithm computes the covariance $\mathbf{P}$ of the estimated parameters using (5.15), which is a similar concept to Cramér-Rao Inequality [33].

$$\mathbf{P} = \mathrm{Var}(\mathbf{e})\left(\mathbf{H}^{\mathrm{T}}\mathbf{H}\right)^{-1} = \sigma_{\mathbf{e}}^2\left(\mathbf{H}^{\mathrm{T}}\mathbf{H}\right)^{-1}, \tag{5.15}$$

where $\sigma_{\mathbf{e}}^2$ is the variance calculated for the last iteration residual error values, $\mathbf{e}$. We take this approach since the variance of the model depends on the magnetometer measurements and the estimated parameters. In addition, since our model computes the squared values, the variance will depend on the absolute values of $\mathbf{B}_e$. Note that for constant expected magnitudes the value of $\sigma_{\mathbf{e}}^2$ will be identical to the model's variance, $\text{Var}\left(\mathbf{f}(\widetilde{\mathbf{B}}, \hat{\mathbf{p}})\right)$. However, that is not true for non-constant magnitudes, and we are required to compute the variance of the residual error vector. Furthermore, we assume all magnetometer measurements have a Gaussian distribution, and as a consequence, so does the error distribution and the model given by (5.8). This assumption is shown in [7] and validated in Appendix A.1.

Finally, the square root of the diagonal elements of the $\mathbf{P}$, a 9×9 covariance matrix, will provide the lower bounds (1σ) of the calibration quality for each parameter. Equation (5.16) displays the uncertainties extracted from the estimated $\mathbf{P}$. These elements allow the evaluation of the algorithm's convergence and the calibration accuracy for a specific set of magnetometer data [7].

$$\mathbf{p}_{1\sigma} = \sqrt{\text{diag}\,(\mathbf{P})} \tag{5.16}$$

5.3.4 About the Initial Estimate $\mathbf{p_0}$ and Possible Solutions

The initial state of $\mathbf{p}$, denoted by $\mathbf{p}_0$, is critical to ensure the algorithm's convergence. In general, the misalignment angles are relatively small ($< 10^\circ$), and if a good initial guess of the offsets and scale factors is provided, the algorithm achieves convergence regardless of the error. Section 5.7.1 demonstrates that. Therefore, we seek an algorithm capable of estimating these parameters using a method that does not depend on an initial starting point and without convergence issues.

The starting guess formulation described in Gebre-Egziabher et al. [1] is an adequate algorithm to solve the problem complying with these conditions. In their algorithm, the authors depicted a method to rewrite the sensor model considering the scale factor and offset using intermediate variables and solving by the batch least squares. That specific formulation of Gebre-Egziabher et al. was the one expanded by Foster and Elkaim to include the misalignment angles [2].

Nonetheless, that formulation has the same limitation as the intermediate solution of the two-step algorithm of Foster and Elkaim, which requires a constant magnitude for all measurements. Consequently, it is not applicable in scenarios with non-constant magnitude. Hence, we propose two alternative solutions.

The first is the formulation of Gebre-Egziabher et al., adapted to estimate the offsets and the scale factors considering measurements with distinct magnitude values. However, the issue with that alternative formulation is that it is unsuitable for constant magnitudes. Therefore, for the sake of simplicity, we propose a second alternative manner to calculate the offset and scale factors that comply with conditions of constant and non-constant magnetic field magnitude measurements.

Section 5.4 further discusses them and presents all three alternatives. Their comparison and error analysis through simulation is left for Appendix A.2.

5.3.5 About the Algorithm Input and Output Units

The most direct way to input data and the expected magnetic field (B_e) in the estimator is to provide their magnitude within a usual magnetic field unit, such as Gauss, mG, μT. Then, the offsets are estimated in the same unit, angles in radians, and the scale factors are unitless. In such cases, the sensor's count measurement is converted to the magnetic field unit before the algorithm; hence, the scale factor is unitless beyond that. One can see that by making a dimensional analysis of (5.8) and (5.9).

Similarly, it is possible to use the algorithm by inputting data directly in the sensor's measurement count and the expected magnitude in the magnetic field unit. For instance, let us assume the sensor's measurement data input in counts (LSB) and the expected field in mG. In such a scenario, the estimated offset is in LSB counts, the angles are in radians, and the scale factor relates the sensor's count and the magnetic field unit (LSB/mG).

5.4 The Initial State Solution for the Scale Factors and Offsets

As mentioned in Section 5.3.4, Gebre-Egziabher et al. [1] proposed an algorithm capable of estimating initial conditions for the scale factor and bias as the starting point to their recursive non-linear least squares estimator. Note that their work did not include misalignment or non-orthogonality parameters. The authors have found that the initial estimation was almost as good as their non-linear least squares; nevertheless, the recursive estimator was necessary to compute the uncertainties of the parameters.

Section 5.4.1 describes that initial estimate solution. However, that procedure is restricted because it relies on the fact that every measurement must have the same magnetic field magnitude value. Hence, we show an adaptation of Gebre-Egziabher et al. to overcome that limitation in Section 5.4.2. At last, Section 5.4.3 depicts a proposed alternative solution, which does not have restraints related to the magnitude value, whether they are constant or not. Furthermore, that solution simplifies the problem by separately estimating the bias and scale factors.

All methods have the same simplified sensor model without misalignment parameters. Therefore, we can rewrite the sensor model of (5.7) without the misalignment matrix $\mathbf{T}$, and each axis measurement, previously given by (5.3)-(5.5), are reduced to:

$$\widetilde{B}_{\mathrm{x}} = aB_{\mathrm{x}} + x_0 + \eta_{\mathrm{x}} \tag{5.17}$$

$$\widetilde{B}_{\mathrm{y}} = bB_{\mathrm{x}} + y_0 + \eta_{\mathrm{y}} \tag{5.18}$$

$$\widetilde{B}_{\mathrm{z}} = cB_{\mathrm{z}} + z_0 + \eta_{\mathrm{z}}. \tag{5.19}$$

Analogously to the NLLS formulation, it is possible to write the expected square magnitude as a function of each axis measurement:

$$B_e^2 = B_x^2 + B_y^2 + B_z^2 = \left(\frac{\tilde{B}_x - x_0}{a}\right)^2 + \left(\frac{\tilde{B}_y - y_0}{b}\right)^2 + \left(\frac{\tilde{B}_z - z_0}{c}\right)^2, \tag{5.20}$$

and assuming m measurements, we seek to find the scale factors and bias parameters that minimize the differ-

ence between the squared expected magnitude of each measurement (B_e^2) and the squared vector components sum ($B_x^2 + B_y^2 + B_z^2$).

5.4.1 The Initial Estimation using the Solution of Gebre-Egziabher et al.

The algorithm proposed by Gebre-Egziabher et al. [1] is a non-linear two-step estimator that rewrites (5.20) using intermediate variables and applies a linear batch estimator. Thereby, the estimation problem becomes linear in the first step and has the desirable properties of a linear system, which allows computing the first-step parameters using the batch linear least squares [33]. Then, in the second step, the parameters (offsets and scale factors) are extracted through algebraic manipulation from the intermediate estimated variables.

To define the first-step formulation, we rewrite (5.20) into:

$$-\tilde{B}_x^2 = -2\tilde{B}_x x_0 - 2\tilde{B}_y y_0 \frac{a^2}{b^2} - 2\tilde{B}_z z_0 \frac{a^2}{c^2} + \tilde{B}_y^2 \frac{a^2}{b^2} + \tilde{B}_z^2 \frac{a^2}{c^2} + x_0^2 + y_0^2 \frac{a^2}{b^2} + z_0^2 \frac{a^2}{c^2} - B_e^2 a^2, \tag{5.21}$$

which is obtained by simply expanding each squared element in (5.20) and then isolating $-\tilde{B}_x^2$. Now, it is necessary to specify the correct intermediate variables to obtain a formulation that holds the properties of linear systems. Therefore, Gebre-Egziabher et al. have defined μ_1, μ_2, and μ_3, respectively given by (5.22)-(5.24).

$$\mu_1 = \frac{a^2}{b^2} \tag{5.22}$$

$$\mu_2 = \frac{a^2}{c^2} \tag{5.23}$$

$$\mu_3 = x_0^2 + \frac{a^2}{b^2} y_0^2 + \frac{a^2}{c^2} z_0^2 - a^2 B_e^2 \tag{5.24a}$$

$$= x_0^2 + \mu_1 y_0^2 + \mu_2 z_0^2 - a^2 B_e^2 \tag{5.24b}$$

Replacing μ_1, μ_2, and μ_3 into (5.21) leads to (5.25). Given m magnetometer measurements, we can put (5.25) into a matrix form following the linear relationship $\mathbf{y}_{\text{ge}} = \mathbf{H}_{\text{ge}}\mathbf{x}_{\text{ge}}$, where $\mathbf{x}_{\text{ge}}$ is a vector formed using the intermediate variables. Therefore, the batch least squares estimator [33] can be used to estimate the elements of $\mathbf{x}_{\text{ge}}$. Equation (5.26) shows the final matrix form proposed by Gebre-Egziabher et al.

$$-\tilde{B}_x^2 = -2\tilde{B}_x x_0 - 2\tilde{B}_y y_0 \mu_1 - 2\tilde{B}_z z_0 \mu_2 + \tilde{B}_y^2 \mu_1 + \tilde{B}_z^2 \mu_2 + \mu_3 \tag{5.25}$$

$$\underbrace{\begin{bmatrix} -\tilde{B}_{x_1}^2 \\ -\tilde{B}_{x_2}^2 \\ \vdots \\ -\tilde{B}_{x_m}^2 \end{bmatrix}}_{\mathbf{y}_{\text{ge}}} = \underbrace{\begin{bmatrix} -2\tilde{B}_{x_1} & -2\tilde{B}_{y_1} & -2\tilde{B}_{z_1} & \tilde{B}_{y_1}^2 & \tilde{B}_{z_1}^2 & 1 \\ -2\tilde{B}_{x_2} & -2\tilde{B}_{y_2} & -2\tilde{B}_{z_2} & \tilde{B}_{y_2}^2 & \tilde{B}_{z_2}^2 & 1 \\ \vdots & \vdots & \vdots & & & \\ -2\tilde{B}_{x_m} & -2\tilde{B}_{y_m} & -2\tilde{B}_{z_m} & \tilde{B}_{y_m}^2 & \tilde{B}_{z_m}^2 & 1 \end{bmatrix}}_{\mathbf{H}_{\text{ge}}} \underbrace{\begin{bmatrix} x_0 \\ \mu_1 y_0 \\ \mu_2 z_0 \\ \mu_1 \\ \mu_2 \\ \mu_3 \end{bmatrix}}_{\mathbf{x}_{\text{ge}}} \tag{5.26}$$

By taking m magnetometer measurements, we can estimate $\mathbf{x}_{\text{ge}}$ using (5.27).

$$\hat{\mathbf{x}}_{\mathrm{ge}} = \left(\mathbf{H}_{\mathrm{ge}}^{\mathsf{T}}\mathbf{H}_{\mathrm{ge}}\right)^{-1}\mathbf{H}_{\mathrm{ge}}^{\mathsf{T}}\mathbf{y}_{\mathrm{ge}} \tag{5.27}$$

Finally, the second step is responsible for the algebraic manipulation that extracts the offsets and scale factors from the estimated intermediate variables, $\hat{\mathbf{x}}_{\mathrm{ge}}$. Equations (5.28)-(5.33) relate x_0, y_0, z_0, a, b, and c, respectively, to the intermediate variables and the elements of $\hat{\mathbf{x}}_{\mathrm{ge}}$.

$$\hat{x}_0 = \hat{\mathbf{x}}_{\mathrm{ge}}(1) \tag{5.28}$$

$$\hat{y}_0 = \frac{\hat{\mathbf{x}}_{\mathrm{ge}}(2)}{\hat{\mathbf{x}}_{\mathrm{ge}}(4)} = \frac{\hat{\mathbf{x}}_{\mathrm{ge}}(2)}{\mu_1} \tag{5.29}$$

$$\hat{z}_0 = \frac{\hat{\mathbf{x}}_{\mathrm{ge}}(3)}{\hat{\mathbf{x}}_{\mathrm{ge}}(5)} = \frac{\hat{\mathbf{x}}_{\mathrm{ge}}(3)}{\mu_2} \tag{5.30}$$

$$\hat{a} = \sqrt{\frac{-\hat{\mathbf{x}}_{\mathrm{ge}}(6) + x_0^2 + \hat{\mathbf{x}}_{\mathrm{ge}}(4)y_0^2 + \hat{\mathbf{x}}_{\mathrm{ge}}(5)z_0^2}{B_e^2}} = \sqrt{\frac{-\mu_3 + x_0^2 + \mu_1 y_0^2 + \mu_2 z_0^2}{B_e^2}} \tag{5.31}$$

$$\hat{b} = \frac{\hat{a}}{\sqrt{\hat{\mathbf{x}}_{\mathrm{ge}}(4)}} = \frac{\hat{a}}{\sqrt{\mu_1}} \tag{5.32}$$

$$\hat{c} = \frac{\hat{a}}{\sqrt{\hat{\mathbf{x}}_{\mathrm{ge}}(5)}} = \frac{\hat{a}}{\sqrt{\mu_2}} \tag{5.33}$$

We must note that the magnitude measurement, B_e, is part of the estimated vector, and its value is necessary to find the non-normalized scale factors parameters. Therefore, it is only possible to correctly calculate the parameters using this procedure if B_e is constant throughout every measurement.

5.4.2 Adaptation of Gebre-Egziabher et al. Formulation for Non-Constant Magnetic Field Magnitudes

The alternative solution capable of solving the parameters for measurements with non-constant magnetic field magnitudes still uses the relationship of (5.21). However, we now seek to define the intermediate variables holding B_e either in the observation matrix $\mathbf{H}$ or the measurement matrix $\mathbf{y}$. Our alternative solution uses four intermediate variables instead of three to achieve that. The variables μ_1 and μ_2 are preserved similarly to the original algorithm seen before; hence, they are given by (5.22) and (5.23), respectively. Then, instead of μ_3, we define two new variables, named α_1 and α_2, and given by (5.34) and (5.35), respectively. Note that we have chosen to use α instead of μ in these new variables to avoid nomenclature divergences compared to the original work of Gebre-Egziabher et al. [1].

$$\alpha_1 = a^2 \tag{5.34}$$

$$\alpha_2 = x_0^2 + \frac{a^2}{b^2}y_0^2 + \frac{a^2}{c^2}z_0^2 = x_0^2 + \mu_1 y_0^2 + \mu_2 z_0^2 \tag{5.35}$$

For a single measurement, (1) can be rewritten into (2) using these new intermediate variables. Then, given m measurements, and similarly to the original solution, it is possible to represent the measurements in

a linear relationship following $\mathbf{y}_{\mathrm{ge}'} = \mathbf{H}_{\mathrm{ge}'}\mathbf{x}_{\mathrm{ge}'}$. Equation (5.37) depicts this matrix form.

$$-\tilde{B}_x^2 = -2\tilde{B}_x x_0 - 2\tilde{B}_y y_0\mu_1 - 2\tilde{B}_z z_0\mu_2 + \tilde{B}_y^2\mu_1 + \tilde{B}_z^2\mu_2 - B_e^2\alpha_1 + \alpha_2 \tag{5.36}$$

$$\underbrace{\begin{bmatrix} -\tilde{B}_{x_1}^2 \\ -\tilde{B}_{x_2}^2 \\ \vdots \\ -\tilde{B}_{x_m}^2 \end{bmatrix}}_{\mathbf{y}_{\mathrm{ge}'}} = \underbrace{\begin{bmatrix} -2\tilde{B}_{x_1} & -2\tilde{B}_{y_1} & -2\tilde{B}_{z_1} & \tilde{B}_{y_1}^2 & \tilde{B}_{z_1}^2 & -B_{e_1}^2 & 1 \\ -2\tilde{B}_{x_2} & -2\tilde{B}_{y_2} & -2\tilde{B}_{z_2} & \tilde{B}_{y_2}^2 & \tilde{B}_{z_2}^2 & -B_{e_2}^2 & 1 \\ \vdots & \vdots & \vdots & & & & \\ -2\tilde{B}_{x_m} & -2\tilde{B}_{y_m} & -2\tilde{B}_{z_m} & \tilde{B}_{y_m}^2 & \tilde{B}_{z_m}^2 & -B_{e_m}^2 & 1 \end{bmatrix}}_{\mathbf{H}_{\mathrm{ge}'}} \underbrace{\begin{bmatrix} x_0 \\ \mu_1 y_0 \\ \mu_2 z_0 \\ \mu_1 \\ \mu_2 \\ \alpha_1 \\ \alpha_2 \end{bmatrix}}_{\mathbf{x}_{\mathrm{ge}'}} \tag{5.37}$$

Again, the batch least squares is used to estimate the vector formed with the intermediate variables:

$$\hat{\mathbf{x}}_{\mathrm{ge}'} = \left(\mathbf{H}_{\mathrm{ge}'}^{\mathsf{T}}\mathbf{H}_{\mathrm{ge}'}\right)^{-1}\mathbf{H}_{\mathrm{ge}'}^{\mathsf{T}}\mathbf{y}_{\mathrm{ge}'} \tag{5.38}$$

With the estimated values of $\mathbf{x}_{\mathrm{ge}'}$, it is possible to calculate the parameters algebraically, similarly to the previous solution. The bias values remains unchanged, and x_0, y_0, and z_0 are extracted from $\mathbf{x}_{\mathrm{ge}'}$ using the same relationships of (5.28)-(5.30). At last, the scale factors of this adapted formulation are calculated using (5.39)-(5.41), respectively, for a, b, and c.

$$\hat{a} = \sqrt{\hat{\mathbf{x}}_{\mathrm{ge}'}(6)} = \sqrt{\alpha_1} \tag{5.39}$$

$$\hat{b} = \sqrt{\frac{\hat{\mathbf{x}}_{\mathrm{ge}'}(6)}{\hat{\mathbf{x}}_{\mathrm{ge}'}(4)}} = \sqrt{\frac{\alpha_1}{\mu_1}} = \frac{a}{\sqrt{\mu_1}} \tag{5.40}$$

$$\hat{c} = \sqrt{\frac{\hat{\mathbf{x}}_{\mathrm{ge}'}(6)}{\hat{\mathbf{x}}_{\mathrm{ge}'}(5)}} = \sqrt{\frac{\alpha_1}{\mu_2}} = \frac{a}{\sqrt{\mu_2}} \tag{5.41}$$

One should note that if the expected magnitude is constant in every measurement, the last two columns of $\mathbf{H}_{\mathrm{ge}'}$ are linearly dependent, and the matrix will not have a full rank. Consequently, computing (5.38) is not possible if the measurements taken by a sensor are subject to a constant magnetic field magnitude.

5.4.3 The Proposed Alternative Simplified Solution

The proposed alternative formulation has the same idea as the previous algorithms. Hence, it rewrites the problem using intermediate variables holding the properties of a linear system. However, the proposed solution simplifies the formulation by separating the bias and scale factor into two separate estimations. Although the bias and scale factors are computed separately, evaluating the latter depends on performing the bias computation first to guarantee convergence. This methodology's advantage in estimating the initial bias and scale factor condition is that it is suitable for cases with constant and non-constant magnetic field magnitude values.

The bias estimation procedure considers a simplified sensor model that only includes the bias parameters.

Therefore, the measurement model of (5.17)-(5.19) is rewritten to include only the bias parameter and is reduced to (5.42).

$$B_e^2 = (\tilde{B}_x - x_0)^2 + (\tilde{B}_y - y_0)^2 + (\tilde{B}_z - z_0)^2 \tag{5.42a}$$

$$B_e^2 - \tilde{B}_x^2 - \tilde{B}_y^2 - \tilde{B}_z^2 = x_0^2 + y_0^2 + z_0^2 - 2\tilde{B}_x x_0 - 2\tilde{B}_y y_0 - 2\tilde{B}_z z_0 \tag{5.42b}$$

Equation (5.42b) is obtained by expanding (5.42a) and subtracting the squared measurements at both sides. However, the problem is non-linear to formulate an estimation problem for x_0, y_0, and z_0. Thus, it is rewritten with the intermediate variables β_0 and $\tilde{\xi}$, resulting the following equation:

$$\tilde{\xi} = \beta_0 - 2\tilde{B}_x x_0 - 2\tilde{B}_y y_0 - 2\tilde{B}_z z_0, \tag{5.43}$$

where $\beta_0 = x_0^2 + y_0^2 + z_0^2$ and $\tilde{\xi} = B_e^2 - \tilde{B}_x^2 - \tilde{B}_y^2 - \tilde{B}_z^2$.

Assuming m magnetometer measurements, (5.43) can be expressed in the matrix form of (5.44), which follows the linear relationship $\mathbf{y}_\mathrm{b} = \mathbf{H}_\mathrm{b}\mathbf{x}_\mathrm{b}$.

$$\underbrace{\begin{bmatrix} \tilde{\xi}_1 \\ \tilde{\xi}_2 \\ \vdots \\ \tilde{\xi}_m \end{bmatrix}}_{\mathbf{y}_\mathrm{b}} = \underbrace{\begin{bmatrix} -2\tilde{B}_{x_1} & -2\tilde{B}_{y_1} & -2\tilde{B}_{z_1} & 1 \\ -2\tilde{B}_{x_2} & -2\tilde{B}_{y_2} & -2\tilde{B}_{z_2} & 1 \\ \vdots & \vdots & \vdots & \vdots \\ -2\tilde{B}_{x_m} & -2\tilde{B}_{y_m} & -2\tilde{B}_{z_m} & 1 \end{bmatrix}}_{\mathbf{H}_\mathrm{b}} \underbrace{\begin{bmatrix} x_0 \\ y_0 \\ z_0 \\ \beta_0 \end{bmatrix}}_{\mathbf{x}_\mathrm{b}}, \tag{5.44}$$

where $\mathbf{y}_\mathrm{b}$ is an $m \times 1$ vector obtained by using the expected magnetic field magnitude and the magnetometer readings from each measurement; $\mathbf{H}_\mathrm{b}$ is a $m \times 4$ matrix obtained using the magnetometer measurements and a column of ones; and $\mathbf{x}_\mathrm{b}$ is the 4×1 vector with the parameters which we seek to estimate. Then, for each $i\text{-}th$ measurement, $\tilde{\xi}_i = B_{e_i}^2 - \tilde{B}_{x_i}^2 - \tilde{B}_{y_i}^2 - \tilde{B}_{z_i}^2$, and each measurement may have an independent value of the expected magnitude.

With the $\mathbf{y}_\mathrm{b}$ vector and the $\mathbf{H}_\mathrm{b}$ matrix, one can compute the estimated parameters of $\mathbf{x}_\mathrm{b}$ using the batch linear square method [33]. The solution of $\mathbf{x_b}$ is obtained by means of (5.45).

$$\hat{\mathbf{x}}_\mathrm{b} = \left(\mathbf{H}_\mathrm{b}^\mathsf{T}\mathbf{H}_\mathrm{b}\right)^{-1}\mathbf{H}_\mathrm{b}^\mathsf{T}\mathbf{y}_\mathrm{b}, \tag{5.45}$$

where the bias estimates for each sensor's axis are given by $\hat{x}_0 = \hat{\mathbf{x}}_\mathrm{b}(1)$, $\hat{y}_0 = \hat{\mathbf{x}}_\mathrm{b}(2)$, and $\hat{z}_0 = \hat{\mathbf{x}}_\mathrm{b}(3)$.

The subsequent step that estimates the initial scale factor for each axis uses the computed bias. That result is vital to ensure the scale factor correct estimation. Returning the sensor model of (5.42a) to include each axis' scale factor results leads once more into:

$$B_e^2 = \left(\frac{\tilde{B}_x - x_0}{a}\right)^2 + \left(\frac{\tilde{B}_y - y_0}{b}\right)^2 + \left(\frac{\tilde{B}_z - z_0}{c}\right)^2, \tag{5.46}$$

where it is possible to compute $\tilde{B}_x - x_0$, $\tilde{B}_y - y_0$, and $\tilde{B}_z - z_0$ for each measurement using the bias estimation

$\hat{x}_0$, $\hat{y}_0$, and $\hat{z}_0$. Renaming these calculated values as B'_x, B'_y, and B'_z, respectively, (5.46) is rewritten as:

$$B_e^2 = \frac{1}{a^2}B_x'^2 + \frac{1}{b^2}B_y'^2 + \frac{1}{c^2}B_z'^2. \tag{5.47}$$

Equation (5.47) can be expanded to a matrix form assuming m measurements, which results in:

$$\underbrace{\begin{bmatrix} B_{e_1}^2 \\ B_{e_2}^2 \\ \vdots \\ B_{e_m}^2 \end{bmatrix}}_{\mathbf{y}_{\text{sf}}} = \underbrace{\begin{bmatrix} B_{x_1}'^2 & B_{y_1}'^2 & B_{z_1}'^2 \\ B_{x_2}'^2 & B_{y_2}'^2 & B_{z_2}'^2 \\ \vdots & \vdots & \vdots \\ B_{x_m}'^2 & B_{y_m}'^2 & B_{z_m}'^2 \end{bmatrix}}_{\mathbf{H}_{\text{sf}}} \underbrace{\begin{bmatrix} 1/a^2 \\ 1/b^2 \\ 1/c^2 \end{bmatrix}}_{\mathbf{x}_{\text{sf}}}, \tag{5.48}$$

where $\mathbf{y}_{\text{sf}}$ is an $m \times 1$ vector containing the squared expected magnetic field magnitude for each measurement; $\mathbf{H}_{\text{sf}}$ is a $m \times 3$ calculated using the magnetometer measurements and the initial bias estimation; and $\mathbf{x}_b$ is the 3×1 vector with the unknown parameters.

Once more, $\mathbf{x}_{\text{sf}}$ can be found using the batch linear least squares estimator. The solution is given by (5.49). Note that the a, b, and c are not obtained directly, as the estimated variables are intermediate.

$$\hat{\mathbf{x}}_{\text{sf}} = \left(\mathbf{H}_{\text{sf}}^{\mathsf{T}}\mathbf{H}_{\text{sf}}\right)^{-1}\mathbf{H}_{\text{sf}}^{\mathsf{T}}\mathbf{y}_{\text{sf}}, \tag{5.49}$$

and the scale factor estimates for each sensor's axis are given by $\{\hat{a}, \hat{b}, \hat{c}\} = \{\hat{\mathbf{x}}_{\text{sf}_i}^{-1/2}\}$, for $i = 1..3$.

Finally, Algorithm 5.1 summarizes the procedure comprehensively.

Algorithm 5.1: The proposed simplified Initial Condition Estimation Algorithm.

Step 1. Calculate $\tilde{\xi}_i$ for each measurement.
Step 2. Form vector $\mathbf{y}_b$ and matrix $\mathbf{H}_{\text{b}}$.
Step 3. Compute (5.45): $\mathbf{x}_{\text{b}} \leftarrow \text{inv}\left(\mathbf{H}_{\text{b}}^{\mathsf{T}}\mathbf{H}_{\text{b}}\right)\mathbf{H}_{\text{b}}^{\mathsf{T}}\mathbf{y}_{\text{b}}$.
Step 4. Extract $\hat{x}_0$, $\hat{y}_0$ and $\hat{z}_0$ from $\hat{\mathbf{x}}_b$.
Step 5. Calculate B'_{x_i}, B'_{y_i}, and B'_{z_i}. for each measurement.
Step 6. Form vector $\mathbf{y}_{\text{sf}}$ and matrix $\mathbf{H}_{\text{sf}}$.
Step 7. Compute (5.49): $\hat{\mathbf{x}}_{\text{sf}} \leftarrow \text{inv}\left(\mathbf{H}_{\text{sf}}^{\mathsf{T}}\mathbf{H}_{\text{sf}}\right)\mathbf{H}_{\text{sf}}^{\mathsf{T}}\mathbf{y}_{\text{sf}}$.
Step 8. Extract $\hat{a}$, $\hat{b}$, and $\hat{c}$ from $\hat{\mathbf{x}}_{\text{sf}}$.

5.5 Simulation to Validate the Time-Invariant Model Solution using the NLLS

The simulation analysis is broken up into five subsections. The first two subsections compare the Non-Linear Least Squares (NLLS) solution to the analytical solution of the extended two-step of Foster and Elkaim [2] described in [36] and referred to as the ETS-A algorithm. Section 5.5.1 demonstrates the calibration for a specific dataset corrupted by a distinct error. Section 5.5.2 presents a Monte Carlo simulation to evaluate both algorithms statistically and to establish a comparison between the parameters estimated by both algorithms. It also discusses the NLLS uncertainties obtained using the Cramér-Rao Inequality, which is complemented

by Section 5.5.3 analysis, where we depict further Monte Carlo simulations to evaluate the parameters' errors and uncertainties computed by the NLLS. At last, Sections 5.5.4 and 5.5.5 assess the NLLS solution to a non-constant magnitude simulation, reproducing an environment similar to that expected by an on-orbit magnetometer calibration. The former displays one calibration example, and the latter exhibits a Monte Carlo simulation to evaluate the error and uncertainties for the non-constant magnitude condition.

The comparison of the NLLS to the ETS-A is strategic, and the introductory part of the chapter has summarized the reasons. Nevertheless, the first motivation is that both algorithms solve the same sensor model. In addition, the work of [36] describes the ETS-A solution and compares its results to other well-known algorithms in the literature and the results seen in [83] and [84]. Therefore, comparing the NLLS and the ETS-A can be extrapolated to infer about the NLLS to other algorithms.

In every simulation, we use the simplified initial guess algorithm of Section 5.4.3 as the starting solution of the NLLS for simplicity since it is suitable for all procedures independent of the magnetic field magnitude. The algorithms and simulations were implemented in MATLAB. In addition, all simulations use the input measurement data and the expected magnitude in milligauss (mG) to simplify the data visualization. Thereby, all results show a unitless scale factor and an offset estimation in mG, as Section 5.3.5 explains. Further details on the methodology are discussed within each subsection.

5.5.1 Calibration Demonstration and Algorithm Comparison

To evaluate the algorithms, we generate a uniform distribution over the attitude sphere comprising 1112 points with a constant magnitude of 500 mG. Figure 5.2(a) shows the vector components plot of the theoretical non-corrupted data, which generates the corrupted dataset. Table 5.1 shows the simulated calibration parameters, and the noise represents the standard deviation value associated independently with each measurement axis. Finally, Fig. 5.2(b) shows the vector component plots in three dimensions of the corrupted dataset.

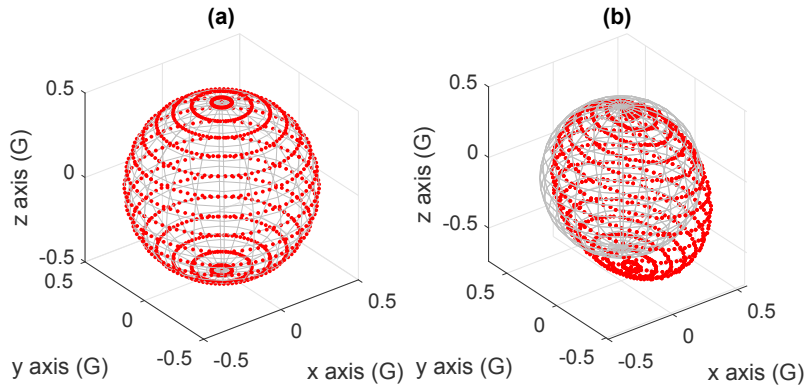

Figure 5.2: Vector components plotted in three dimensions of the simulated data in Section 5.5.1. (a) Theoretical data. (b) Uncalibrated data.

Table 5.1: Simulated calibration parameters that generates the corrupted dataset in Fig. 5.2(b).

Scale Factor (unitless)			**Offsets** (milligauss)			**Misalignment** (degrees)			**Noise SD** (milligauss)
a	b	c	x_0	y_0	z_0	ρ	ϕ	λ	σ_x, σ_y, σ_z
0.85	1.20	1.10	145	85	-180	2.50	-3.20	1.80	3

We apply the corrupted dataset as input to the NLLS and the ETS-A algorithms. Table 5.2 shows the estimated parameters for both solutions and Figs. 5.3(a) and 5.3(b) show the vector components calibrated data obtained from the NLLS and the ETS-A, respectively. Table 5.2 also includes the initial offset and scale factor state of the NLLS, which is calculated through the initial state algorithm of Section 5.4.3.[2]

Table 5.2: Calibration parameters obtained using the uncalibrated dataset seen in Fig. 5.2(b).

Param.	True Value	NLLS[1] $\mathbf{p_0}$	NLLS[2]	ETS-A[3]	Unit
a	0.85	0.85174	0.85036	0.85050	unitless
b	1.20	1.19994	1.19937	1.19867	unitless
c	1.10	1.09923	1.09996	1.10005	unitless
x_0	145	145.1571	145.2061	145.2060	mG
y_0	85	85.1114	85.1075	85.1075	mG
z_0	-180	-179.9694	-180.0420	-180.0420	mG
ρ	2.50	-	2.4420	2.4434	degrees
ϕ	-3.20	-	-3.1539	-3.1537	degrees
λ	1.80	-	1.8127	1.8136	degrees

[1] NLLS p_0 refers to the initial algorithm estimation of Section 5.4.3.
[2] NLLS stands for the last iteration of the proposed NLLS solution.
[3] ETS-A for the analytical two-step solution of [36].

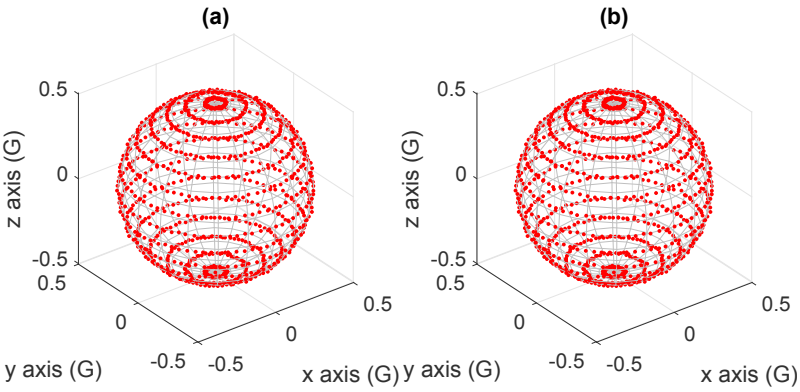

Figure 5.3: Three dimensions plot of the calibrated vector components of the Simulated Data of Section 5.5.1. (a) NLLS Calibrated Data. (b) ETS-A Calibrated Data.

The analysis of both representations in Fig. 5.3 shows that the NLLS and ETS-A data have similar results for the vector components plot over the sphere, and the calibrated data distribution is, visually, close to the theoretical data of Fig. 5.2(a). Table 5.2 also shows that both algorithms have similar estimations. The estimation differences between the NLLS and the ETS-A are in the 10^{-4} order for scale factors (unitless), 1 μG order for the offset, and in the order of 10^{-3} degrees for the misalignment angles. Therefore, it shows that both algorithms have similar estimations. However, comparing the estimated parameters to the true ones for a single run would not provide an accurate analysis.

Although these results are indicators of the calibration effectiveness of the algorithms, it is unreasonable to distinguish their performance using a single set of data, as observed in [36] and [83]. Therefore, the error comparison of both algorithms is left for the Monte Carlo simulation in the following analysis, in Section 5.5.2. At last, we note that the initial guess algorithm, indicated by the NLLS p_0 column in Table 5.2, does have an accurate offset and scale factor estimation. Again, the Monte Carlo analysis has additional comparisons.

[2] We use the **NLLS p0** nomenclature to indicate the parameters calculated using the proposed initial guess algorithm.

At last, we can also assess the calibration and each algorithm by inspecting the uncalibrated and calibrated data. Figure 5.4 shows the magnitude of each simulated measurement for the uncalibrated data (a) and the NLLS and ETS-A calibrated data (b). It is notorious that the resulting magnitude of the uncalibrated measures (Fig. 5.2(a)) is far off from the expected value of 500 mG. However, that is corrected by the calibration procedure. The calibrated results of the NLLS and ETS-A magnitude are almost identical; hence, Table 5.3 shows the magnitude data analysis and the error analysis. The error is obtained by subtracting the expected magnitude of 500 mG from the magnitude measurements.

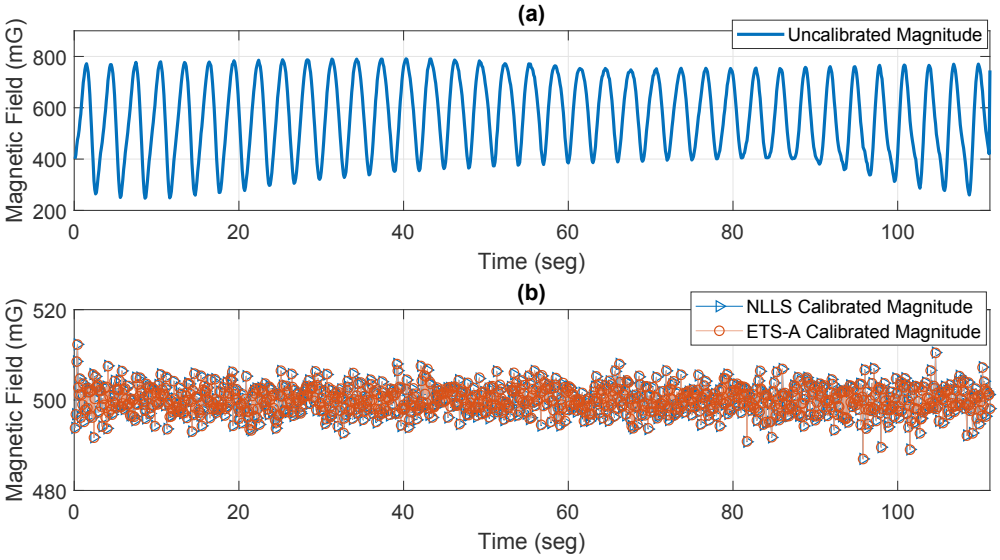

Figure 5.4: Magnitude of the uncalibrated data (a) and calibrated data for both algorithms (b).

Table 5.3: Numerical analysis of the magnitude data and its error for the results seen in Fig. 5.4.

Data	Magnitude Analysis (mG)		Error Analysis (mG)	
	Mean	SD (σ)	RMSE	Worst measure absolute error
Uncalibrated	567.90	151.87	166.31	290.90
NLLS	499.96	2.95	2.95	13.03
ETS-A	499.99	2.96	2.96	13.06

Table 5.3 analysis verifies how similar the algorithms performed. The ETS-A and the NLLS have a mean calibrated magnitude very close to the expected value, but the latter has a negligibly lower RMSE. We also note that since the mean calibrated value is close to the true magnitude and the number of measurements is large, the standard deviation of the magnitude and the RMSE error are almost identical.

These results demonstrate that the NLLS algorithm has estimated values very close to the ones of the ETS-A method. Still, a Monte Carlo simulation is essential and allows us to assess the algorithm's performance more accurately.

5.5.2 Monte Carlo Simulation Analysis

The Monte Carlo analysis seeks to identify the estimation error distribution and to check the algorithm convergence. We perform a simulation with 5000 runs, and each one randomly generates the calibration parameters and the expected magnitude (constant during each run). The parameters and the expected

magnetic field magnitude have a uniform distribution, and the range associated with each one is shown in Table 5.4. Every run has the same 1112 theoretical points and the vector components used in the previous simulation. All sensor measurements have a normal distribution with a standard deviation of 1.5 mG, similar to the RMS noise obtained from an HMC5883L magnetometer, as seen in Appendix A.1.

Table 5.4: Uniform distribution range of the calibration parameters used in the Monte Carlo simulation.

Parameter	Range	Unit
Expected Magnitude (B_e)	$300 - 500$	mG
Scale Factor - a, b, c	$0.75 - 1.25$	unitless
Bias - x_0, y_0, z_0	± 500	mG
Angles - ρ, ϕ, λ	± 3	degrees

For each run, we evaluate the estimated parameters of the initial guess, the NLLS, and the ETS-A algorithms. The data is used to plot the probability distribution of the error of the parameters to each algorithm. Figure 5.5 illustrates this result. For the NLLS algorithm, we also calculate the 1σ uncertainties using (5.16) and the 3σ value for every run. Table 5.5 shows the average value of the uncertainties for each parameter calculated using all runs data. Figure 5.5 also includes the average uncertainties boundary limits computed using the 3σ value of all Monte Carlo runs. For further comparisons between the uncertainties calculated by the NLLS displayed in Table 5.5 and the error distribution, Table 5.6 depicts the standard deviation of the normal distribution fit for the probability distribution data of the error seen in Fig. 5.5. It also includes the average values of the errors.

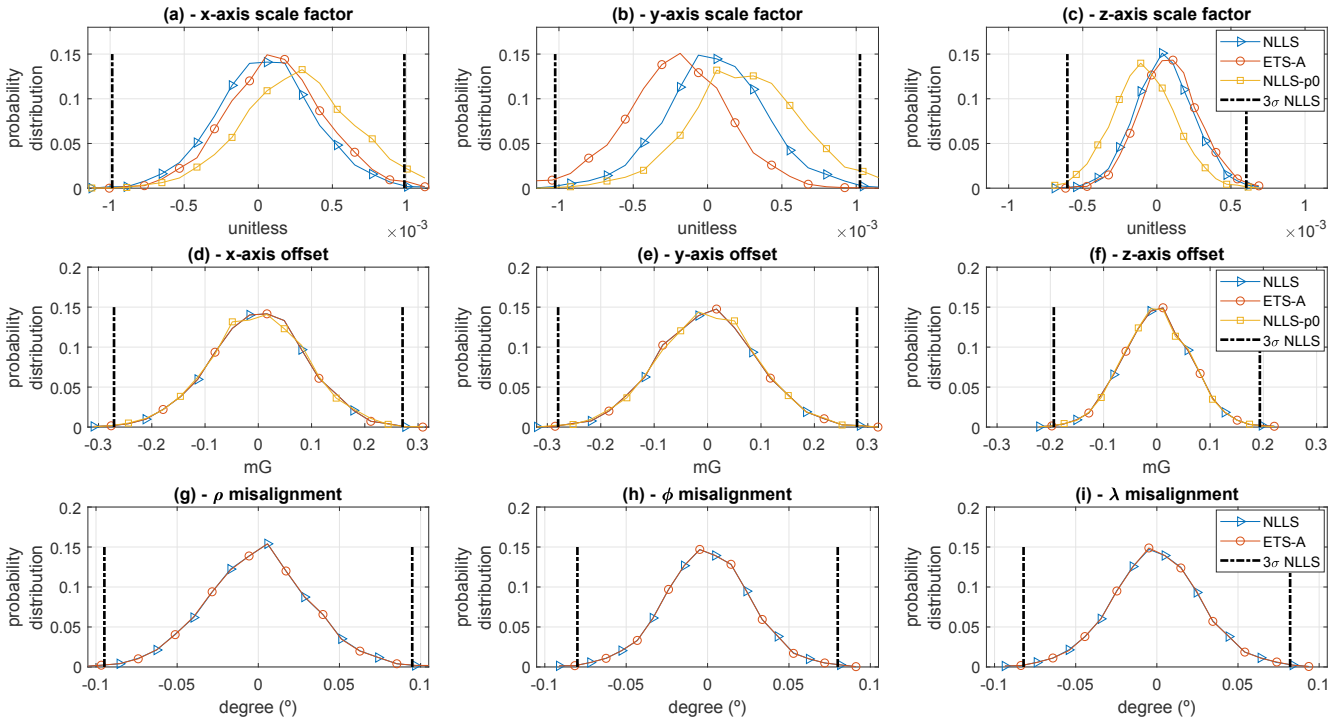

Figure 5.5: Probability distribution of the estimation error from the Monte Carlo simulation for the proposed algorithm (NLLS), the initial guess algorithm (NLLS-p0), the ETS-A of [36], and the 3σ uncertainties bounds of the NLLS. (a) x-axis scale factor. (b) y-axis scale factor. (c) z-axis scale factor. (d) x_0 offset. (e) y_0 offset. (f) z_0 offset. (g) ρ misalignment. (h) ϕ misalignment. (i) λ misalignment.

Table 5.5: Average 1σ and 3σ uncertainties of the NLLS algorithm calculated using the 5000 runs data.

Param.	5000 Runs Avg. Uncertanties		Unit
	1σ	3σ	
a	3.28E-4	9.85E-4	unitless
b	3.42E-4	10.26E-4	unitless
c	2.01E-4	6.04E-4	unitless
x_0	0.0903	0.2709	mG
y_0	0.0933	0.2798	mG
z_0	0.0645	0.1935	mG
ρ	0.0316	0.0948	degrees
ϕ	0.0267	0.0800	degrees
λ	0.0274	0.0821	degrees

Table 5.6: Normal distribution fit of the error data results seen in Fig. 5.5 for each parameter.

Calib. Param.	Normal Distribution Fit - Mean (μ) and STD (σ)						Unit
	NLLS		ETS-A		NLLS-p0		
	(μ)	(σ)	(μ)	(σ)	(μ)	(σ)	
a	0.5E-4	3.32E-4	1.2E-4	3.35E-4	2.8E-4	3.82E-4	unitless
b	0.5E-4	3.43E-4	-2.2E-4	3.55E-4	2.6E-4	3.88E-4	unitless
c	0.5E-4	2.01E-4	0.8E-4	2.02E-4	-0.8E-4	2.17E-4	unitless
$x0$	2.2E-4	0.0896	2.3E-4	0.0896	-3.0E-4	0.0906	mG
$y0$	-4.5E-4	0.0923	-4.5E-4	0.0923	-8.0E-6	0.0928	mG
$z0$	-2.6E-4	0.0637	-2.6E-4	0.0637	-8.0E-5	0.0634	mG
ρ	-8.9E-5	0.0326	-8.9E-5	0.0326	-	-	degrees
ϕ	-1.5E-4	0.0269	-1.6E-4	0.0269	-	-	degrees
λ	-3.0E-4	0.0281	-3.0E-4	0.0281	-	-	degrees

Before comparing the parameters among the methods, it is evident by comparing the 1σ uncertainties, seen in Table 5.5, and the σ calculated for the error distribution of Fig. 5.5, shown in Table 5.6, that they are very close. Thus, it shows that the estimation of the uncertainties and the assumption of using the residual error variance is correct to extract the lower bounds of the estimated parameters. Note that the z-axis offset and its scale factor have lower uncertainties than the other axes, which is related to the data distribution over the *attitude sphere* of Fig. 5.2(a). Section 5.5.3 analysis corroborates this hypothesis.

We begin the analysis of the parameters with the offsets data. Notably, the data shown in Figs. 5.5(d), (e), and (f) demonstrate that the NLLS and ETS-A solutions have visually identical error distributions. Furthermore, the initial guess algorithm (NLLS-p0) performs similarly to the other two. These observations are supported by the fit data presented in Table 5.6, which shows that the ETS-A and NLLS solutions have nearly identical numerical results for the error distribution's mean and standard deviation of the offsets. In contrast, the initial guess algorithm has slightly different values, with differences in the calculated standard deviation σ around an order of 10^{-3}, or 0.001 mG.

We also observe a similar behavior between the misalignment angles error distribution computed for both algorithms. Figs. 5.5(g), (h), and (i), along with their normal distribution shown in Table 5.6, reveal that both solutions performed almost identically in estimating these parameters. The differences in the normal fit's sigma (σ) values were on the order of 10^{-5} between the algorithms for all axes, which is too small to be noticed with the table's precision of four decimal places.

On the contrary, we observed a different behavior for the scale factor parameters. In comparison, the NLLS

estimate was the only one whose error distribution has an approximate zero mean. In contrast, the ETS-A had a slightly worse distribution, as shown in the μ and σ values from the graphical and fit distribution data. This finding is similar to what was reported in [36], where the scale factor estimation had the same behavior, and especially for the y-axis scale factor estimates, the error distribution was not centered around zero compared to other algorithms like [78, 80, 81]. Despite having a worse distribution, the initial guess algorithm performed well. Its error distribution had the same order of magnitude, indicating that the procedure provides a correct initial estimation of the scale factor for the NLLS solution.

For a complementary analysis of the proposed NLLS algorithm estimation error and the computed uncertainties, Fig. 5.6 depicts each parameter error for every Monte Carlo run and the $\pm 3\sigma$ boundaries of the uncertainties using the values in Table 5.5.

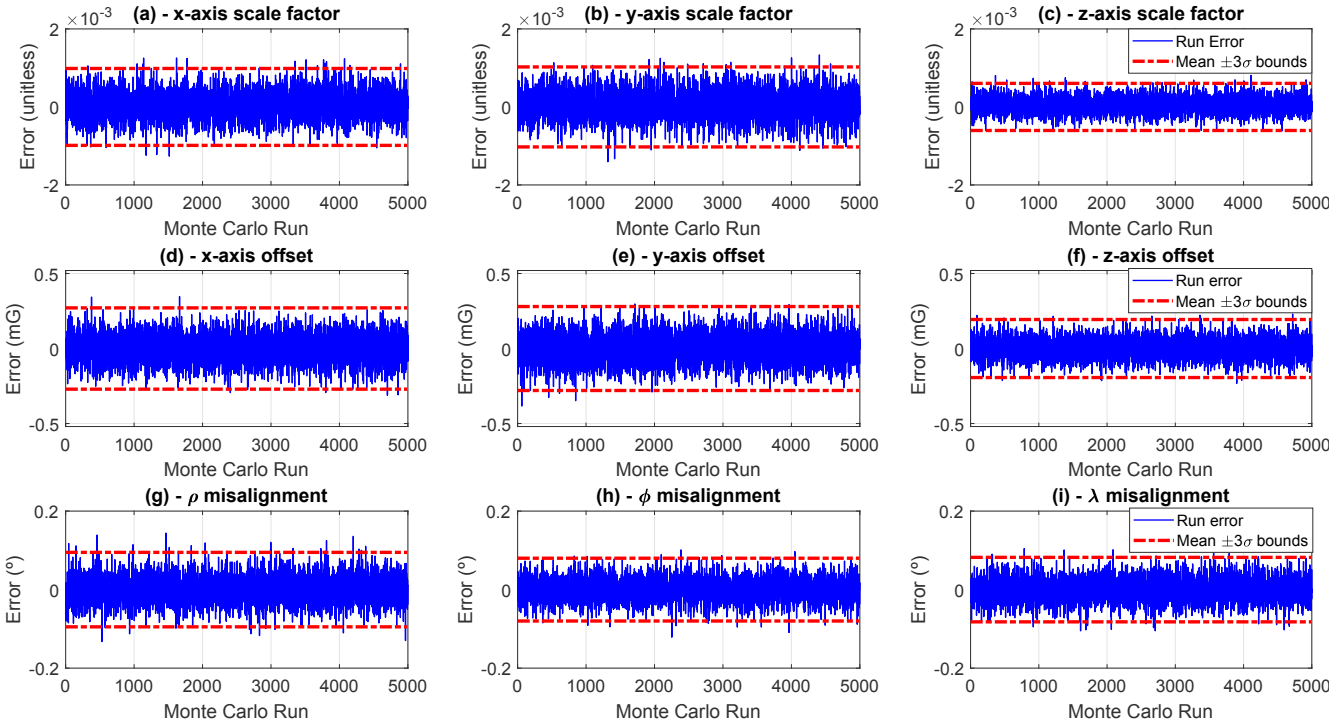

Figure 5.6: Estimated parameters errors of each Monte Carlo run and the average $\pm 3\sigma$ bounds of the uncertainties obtained via the Fisher information Matrix.

Figure 5.6 results corroborate the analysis above. The z-axis offset and scale factor of the NLLS algorithm has a slightly better outcome than the other axes. More importantly, it shows that the errors of the majority of the Monte Carlo trials are inside the 3σ boundary of the average value of the uncertainties. Such a result is compatible with the theoretical concept of the uncertainties, where we expect that 99.7% of the data error should be contained within the three standard deviation boundary.

Another metric to evaluate the Monte Carlo simulation results is using the RMSE of the magnetic field magnitude calibrated data of the algorithms for each run. Figure 5.7 shows that both methods produced similar calibrated RMSEs per run. The numerical analysis of the data in Table 5.7 reveals that NLLS estimates have a smaller RMSE, but the difference between them is minimal. The average difference in RMSE between the two algorithms is 0.0003 mG, which is smaller than the effective resolution of typical low-cost magnetometers. Hence, we can infer that the calibrated magnitude data from both algorithms are almost identical.

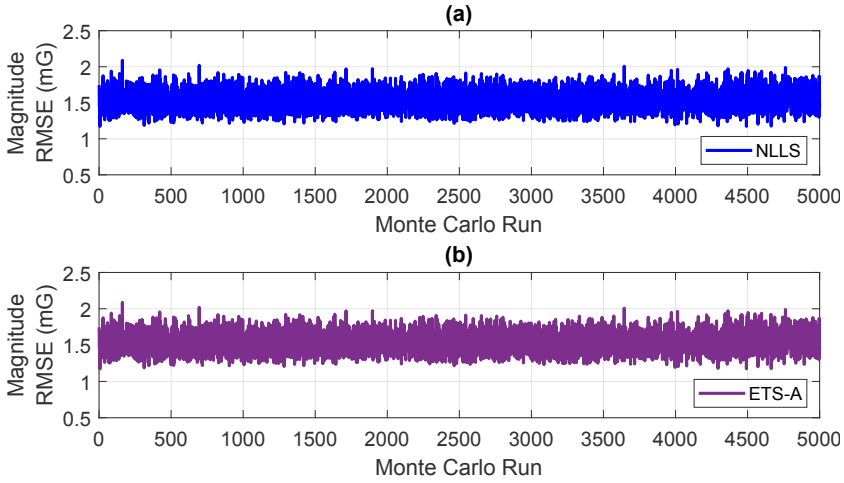

Figure 5.7: Magnitude RMSE for each run of the Monte Carlo simulation.

Table 5.7: Magnitude RMSE numerical analysis for the results in Fig. 5.7.

Calibration Method	Average RMSE (mG)	Worst Run RMSE (mG)
NLLS	1.5393	2.0880
ETS-A	1.5396	2.0886

To conclude the analysis, Table 5.8 compares the time required to execute each algorithm and the number of iterations of the NLLS. These results were collected by the simulation script running in MATLAB in a Windows 10 using an Intel I5-10400F processor with 32 GB of RAM. The NLLS and ETS-A timing includes the steps that calculate the calibrated measurements. The combined execution time of the initial guess algorithm and the NLLS solution compared to the ETS-A algorithm shows that our solution performs approximately 25% faster in the average.

Table 5.8: Mean time and number of iterations took by each algorithm to complete the procedure.

Algorithm	Mean Time (ms)	Mean No. of Iterations
NLLS p0	5.1×10^{-4}	1
NLLS[1]	9.8×10^{-4}	3.050
ETS-A	2.1×10^{-3}	1

[1] The NLLS time does not include the time needed by NLLS-p0.

Table 5.8 shows that out of 5000 runs, the NLLS algorithm reached the stop criterion within three iterations in 4752 runs, while the remaining 248 runs required four iterations. On average, the NLLS algorithm required 3.050 iterations to converge. The stopping criterion was set to a threshold of 0.1% for all simulations ($\varepsilon = 0.1\%$). We chose this threshold based on our analysis that showed values above 0.2% could result in worse error distributions than those observed in Fig. 5.5. Conversely, a tighter criterion than 0.05% would not improve the results, and differences in the estimated values were at least two orders of magnitude smaller than the actual uncertainties.

Now that our analysis is concluded, we can further extrapolate our algorithm's results compared to other well-known solutions in the literature using the observations of [36]. Overall, the authors observed that the ETS-A performed satisfactorily compared to most algorithms at a lower (better) computational cost. Its bias error distribution performed similarly compared to other well-known and typical algorithms [77,78,80,81]. The

scale factor error distribution was not around a mean zero value compared to the solutions of [78, 80, 81] but had a similar standard deviation value. Therefore, we could expect our algorithm to perform almost identically as these others since, in our evaluation, the NLLS outperformed the ETS-A by a small margin. About the misalignment angles, the ETS-A was only outperformed by Wu and Shi's algorithm [81]; consequently, we would expect the same result of our NLLS solution as it performed almost identically to the ETS-A.

The findings in [36] on the computational effort required by the different algorithms were similar to those of [83] and [84]. Our results show that the proposed NLLS algorithm matches the computational performance of the ETS-A while having an estimation error evaluated in our Monte Carlo simulation that is almost identical to that algorithm. Still, it outperformed the ETS-A in terms of scale factor estimation. In general, we could conclude that only Wu and Shi's solution [81] would provide better misalignment angle estimations, but at a much higher computing time.

Finally, we must note that the performance of magnetometer calibration algorithms depends significantly on the spatial distribution of the data [1, 98], as evidenced by the additional uncertainties analysis presented in the following subsection. Hence, a detailed comparison of different algorithms, including ours, with input data of limited spatial range may be the subject of future research.

5.5.3 Complementary Analysis of the Parameter Estimation Errors and Uncertainties

This section seeks to complement the analysis of the calibration parameters uncertainties using magnetic fields with a distinct spatial distribution compared to the one previously reported in Section 5.5.2. The simulation methodology is identical to the Monte Carlo simulation above; there are 5000 trials, and the parameters are randomized every run and have the same uniform distribution reported in Table 5.4.

Figure 5.8 shows the vector components plot over the sphere for the first two additional simulations. They have a spatial distribution equivalent to that used in the previous simulation, but the data distribution around each axis is distinct for all three cases. Consequently, we can use these distributions to evaluate and confirm the hypothesis that the differences in the uncertainties observed in the previous Monte Carlo simulation were due to the spatial distribution of the data and not related to the NLLS algorithm. In addition, it allows further comparison between the ETA-S and the NLLS solutions.

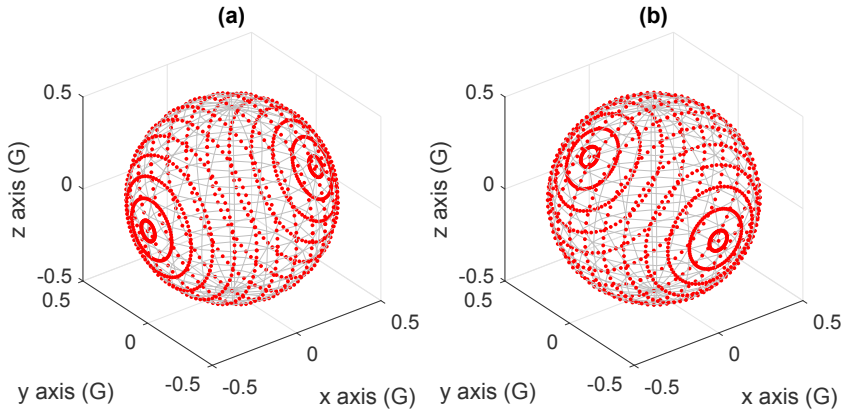

Figure 5.8: Theoretical three dimensions vector components plot of the first (a) and second (b) additional datasets used to evaluate the NLLS algorithm uncertainties.

The calibration parameters for both Monte Carlo simulations are estimated using the NLLS and the ETS-A algorithms for every run. Using this data, we calculate each parameter's error, generate the error distribution, and extract the 1σ and 3σ uncertainties using the Fisher information matrix from the NLLS solution, as done before. Figures 5.9 and 5.10 display the error distribution and the 3σ uncertainties boundary of the NLLS, respectively, for the spatial distribution of Figs. 5.8 (a) and 5.8(b).

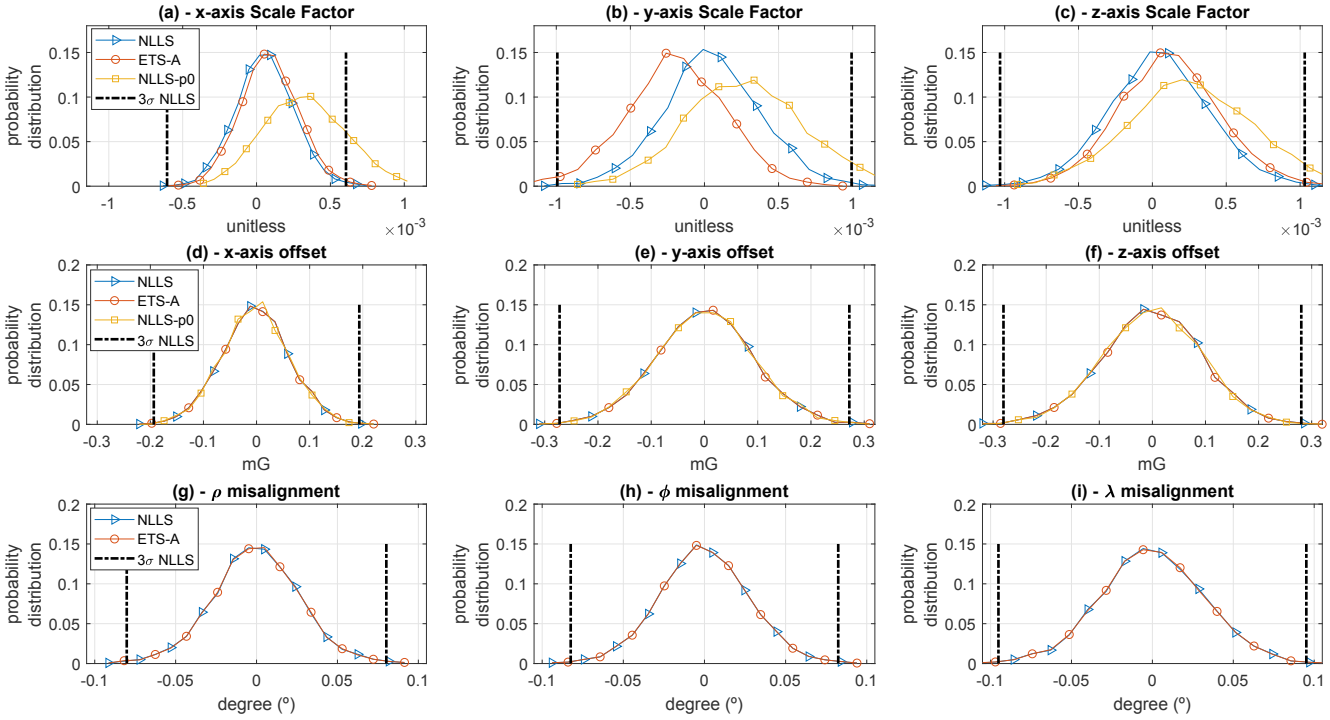

Figure 5.9: Probability distribution of the estimation error for every parameter for the Monte Carlo simulation using the data distribution of Fig. 5.8(a).

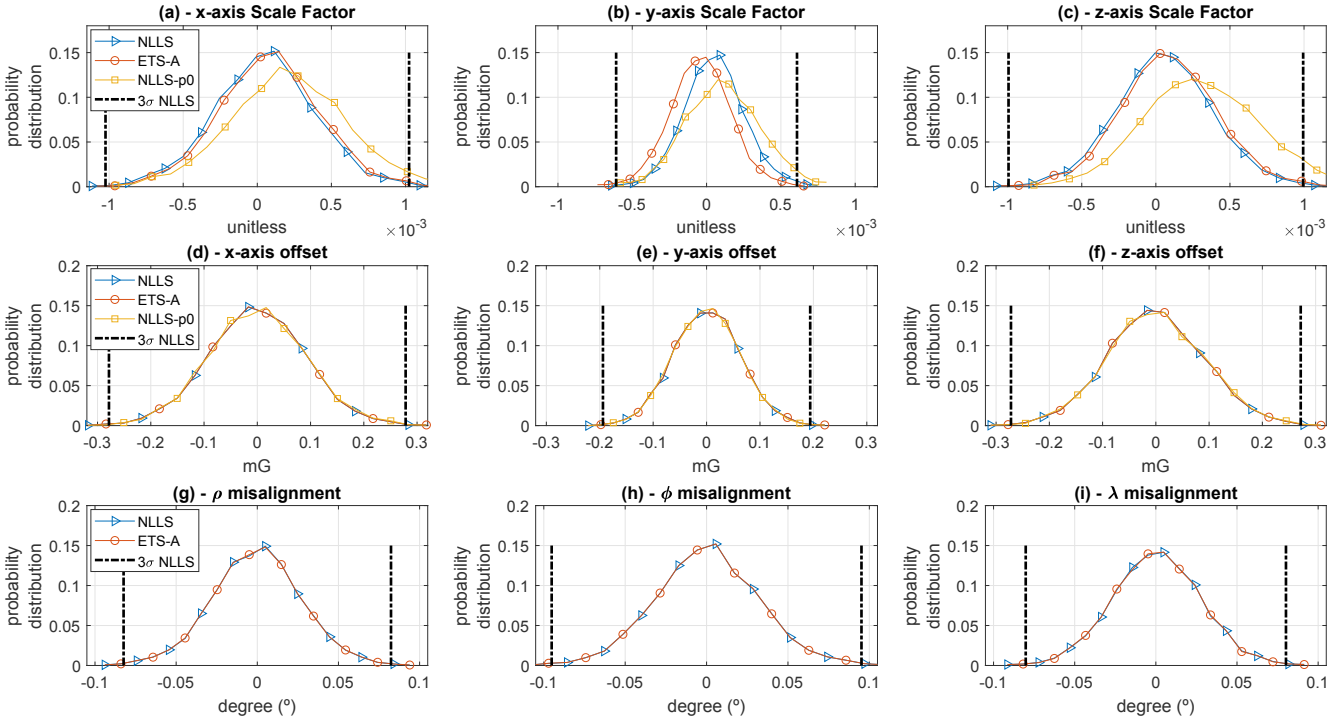

Figure 5.10: Probability distribution of the estimation error for every parameter for the Monte Carlo simulation using the data distribution of Fig. 5.8(b).

The analysis of Figs. 5.9 and 5.10 corroborates the findings and conclusions from the previous Monte Carlo simulation. The offset and misalignment estimations are almost identical regardless of the estimator. On the contrary, the scale factors errors' distributions have a more considerable difference, especially in the y-axis offset. For illustration, the distributions in Figs. 5.9(b) and 5.10(b) confirm that.

Nevertheless, these results establish that the previous error distribution, and consequently, the standard deviation of the normal fit, were related to the spatial distribution of the data and not the estimators. For instance, the offsets and scale factors uncertainties were inferior for the z-axis in the previous Monte Carlo simulation. In contrast, they are smaller than the other axes in the x-axis and y-axis, respectively, for the data distribution (a) and (b) seen in Fig. 5.8. To further prove that, Table 5.9 reports the average 1σ uncertainties extracted from the Fisher information matrix for all 5000 runs for each data distribution. It also includes the previous simulation results to facilitate the comparison.

Table 5.9: Average 1σ bound uncertainties of the NLLS algorithm calculated using the data of all 5000 runs for the vector components distributions of Figs. 5.8(a), 5.8(b), and 5.3(a).

Param.	5000 Runs Avg 1σ Uncertainties			Unit
	Input Data			
	Fig. 5.3(a)	Fig. 5.8(a)	Fig. 5.8(b)	
a	3.28E-4	2.01E-4	3.41E-4	unitless
b	3.42E-4	3.30E-4	2.03E-4	unitless
c	2.01E-4	3.43E-4	3.31E-4	unitless
x_0	0.0903	0.0644	0.0927	mG
y_0	0.0933	0.9062	0.0646	mG
z_0	0.0645	0.9343	0.0906	mG
ρ	0.0316	0.0267	0.0274	degrees
ϕ	0.0267	0.0274	0.0317	degrees
λ	0.0274	0.0317	0.0267	degrees

First, Table 5.9 shows that the NLLS uncertainties are identical in every scenario, taking the respective data rotation among each axis. For instance, the 1σ numerical average value of ϕ, ρ, and λ are identical in the four decimal places for each input data, respectively. At last, although we omit the probability distribution of the error as we presented in the Monte Carlo section, the normal distribution error standard deviation was compatible with the estimated uncertainties. Hence, it endorses the last section's result and the methodology to calculate the uncertainties extracted from the covariance matrix $\mathbf{P}$.

For the sake of completeness, we evaluate the uncertainties of the NLLS using three additional cases whose spatial distributions of the data over the *attitude sphere* are seen in Fig. 5.11.

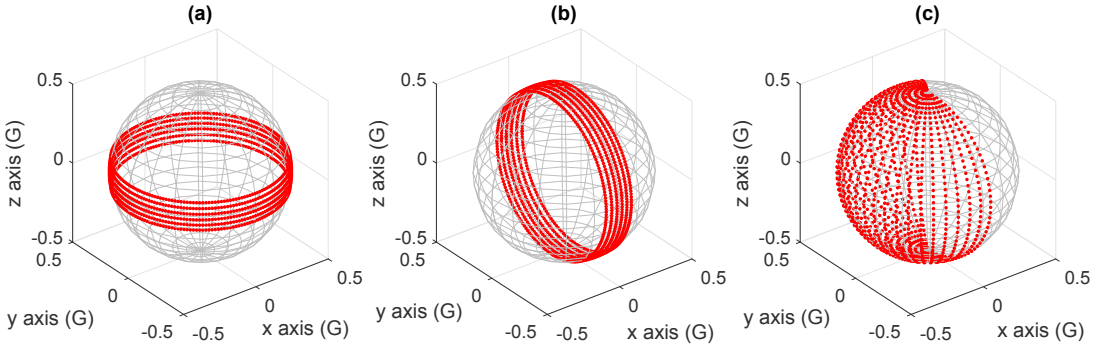

Figure 5.11: Theoretical three dimensions vector components plot of the third (a), fourth (b), and fifth (c) additional datasets used to evaluate the NLLS algorithm uncertainties.

We run a Monte Carlo simulation for each distribution and calculate the parameters' 1σ uncertainties, depicted in Table 5.10. The results for Figs. 5.11(a) and (b) demonstrate that data distribution less sparse in the *attitude sphere* increases the uncertainties. The first has a lousy distribution over the z-axis, and the second over the x-axis, and the respective columns in Table 5.10 show that the order of magnitude of the scale factor and offset errors in those axes are much worse than those of the others. Furthermore, two misalignment angle uncertainties are worse in those cases. At last, Fig. 5.11(c) shows another case that shows the reader the impact of the distribution, which is also somewhat lousy on the x-axis, supported by the numerical analysis.

Table 5.10: Average 1σ bound uncertainties of the NLLS algorithm calculated using the data of all 5000 runs the vector components distributions of Fig. 5.11.

Param.	**5000 Runs Avg 1σ Uncertainties**			**Unit**
	Vector Components Distribution (Waveform)			
	Fig. 5.11(a)	Fig. 5.11(b)	Fig. 5.11(c)	
a	2.47E-4	9.51E-3	9.88E-4	unitless
b	2.48E-4	2.47E-4	2.98E-4	unitless
c	9.49E-3	2.48E-4	2.14E-4	unitless
x_0	0.0656	0.3860	0.3034	mG
y_0	0.0656	0.0661	0.1124	mG
z_0	0.3856	0.0662	0.0811	mG
ρ	0.0196	0.0822	0.0423	degrees
ϕ	0.0821	0.0826	0.0361	degrees
λ	0.0825	0.0197	0.0241	degrees

Therefore, these results validate the methodology to estimate the uncertainties discussed in Section 5.3. More importantly, it depicts that the uncertainty data can be used to assess the calibration quality. For example, suppose the NLLS algorithm results in a poor estimation due to the data scattering over the *attitude sphere* or an inadequate initial guess. In that case, it will be identified by the computed uncertainties using the Fisher information matrix.

5.5.4 Calibration Simulation for a Magnetic Field with Non-Constant Magnitude

The calibration procedure to a magnetic field with a non-constant magnitude is demonstrated using Fig. 5.12(a) waveform, which has a magnitude that varies from 300 to 500 mG during the simulation. Figure 5.12(b) exhibits the normalized (dimensionless) vector components plot.

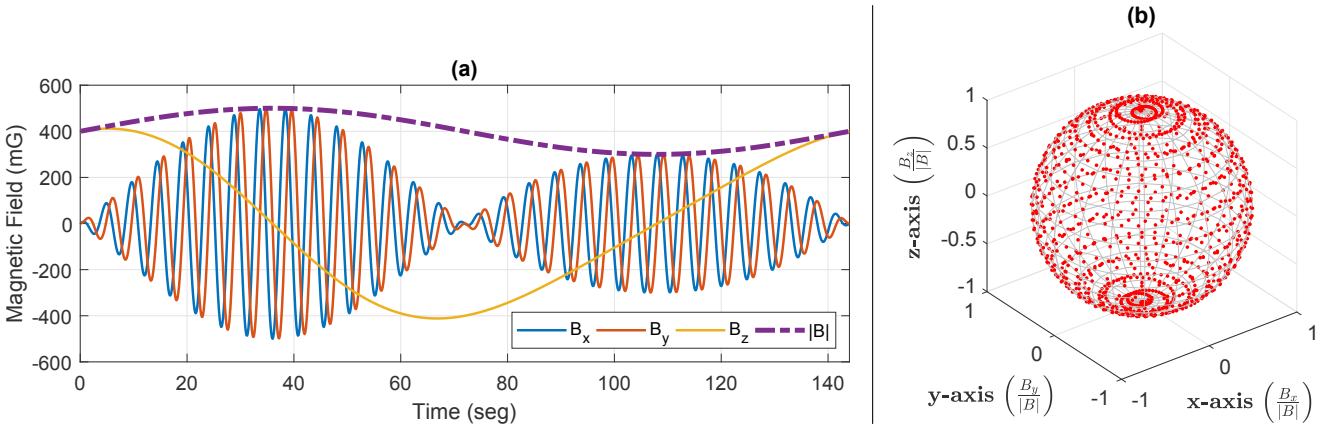

Figure 5.12: Simulated magnetic field used to evaluate the non-constant magnitude calibration.

Such a waveform simulates an effect similar to that expected in the on-orbit magnetometer calibration problem, where the field's strength magnitude varies accordingly to the spacecraft position. Simulating the measurements of Fig. 5.12(a) simplifies the calibration demonstration and avoids a complete nanosatellite orbit, for example. The simulation generates 8 magnetometer measurements per second; thus, 1152 points are simulated and generate the spatial distribution seen in Fig. 5.12(b). The corrupted measurements are generated using the parameters seen in the true value column of Table 5.11. The parameter estimation results using the NLLS solution are also presented in Table 5.11.

Table 5.11: Calibration parameters data for the non-constant magnitude simulation.

Par.	True Value	NLLS $\mathbf{p_0}$	NLLS	NLLS Error	NLLS 3σ	Unit
a	0.90	0.9005	0.9005	0.0005	0.0010	unitless
b	1.15	1.1508	1.1501	0.0001	0.0013	unitless
c	0.95	0.9496	0.9497	-0.0003	0.0007	unitless
x_0	-100.0	-100.011	-99.982	0.018	0.318	mG
y_0	-65.0	-64.860	-64.960	0.140	0.406	mG
z_0	85.0	84.833	85.065	0.065	0.241	mG
ρ	1.20	-	1.182	-0.018	0.104	degrees
ϕ	-0.50	-	-0.468	0.032	0.096	degrees
λ	2.20	-	2.110	-0.090	0.095	degrees

The results seen in Table 5.11 are similar to those already reported in the constant magnitude analysis. The initial guess algorithm and the NLLS have estimated the parameters correctly, and every parameter's error is within the $\pm 3\sigma$ uncertainties boundary extracted from the Fisher information matrix. In the following section, a Monte Carlo simulation complements the error analysis.

At last, Fig. 5.13(a) shows the uncalibrated and calibrated magnitude and Fig. 5.13(b) the calibrated magnitude error, obtained by subtracting the calibrated magnitude measurements minus the theoretical magnitude of Fig. 5.12(a). The resulting RMSE of the magnitude error of Fig. 5.13(b) is 2.02 mG, verifying the effectiveness of the calibration and evidencing that the NLLS is adequate for calibration with non-constant magnitude.

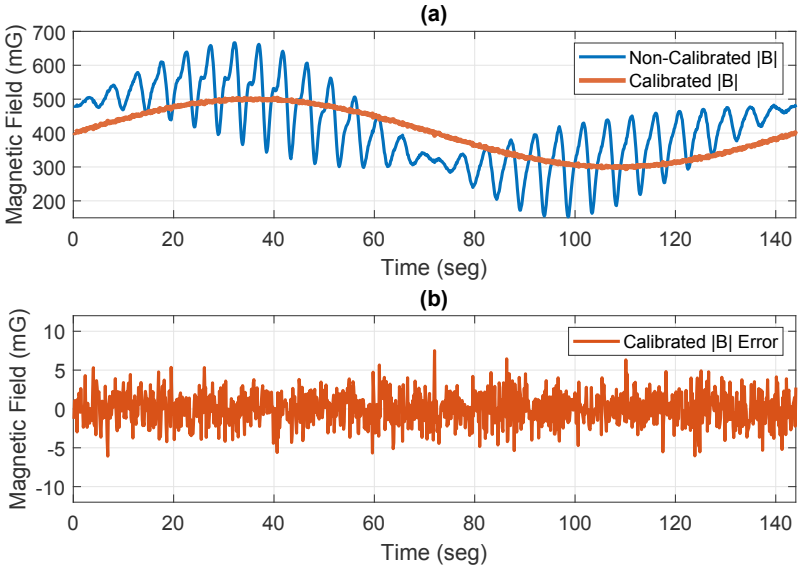

Figure 5.13: Magnitude plots of the non-constant field simulation. (a) Uncalibrated and calibrated magnitude. (b) Calibrated magnitude error.

5.5.5 Monte Carlo Simulation for a Non-Constant Magnetic Field Magnitude

The Monte Carlo simulation uses the magnetic field of Fig. 5.12 and the methodology of Section 5.5.2. Therefore, the simulation randomly generates each bias, scale factor, and misalignment angle for each Monte Carlo trial. As a result, the parameters have a uniform distribution ranging from ± 300 milligauss, $0.75 - 1.25$ dimensionless, and ± 3 degrees, similarly to Table 5.4 values of the constant magnitude Monte Carlo test.

Figure 5.14 and Table 5.12 summarize the simulation results. The former shows each parameter error for every run and the average $\pm 3\sigma$ boundaries calculated using the values extracted from the Fisher information matrix for all trials. The latter displays the average numeric values of the 1σ and the 3σ uncertainties.

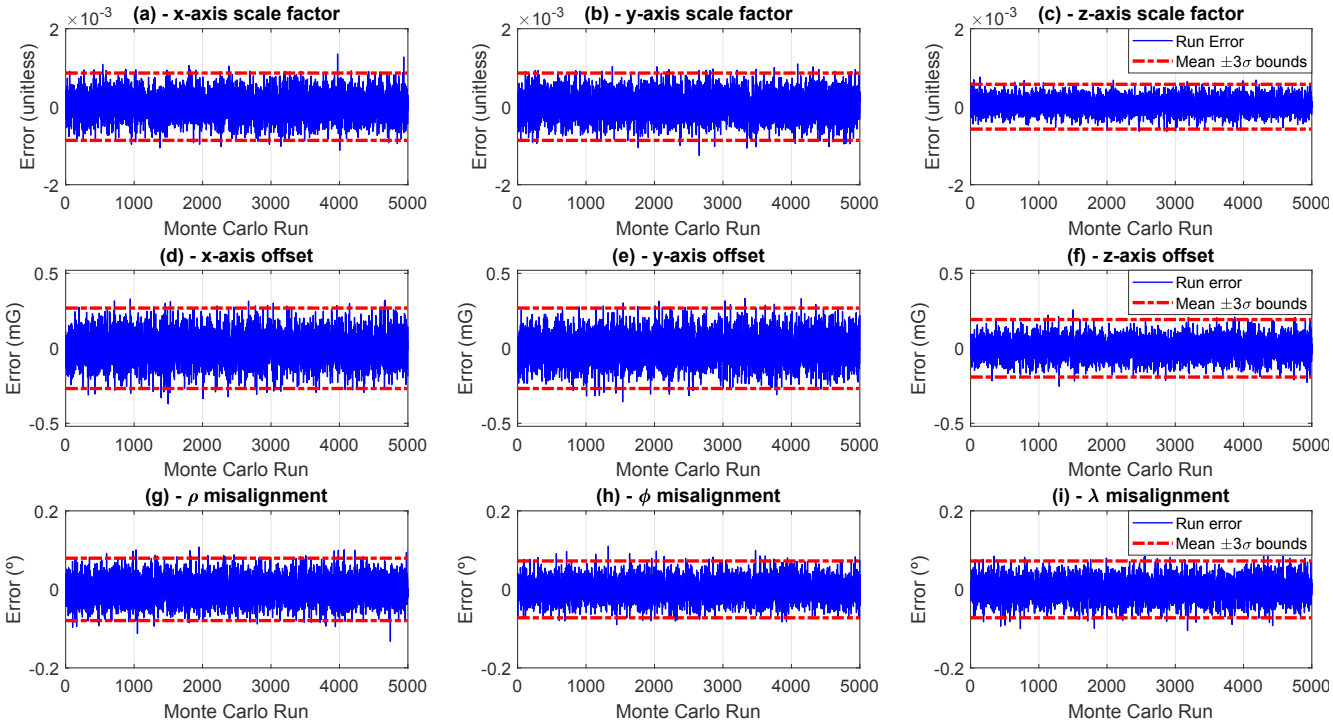

Figure 5.14: Estimated parameters errors of each Monte Carlo run and the average $\pm 3\sigma$ bounds of the uncertainties obtained via the Fisher information Matrix for the non-constant magnitude simulation.

Table 5.12: Average 1σ and 3σ uncertainties from the 5000 runs of the NLLS Monte Carlo simulation with non-constant magnitude values.

Param.	5000 Runs Avg. Uncertanties		Unit
	1σ	3σ	
a	2.88E-4	8.63E-4	unitless
b	2.87E-4	8.63E-4	unitless
c	1.91E-4	5.74E-4	unitless
x_0	0.0894	0.2681	mG
y_0	0.0893	0.2680	mG
z_0	0.0639	0.1917	mG
ρ	0.0265	0.0795	degrees
ϕ	0.0241	0.0724	degrees
λ	0.0242	0.0726	degrees

Firstly, we must observe the similarity between these results and those reported in Section 5.5.2, more specifically, the ones seen in Fig. 5.6 and Table 5.5. These similarities in the results are expected since the spatial distribution (the data scattering) of the vector components and the number of measurements are

similar, although not identical. Consequently, the uncertainties values are in the same order of magnitude and alike, independent of the non-constant magnitude values of the magnetic field.

Furthermore, as both tests have a similar spatial distribution of the vector components, we observe the same behavior in the z-axis scale factor and bias, whose estimations have better uncertainties. Aside from that, this test has no essential observations compared to the conclusions outlined in Section 5.5.2. Finally, we can point out that this Monte Carlo simulation endorses the NLLS algorithm's effectiveness in a non-constant magnitude situation and that the estimation was barely affected by this circumstance compared to the constant case reported previously.

5.6 Experimental Validation of the NLLS Algorithm using the Magnetic Field Simulator

The experimental calibration tests use the magnetic field simulator operating in the closed-loop topology described in reference [25], whose results were validated in Section 4.7. Using the simulator allows us to evaluate the proposed algorithm estimation utilizing real magnetometer data and demonstrate the use of the simulator in the calibration process.

As discussed in the Chapters 2 and 4, the closed-loop topology is a more straightforward and logical solution to assess the algorithms. Furthermore, we are not interested in evaluating any time-varying interference (or bias) in the current experimental procedure; consequently, the closed-loop topology, using the fluxgate measurements as the ground truth, is suitable. Moreover, Chapter 6, which addresses the time-varying bias calibration, exhibits the magnetometer calibration using the open-loop field operation of the simulator. Consequently, that particular condition is left for that chapter.

Results are divided into two tests. The first generates a constant magnitude magnetic field and compares the ETS-A and the NLLS algorithms. The second assesses the calibration for a non-constant magnitude waveform. Complementary, a calibration procedure without the simulator and using only Earth's geomagnetic field is seen in [35]. All measurements are converted to milligauss utilizing the theoretical sensitivity of the sensor [44]; thus, we maintain the unitless scale factor in the analysis. The HMC5883L low-cost magnetometer, available at the dedicated electronic embedded system, is used in both situations. It is placed within the coil's uniformity region and is subject to the same magnetic field observed by the FGM3D fluxgate sensor.

5.6.1 Constant Magnitude Test - NLLS and ETS-A Comparison

In the first test, the HiL simulation is programmed to generate the magnetic field of Fig. 5.15(a), which has a constant magnitude of 500 mG and a spatial data distribution displayed in Fig. 5.15(b), somewhat similar to the previous theoretical simulations. The setup simulates 4 distinct magnetic field values per second for 144 seconds, resulting in 576 points. During the procedure, the HiL simulation disregards any acquisition made during the transient time of the setup, in compliance with timing analysis in Section 2.6. Therefore, for each point, using the HMC5883L sensor with an ODR of 40 Hz, there are 8 measures taken during the steady state of the generated magnetic field, resulting in 4608 valid measurements during the procedure.

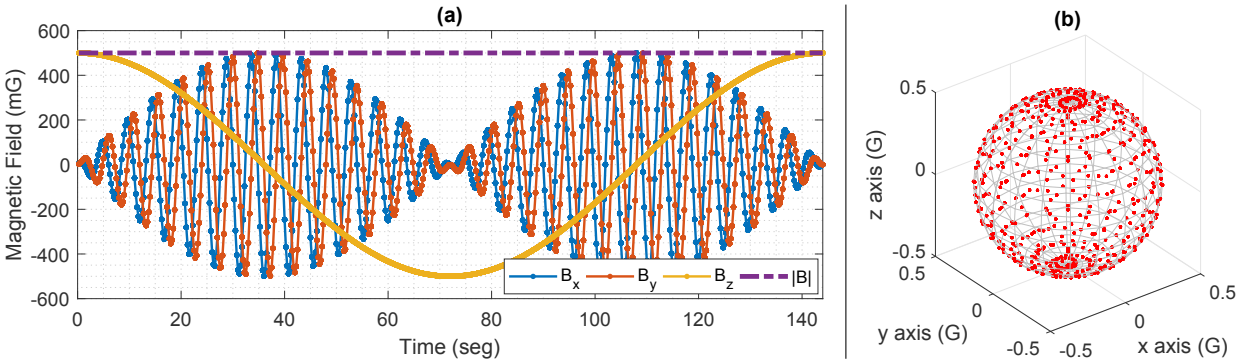

Figure 5.15: Magnetic field input for the constant magnitude experimental test. (a) Vector components versus time. (b) Vector components plot in three dimensions.

We employ the ETS-A and the NLLS algorithms to calibrate the HMC5883L raw measurements. Figure 5.16 exhibits the vector components plot of the uncalibrated (a), the NLLS (b), and the ETS-A (c) calibrated measurements. Table 5.13 shows the calibration parameters obtained for both methods. It also displays the uncertainties calculated for the NLLS solution and the proposed initial guess algorithm estimation parameters.

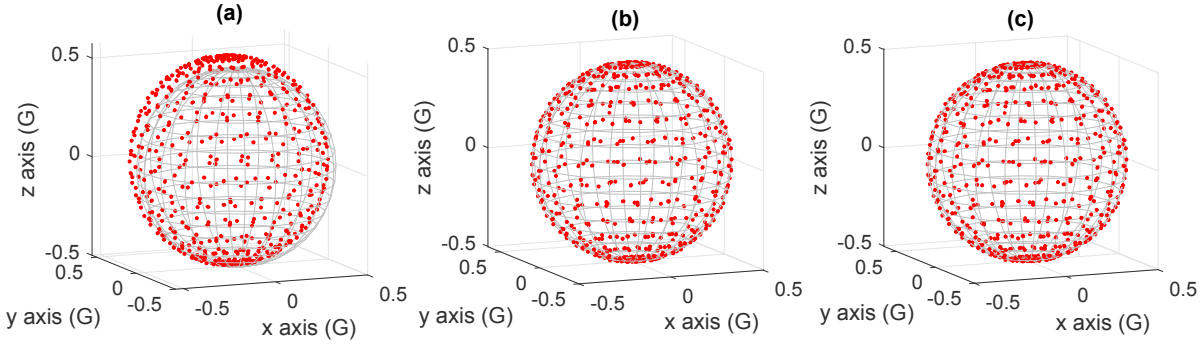

Figure 5.16: Vector components plot in three dimensions for the constant magnitude experimental test. (a) uncalibrated data. (b) NLLS calibrated data. (c) ETS-A calibrated data.

Table 5.13: Calibration parameters obtained for the experimental test of Fig. 5.15 with the constant magnetic field magnitude.

Param.	NLLS	NLLS		ETS-A	Unit
	$\mathbf{p_0}$	$\mathbf{p}$	$\mathbf{3\sigma}$	$\mathbf{p}$	
a	0.99440	0.99351	3.9E-4	0.99377	unitless
b	0.88832	0.88777	3.5E-4	0.88695	unitless
c	1.05807	1.05818	2.5E-4	1.05830	unitless
x_0	-48.1764	-48.15023	0.136	-48.15026	mG
y_0	-18.7113	-18.67956	0.121	-18.67953	mG
z_0	41.7253	41.73535	0.102	41.73539	mG
ρ	-	-2.8710	0.036	-2.8743	degrees
ϕ	-	-0.7606	0.031	-0.7603	degrees
λ	-	-0.2478	0.031	-0.2477	degrees

The same analysis of the simulated results is replicated using the experimental data. The initial guess estimation provides offset and scale factor values relatively close to the NLLS and the ETS-A estimations. Furthermore, the results between these two algorithms are numerically close. Differences are in the order of 10^{-4} (dimensionless) for scale factors, 10^{-5} milligauss for offsets, and 10^{-4} degrees for angles, and are all considerably smaller than the estimated parameters' uncertainties of the NLLS algorithm.

The extracted 3σ values for the uncertainties of the NLLS are in the same order of magnitude, however

smaller, compared to the Monte Carlo simulation. Although we have simulated a similar RMS noise to the experimental HMC5883L evaluation reported in Appendix A.1, the experimental analysis has four times more measurements than that simulation. Consequently, better uncertainties numbers are befitting with the test. Moreover, we observe that the z-axis parameters' uncertainties are the smallest, which shows that the spatial distribution of the data has the same effect observed in the simulations.

Figure 5.17 displays the test visual magnetic field magnitude results. Subfigure (a) shows that the magnitude of the uncalibrated measurements deviates considerably from the expected value, whereas the calibrated data of both algorithms are closer to the 500 mG value. Fig. 5.17(b) presents the calibrated measurements' magnitude error for both algorithms and the fluxgate sensor. In addition, the error data in Fig 5.17(b) verifies that the ETS-A and NLLS magnitudes are almost identical throughout the simulation and they vary from ± 5 mG, approximately. Finally, subfigure (c) displays a magnified portion of (b) to exhibit that although both algorithms calibrated data are close, they are not identical.

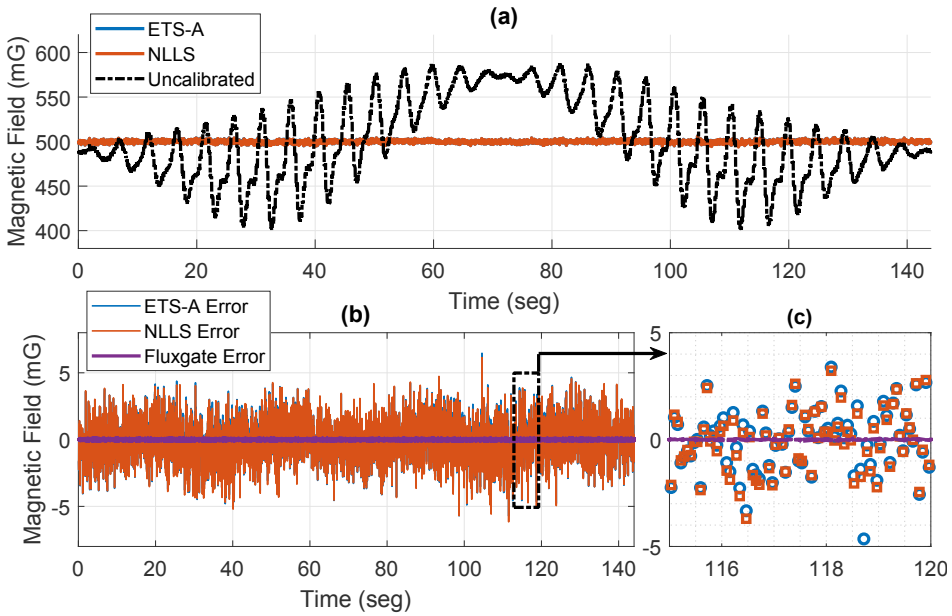

Figure 5.17: Results for the magnitude of the constant magnitude experimental test. (a) Uncalibrated and calibrated measurements. (b) ETS-A and NLLS calibrated error and the FGM3D sensor error. (c) Magnitude errors magnified for a better visualization.

At last, Table 5.14 has the magnitude error numerical data, which shows that both solutions reduced the uncalibrated RMSE of the magnitude measurements from 46.56 mG to 1.55 mG after the calibration procedure. In addition, the fluxgate measurements have an absolute maximum error of ± 150 μG, corroborating the closed-loop accuracy of the setup reported earlier. Hence, the analysis confirms the effectiveness of the practical calibration analogous to the simulated study reported before.

Table 5.14: Magnitude error analysis of the experimental test with constant magnetic field magnitude.

Data	Mean Error (mG)	RMSE (mG)	Absolute Max. (mG)
Fluxgate Data (Reference)	0.00	0.03	0.15
HMC Data - Uncalibrated	3.15	46.56	99.12
HMC Data - NLLS	-0.11	1.55	6.16
HMC Data - ETS-A	-0.05	1.55	6.46

5.6.2 Non-Constant Magnitude Calibration Test

The last test seeks to confirm the NLLS algorithm estimation using experimental data for a magnetic field with a non-constant magnitude. The methodology is the same as the previous test except that we generate the magnitude field of Fig. 5.12(a), whose magnitude values vary between 300 and 500 mG. The waveform is similar to that used in the non-constant magnitude simulation. Likewise to Section 5.6.1, the magnetic field simulator generates 576 points during the 144 seconds of the simulation, which results in the normalized data plot over the sphere seen in Fig. 5.12(b).

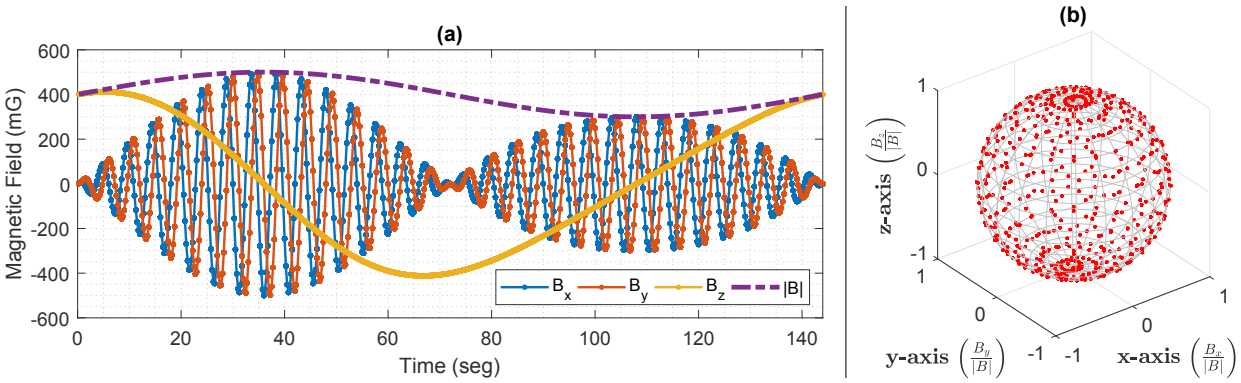

Figure 5.18: Magnetic field input for the non-constant magnitude experimental test. (a) Representation over time. (b) Normalized vector components plot in three dimensions.

Once more, the system collects 8 valid measurements for each of the 144 points simulated. The NLLS algorithm applied to the uncalibrated HMC5883L data results in the parameters and the uncertainties seen in Table 5.15, which also includes the estimation of the initial guess algorithm. The similarity of the data is notable compared to that reported above for the constant magnitude experimental test (Table 5.13). The estimation's uncertainties are in the same order of magnitude, and the conclusions are identical to those outlined in the previous test.

Table 5.15: Calibration parameters for the experimental test with non-constant magnetic field magnitude.

Param.	NLLS	NLLS		Unit
	$\mathbf{p_0}$	$\mathbf{p}$	$\mathbf{3\sigma}$	
a	0.9950	0.9942	4.3E-4	unitless
b	0.8872	0.8866	3.8E-4	unitless
c	1.0595	1.0596	3.1E-4	unitless
x_0	-48.269	-48.244	0.133	mG
y_0	-18.984	-18.970	0.119	mG
z_0	41.663	41.669	0.102	mG
ρ	-	-2.893	0.039	degrees
ϕ	-	-0.807	0.036	degrees
λ	-	-0.256	0.036	degrees

Regardless of the previous validation, Figs 5.19 and 5.20 assess the magnitude of the magnetic field measurements. The first exhibits the uncalibrated and calibrated magnitude data of the HMC5883L, and the other shows the HMC5883L calibrated data and the fluxgate measurements.

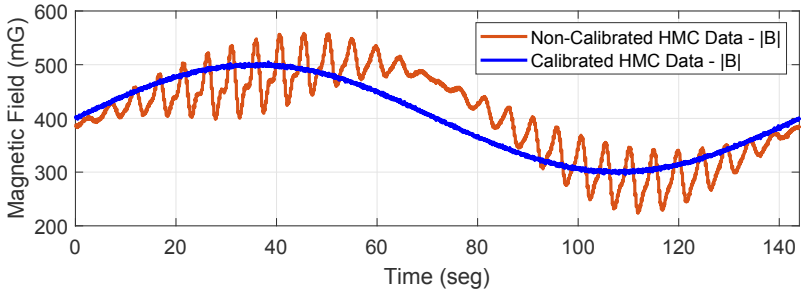

Figure 5.19: Uncalibrated and calibrated magnitude of the HMC5883L sensor for the non-constant magnitude experimental test.

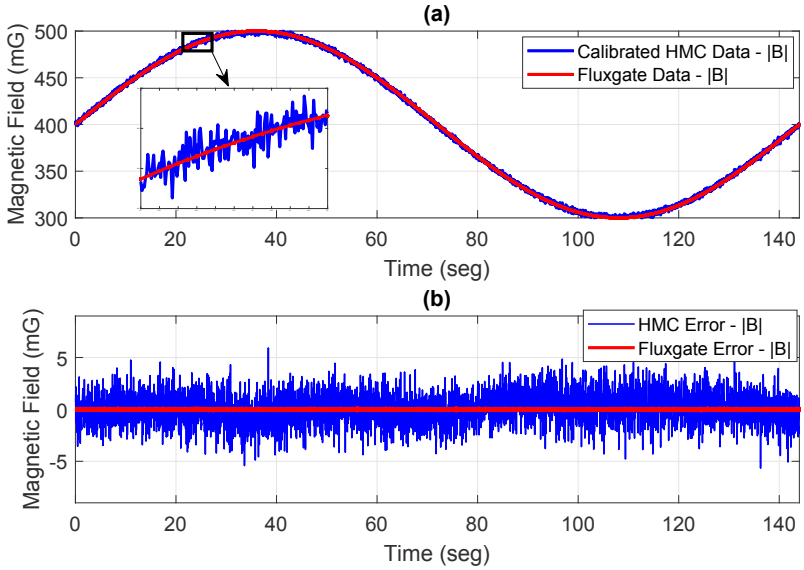

Figure 5.20: Magnitude results of the non-constant experimental test. (a) Uncalibrated and calibrated data of the HCM5883L measurements. (b) Magnitude error for the calibrated data of the HMC5883L sensor and the raw fluxgate measurements.

Figure 5.19 data shows that the uncalibrated magnitude deviates from the programmed field's magnitude of Fig. 5.18(a) and is, visually, identical to that waveform after the calibration procedure. Figure 5.20(a) shows the calibrated data and includes the fluxgate measurements, corroborating that the calibrated data is closer to the expected value. Figure 5.20(b) supports that affirmation by displaying the magnitude error of the HMC5883L calibrated measurements and the fluxgate data. Once more, all these graphical results are equivalent to those reported in the constant magnitude experimental test. Lastly, Table 5.16 features the numerical analysis of the magnitude error seen in Fig. 5.20(b).

Table 5.16: Numerical error analysis of the magnitude data of the experimental test with non-constant magnetic field magnitude.

Data	Mean Error (mG)	RMSE (mG)	Absolute Max. (mG)
Fluxgate Data (Reference)	0.00	0.039	0.17
HMC Data - Uncalibrated	4.35	44.45	98.76
HMC Data - NLLS	0.11	1.54	5.92

Table 5.16 data has similar values to those reported in the constant magnitude experimental test (Table 5.14). The fluxgate error is in the same order of magnitude, and the RMSE of the HMC5883L sensor calibrated magnitude data was almost identical (1.54 rather than 1.55 milligauss in the previous test). Hence, it confirms

that the experimental estimation does not depend on whether the magnitude is constant.

Further analysis of this data is identical to those reported in the simulation study of Section 5.5.4 and the previous experimental test with a constant magnetic field magnitude. Therefore, it reinforces previous conclusions drawn about the NLLS performance. Nevertheless, and more notably, the test outcome demonstrates the effectiveness of using the closed-loop topology to generate a magnetic field using the simulator to evaluate the magnetometer calibration.

5.7 Complementary Analysis of the NLLS Algorithm

This section brings a complementary examination of the calibration using the NLLS algorithm. First, Section 5.7.1 compares the proposed calibration method convergence with and without using an initial estimate of the offsets and scale factors, presenting evidence of the convergence problems mentioned throughout the chapter. Next, Section 5.7.2 depicts the number of iterations the NLLS solution takes to reach convergence depending on the initial estimate, which shows that a reasonable initial guess also reduces the number of iterations of the NLLS, improving the computational cost of the algorithm.

5.7.1 The NLLS Algorithm Convergence Problem

The loss function of the NLLS formulation is quartic; thus, the algorithm is not guaranteed to estimate the correct minima. Although we do not provide a formal study of the problem, we show that the NLLS has convergences issues without an appropriate initial condition estimate. We discuss this problem since Springmann and Cutler's work [7] indicates they found no convergence issues with a similar non-linear least squares formulation, which is an incorrect statement for the NLLS algorithm proposed here. Nevertheless, in their work, the authors did not explicitly present their solution; hence, it may have differences from our implementation.

We repeat the Monte Carlo simulation of Section 5.5.2 to assess the NLLS convergence with and without the initial condition algorithm. Table 5.17 shows the results for nine different conditions of the uniform distribution range of the calibration parameters. Regardless of the condition, each run may have a constant magnetic field magnitude value of 300 or 500 mG in each case, as indicated in that table. These values are compatible with Earth's magnetic field intensity and represent actual values expected in an experimental test. We assume that the offsets and angles are zero and the scale factors are unitary to evaluate the NLLS without an estimated starting condition, representing the ideal condition of a sensor. Furthermore, a run is considered a convergence if the RMSE of the calibrated data of the magnetic field magnitude is within a specified absolute value and if every computed parameter is within a percentage threshold of the true value in that run.

Table 5.17: Monte Carlo simulation results to evaluate the NLLS algorithm convergence versus the uniform distribution range of the simulated calibration parameters for nine different conditions.

Test	Uniform distribution of the Parameters and Magnitude Value				No of Runs	Number of Convergences	
	a, b, c (unitless)	x_0, y_0, z_0 (mG)	ρ, ϕ, λ (º)	B_e (mG)		Without $\mathbf{p0}$ estimate[1]	With $\mathbf{p0}$ estimate[2]
1	0.70-1.30	± 100	± 5	500	5000	5000	5000
2	0,70-1,30	± 100	± 5	300	5000	4955	5000
3	0,70-1,30	± 150	± 5	500	5000	4989	5000
4	0,80-1,20	± 150	± 5	300	5000	4215	5000
5	0,80-1,20	± 200	± 3	500	5000	4972	5000
6	0,70-1,30	± 200	± 5	500	5000	4714	5000
7	0,70-1,30	± 300	± 3	500	5000	3415	5000
8	0,70-1,30	± 400	± 3	500	5000	2449	5000
9	0,70-1,30	± 400	± 3	300	5000	2134	5000

[1] Column *Without* $\mathbf{p0}$ *estimate* indicates the NLLS without the initial guess algorithm, using $x_0{=}y_0{=}z_0{=}0$, $a{=}b{=}c{=}1$, and $\rho{=}\phi{=}\lambda{=}0$ for $\mathbf{p}_o$.
[2] Column *With* $\mathbf{p0}$ *estimate* refers to the NLLS solution using the the initial condition described in Section 5.4.3.

Table 5.17 data verify that the NLLS may have convergence problems depending on the parameters and that the issue is more critical for higher offset ranges. For instance, no convergence problems were observed in the first case, despite having a significant error range associated with the scale factors and the angles. Still, cases 5 and 6 reveal that the angles and scale factors may impact the convergence for a constant offset range. Nevertheless, it is notable that the offset value (or a decrease in the offset and the expected magnitude value ratio) is more critical to the NLLS solution and can significantly impact the convergence capacity of the algorithm. The comparisons of the last four cases prove that analysis.

However, using the NLLS solution with either of the techniques described in Section 5.4 to calculate an initial condition for scale factors and offsets, the algorithm has shown 100% convergence in all scenarios. Thus, ensuring a proper initial guess to the offsets and scale factors parameters is vital.

At last, we must observe that the parameters' values in the tests are compatible with those obtained in low-cost magnetometer systems and reported by many authors. For instance, hard iron effects and the null shift inherent to the sensor may sometimes lead to offset values higher than the magnetic field's expected magnitude. An example is the E-MEMS device [26], an embedded platform designed for attitude determination studies using multiple sensors, four of which are HMC5883L magnetometers, which experienced these conditions. Additionally, the angle and scale factor range are compatible with errors caused by soft iron effects combined with the scale factor and non-orthogonality errors inherent to the sensor.

5.7.2 Number of Iterations Analysis of the NLLS

We use the previous Monte Carlo simulation to discuss the number of loops the algorithm requires to reach convergence, specifically Test Number 5 results. Table 5.18 reports the total number of runs (of the Monte Carlo simulation) separated by the number of iterations. Once more, without $\mathbf{p0}$ denotes the NLLS solution using the ideal parameters, and with $\mathbf{p0}$, the one including the initial estimate of the scale factors and offsets.

Table 5.18: Number of iterations required by the Monte Carlo simulation to reach convergence, using the conditions of the fifth test resported in Table 5.17.

Solution	Number of Runs counter (convergence only)							Total Runs without Convergence
	Iteration Numbers (n)							
	$n=3$	$n=4$	$n=5$	$n=6$	$n=7$	$n=8$	$n>9$	
Without $\mathbf{p0}$[1]	0	119	2167	1773	679	172	62	28
With $\mathbf{p0}$[2]	4763	237	0	0	0	0	0	0

[1] Row *Without* $\mathbf{p0}$ *estimate* indicates the NLLS without the initial guess algorithm, using $x_0{=}y_0{=}z_0{=}0$, $a{=}b{=}c{=}1$, and $\rho{=}\phi{=}\lambda{=}0$ for $\mathbf{p}_o$.
[2] Row *With* $\mathbf{p0}$ *estimate* refers to the NLLS solution using the the initial condition described in Section 5.4.3.

Not only does the initial state ensures convergence, but it also significantly impacts the number of iterations. For instance, when starting the offsets and scale factors parameters using the proposed method, most runs required three loops and only a few four iterations to reach the stopping criteria, a similar result to the Monte Carlo simulation discussed in Section 5.5.2. On the contrary, most runs needed between 5 and 7 loops without the initial state before reaching the convergence criterion. Moreover, not a single run converged within the third loop, and a few of them required more than ten loops.

Therefore, these results show that the initial state solution guarantees the convergence of the NLLS method and improves its computational cost, as it can significantly impact the number of iterations.

5.8 Chapter Conclusions

This chapter presented an alternative formulation to estimate the calibration parameters using the magnetometer sensor model proposed by Foster and Elkaim [2]. The theoretical part of the chapter shows the formulation to use the direct application of the Non-Linear Least Squares (NLLS) estimator rather than rewriting the problem into auxiliary variables to use the batch linear least squares estimator.

The simulations and experimental tests have shown that the NLLS algorithm performs very similarly to the analytical solution of the extended two-step, reported by Menezes Filho et al. in reference [36]. Nevertheless, the proposed algorithm allows the parameter estimation for measurements with different magnitudes, which, for instance, may be required by the on-orbit magnetometer calibration procedure for nanosatellites.

Furthermore, the NLLS solution has a few advantages over the ETS and is more straightforward to implement than other alternatives. The NLLS approach allows for an easy expansion of the sensor's model to include new parameters compared to the two-step problem. For example, the time-varying bias model of [7] is easily solved by the non-linear Least Squares-based estimator presented here, where the solution remains the same, only requiring computing the additional gradient parameters in each iteration. Future authors may also expand the NLLS for other parameters, such as calibration to a vehicle's or another sensor's frame, a calibration considering temperature coefficients, or any other model requiring an attitude-independent calibration.

The drawback of the NLLS is the convergence problems depending on the initial state of the parameters. Nevertheless, we have shown that a good condition of the offsets and scale factors to initialize the NLLS algorithm circumvents the matter. In this direction, we have reported three different algorithms capable of

providing that estimate.

The first two algorithms are the Gebre-Egziabher et al. estimator [1] and an alternative formulation based on that. The first is viable for measurements subject to a magnetic field with constant magnitude, and the latter is an adaptation suitable for non-constant magnitudes. In addition, we have presented a new approach, which estimates the offsets and scale factors parameters separately. The advantage of this simplified solution is that it does not have limitations on whether the measurements' magnitude is constant or variable.

Lastly, the experimental tests demonstrate the effectiveness of the magnetic field simulator in evaluating sensors and algorithms when generating a magnetic field in the closed-loop topology. Thus, for example, future works can use the simulator to assess other conditions and generate magnetic fields with the specific spatial distribution of the data to evaluate an algorithm's performance in such circumstances.

6 The Magnetometer Calibration including Time-Varying Bias

In this chapter, we display the analysis of the magnetometer calibration, including time-varying bias, and a methodology to evaluate that calibration experimentally using the magnetic field simulator. With the advance of technology in the past decades, a new set of systems have emerged using low-cost magnetic sensors. For instance, these include small satellite missions, unmanned aerial vehicles, small-sized attitude and heading reference systems, and even daily gadgets or devices. Unfortunately, magnetometers will likely be exposed to more sources of soft and hard iron errors in these applications due to their characteristics, such as having a low-cost and small-sized design and reduced development time and resources. For example, many small satellite missions neither isolate the magnetometer from other electronics nor employ a boom mechanism.

More problematic, some sources of errors could end up causing non-constant interference in the sensor measurements. Therefore, magnetometers might be subject to time-varying errors in some applications. In nanosatellites missions, for example, some authors [7, 11, 12] have identified that varying electrical currents from solar panels and batteries systems and magnetorquers could lead to time-varying errors. Hence, a few works have displayed that the time-varying interference would cause additional errors in magnetometer readings [7,8,10–13]. In such conditions, the typical time-invariant calibration is sub-optimal, leading to worse estimated calibrated magnetic field values and negatively impacting any system dependent on the Earth's magnetic field measurement acquired by a magnetometer. For instance, these time-varying interference could affect the accuracy of attitude determination and control systems. Hence, some of those works have shown that accounting for the time-varying interference in small satellites would lead to a better outcome in magnetometer calibration [7,8,11,13].

Although the aforementioned works discuss the calibration, they focus on their specific mission, except for [11]. In addition, some only assess the magnetometer calibration using in-flight data and do not discuss a procedure to evaluate or test the time-varying interference in a controlled pre-flight environment. For instance, Springmann and Cutler [7] use in-flight data of the RAX-1 satellite [99] to demonstrate that a sensor model including time-varying biases could compensate for the errors occasioned due to electrical currents of the solar panels and the battery system. However, they barely discuss the algorithm or the methodological calibration process and do not have a ground test or pre-launch calibration procedure. Kim, Bang, and Lee [10] use a measurement model to compensate for magnetic torques in the KOMPSAT-1. Nonetheless, their discussion is limited to a simulation study followed by flight data analysis without any pre-flight examination.

Han et al. [8] evaluate, prior to launch, the effects of the CDPS-1A Pico-satellite's electronics in the magnetometer calibration. Nevertheless, they used a dedicated zero magnetic laboratory to map the dynamic

bias induced by other electronics and a manual experiment to assess the solar panel influence afterward. Then, the authors can pre-launch calibrate and estimate the dynamic (time-varying) bias coefficients. Frey, Hawkins, and Thorsen [12] discuss a calibration procedure to compensate for magnetic torques using a three-axial magnetic field simulator. However, that procedure requires a specific predefined sequence of the Helmholtz Cage to find a set of coefficients. Hence, the solution is not attitude-independent, and the coefficients are estimated only pre-flight.

At last, Allen et al. [11] propose an algorithm for accurate geomagnetic measurements considering the time-varying onboard field contribution of electrical currents. They also show a HiL setup to validate and test the proposed algorithm. However, their method requires multiple magnetometers to perform the joint calibration of the sensors. In addition, the algorithm requires training and specific data during orbit, requiring the varying current sources to be turned off for short periods during the spacecraft orbit.

In the direction of the time-varying bias study due to electrical currents and electronics, this chapter presents an experimental methodology to assess time-varying interference in any system requiring attitude-independent magnetometer calibration. Therefore, our contribution is to propose an experimental Hardware-in-the-Loop (HiL) setup using the magnetic field simulator capable of testing, simulating, and evaluating the effect of time-varying sources of magnetic disturbances in a magnetometer. Furthermore, the proposed HiL setup can generate and simulate electrical currents while generating the magnetic field. Hence, not only can we evaluate a calibration algorithm, but it is also possible to reproduce the effect of electrical currents, for example, by generating currents equivalent to that of solar panels while in a controlled environment. For example, our methodology circumvents the limitations of the test performed by Han et al. [8].

As a result, we present a more generic approach to evaluate the calibration of magnetometers subject to time-varying errors, as the procedure allows simulating time-varying currents and generating magnetic fields simultaneously. Thus, it is possible to replicate any condition, such as those expected in a small satellite mission, and evaluate any proposed calibration algorithm. Therefore, it is possible to use the setup to perform a pre-flight assessment of low-cost magnetometers in multiple scenarios.

In addition, we also present a thorough discussion on the attitude-independent calibration, including the time-varying bias parameters using the Non-Linear Least Squares (NLLS) solution. Before addressing the experimental methodology, we present the theory and simulations of the NLLS algorithm. Theoretically, Springmann and Cutler [7] have used a similar solution. However, as discussed in Chapter 5, they reported a solution without convergence problems due to the initial point of the parameters. Thus, perfectly inferring these authors' algorithm is impossible as the NLLS has convergence problems.

The remainder of the chapter is organized as follows. Section 6.1 depicts the sensor model and the NLLS solution, including the time-varying bias. The NLSS algorithm validation and simulation results are reported in Section 6.2. Then, Section 6.3 shows the methodology and the hardware-in-the-loop setup to use the magnetic field simulator to evaluate the calibration and simulate the time-varying electrical currents or error conditions. At last, the conclusions of the chapter are seen in Section 6.4.

6.1 The Sensor Model and the NLLS Solution including the Time-Varying Bias

As mentioned, the inclusion of the time-varying bias follows the model proposed by Springmann and Cutler [7], which is an expansion of Foster and Elkaim's sensor model [2]. Therefore, our model is similar to those discussed in Chapter 5 with the additional parameters related to the time-varying source of errors. The NLLS solution also remains similar to the previous chapter discussion, which is a remarkable advantage of that algorithm compared to other solutions, such as those which rewrite the problem using the intermediate variables before estimating the parameters.

6.1.1 The Sensor Model including the Time-Varying Bias

The model proposed by Springmann and Cutler [7], and other authors that addressed the calibration with time-varying errors, considers that each source of interference generates a time-varying hard iron distortion in the magnetometer measurements. In other words, if an electronic system or a current-carrying wire, which is rigidly mounted to the sensor frame, has a time-varying electrical current, it results in a time-varying hard iron error in each axis sensing element of the sensor. Therefore, it is possible to map each varying source of error to a time-varying bias parameter in each axis.

Springmann and Cutler [7] approach sought to compensate for known time-varying electrical currents measured by the RAX-1 satellite. Therefore, for every magnetometer measurement, a current measurement was associated with each source of time-varying errors. Nevertheless, that concept can be generalized so that current measurements are not the only viable mapping element between the magnetometer measurement and the source of error. For example, Han et al. [8] considered available and measured electrical currents and other subsystems' states, which could be either on or off (0 or 1) in their picosatellite. In addition, even if the current is unknown, but the source of error is proportional to a signal value controlled by another subsystem that has that information available, it is possible to use that data instead of an actual electrical current measurement value. To exemplify, assuming an electrical current proportional to a PWM signal, the PWM value could be associated with each magnetometer data instead of a current measurement.

Assuming this generalization, the model requires that for each magnetometer measurement, there is another measurement (or state) for the varying electrical current (or any unit of the physical measurement responsible for the time-varying hard iron error). If mapping each sensor acquisition to the current state, it is possible to expand the time-invariant sensor model discussed in Chapter 5 to:

$$\tilde{\mathbf{u}} = \mathbf{STu} + \mathbf{b_0} + \sum_{i=1}^{n} \tilde{I}_i \mathbf{b_i} + \eta, \tag{6.1}$$

where i represents the *i-th* varying element in the sensor model, $\tilde{I}_i$ the current measurement, or the known state value, associated with the *i-th* element, and $\mathbf{b_i}$ the *i-th* 3×1 vector containing the time-varying bias parameter of each axis. This model has three additional parameters to each known internal source of variable hard iron errors in the system.

Expanding the matrix form for each of the axes, the sensor model with the time-varying bias parameters

is given by:

$$\tilde{B}_{\mathrm{x}} = aB_{\mathrm{x}} + x_0 + \sum_{i=1}^{n} x_i \tilde{I}_i + \eta_{\mathrm{x}} \tag{6.2}$$

$$\tilde{B}_{\mathrm{y}} = b\Big(B_{\mathrm{x}}\sin(\rho) + B_{\mathrm{y}}\cos(\rho)\Big) + y_0 + \sum_{i=1}^{n} y_i \tilde{I}_i + \eta_{\mathrm{y}} \tag{6.3}$$

$$\tilde{B}_{\mathrm{z}} = c\Big(B_{\mathrm{x}}\sin(\phi)\cos(\lambda) + B_{\mathrm{y}}\sin(\lambda) + B_{\mathrm{z}}\cos(\phi)\cos(\lambda)\Big) + z_0 + \sum_{i=1}^{n} z_i \tilde{I}_i + \eta_{\mathrm{z}}, \tag{6.4}$$

where x_i, y_i and z_i represent the i-*th* time-varying bias parameter mapped to the i-*th* source of the time-varying error by $\tilde{I}_i$.

There are a few noteworthy characteristics of the formulation above. First, as elucidated in [7], the model is effective only if it is physically possible to map the varying electrical current (or a device or system's state) to a variation in the magnetic sensor measurement. On the contrary, the model is non-observable, and the calibration accuracy will decrease. Secondly, each I_i must be linearly independent of each other, or the non-linear least squares solution will have a rank-deficient Jacobian matrix. Lastly, the model assumes that the current measurements (or state values) are acquired (or updated) concurrently with the magnetometer measurements and at the same rates. If that is not true in a system, it would require an interpolation method [7] or an approximation technique that would lead to sub-optimum results.

6.1.2 The NLLS Solution including the Time-Varying Bias Parameters

The time-varying bias solution follows the same procedure elucidated in Section 5.3, but now including the additional parameters $\mathbf{b_i}$ and the associated current/state measurement $\tilde{I}_i$ given in the sensor model of (6.2)-(6.4). Therefore, the expected magnetic field is a function of:

$$B_e^2 = B_x^2 + B_y^2 + B_z^2 = f(\tilde{\mathbf{B}}, \mathbf{p}, \tilde{\mathbf{I}}), \tag{6.5}$$

where $\mathbf{p}$ has $9+3i$ parameters, which includes the nine time-invariant ones plus one time-varying bias per axis for every source of known time-varying errors[1].

The new system model $f\left(\tilde{\mathbf{B}}, \mathbf{p}, \tilde{\mathbf{I}}\right)$, as a function of the sensor measurements, the parameters, and the current/state measurement, is now given by (6.6), which is obtained using (6.2)-(6.4).

$$f\left(\tilde{\mathbf{B}}, \mathbf{p}, \tilde{\mathbf{I}}\right) = B_x^2 + B_y^2 + B_z^2 = \left(\frac{\widetilde{B}_{\mathrm{x}} - \mathrm{O}_x}{a}\right)^2 + \left(\frac{a(\widetilde{B}_{\mathrm{y}} - \mathrm{O}_y) - b\sin(\rho)(\widetilde{B}_{\mathrm{x}} - \mathrm{O}_x)}{ab\cos(\rho)}\right)^2 + \left(\frac{ab\cos(\rho)\left(\widetilde{B}_{\mathrm{z}} - \mathrm{O}_z\right) - ac\sin(\lambda)\left(\widetilde{B}_{\mathrm{y}} - \mathrm{O}_y\right) + bc\Big(\sin(\lambda)\sin(\rho) - \cos(\rho)\sin(\phi)\cos(\lambda)\Big)\left(\widetilde{B}_{\mathrm{x}} - \mathrm{O}_x\right)}{abc\cos(\rho)\cos(\phi)\cos(\lambda)}\right)^2, \tag{6.6}$$

where O_x, O_y, and O_z, are given by (6.7)-(6.9), respectively.

[1] In the remainder of the thesis, we use the nomenclature offset to refer to the time-invariant offset error, and the nomenclature bias to refer to the time-varying bias to facilitate the thesis comprehension and readability.

$$\mathrm{O}_x = x_0 + \sum_{i=1}^{n} x_i \tilde{I}_i \tag{6.7}$$

$$\mathrm{O}_y = y_0 + \sum_{i=1}^{n} y_i \tilde{I}_i \tag{6.8}$$

$$\mathrm{O}_z = z_0 + \sum_{i=1}^{n} z_i \tilde{I}_i \tag{6.9}$$

The updated loss function of the NLLS formulation is given by:

$$J = \frac{1}{2}\left[\mathbf{B}_e^2 - \mathbf{f}(\tilde{\mathbf{B}}, \mathbf{p}, \tilde{\mathbf{I}})\right]^{\mathsf{T}} \left[\mathbf{B}_e^2 - \mathbf{f}(\tilde{\mathbf{B}}, \mathbf{p}, \tilde{\mathbf{I}})\right] \tag{6.10}$$

The algorithm estimates the parameters following the same procedure defined in Chapter 5. Equations (5.10) and (5.13) are maintained, but in this new solution $\mathbf{p}$ is a $(9+3i)\times 1$ vector, the Jacobian matrix now has a dimension of $m \times (9+3i)$ and is given by (6.11), and the residual error maintains the $m \times 1$ calculated using (6.12).

$$\mathbf{H} = \left.\frac{\partial \mathbf{f}(\tilde{\mathbf{B}}, \mathbf{p}, \tilde{\mathbf{I}})}{\partial \mathbf{p}}\right|_{\hat{\mathbf{p}}} \tag{6.11}$$

$$\mathbf{e} = \mathbf{B}_e^2 - \mathbf{f}(\tilde{\mathbf{B}}, \mathbf{p}, \tilde{\mathbf{I}}) \tag{6.12}$$

Therefore, the estimation considering the additional time-varying parameters follows the same steps of the time-invariant NLLS solution described in Fig. 5.1's flowchart. The algorithm repeats the loops until it reaches the stopping criteria, whose values and considerations are independent of the additional parameters, and follows the criteria described in Chapter 5.

6.1.3 The Uncertainties Calculation using the Fisher Information Matrix

After reaching the stopping condition, the NLLS algorithm computes the Fisher information matrix similarly to the time-invariant solution. The only difference is that now the covariance matrix, $\mathbf{P}$, has a dimension of $(9+3i)\times(9+3i)$. The square root of its diagonal elements will provide the 1σ lower bound uncertainties of the nine time-invariant parameters plus the other three time-varying biases per i-*th* source of varying error.

It is important to note that in our formulation, which uses the residual error variance, $\mathrm{Var}(\mathbf{e})$, to calculate the uncertainties, it is not necessary to consider the standard deviations of the time-varying currents $\tilde{I}_i$. Section 6.2.4 displays the results of three Monte Carlo simulations with distinct standard deviation values associated with the noise of the time-varying measurement I_1. Those results demonstrate that our assumption is reasonable to calculate the uncertainties regardless of the measurement noise of the varying current.

In addition to that, as it is also discussed by Springmann and Cutler [7] in their work's Appendix, the uncertainties values calculated using the Cramér-Rao inequality (or the Fisher information Matrix) are optimistic and provide a lower bound of the state covariance, not its actual covariance. The non-linear least squares is not an optimal estimator in the magnetometer calibration, despite the excellent results achieved in Chapter 5. Furthermore, the NLLS solution does not consider the probability density function of the error. Nevertheless,

as it has already been shown in the previous chapter and indicated in [7], the lower bound of the uncertainties provides insight into the accuracy of the parameters and eventual identification of a poor spatial distribution of a specific set of measurements.

6.1.4 The Convergence Problem and the Initial Solution for the Time-Varying Calibration

Compared to the time-invariant solution, differences arise due to the initial estimate of the parameters, $\mathbf{p_0}$, which impacts the convergence of the time-varying NLLS. Naturally, it will depend on the initial value of the time-varying biases and the time-invariant parameters. Therefore, it is necessary to investigate the time-varying NLLS convergence.

The most straightforward alternative is to initialize the $\mathbf{p_0}$ using the offsets and scale factors computed using the algorithm proposed in Section 5.4.3 regardless of the new errors and assume a starting point of $\mathbf{p_0}$ where all time-varying biases and misalignment angles are 0. Generally, we have observed that using that initial state solution ensures the time-varying bias solution convergence in most conditions. The matter is addressed in Section 6.2.5 and shows that the time-varying bias NLLS converges in every simulation with time-varying bias magnitudes compatible with the findings reported in the literature [7, 8, 10, 13].

Despite that, it is also possible to expand the algorithm proposed to estimate the offsets and scale factors in Section 5.4.3 to include the time-varying biases. However, we have found that unless a time-varying bias magnitude value is considerably high (higher than those reported in the literature in the aforementioned works), the adaptation of the algorithm has a poor estimate. Consequently, we left the discussion of the matter for Appendix A.3 and chose not to employ that algorithm except for the tests reported in that appendix.

Therefore, authors may evaluate what the best alternative in each case is. The remainder of this chapter always initiates the time-varying bias NLLS $\mathbf{p_0}$ parameters using the values computed using the time-invariant scale factors and offsets solution reported in Section 5.4.3. Therefore, the angles (ρ, ϕ, and λ) and the time-varying biases (x_i, y_i, and z_i) values are 0 in the initial estimate vector ($\mathbf{p_0}$).

6.2 Simulation to Validate the Time-Varying Bias Model and Solution using the NLLS

The simulation analysis is broken down into six examinations, each reported in the following subsections. The first one, shown in Section 6.2.1, demonstrates the time-varying magnetometer calibration and establishes a comparison with the time-invariant solution for a single source of time-varying bias. Next, Section 6.2.2 presents the NLLS algorithm expanded to compensate for a couple of time-varying electrical currents. The third and fourth tests, reported in Sections 6.2.3 and 6.2.4, are Monte Carlo simulations to examine the algorithm. The former assesses the solution robustness and the error distribution of the estimated parameters, and the latter evaluates the impact of the time-varying current noise in the estimation process and the uncertainties. The fifth test, reported in Section 6.2.5, depicts the algorithm robustness using the time-invariant initial guess in the offsets and scale factors. At last, Section 6.2.6 displays the RMSE error of the calibrated magnetic field magnitude for different conditions of the time-varying bias and with distinct amplitudes.

In every simulation, we use the magnetic field uncorrupted measurements seen in Fig. 6.1 to generate the corrupted data, which has 8 simulated measurements per second in the magnetic field waveform of Fig. 6.1(a). That generates a total of 1152 measurements per test, whose ideal vector components plot (data scattering over the attitude sphere) is seen in Fig. 6.1(b).

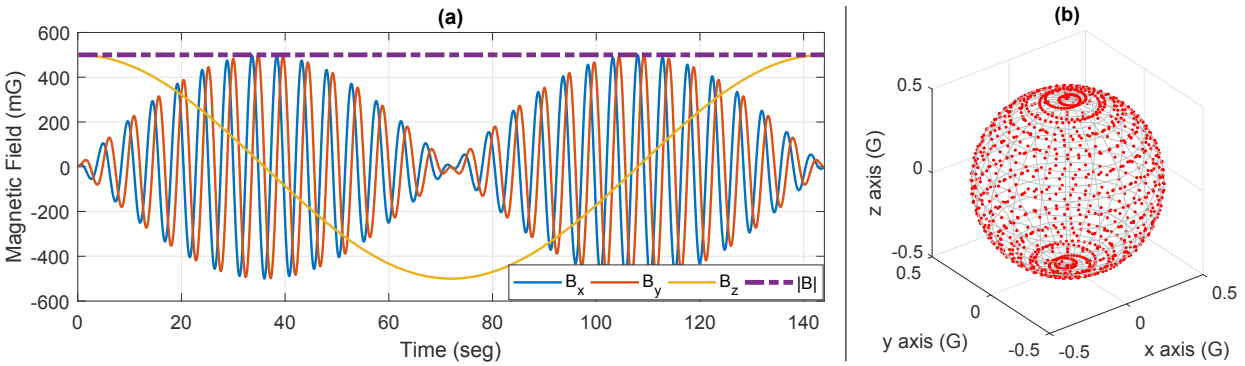

Figure 6.1: Theoretical magnetic field used in the time-varying bias simulation analysis. (a) Vector components versus time. (b) Vector components plot in three dimensions.

The error value of the parameters and specific methodological details of each test are discussed within the respective subsection. Each test analysis, graphically and numerically, follows the same idea of the time-invariant chapter. We show the estimated parameters, their uncertainties in each test, and the magnetic field magnitude RMSE analysis. Naturally, the error analysis is discussed more deeply in the Monte Carlo simulation, shown in Section 6.2.3.

Moreover, the behavior of the algorithm and the uncertainties computed also depend on the spatial data distribution, as established in the time-invariant analysis. However, we do not replicate that analysis here, as they would not provide new insights compared to the time-invariant results reported in Chapter 5. At last, we also limit the test for a constant magnetic field magnitude for the same reason, as the previous chapter examination yielded similar results regardless of the magnitude condition.

6.2.1 Demonstration of the Time-Varying Bias Calibration and Comparison with the Time-Invariant Procedure

In this first simulation, we seek to demonstrate the time-varying bias calibration and establish a comparison with the invariant solution. Thus, we simulate the magnetometer measurements corrupted by the time-invariant model and the one including the time-varying bias. In both cases, they are corrupted by the same invariant parameters and have precisely the same noise associated with each measurement. Therefore, it is possible to analyze the results by comparing the time-invariant and time-varying calibration estimation and the residual RMSE value from the expected magnitude field in a theoretical scenario to establish a comparison.

In a real problem, the time-varying source of interference (and error) could lead to an additional noise associated with each sensor measurement. Furthermore, each varying signal measurement ($\tilde{I}_i$) may have noise. For instance, Springmann and Cluter [7] discuss that their electronics responsible for measuring the electrical current have noise with a standard deviation of 5 mA, approximately. However, if the time-varying bias signal is obtained without a measurement system, no noises are associated with it. For example, that would be the case of an on/off electronics system state or a PWM signal generated by a microcontroller. In these cases, $\tilde{I}_i$

is the expected theoretical value instead of an actual measurement.

However, to generate two datasets that are as identical as possible to compare the calibration, we do not consider any other error or noise except for the time-varying bias. Based on Fig. 6.1 theoretical data, we apply the errors seen in Table 6.1 to generate the datasets.

Table 6.1: Simulated parameters in the first test to demonstrate the time-varying bias calibration.

Scale Factor (unitless)			**Offsets** (milligauss)			**Misalignment** (degrees)			**Varying Bias** (mG/A)			**Noise SD** (milligauss)
a	b	c	x_0	y_0	z_0	ρ	ϕ	λ	x_1	y_1	z_1	σ_x, σ_y, σ_z
0.85	1.20	1.10	145	85	-180	2.50	-3.20	1.80	18	-12	10	2

We generate the time-invariant data based on the calibration parameters, whose uncalibrated magnitudes are seen in Fig. 6.2(a). We can observe that the time-varying electrical current on the right side of the y-axis of the plot is zero throughout the simulation. In Fig. 6.2(b), we have the simulated varying current measurements, which are associated with the varying bias values of Table 6.1. The same plot shows the uncalibrated data of the time-varying dataset. Although both waveforms are very similar, Fig. 6.2(c) depicts the time-invariant magnitude minus the time-varying one, where it is evident that the magnitude differs between them during the moments subject to the time-varying current interference. However, in the remainder of the simulated measurements, they are identical; thus, it shows that both data have the same noise associated with them.

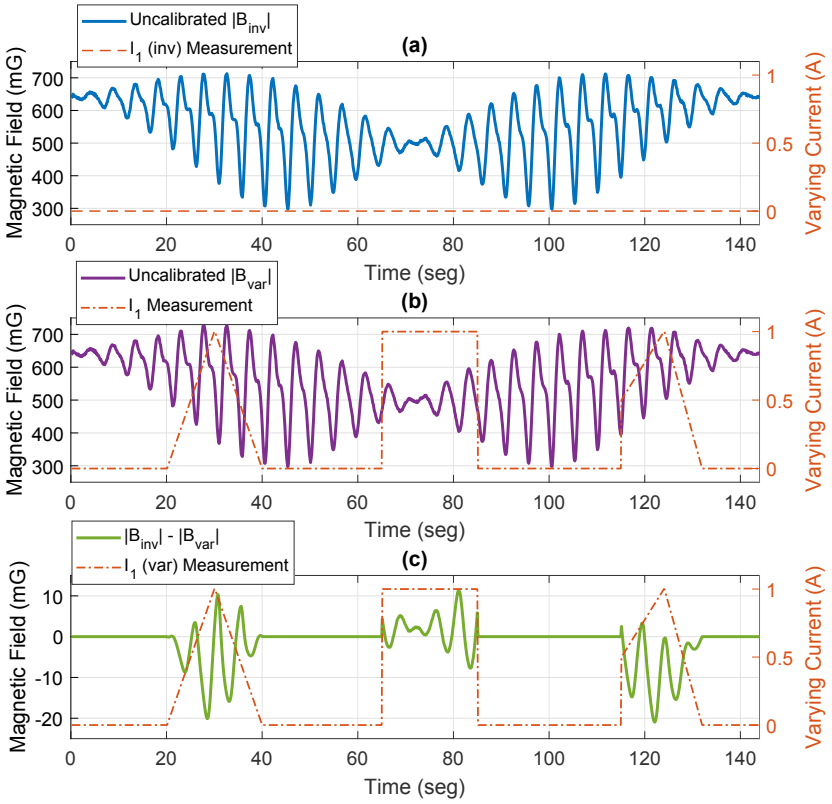

Figure 6.2: Magnitude values of the simulated measurements. (a) Time-invariant sensor model. (b) Time-varying bias sensor model. (c) Difference between the time-varying and the time-invariant magnitudes.

The time-invariant NLLS solution discussed in Chapter 5 is applied in the time-invariant simulated measurements. Table 6.2 displays the calibration parameters obtained. Once more, we see that the initial algorithm and the NLLS have converged to values close to the true one. Furthermore, the NLLS 3σ uncertainties ex-

tracted from the Fisher information matrix are smaller than the error. Naturally, these results are almost identical to the time-invariant ones reported in Section 5.5.1, which is expected since the dataset has a similar spatial distribution. The objective is to use these results as a reference for the time-varying calibration analysis.

Table 6.2: Calibration parameters results for the time-invariant simulated dataset seen in Fig. 6.2(a).

Param.	True Value	Time-Invariant Calib. Model				Unit
		NLLS[1] $\mathbf{p_0}$	NLLS[2] $\mathbf{p}$	NLLS Error	NLLS[3] 3σ	
a	0.90	0.9000	0.8995	-0.0005	0.0008	unitless
b	1.20	1.2006	1.1994	-0.0006	0.0011	unitless
c	1.10	1.0993	1.1001	0.0001	0.0006	unitless
x_0	125	125.08	125.09	0.09	0.29	mG
y_0	-90	-89.93	-89.89	0.11	0.38	mG
z_0	75	75.11	75.11	0.11	0.25	mG
ρ	1.5	-	1.498	-0.002	0.085	degrees
ϕ	-2.5	-	-2.534	-0.034	0.073	degrees
λ	3.2	-	3.222	0.022	0.073	degrees

[1] NLLS p_0 refers to the initial algorithm estimation of Section 5.4.3.
[2] NLLS stands for the last iteration of the proposed NLLS solution.
[3] NLLS 3σ refers to the computed 3σ bounds of the uncertainties.

Next, we apply the time-invariant NLLS algorithm and the varying one to calibrate the magnetometer data corrupted with the time-varying bias. The numerical results of the parameters and uncertainties are seen in Table 6.3, which also includes the initial guess estimation of the scale factors and the offsets.

Table 6.3: Calibration parameters results for the time-varying dataset seen in Fig. 6.2(b), using the time-invariant NLLS solution and the NLLS solution including the time-varying bias parameters.

Param.	True Value	NLLS $\mathbf{p_0}$	Time-Invariant NLLS			Time-Varying NLLS			Unit
			NLLS $\mathbf{p}$	NLLS Error	NLLS 3σ	NLLS $\mathbf{p}$	NLLS Error	NLLS 3σ	
a	0.90	0.9037	0.9039	0.0039	0.0021	0.8994	-0.0006	0.0009	unitless
b	1.20	1.2051	1.2045	0.0045	0.0029	1.1992	-0.0008	0.0012	unitless
c	1.10	1.0929	1.0922	-0.0078	0.0015	1.1004	0.0004	0.008	unitless
x_0	125	129.28	129.27	4.27	0.74	125.08	0.08	0.36	mG
y_0	-90	-92.77	-92.61	-2.61	0.98	-89.98	0.02	0.48	mG
z_0	75	78.15	78.20	3.20	0.63	74.98	-0.02	0.35	mG
ρ	1.5	-	1.403	-0.097	0.217	1.498	-0.002	0.085	degrees
ϕ	-2.5	-	-1.899	0.601	0.186	-2.535	-0.035	0.079	degrees
λ	3.2	-	2.887	-0.313	0.185	3.213	0.013	0.078	degrees
x_1	18	-	-	-	-	18.043	0.043	0.903	mG/A
y_1	-12	-	-	-	-	-11.650	0.350	1.196	mG/A
z_1	10	-	-	-	-	10.405	0.405	0.738	mG/A

There are a few essential observations from Table 6.3 data. First, the initial solution algorithm offsets and scale factors estimate is further away from the true value compared to Table 6.2 solution. Nevertheless, they converged to a value sufficient to ensure the NLLS algorithm convergence, and further investigations of that matter using the time-invariant initial guess are made in Section 6.2.5. However, despite the new varying bias, the solution still works to find a relatively good initial guess for the scale factors and offsets.

The convergence of the time-varying NLLS solution is evident by inspecting the results under the *Time-Varying NLLS* column. Every error and uncertainty computed are in the same order of magnitude and very close to those of the time-invariant estimation seen in Table 6.2. Furthermore, the time-varying bias parameters converged to a value near the simulated one, confirming the procedure's effectiveness.

Lastly, we must assess the estimated calibration parameters of the NLLS solution using the time-invariant model when applied to the measurements corrupted by the time-varying bias interference. The errors of the estimated parameters and their uncertainties increased considerably. However, the notable result is that we have a 3σ value smaller than the actual estimate errors for every parameter besides the misalignment angle ρ. For instance, the z-axis scale factor, x_0, y_0, and the misalignment angle ϕ errors are three times superior considering the boundary value of $\pm 3\sigma$. Therefore, although the uncertainties values are considerably worse than the time-invariant reference estimation, indicating a degradation in the computed values, it does not reflect the actual value of the error as it does without the time-varying interference effect.

That is a consequence of having a sensor model that is no longer accurate, which also impacts the accuracy of the uncertainties. Hence, if a sensor is subject to an unknown time-varying error, the estimated uncertainties might be inaccurate and unfit to reflect the effect of these errors. In such conditions, the magnitude analysis of the calibrated data is another option to identify a poor calibration result or a deficient error model for a set of measurements. Nevertheless, future authors may seek an alternative formulation capable of detecting time-varying interference in cases where it is not viable to model them and where the computed uncertainties would reflect these errors.

Finally, we evaluate the calibrated magnetic field magnitude in each condition. The time-invariant measurements are correct only by the respective invariant algorithm, and Fig. 6.3(a) shows the calibrated sensor magnitude. The time-varying results after calibration are shown in Figs. 6.3(b) and (c). The former has the measurements corrected by the nine parameters sensor model, and the latter by the one with the additional bias parameters.

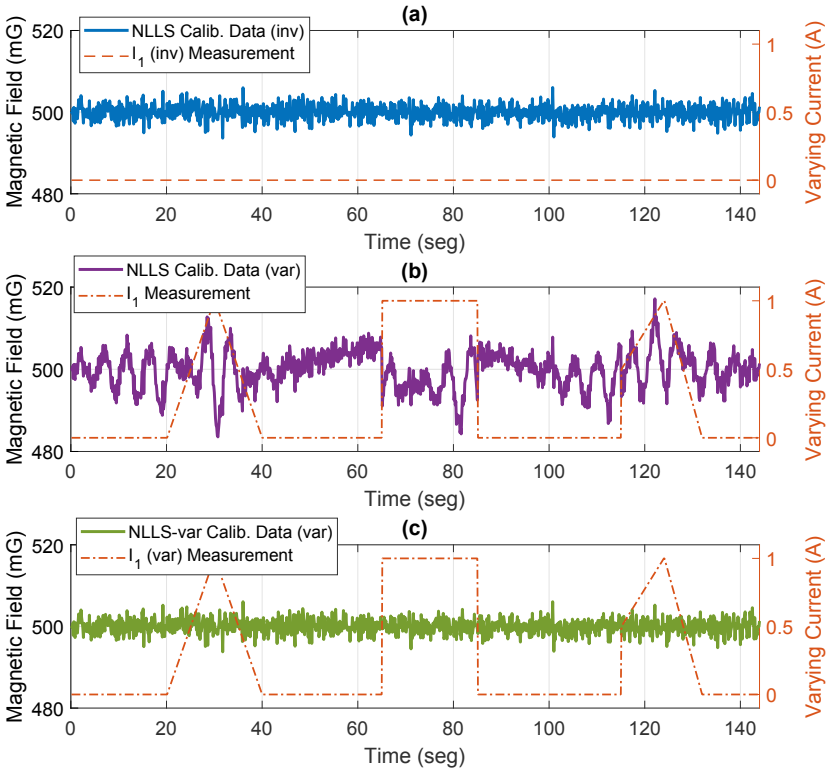

Figure 6.3: Magnitude of the calibrated data of the first simulation. (a) Time-invariant data and sensor model. (b) Time-varying measurements calibrated by the time-invariant model. (c) Time-varying measurements and varying bias sensor model.

The graphical results indicate how the performance of the calibrated data degrades when the typical time-invariant is used in a dataset corrupted by the time-varying hard iron errors. However, Fig. 6.3(c) proves that the NLLS algorithm using the sensor model with the time-varying bias, reduces the magnitude error to the same order of magnitude as seen in Fig. 6.3(a), corroborating that the model and the estimation were effective. Table 6.4 displays the numerical analysis of magnetic field magnitude data.

Table 6.4: Numerical analysis of the magnetic field magnitude and its errors obtained in the first simulation with the time-varying bias.

Sensor Simulated Data Type	Calibration Algorithm	Mean Magnitude (mG)	RMSE (mG)	Absolute Max. Error (mG)	Pk-Pk Error (mG)
Time Invariant	Uncalib.	558.29	111.62	213.33	418.13
	NLLS-Inv	499.98	1.820	6.37	12.40
With Time-Varying bias	Uncalib.	559.50	113.96	228.37	432.16
	NLLS-Inv	499.89	4.629	17.14	33.58
	NLLS-Var	499.98	1.818	6.22	12.27

Table 6.4 supports the graphical result above. The time-invariant data in the first two rows show that the calibration procedure reduced the RMSE value of the magnitude from approximately 110 to 1.82 milligauss. The last three rows of Table 6.4, with the time-varying data, prove the efficiency of the sensor model in such circumstances. On the contrary, the calibration using the typical sensor model led to a measurements magnitude RMSE value of 4.62 mG and higher than 30 mG from peak-to-peak. Consequently, the RMSE value and the magnitude error seen in Fig. 6.3(b) are indications of the poor estimate of the time-invariant solution and that the calibrated data deviated from the expected magnitude value. Notably, the magnitude does not oscillate around the expected magnitude value as the time-invariant data of Fig. 6.3(a). Instead, it drifts distinctively from the behavior expected from a Gaussian distribution, as reported in the time-invariant results.

Moreover, the NLLS approach using the time-varying bias sensor model improved the calibration to a nearly identical outcome compared to the time-invariant analysis. Hence, it also confirms the efficacy of the expanded NLLS algorithm, including the time-varying bias parameters.

6.2.2 Demonstration of the Time-Varying Calibration for Simultaneous Interference

Now that we have established the comparison between the time-invariant NLLS and the time-varying bias one, we expand the demonstration to include the calibration with a couple of simultaneous interference. Theoretically, the sensor model and the NLLS solution allow any number of time-varying bias terms. However, we limit the tests to two sources of time-varying bias to facilitate the graphical visualization and the data analysis.

The tests simulate two-independent time-varying electrical currents. The first is mapped through a current sensor, which measures the current value for each magnetometer measurement. The second time-varying bias is caused by a subsystem with an on/off state; therefore, it is an electrical current with two states. In this second condition, the current measurement is not essential to perform the estimation, and the estimator can input binary data reflecting the current state in the variable I_2. In addition, we associate a Gaussian noise with

the electrical current measurements of I_1. In the second system, we add Gaussian noise (in addition to the time-invariant noise) in the magnetometer measurement if the system's state is on during that measurement.

Table 6.5 shows the simulated time-invariant parameters, and Table 6.6 the time-varying bias characteristics. Note that the resulting magnitude of the time-varying bias is approximately 30 mG/A and 23 mG, respectively, for the first and the second time-varying signal. Also, we should observe that each axis time-varying bias owing to the current I_1 is given in milligauss per ampere, as I_1 measurements are given in ampere. In turn, the second varying bias parameters unit is direct a milligauss value, as the state does not have a known current measurement; hence, I_2 inputs are unitless and are either 0 or 1.

Table 6.5: Time-invariant parameters simulated for the simulation with multiple sources of interference.

Time-Invariant Parameters									
Scale Factor (unitless)			Offset (milligauss)			Misalignment (degrees)			Noise SD (milligauss)
a	b	c	x_0	y_0	z_0	ρ	ϕ	λ	σ_x, σ_y, σ_z
1.15	1.05	0.90	-105	75	-120	2.5	-1.6	2.4	2

Table 6.6: Time-varying bias parameters and its characteristics for the simulation with multiple sources of interference.

First Time-Varying Bias					**Second Time-Varying Bias**				
First Varying Bias (mG/A)			I_1 Meas. SD (mA)	Noise SD (mG)	Second Varying Bias (mG)			I_2 Meas. SD (mA)	Noise SD (mG)
x_1	y_1	z_1	I_1	σ_x, σ_y, σ_z	x_2	y_2	z_2	I_2	σ_x, σ_y, σ_z
12	-15	24	2	0	-15	-8	16	0	1

Using the parameters described above and the theoretical points described in the methodology, seen in Fig. 6.1, we simulate 1152 measurements. Figure 6.4 depicts the simulated current measurement for I_1, the state of the second varying current I_2, and the uncalibrated magnitude of the magnetometer measurements.

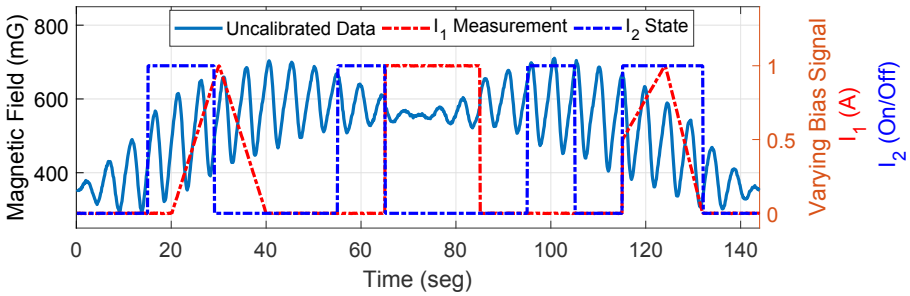

Figure 6.4: Magnitude of the uncalibrated data in the simulation with multiple sources of time-varying electrical currents and the measurements of I_1 and signal state of I_2.

To evaluate and compare the invariant and the time-varying algorithms, we calibrate the simulated measurements using the time-invariant NLLS and the one expanded to include the six time-varying biases. Table 6.7 shows the results for the calibration, including the offset and scale factor initial state solution, the time-invariant NLLS, and the one including the time-varying parameters.

Table 6.7: Calibration parameters results for the simulated measurements subject to multiple sources of time-varying bias whose uncalibrated data is seen in Fig. 6.4.

Param.	True Value	NLLS $\mathbf{p_0}$	Time-Invariant NLLS		Time-Varying NLLS		Unit
			NLLS-inv $\mathbf{p}$	NLLS-inv $\mathbf{3\sigma}$	NLLS-inv $\mathbf{p}$	NLLS-inv $\mathbf{3\sigma}$	
a	1.15	1.1691	1.1683	0.0055	1.1499	0.0013	unitless
b	1.05	1.0686	1.0682	0.0050	1.0502	0.0012	unitless
c	0.90	0.8838	0.8836	0.0024	0.8995	0.0007	unitless
x_0	-105	-109.45	-109.20	1.871	-104.91	0.616	mG
y_0	75	67.89	67.82	1.713	75.01	0.567	mG
z_0	-120	-107.50	-107.38	0.974	-119.72	0.379	mG
ρ	2.5	-	2.5247	0.4298	2.4655	0.094	degrees
ϕ	-1.6	-	-1.8234	0.3514	-1.5789	0.091	degrees
λ	2.4	-	1.4800	0.3519	2.3768	0.091	degrees
x_1	12	-	-	-	11.704	1.302	mG/A
y_1	-15	-	-	-	-15.441	1.175	mG/A
z_1	24	-	-	-	23.702	0.696	mG/A
x_2	-15	-	-	-	-15.361	0.886	mG
y_2	-8	-	-	-	-7.933	0.809	mG
z_2	16	-	-	-	16.091	0.537	mG

The conclusions extracted from Table 6.7 are similar to the previous section's analysis. Once more, the initial guess algorithm solution adequately estimates the scale factors and the offsets, ensuring the NLLS algorithm convergence. Nonetheless, the parameters computed by the initial estimate are less accurate compared to the time-invariant results reported in Chapter 5.

The same is seen for the time-invariant algorithm results. The calibrated parameters are far from the true value compared to errors obtained in the time-invariant simulations examined in Chapter 5. In addition, although we omit the numerical values of the errors, they are higher than the 3σ uncertainties for every axis scale factor and offset and for the misalignment angle λ. That emphasizes that the uncertainties estimation may not reflect the actual error if the sensor is subject to time-varying interference.

Finally, the time-varying NLLS correctly estimated every parameter, and the numerical values of the errors are smaller than the 3σ uncertainties extracted from the Fisher Information Matrix. Nevertheless, as Chapter 5 and [36] pointed out, the error examination for a single case does not provide enough information to conclude the algorithm's accuracy. Therefore, the detailed error analysis is left for the Monte Carlo simulation ahead.

Figure 6.5 displays the magnetic field magnitude obtained for both situations, allowing further investigation of the effectiveness of the time-varying bias calibration. In addition, the numerical analysis of the magnitude data results and their error are reported in Table 6.8, which also depicts the uncalibrated magnitude analysis.

Table 6.8: Numerical analysis of the uncalibrated (Fig. 6.4) and calibrated (Fig. 6.5) data obtained for the test with multiple sources of time-varying bias.

Sensor Simulated Data Type	Calibration Algorithm	Mean Magnitude (mG)	RMSE (mG)	Absolute Max. Error (mG)	Pk-Pk Error (mG)
With Time-Varying bias	Uncalib.	518.38	106.82	210.45	418.13
	NLLS-Inv	499.60	8.94	24.43	45.10
	NLLS-Var	499.98	2.03	8.30	14.55

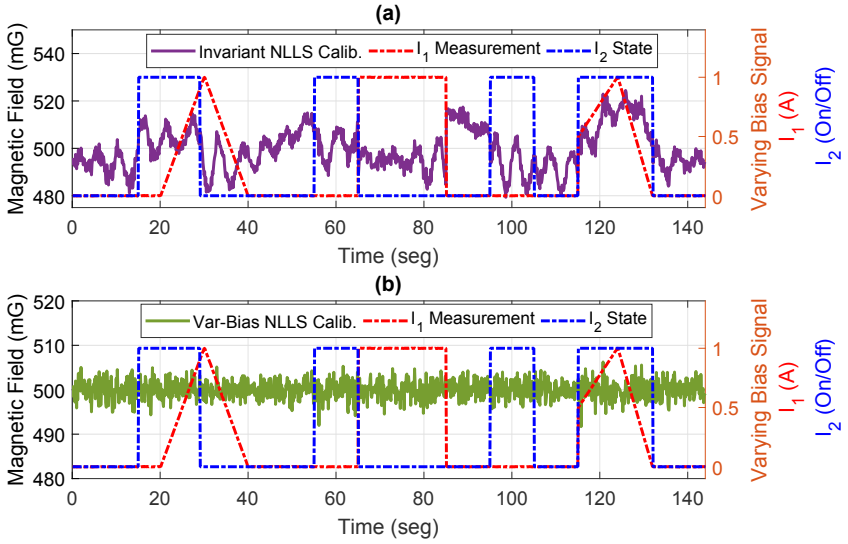

Figure 6.5: Magnitude of the calibrated data in the simulation with multiple time-varying electrical currents. (a) Results without the time-varying bias model. (b) Results with the time-varying bias model.

The calibrated magnitude using the time-invariant model deviates considerably from the 500 milligauss value, reaching a peak-to-peak error of approximately 45 mG and having an RMSE of 8.94 mG. On the contrary, the time-varying bias solution oscillates much closer to the expected magnitude, reducing the RMSE to 2.03 mG and the peak-to-peak error below 15 mG. At last, the vector components plots (spatial distribution over the *attitude sphere*) of the uncalibrated and the calibrated data are seen in Fig. 6.6.

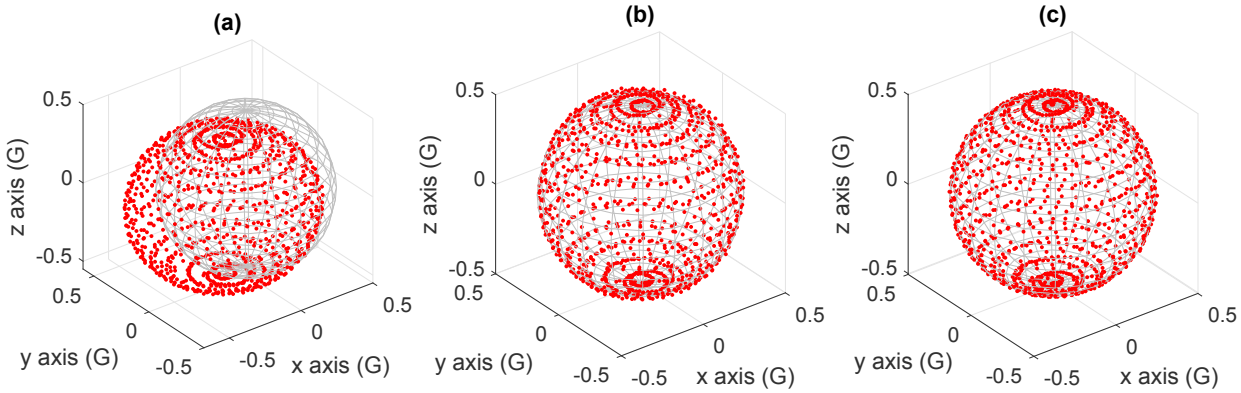

Figure 6.6: Vector components plot in three dimensions of the simulation with multiple time-varying electrical currents. (a) Uncalibrated Data. (b) NLLS calibrated data without the varying bias parameters. (c) NLLS calibrated data with the time-varying bias sensor model.

While the uncalibrated data is far from the 500 milligauss reference sphere, both solutions compensate for most errors regardless of additional time-varying interference. It is evident that the data seen in Figs. 6.6(b) and (c) are much closer to the theoretical distribution, which was plotted in Fig. 6.1(b). Although it is possible to visually identify that the time-varying data (c) has a better coincidence with the theoretical points than (b), it is perceptible that the magnitude and the parameters data analyses are much better at identifying the improvement in the calibration.

The results above display the effectiveness of the calibration considering multiple sources of time-varying bias. Therefore, as Springmann and Cutler [7] observed, the system may have numerous sources of varying currents, which can be modeled as a time-varying bias in the sensor model. Nevertheless, to be feasible

to perform the time-varying bias calibration, these electrical currents (or electronic systems states) must be known or mapped and must be uncorrelated to one another.

6.2.3 Monte Carlo Simulation Analysis

The Monte Carlo analysis seeks to identify the estimated parameters error distribution with the time-varying interference. Although it also evaluates the procedure convergence, the specific study of the time-varying bias NLLS convergence for different scenarios and conditions is discussed in Section 6.2.5. The Monte Carlo examination follows the same idea as the time-invariant one reported in Chapter 5. We perform a simulation with 5000 runs, and each one randomly generates the time-invariant parameters, the expected magnitude value (constant within each run), and the time-varying bias electrical current and, consequently, the varying bias. The time-invariant parameters and the expected magnitude values have the same uniform distribution used in the time-invariant analysis in Section 5.5.2. However, the time-varying interference and its resulting bias have many conditions, and we must establish a methodology to simplify the study.

To make the examination easier to comprehend and more straightforward, we simplify the problem by using only a binary (on/off) time-varying interference. In each run, the simulation randomly generates the magnitude (using a uniform distribution) of the time-varying bias ($|b_i|$) and a rotation matrix [100]; therefore, we have a random value in each axis varying bias (x_1, y_1, and z_1). In addition, the simulation randomly generates one value per run that dictates the probability of the time-varying signal (I_1) being on ($I_1 == 1$) in each magnetometer data. Then, the system generates another number for every simulated measurement in that run and verifies if this second value is higher than the one that dictates the probability. If the condition is satisfied, the signal $I_1 = 1$ for that measurement and, consequently, the time-varying bias is added in all axes.

Table 6.9 shows the time-varying parameters range and the characteristics of the time-varying bias. It also includes the range of the expected magnitude and the time-invariant parameters. Every run has the same 1152 theoretical points described previously, and all sensor measurements have a normal distribution with a standard deviation of 1.5 mG. This value is similar to the RMS noise used in the other Monte Carlo simulations and equivalent to that observed in the SUT's HMC5883L magnetometer, as seen in Appendix A.1.

Table 6.9: Uniform distribution range of the calibration parameters and the characteristics of the time-varying bias used in the Monte Carlo simulation with one source of time-varying bias.

Parameter	Range	Unit
Expected Magnitude (B_e)	$300 - 500$	mG
Scale Factor - a, b, c	$0.75 - 1.25$	unitless
Bias - x_0, y_0, z_0	± 500	mG
Angles - ρ, ϕ, λ	± 3	degrees
b_i magnitude - $\left(\sqrt{x_1^2 + y_1^2 + z_1^2}\right)$	$10 - 50$	mG
Probability of $I_1 == 1$ in each measurement	$30 - 70$	%

For each run, the uncalibrated data is corrected using both solutions, the time-invariant NLLS and time-varying bias one, which allow us to compute the parameters and their errors for every run and to compare the results for both algorithms. In addition, we extract the 1σ uncertainties of the estimation using the Fisher

Information matrix, and consequently, the 3σ values and the $\pm 3\sigma$ boundaries are available for each run. Lastly, the simulation also computes the magnetic field magnitude for each measurement and the resulting magnitude RMSE for both algorithms.

We begin the simulation analysis by depicting the graphical results of the error of the parameters. The errors versus each trial of the Monte Carlo simulation and the $\pm 3\sigma$ uncertainties boundary for each parameter are shown in Figs. 6.7, 6.8, 6.9, and 6.10. The first three figures show the error for the scale factors, offsets, and misalignment angles, respectively. In each one, (a)-(c) describe the time-invariant error for the x, y, and z axis, respectively, and (d)-(f) that for the time-varying bias solution, respectively, for the same axes. Lastly, Fig. 6.10 depicts the error of time-varying biases, computed only for the time-varying sensor model.

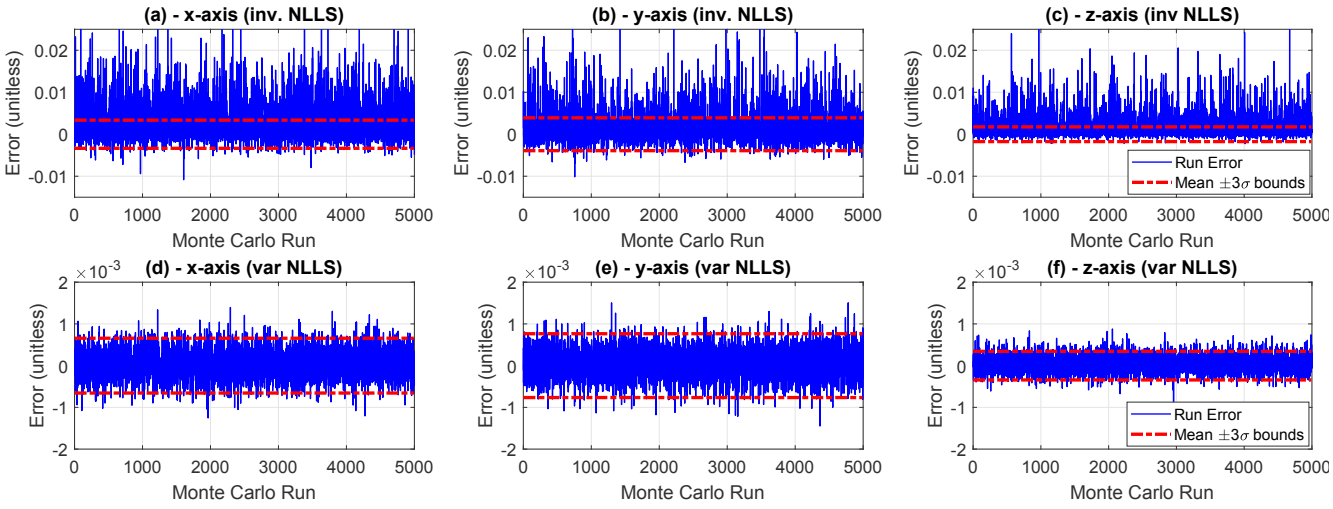

Figure 6.7: Errors of the scale factors estimation for each run and the average $\pm 3\sigma$ bounds of the uncertainties for the time-varying bias Monte Carlo simulation. (a)-(c) shows the time-invariant solution and (d)-(f) the results of the time-varying bias estimator.

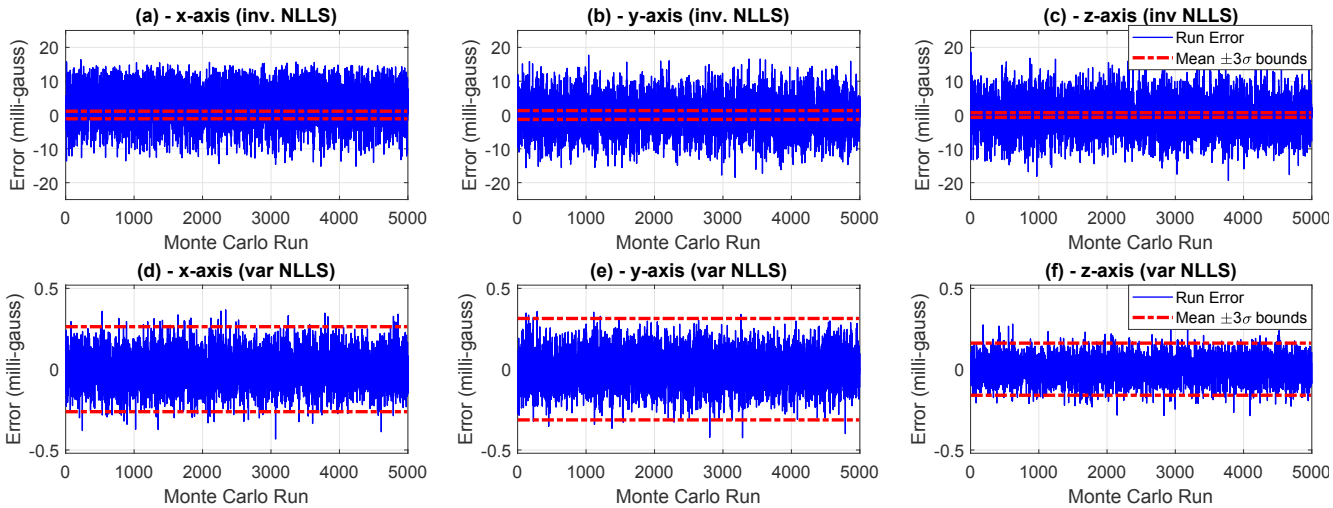

Figure 6.8: Errors of the offsets estimation for each run and the average $\pm 3\sigma$ bounds of the uncertainties for the time-varying bias Monte Carlo simulation. (a)-(c) shows the time-invariant solution and (d)-(f) the results of the time-varying bias estimator.

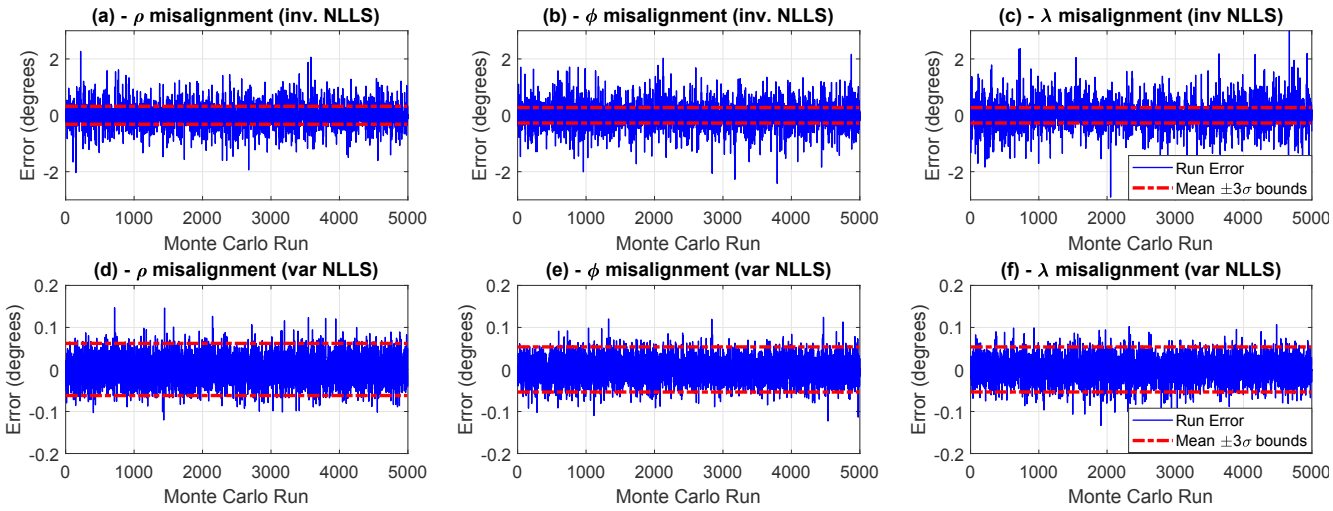

Figure 6.9: Errors of the misalignment angles estimation for each run and the average $\pm 3\sigma$ bounds of the uncertainties for the time-varying bias Monte Carlo simulation. (a)-(c) shows the time-invariant solution and (d)-(f) the results of the time-varying bias estimator.

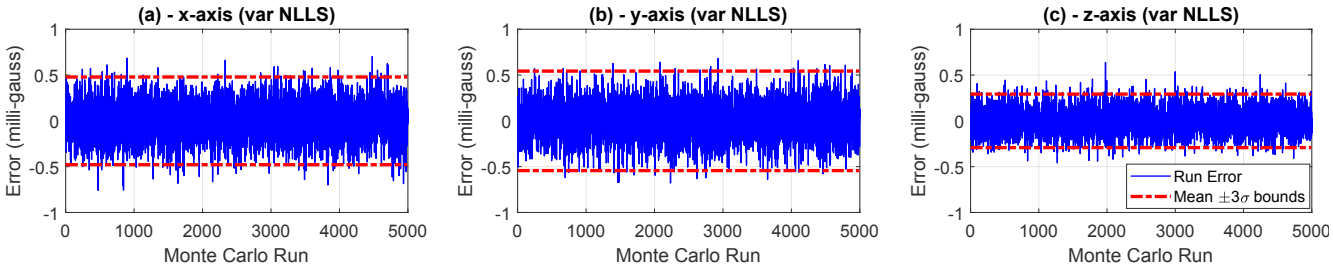

Figure 6.10: Errors of the time-varying biases estimation for each run and the average $\pm 3\sigma$ bounds of the uncertainties for the time-varying bias Monte Carlo simulation. (a) x-axis time-varying bias. (b) y-axis time-varying bias. (c) z-axis time-varying bias.

The first thing that should be pointed out is that the time-varying bias results in Figs. 6.7-6.9, seen in subfigures (d), (e), and (f), are plotted in the same y-axis scale compared to the time-invariant results reported in Section 5.5.2 of Chapter 5. Therefore, it shows that the calibration using the model expanded to the time-varying bias has an estimation error in the same order of magnitude. In addition, we also observe that the z-axis offset and scale factor error are smaller than the other axes, which is a consequence of the data spatial distribution, as established in the time-invariant study.

Once more, we observe that the average value of the 3σ used to plot the $\pm 3\sigma$ boundaries is befitting for all twelve parameters, including the three time-varying biases seen in Fig. 6.10. Moreover, the errors in most runs are within those boundaries, validating the methodology to estimate the uncertainties regardless of the addition of the time-varying biases. Nevertheless, the simulated data does not consider any noise associated with the current measurement $\tilde{I}_1$; thus, Section 6.2.4 examines the matter and additional Monte Carlo simulations with such noise.

On the contrary, the time-invariant NLLS results are inferior, as seen in subfigures (a)-(c) of Figs. 6.7-6.9. These show that the errors increase considerably, and the uncertainties extracted from the Fisher information matrix are not befitting with the actual errors. Hence, the Monte Carlo analysis confirms that if the sensor is subject to time-varying interference, the typical time-invariant model calibration worsens, and the computed uncertainties using the time-invariant NLLS algorithm do not provide accurate information.

The numerical analysis of the Monte Carlo simulation data follows in Tables 6.10 and 6.11. The former shows the parameters error analysis for all 5000 runs, which includes the average value of each parameter for all runs, their standard deviation (SD) value, and the error value of the worst run. The latter depicts the 3σ uncertainties analysis for all 5000 runs for every parameter, showing their average 3σ values, the uncertainties standard deviation (SD) values, and the worst run uncertainties values. In addition, both tables show the data for the time-invariant NLLS solution and the one including the time-varying bias.

Table 6.10: Error analysis of the Monte Carlo simulation with time-varying bias per parameter for all 5000 runs: average value (mean value of every run error modulus); the error standard deviation (SD) value; and the worst run error value.

Param.	**Error Analysis of the Parameters**						**Unit**
	Time-Invariant NLLS			Varying Bias NLLS			
	Mean Abs. Value	SD Value	Worst Run Value	Mean Abs. Value	SD Value	Worst Run Value	
a	3.2E-3	4.5E-3	37.1E-3	2.6E-4	3.3E-4	13.9E-4	unitless
b	2.3E-3	3.7E-3	34.5E-3	2.7E-4	3.4E-4	15.1E-4	unitless
c	1.7E-3	2.7E-3	33.1E-3	1.6E-4	2.0E-4	8.8E-4	unitless
x_0	5.22	5.64	16.37	0.086	0.109	0.367	mG
y_0	3.91	5.13	17.70	0.087	0.109	0.357	mG
z_0	3.85	5.06	18.59	0.060	0.075	0.279	mG
ρ	0.225	0.338	2.268	0.025	0.031	0.147	degrees
ϕ	0.232	0.359	2.163	0.021	0.027	0.124	degrees
λ	0.219	0.362	3.70	0.021	0.027	0.107	degrees
x_1	-	-	-	0.160	0.201	0.703	mG
y_1	-	-	-	0.157	0.197	0.681	mG
z_1	-	-	-	0.110	0.138	0.637	mG

Table 6.11: 3σ uncertainties analysis of the Monte Carlo simulation with time-varying bias per parameter for all 5000 runs: average value; standard deviation (SD) value; and the worst run value.

Param.	**3σ Uncertainties Analysis**						**Unit**
	Time-Invariant NLLS			Varying Bias NLLS			
	Mean Value	SD Value	Higher Value	Mean Value	SD Value	Higher Value	
a	3.4E-3	1.5E-3	10.9E-3	6.6E-4	1.1E-4	10.2E-4	unitless
b	3.9E-3	1.8E-3	12.7E-3	7.6E-4	1.3E-4	11.9E-4	unitless
c	1.8E-3	0.8E-3	5.7E-3	3.4E-4	0.6E-4	5.3E-4	unitless
x_0	1.122	0.505	3.650	0.263	0.046	0.408	mG
y_0	1.310	0.589	4.262	0.314	0.055	0.488	mG
z_0	0.688	0.309	2.238	0.161	0.028	0.251	mG
ρ	0.318	0.143	1.035	0.062	0.011	0.096	degrees
ϕ	0.275	0.123	0.893	0.054	0.009	0.084	degrees
λ	0.274	0.123	0.891	0.054	0.009	0.083	degrees
x_1	-	-	-	0.478	0.083	0.744	mG
y_1	-	-	-	0.543	0.094	0.844	mG
z_1	-	-	-	0.292	0.051	0.454	mG

Tables 6.10 and 6.11 data confirm how significantly better the estimation was using the time-varying bias sensor model. The time-varying bias estimation errors and uncertainties are in the same order of magnitude and very close to that of the time-invariant tests. Furthermore, the SD values of that solution's uncertainties are approximately 5 to 6 times smaller than the average values of the 5000 runs. In contrast, in the time-invariant solution, the SD values are 2 to 3 times smaller than the mean value, revealing a decrease in the repeatability among runs. Consequently, the data depicts that the time-varying interference impacted the

accuracy of the parameters estimated with the time-invariant sensor model.

In addition, we can compare the worst run value of the errors, seen in Table 6.10, and the run with the higher uncertainties values in Table 6.11. For the time-varying bias process, the error values are compatible with the uncertainties. For instance, every parameter has an error value in the worst run around 10-40% higher than the respective worst uncertainty value. However, for the time-invariant solution, they are proportionally much higher, up to almost nine times (900% higher) for the z_0 offset. It is also notable how the misalignment angles estimation deteriorates if the system suffers from a time-varying interference. For the misalignment angle λ, the worst run has an estimation error of 3.70 degrees, which is higher than the simulated angle range (± 3 degrees) in each run, and the 3σ uncertainty value does not reflect the estimation error, as already discussed.

Although the Monte Carlo simulation displays the inaccuracy of the time-invariant solution when using measurements corrupted by time-varying bias, a single Monte Carlo simulation does not allow us to evaluate the time-invariant error as a function of the time-varying bias magnitude. Consequently, Section 6.2.6 shows a test whose methodology aims explicitly at quantifying the time-invariant calibration accuracy and errors depending on the conditions of the time-varying bias.

At last, we conclude the analysis by inspecting the magnetic field magnitude RMSE in each run. Figure 6.11 exhibits the graphical results of the RMSE versus each run and the histogram plot computed using all values. The numerical analysis of the data follows in Table 6.12, which shows the average RMSE value and the worst run data.

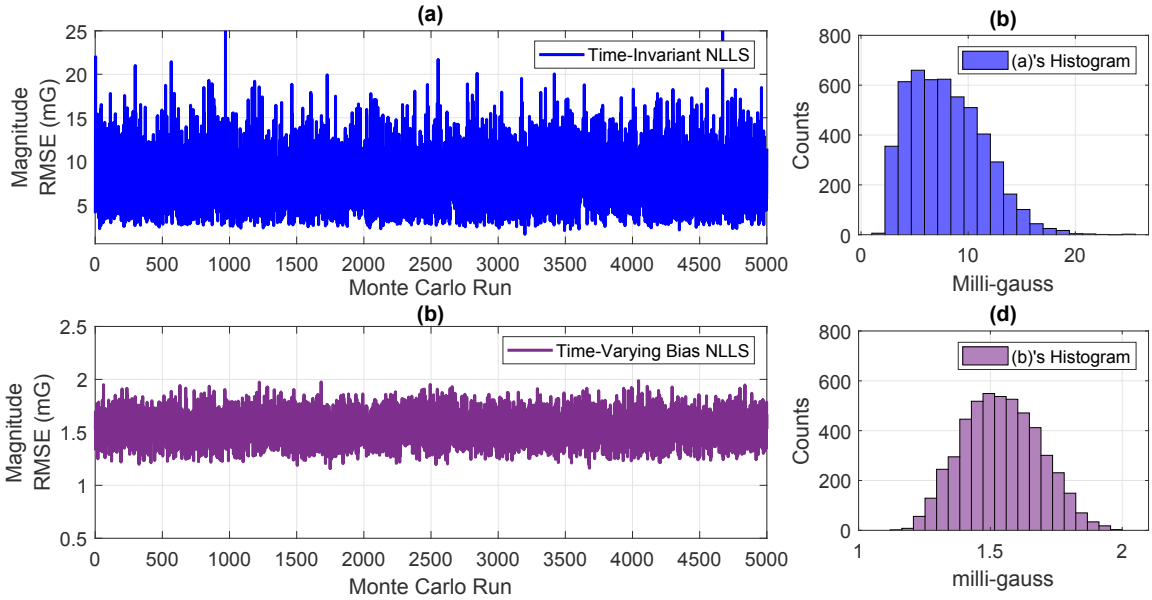

Figure 6.11: Magnitude RMSE in each run of the Monte Carlo simulation.

Table 6.12: Magnitude RMSE analysis for the Monte Carlo simulation with the time-varying bias.

Calibration Method	Average RMSE (mG)	Worst Run RMSE (mG)
Time-Invariant	7.98	25.57
Time-Varying Bias	1.54	1.99

The time-invariant solution data displays how the magnitude RMSE deteriorates due to the time-varying

bias interference, similar to the analysis of the parameters above. Furthermore, the histogram in Fig. 6.11(b) reveals that the RMSE data using the invariant NLLS does not have a Gaussian distribution. Although we do not investigate the matter formally, it is evident that the typical nine-parameters sensor model is inaccurate to the time-varying bias condition. Therefore, the resulting calibrated RMSE error in each Monte Carlo run is not dependent only on the noise of each simulated measurement. On the contrary, the solution using the complete model reduces the RMSE to the same magnitude of the time-invariant simulations in Chapter 5, and Fig. 6.11(d) shows that the RMSE, in that case, has the expected Gaussian distribution.

The Monte Carlo simulation analysis shows the effectiveness of the expanded sensor model and the NLLS solution with the time-varying bias in estimating the calibration parameters in such conditions. Also, it demonstrates that the time-invariant solution is inadequate and can have lousy estimation under conditions with time-varying interference. Besides, Section 6.2.6 establishes a methodology to better identify the calibrated magnetic field error depending on the time-varying bias characteristics and ranges.

6.2.4 Monte Carlo Simulation to Demonstrate the Standard Deviation of $\tilde{I}_i$ Measurements in the Error and Uncertainties Estimation

In the proposed NLLS algorithm with the time-varying biases, the uncertainties computation does not require any knowledge about the noise associated with each time-varying electrical current $\tilde{I}_i$. Hence, the values depend only on the $\mathbf{H}$ matrix values and the variance of the residual error ($\mathbf{e}$) calculated once the algorithm reaches the stopping criteria.

Consequently, for the sake of completeness, we perform three Monte Carlo simulations to understand and evaluate the outcome in the estimation and its uncertainties depending on the noise associated with the measurements of the time-varying currents $\tilde{I}_i$. Apart from the noise, every simulation aspect is identical to that reported in Section 6.2.3. Therefore, the time-varying bias has a magnitude randomized in each run and a probability of each measurement being corrupted by the time-varying error.

In the first case, we maintain the conditions of $\tilde{I}_1$ measurements reported in Section 6.2.3; hence, no noises are associated with them. However, in the second and third Monte Carlo simulations performed now, we add noise to each $\tilde{I}_1$ measurement, regardless of its state. As a result, these two simulations have noise with a standard deviation of 10 and 50 mA, respectively.

To compare the results for all three conditions, we display the error evolution per run of every parameter and the 3σ boundaries computed using the Cramér-Rao inequality. Unlike previous results, we exhibit the calculated uncertainty per run, not the average value. Hence, comparing the current measurement influence in the parameters and their uncertainties is easier. There are 36 graphics to depict that, 27 for the time-invariant parameters and 9 for the time-varying biases. They are shown separately by parameters, respectively, in Figs. 6.12-6.23. In each one, subplots (a), (b), and (c) display the results for $\tilde{I}_1$ measurements without noise, with a noise of 10 mA, and the last case with 50 mA, respectively.

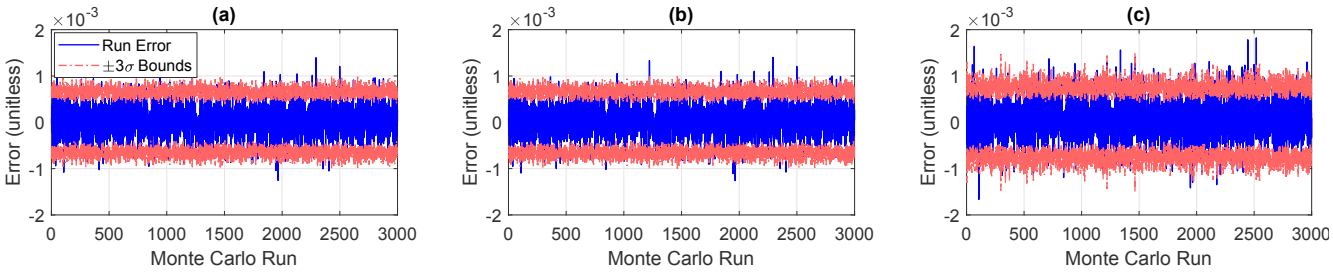

Figure 6.12: x-axis scale factor error and uncertainties results for the Monte Carlo simulation to evaluate the current measurement noise impact. (a) $\sigma_{\tilde{I}_1} = 0$ mA. (b) $\sigma_{\tilde{I}_1} = 10$ mA. (c) $\sigma_{\tilde{I}_1} = 50$ mA.

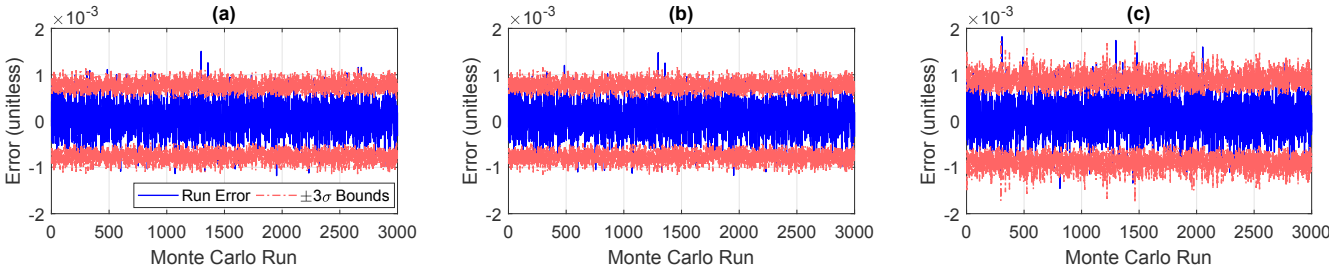

Figure 6.13: y-axis scale factor error and uncertainties results for the Monte Carlo simulation to evaluate the current measurement noise impact. (a) $\sigma_{\tilde{I}_1} = 0$ mA. (b) $\sigma_{\tilde{I}_1} = 10$ mA. (c) $\sigma_{\tilde{I}_1} = 50$ mA.

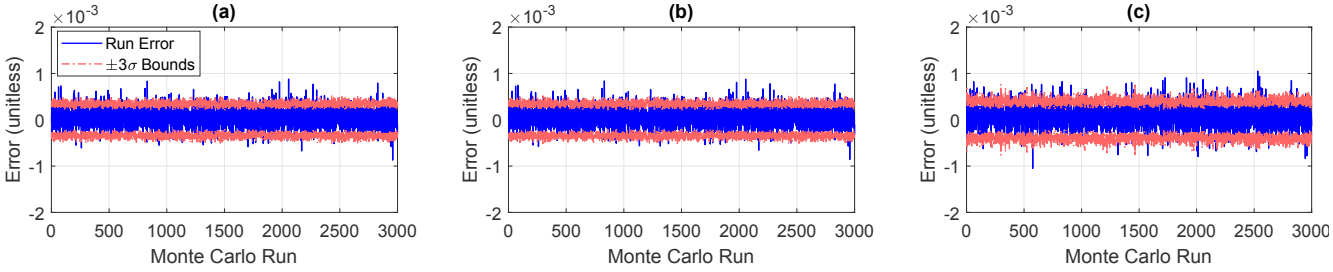

Figure 6.14: z-axis scale factor error and uncertainties results for the Monte Carlo simulation to evaluate the current measurement noise impact. (a) $\sigma_{\tilde{I}_1} = 0$ mA. (b) $\sigma_{\tilde{I}_1} = 10$ mA. (c) $\sigma_{\tilde{I}_1} = 50$ mA.

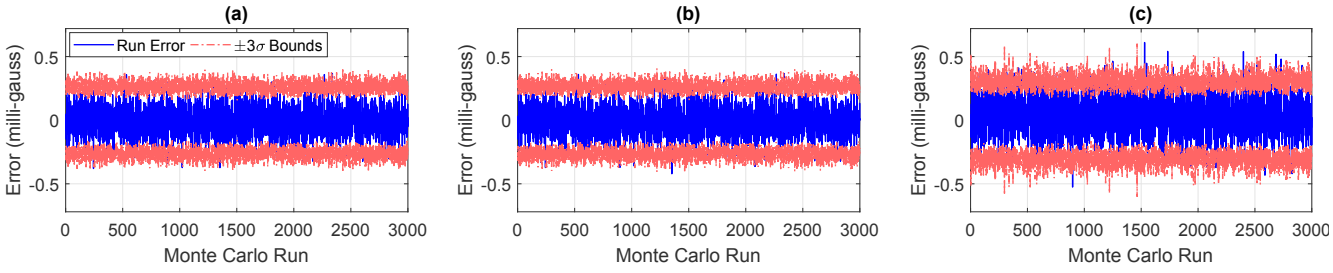

Figure 6.15: x-axis offset error and uncertainties results for the Monte Carlo simulation to evaluate the current measurement noise impact. (a) $\sigma_{\tilde{I}_1} = 0$ mA. (b) $\sigma_{\tilde{I}_1} = 10$ mA. (c) $\sigma_{\tilde{I}_1} = 50$ mA.

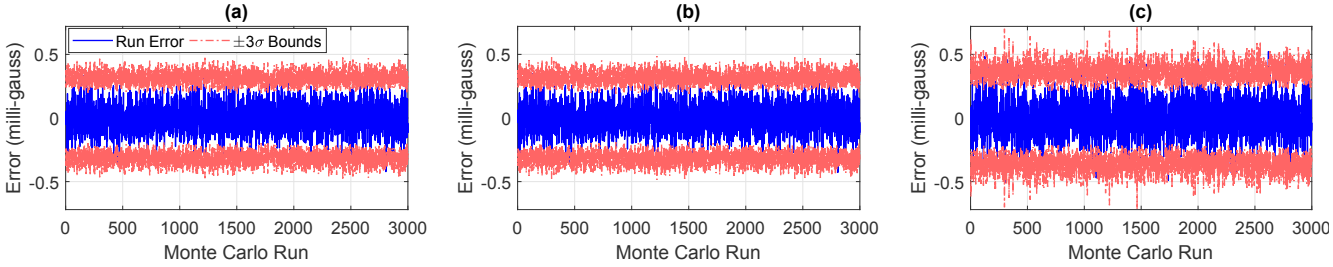

Figure 6.16: y-axis offset error and uncertainties results for the Monte Carlo simulation to evaluate the current measurement noise impact. (a) $\sigma_{\tilde{I}_1} = 0$ mA. (b) $\sigma_{\tilde{I}_1} = 10$ mA. (c) $\sigma_{\tilde{I}_1} = 50$ mA.

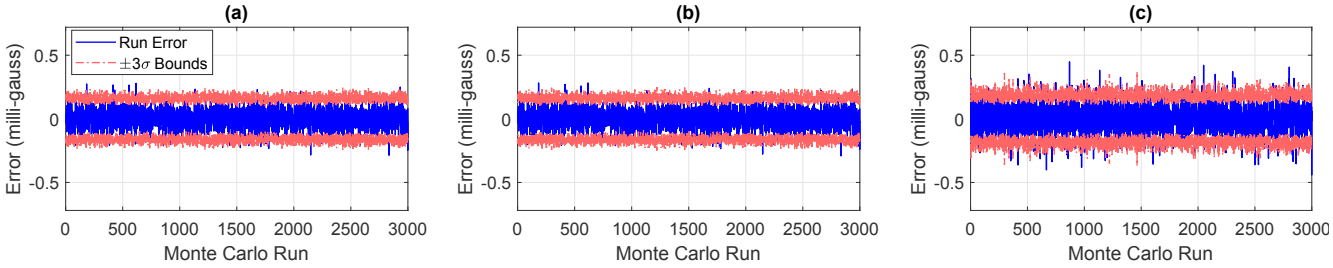

Figure 6.17: z-axis offset error and uncertainties results for the Monte Carlo simulation to evaluate the current measurement noise impact. (a) $\sigma_{\tilde{I}_1} = 0$ mA. (b) $\sigma_{\tilde{I}_1} = 10$ mA. (c) $\sigma_{\tilde{I}_1} = 50$ mA.

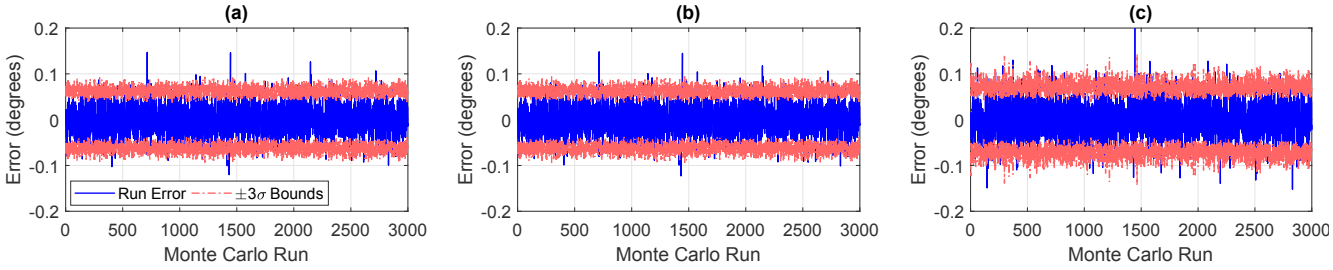

Figure 6.18: ρ misalignment angle error and uncertainties results for the Monte Carlo simulation to evaluate the current measurement noise impact. (a) $\sigma_{\tilde{I}_1} = 0$ mA. (b) $\sigma_{\tilde{I}_1} = 10$ mA. (c) $\sigma_{\tilde{I}_1} = 50$ mA.

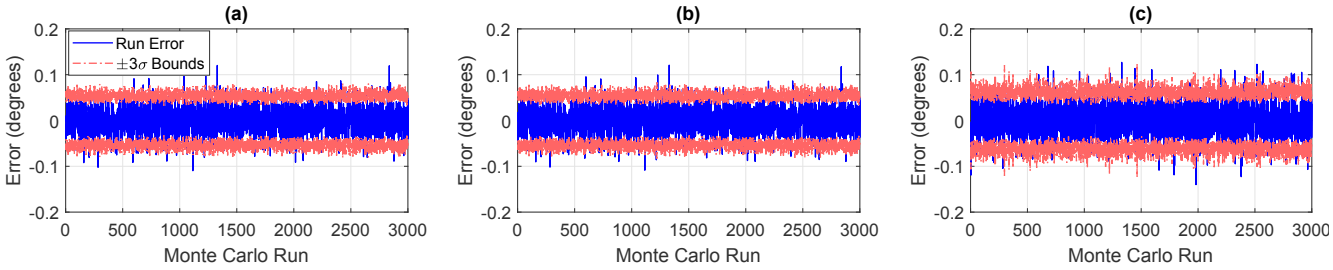

Figure 6.19: ϕ misalignment angle error and uncertainties results for the Monte Carlo simulation to evaluate the current measurement noise impact. (a) $\sigma_{\tilde{I}_1} = 0$ mA. (b) $\sigma_{\tilde{I}_1} = 10$ mA. (c) $\sigma_{\tilde{I}_1} = 50$ mA.

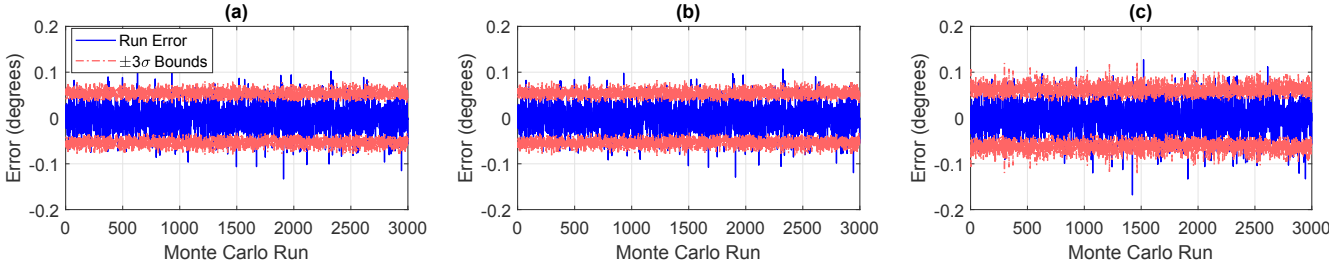

Figure 6.20: λ misalignment angle error and uncertainties results for the Monte Carlo simulation to evaluate the current measurement noise impact. (a) $\sigma_{\tilde{I}_1} = 0$ mA. (b) $\sigma_{\tilde{I}_1} = 10$ mA. (c) $\sigma_{\tilde{I}_1} = 50$ mA.

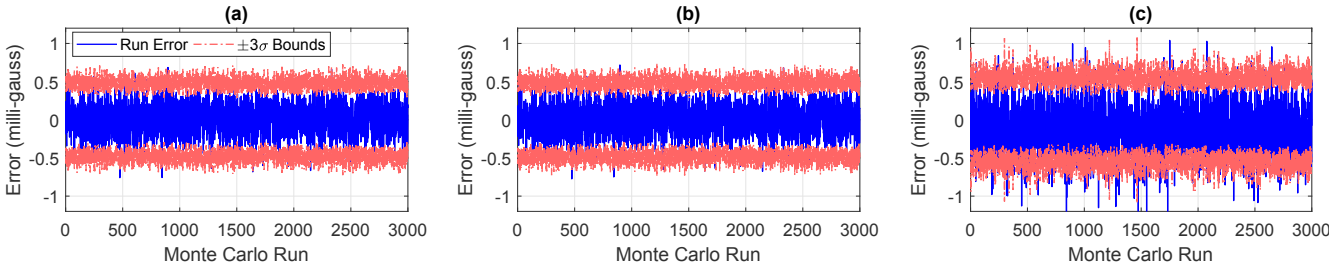

Figure 6.21: x-axis varying bias error and uncertainties results for the Monte Carlo simulation to evaluate the current measurement noise impact. (a) $\sigma_{\tilde{I}_1} = 0$ mA. (b) $\sigma_{\tilde{I}_1} = 10$ mA. (c) $\sigma_{\tilde{I}_1} = 50$ mA.

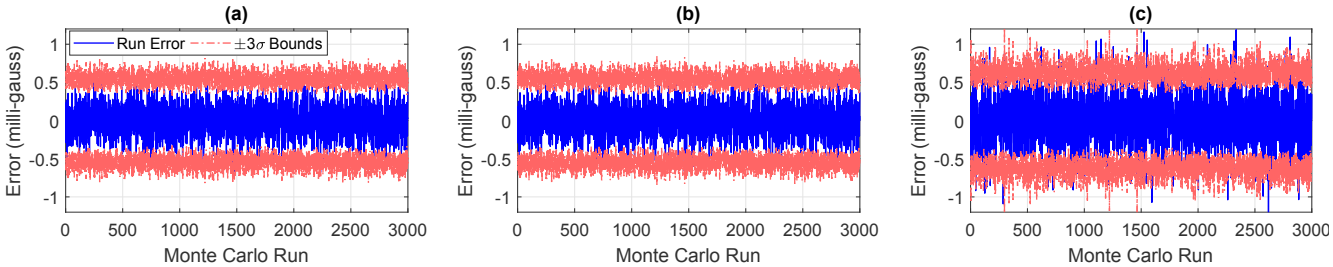

Figure 6.22: y-axis varying bias error and uncertainties results for the Monte Carlo simulation to evaluate the current measurement noise impact. (a) $\sigma_{\tilde{I}_1} = 0$ mA. (b) $\sigma_{\tilde{I}_1} = 10$ mA. (c) $\sigma_{\tilde{I}_1} = 50$ mA.

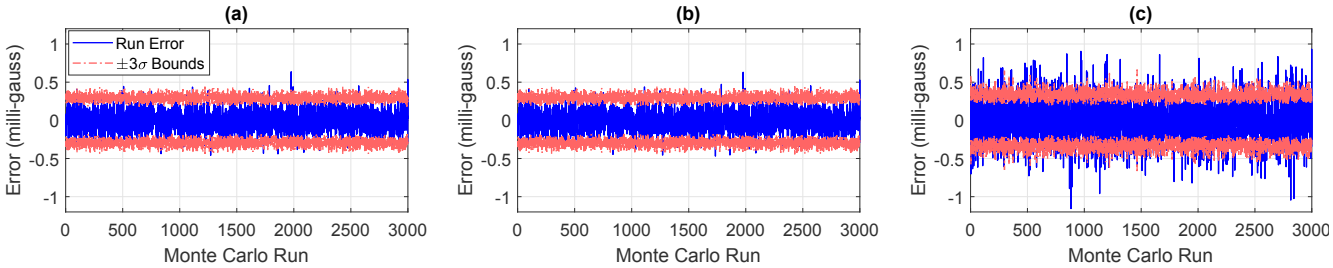

Figure 6.23: z-axis varying bias error and uncertainties results for the Monte Carlo simulation to evaluate the current measurement noise impact. (a) $\sigma_{\tilde{I}_1} = 0$ mA. (b) $\sigma_{\tilde{I}_1} = 10$ mA. (c) $\sigma_{\tilde{I}_1} = 50$ mA.

The results are not going to be assessed separately per parameters. Instead, we can make general comments about Figs. 6.12-6.23 as their behavior is similar as a function of the associated noise. Overall, we can see that in every parameter, the results for no noise, seen in subplots (a), and that with a standard deviation of 10 mA in the current measurements $\tilde{I}_1$, seen in subplots (b) are almost identical. Graphically, there are very few barely observable differences.

The differences are more notable for the last simulation, where $\tilde{I}_1$ has a noise with a standard deviation

of 50 mA. In this case, the parameter errors and their uncertainties are slightly worse; nevertheless, they are in the same order of magnitude, which indicates that the overall impact in the estimation is minimal despite using a Gaussian noise with a significant standard deviation value.

For instance, even the second simulation, with $\tilde{I}_1 = 10$ mA, is already a poor noise if we take typical current sensing electronics. For example, in the RAX-1 satellite [99], Springmann and Cutler [7] reported that their current sensing instrumentation had a standard deviation noise of 5 mA. In addition, with the current technology, one can assume that a few milliamperes, such as the value used in the second simulation or lower, are compatible with the expected in experimental systems and applications. Thus, not only the last case has barely affected the estimation, as it simulated a noise value somewhat unreasonable compared to what could be observed in experimental systems.

On the contrary, the second simulation established that the noise associated with $\tilde{I}_1$ barely affected the estimation outcome compared to the simulation without any noise. Therefore, these results corroborate the uncertainties extracted by the Fisher Information matrix, and the time-varying NLLS reasonably estimates the parameters' uncertainties.

At last, as discussed in Section 6.1, we must bare in mind that the uncertainties values calculated using the Cramér-Rao inequality (or the Fisher information Matrix) are optimistic and provide a lower bound of the state covariance, not its actual covariance. Hence, they do not reflect the actual error but serve as an indication of the estimation quality, which provides insight into the accuracy of the parameters and the eventual identification of a poor spatial distribution of a specific set of measurements.

6.2.5 Convergence of the Time-Varying Bias Algorithm and Number of Iterations Analysis

Although expanding the initial estimate algorithm to include the time-varying bias parameters is possible, as discussed in the theoretical section, Appendix A.3 shows that the solution is only effective if the time-varying bias magnitude has a relatively high value. Consequently, evaluating the solution convergence and establishing an approximate boundary where the convergence problems may arise due to the bias magnitude is essential. We also use the test to assess the number of iterations and average processing time of the NLLS algorithm with time-varying parameters.

To perform this test, we run a few Monte Carlo simulations in different conditions of the time-varying bias. Each simulation has 5000 runs and a methodology similar to that reported in Section 6.2.3. The scale factors, misalignment angles, and the expected magnitude value are randomly selected using a uniform distribution with values identical to those seen in Table 6.9. However, we vary the time-invariant offset range and the time-varying bias magnitude value between simulations. The remainder of the methodology is identical to the Monte Carlo test reported above. Besides, no noises are associated with $\tilde{I}_1$, since Section 6.2.4 demonstrated it has a minor impact on the estimation.

The results are summarized for eight cases, and Table 6.13 depicts the conditions (offset and varying bias range) in each one. The selected instances describe four different ranges of the time-varying bias magnitude, and for each of these, there are two cases with distinct values of the distribution range for the time-invariant offset parameters. Furthermore, Table 6.13 also reports the results in all eight scenarios.

Table 6.13: Conditions and results of the Monte Carlo simulation to assess the time-varying bias NLLS algorithm convergence and number of iterations.

Case	Offset and Varying Bias Range Values		No. of Runs	Data Results						
	x_0, y_0, z_0 (mG)	$\|b_1\|$ (mG)		No. of Converg.	Number of Iterations[1]					Avg. Time (ms)[1]
					n=3	n=4	n=5	n=6	n>6	
1	± 50	$50-100$	5000	5000	39	4938	23	0	0	0.0012
2	± 500	$50-100$	5000	5000	48	4942	10	0	0	0.0013
3	± 50	$100-150$	5000	5000	0	4027	950	23	0	0.0015
4	± 500	$100-150$	5000	5000	0	3995	987	18	0	0.0015
5	± 50	$150-200$	5000	5000	0	1526	3020	398	54	0.0017
6	± 500	$150-200$	5000	5000	0	1570	3023	348	59	0.0018
7	± 50	$200-250$	5000	4878	0	68	1718	1736	1356	0.0024
8	± 500	$200-250$	5000	4873	0	77	1675	1689	1432	0.0024

[1] The number of iterations and the average processing time only consider the runs with a convergence outcome.

The outcome of the simulations shows that using the initial estimate of the scale factor and offset, using the algorithm reported Section 5.4.3, is accurate in most of the time-varying scenarios. Convergence problems appeared only during the seventh and eighth cases, whose time-varying bias magnitude ranges from 200 to 250 milligauss. However, these time-varying bias magnitudes values are exceptionally high and unlikely to occur in a typical application.

For instance, most time-varying bias authors report interference considerably smaller than those, ranging from a few [11] to a few dozens of milligauss [7,8,13]. Therefore, in conditions likely to occur in an experimental situation, the time-varying bias NLLS would have no convergence problems using an accurate initial estimate of time-invariant offsets and scale factors.

Nevertheless, if a magnetometer is susceptible to a time-varying bias with such a magnitude (> 200 mG, or 20 μT), a possible alternative would be to use an initial algorithm expanded to include the time-varying bias, such as seen in Appendix A.3. Another option would be to experimentally define an initial estimate of these parameters [8]; since the time-varying bias is attitude-independent, measurements with varying currents in distinctive states in any attitude would be sufficient to define an approximate estimate.

Another observation from the tests is that the time-invariant offset range value barely affects (if it impacts) the Monte Carlo simulation results. For example, cases 1 and 2, 3 and 4, and so on, are similar to their respective pair in every aspect regarding the number of iterations and the average processing time. At last, we see that the time-varying bias impacts the number of iterations and, consequently, the processing time of the algorithm. Nevertheless, for values of time-varying bias with magnitudes inferior to 100 milligauss, most runs reached convergence within the fourth loop, an average of a single extra loop compared to the time-invariant solution, approximately (see Table 5.18).

6.2.6 Characterization of the Time-Varying Bias effect in the Time-Invariant Calibration

The time-varying bias magnitude impact in the typical time-invariant calibration is assessed using a new set of Monte Carlo simulations with different conditions of the time-varying bias. Thus, the test allows us to put

the errors into perspective depending on the time-varying bias conditions and to identify the RMSE order of magnitude for different scenarios of the time-varying bias error. Besides, Section 6.3.5 complements the current one with an experimental test that examines the magnetic field magnitude error versus each measurement.

Furthermore, the Monte Carlo validation in Section 6.2.3 has shown (Fig. 6.11) that the time-invariant calibration RMSE per run distribution does not follow a Gaussian distribution, which indicates the dependency of the error in the overall conditions of the calibration parameters. Hence, addressing every possible condition here is not viable. Instead, we suggest future works to define a methodology to examine the time-varying bias effect in attitude determination systems, *i.e.*, the attitude error versus the conditions of varying interference.

Here, we report two separate sets of tests. The first test assesses six cases, each with a different time-varying bias magnitude. However, the probability of the time-varying electrical current being one ($\tilde{I}_1 = 1$) is constant throughout them. The remainder of the simulation conditions follows the methodology in Section 6.2.3, the parameters distribution values reported in Table 6.9, and the probability of a measurement being corrupted by the time-varying bias is always 50%, $P(\tilde{I}_1 == \text{On}) = 50\%$. The simulated time-varying bias magnitude for each case is 2, 5, 10, 15, 25, and 50 mG, respectively.

Figure 6.24 shows the RMSE results of the test using the time-invariant and the time-varying solution. The first case, subject to a time-varying bias with 2 mG of magnitude, reveals a minor impact in the RMSE in most runs using the typical invariant sensor model. However, increasing that magnitude to 5 mG already significantly impacts the RMSE, evidenced by the result in Fig. 6.24(b). Beyond that value, it is notable that the impact on the RMSE of the calibrated data is significant when using the time-invariant sensor model. For example, in the worst simulated scenario, with $|B_1| = 50$ mG, we have an RMSE that visually varies from 10 to 20 mG in most runs, reaching a peak superior to 25 mG. Therefore, it is noticeable that time-varying bias with magnitude compatible with those reported in small satellites works [7, 8, 10, 13] have a significant impact on the calibrated measurements if one assumes a time-invariant sensor model.

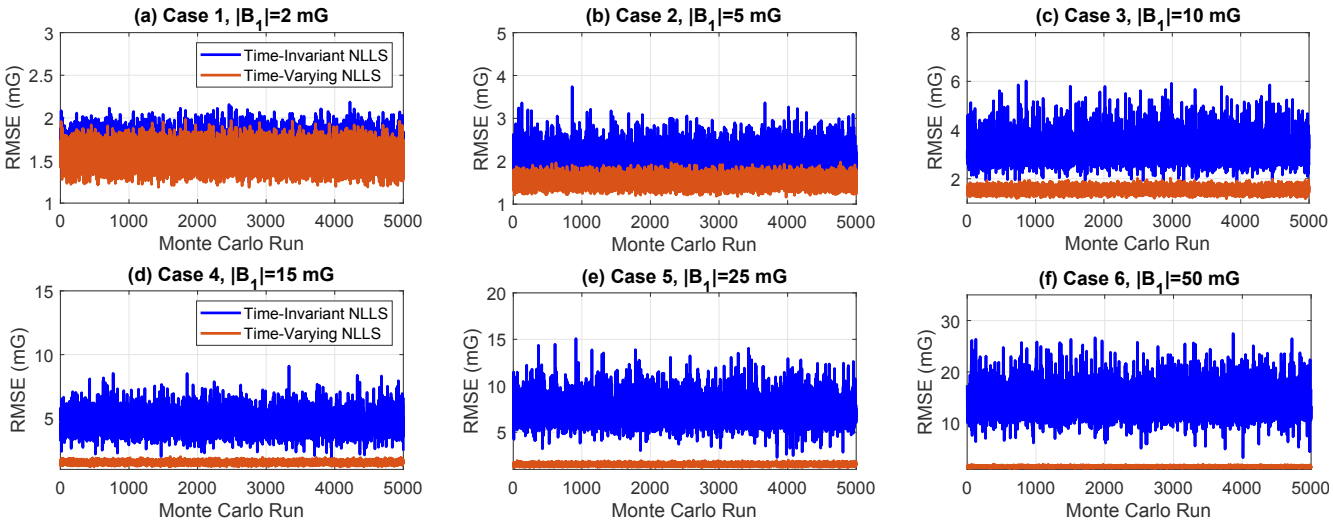

Figure 6.24: Magnitude RMSE obtained in the Monte Carlo simulation for six distinct values of the time-varying bias magnitude value. (a) $|B_1| = 2$ mG. (b) $|B_1| = 5$ mG. (c) $|B_1| = 10$ mG. (d) $|B_1| = 15$ mG. (e) $|B_1| = 25$ mG. (f) $|B_1| = 50$ mG.

On the contrary, the RMSE magnitude ranges when employing the time-varying bias calibration model has a similar outcome regardless of the conditions of the time-varying bias magnitude. Table 6.14 shows the numerical data of the RMSE for a more conclusive examination. It includes, per case and for both algorithms, the average RMSE value computed using all runs data, its standard deviation value, and the worst run data.

Table 6.14: Magnitude error analysis of the results, seen in Fig. 6.24, for cases 1 to 6.

Case	Time-Invariant NLLS			Time-Varying Bias NLLS			Unit
	Mean RMSE	RMSE SD	Worst Run	Mean RMSE	RMSE SD	Worst Run	
1 - $\|B_1\| = 2$ mG	1.646	0.162	2.196	1.538	0.148	1.982	mG
2 - $\|B_1\| = 5$ mG	2.108	0.272	3.740	1.537	0.149	1.983	mG
3 - $\|B_1\| = 10$ mG	3.264	0.569	6.017	1.539	0.147	2.027	mG
4 - $\|B_1\| = 15$ mG	4.560	0.854	9.106	1.538	0.147	2.016	mG
5 - $\|B_1\| = 25$ mG	7.307	1.479	15.078	1.539	0.149	2.007	mG
6 - $\|B_1\| = 50$ mG	14.271	2.924	27.476	1.539	0.148	2.009	mG

First, Table 6.14 corroborates that the time-varying NLLS solution yields similar results regardless of the case. The data displays that the average value of the RMSE is approximately 1.54 mG for all cases, the standard deviation is about 0.15 mG, and the worst run is roughly 2 mG. Hence, it verifies that the solution is adequate and that the outcome does not depend on the distribution and values of the parameters.

On the contrary, the numerical data evidence the estimation process accuracy declining for higher magnitude values when using the algorithm without the time-varying bias compensation. In the second case, with 5 mG of varying bias magnitude, we can see that the average RMSE is almost 40% higher than the other solution, and the worst run RMSE increases to 3.74 mG. Beyond that, the average RMSE is approximately 210%, 300%, 475%, and 925% higher than the counterpart estimation with the varying bias element, respectively, for $|B_1| = 10$, 15, 25, and 50 mG.

Therefore, the first test results demonstrate that the time-varying bias observed in a few nanosatellites [7, 8, 10, 13] can significantly impact the calibrated magnitude if the model does not account for time-varying bias due to the varying electrical currents. Consequently, they exhibit the importance of developing a methodology to evaluate the effect of time-varying electrical currents in small satellite missions and other applications where the magnetometer might sense such interference.

Next, in the second test, we performed six more Monte Carlo simulations with a similar methodology to those reported above. However, instead of modifying the bias magnitude, the altering variable between each case is the chance of a measurement being corrupted by the time-varying bias. Hence, during this test, we set a constant $|B_1|$ value of 10 milligauss, and the probability in each measurement sensing interference from the time-varying current is 5, 10, 25, 50, 75, and 90%, respectively.

Figure 6.25 and Table 6.15 exhibit the results per case. The former shows the RMSE graphical data of the magnitude per run of the Monte Carlo simulation, and the latter depicts the numerical data analysis, including the average RMSE, the RMSE standard deviation, and the worst run values.

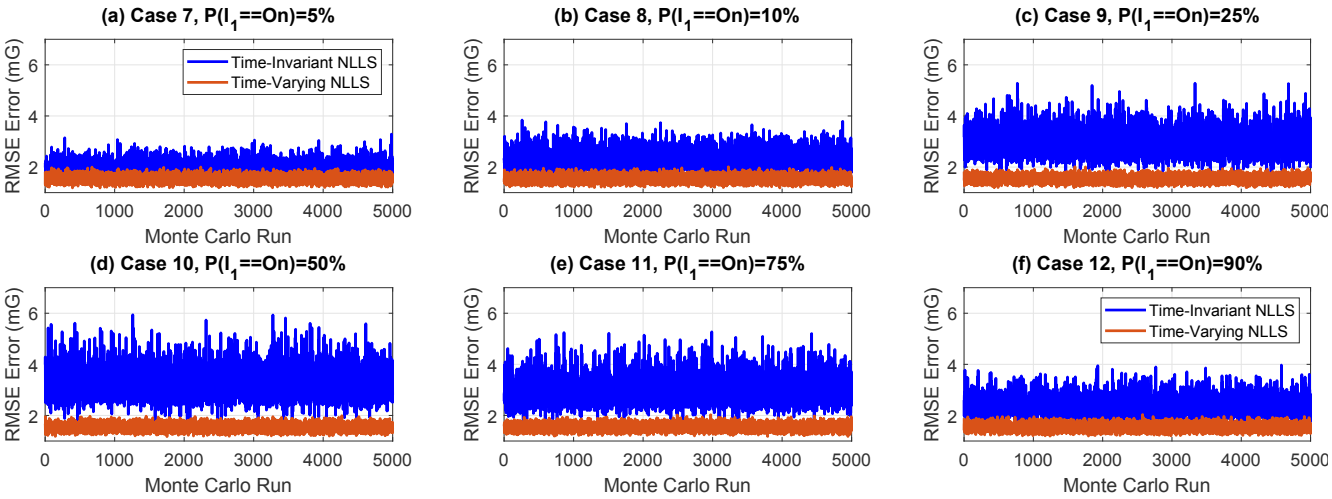

Figure 6.25: Magnitude RMSE obtained in the Monte Carlo simulation for six distinct values of the probability of each measurement being subject to the time-varying current. (a) 5% chance. (b) 10% chance. (c) 25% chance. (d) 50% chance. (e) 75% chance. (f) 90% chance.

Table 6.15: Magnitude error analysis of the results, seen in Fig. 6.25, for cases 7 to 12.

Case	Time-Invariant NLLS			Time-Varying Bias NLLS			Unit
	Mean RMSE	RMSE SD	Worst Run	Mean RMSE	RMSE SD	Worst Run	
7 - 5%	1.985	0.247	3.299	1.538	0.145	2.002	mG
8 - 10%	2.310	0.330	3.840	1.541	0.144	2.010	mG
9 - 25%	2.915	0.482	5.920	1.537	0.149	1.984	mG
10 - 50%	3.253	0.564	5.940	1.539	0.148	1.990	mG
11 - 75%	2.952	0.494	5.272	1.539	0.147	2.028	mG
12 - 90%	2.364	0.347	3.973	1.538	0.148	2.035	mG

Once more, the calibrated data using the time-varying bias solution RMSE perform independently of the case. The numerical results are similar to all previous Monte Carlo simulations, and the mean RMSE value was roughly 1.54 for cases 7 to 12, as the other six simulations with different magnitude values. Oppositely, the outcome when employing the time-invariant sensor model was affected by the probability of each measurement being corrupted by the time-varying bias.

The analysis of the graphical data in Fig. 6.25 and the numerical data in Table 6.15 depict that the worst case happens when the time-varying bias influences half of the measurements. Nevertheless, even for lower probability values (5-10%), the RMSE values of the magnitude are significantly impacted compared to the time-varying bias solution. Moreover, it is logical that the worst-case scenario happens with a 50% probability. For instance, if an electrical current corrupted all measurements, it would become a systematic error (a constant offset) and not a time-varying bias. Thus, the RMSE should increase between 0-50% and decreases in the same ratio beyond that until 100%, which is compatible with the test results.

At last, we reiterate that this analysis put the RMSE of the magnetic field magnitude values into perspective for distinct conditions and is complemented in Section 6.3.5, which addresses the time-varying bias using experimental data and the magnetic field simulator and investigates the same conditions simulated here. Nevertheless, it is suggested that future authors thoroughly examine the impact of time-varying bias in typical attitude determination systems.

6.3 Experimental Time-Varying Bias Calibration Methodology and Analysis using the Magnetic Field Simulator

This section describes the proposed setup and methodology to evaluate magnetic sensor calibration, including time-varying bias. It also demonstrates and assesses the experimental calibration using the magnetic field simulator and the proposed methodology.

First, Section 6.3.1 shows the proposed HiL setup, the supporting electronics for the experimental time-varying study, and the testing methodology to have a generic environment to simulate, test, and evaluate a time-varying bias for any application or system. It also defines the procedure for using the open-loop magnetic field simulator to evaluate sensors subject to time-varying interference. Next, Section 6.3.2 describes the specific setup used in this thesis to demonstrate the experimental calibration utilizing the platform and the HMC5883L magnetometer.

The succeeding subsections show the experimental tests and results, following similar conditions to those simulated during Section 6.2 analysis. Hence, Section 6.3.3 demonstrates and compares the time-varying bias calibration to the time-invariant procedure. Section 6.3.4 displays an experimental test for two time-varying electrical currents. At last, Section 6.3.5 depicts the calibration of the time-invariant and the time-varying bias models for different conditions of the time-varying bias magnitude and probability.

6.3.1 The HiL Setup and Test Methodology to Evaluate the Time-Varying Bias

As stated in the chapter's introduction, our goal is not only to evaluate the time-varying bias experimentally but to develop a Hardware-in-the-Loop (HiL) simulation that can be employed as a platform in the study of the magnetometer calibration subject to any conditions of time-varying interference. Hence, the platform can be used to reproduce several environments expected in a magnetic sensor operation and, more importantly, act as a tool in evaluating several systems under test.

In conjunction with the magnetic field generation, the proposed platform must be able to provide the auxiliary signals and electronics required to test a SUT under the desired time-varying interference conditions. Therefore, it is necessary to improve the magnetic field simulator compared to the elements described in Chapter 2. To achieve that, we have designed a HiL setup with one or more auxiliaries microcontrollers responsible for controlling the additional electronics required to evaluate the time-varying bias experimentally. In addition, a serial interface connects these new microcontrollers to the dSPACE modular hardware, allowing the Simulink model to control the auxiliary devices and its environment.

Figure 6.26 shows the diagram of the proposed time-varying interference test platform. The auxiliary (supporting) electronics may have one or more microcontrollers that manage the additional interfaces to provide the test bench environment of the time-varying bias. Therefore, these microcontrollers handle the digital and analog signals that generate the time-varying electrical currents or interference and interface with the current sensing circuits and instrumentations. The auxiliary electrical currents may be analog (provided by voltage-controlled current sources) or have an on/off state (utilizing relays). Besides, high-power rheostats are used to tune a time-varying current magnitude.

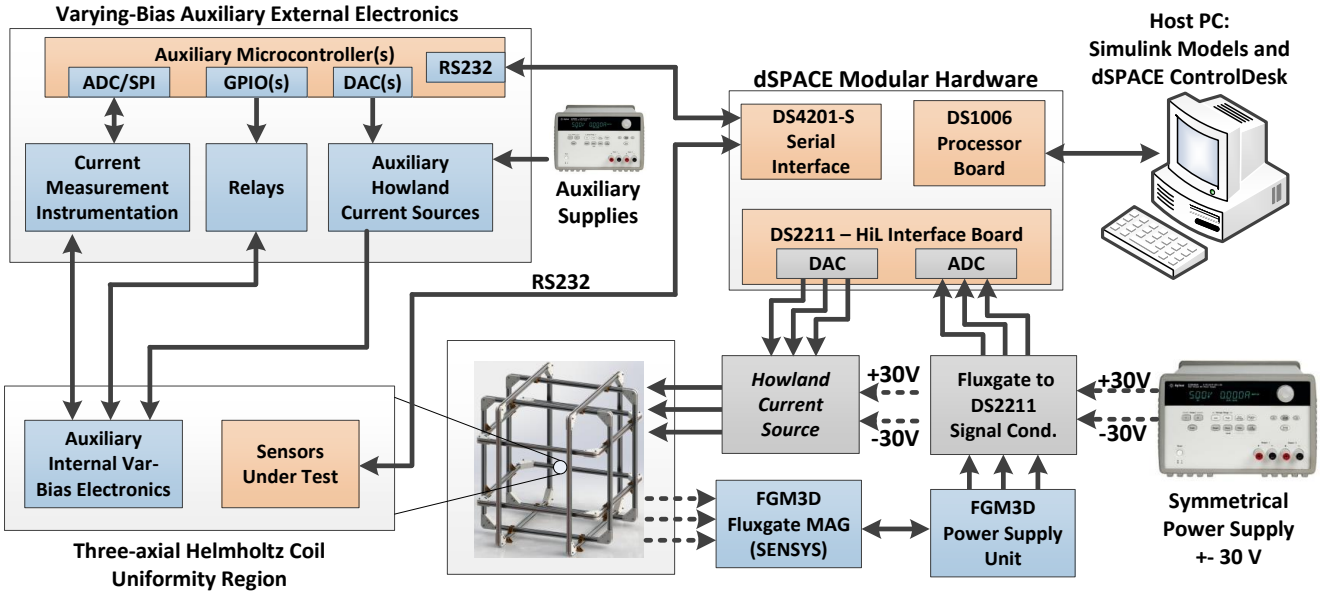

Figure 6.26: Proposed HiL platform with auxiliary electronics to perform experimental tests with time-varying interference and electrical currents.

It is essential to observe that platform can be used in multiple ways. For instance, let us assume that the SUT is a fully built nanosatellite with its own current measurement electronics. Then, the setup can use the auxiliary voltage-controlled current sources to generate an electrical current through a wire, or a PCB, simulating the electrical currents of a solar panel, for example. It is also possible to use the setup in much more generic conditions. In another example, the SUT could be responsible only for the magnetometer readings, and the auxiliary electronics would generate the varying interference and measure the current values. Furthermore, relays could simulate other electronics' state, for instance.

Now that the platform hardware has been explained, it is necessary to establish the experimental methodology of the testing. The magnetic field simulator must generate the magnetic field using the open-loop (non-compensated) topology. Consequently, it is necessary to calibrate the system before the experimental tests with the magnetometers.

Figure 6.27 summarizes the procedure to test the time-varying bias calibration. First, the system calibrates and validates the open-loop magnetic field generation approach described in Chapter 4. During that calibration, only the fluxgate sensor should be inside the coil. Next, the SUT is placed within the uniform magnetic field region, and maintaining the fluxgate sensor is optional. Removing the fluxgate sensor is only required if the SUT needs the entire uniformity region volume of the generated field. Then the setup generates the open-loop calibrated field and controls the auxiliary electronics and signals responsible for the varying electrical currents.

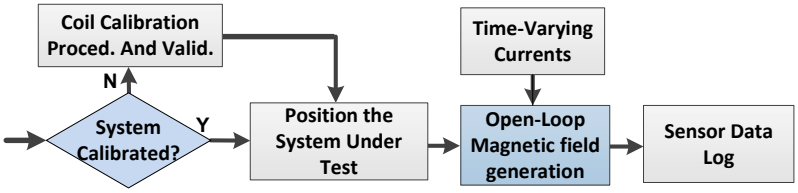

Figure 6.27: Simplified diagram of the procedure to perform tests with time-varying interference.

6.3.2 The HiL Setup used to Demonstrate the Experimental Calibration

To demonstrate the calibration, we use a setup with one auxiliary microcontroller to generate up to two controlled electrical currents that cause time-varying biases errors in the HMC5883L sensor. Each current flows through two distinct PCBs installed close to the HMC5883L sensor. The first current is either on or off and is controlled by one of the relays in the platform. The other is an analog current that can go up to 1.30 A and is generated by an auxiliary HCS circuit. In addition, an INA219-based current sense circuit measures this second current generated by the additional HCS. The dSPACE HiL simulation sends the commands to the microcontroller, which controls the relay's state and the DAC output voltage value. In turn, the microcontroller sends the electrical current measurements value to the dSPACE at the same rate that the SUT samples the magnetometers.

During this process, the dSPACE generates the time-varying signals that control the relay state and the DAC value and sends them to the auxiliary microcontroller. In addition, it generates a magnetic field identical to that used in the experimental tests reported in Chapter 5. To facilitate, Fig. 6.28(a) shows, once more, the theoretical magnetic field programmed at the HiL simulation and used in all experiments reported next. Again, there are 576 distinct points in Fig. 6.28(a) waveform, represented in the vector components plot seen in (b). For each point, eight valid magnetometer measurements are obtained by the HMC5883L sensor.

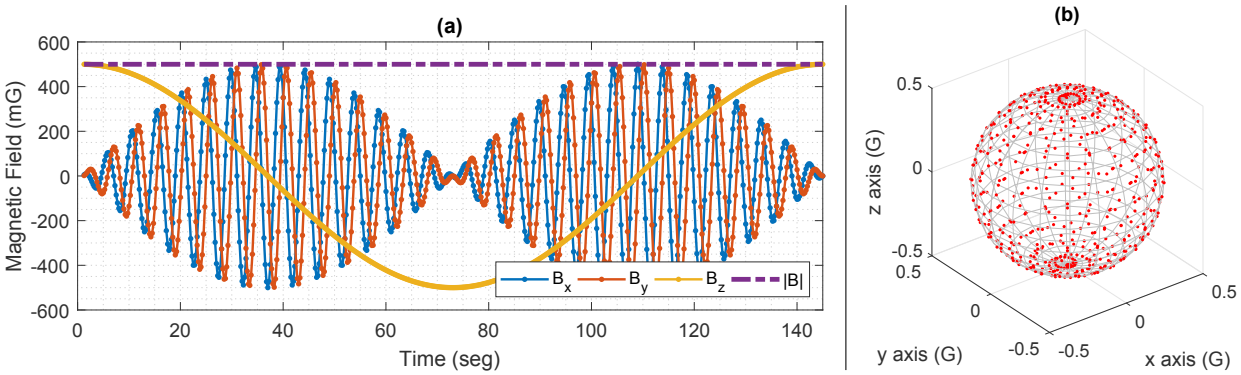

Figure 6.28: Magnetic field input for the first time-varying bias experimental test. (a) Vector components versus time. (b) Vector components plot in three dimensions.

6.3.3 Demonstration of the Experimental Time-Varying Bias Calibration and Comparison with the Time-Invariant Procedure

This experimental test has a similar methodology and objectives to the simulation reported in Section 6.2.1. Hence, it seeks to validate the experimental time-invariant sensor calibration with the open-loop methodology and also works as a benchmark result for the subsequent experimental analysis with the time-varying bias.

Therefore, we generate the magnetic field of Fig. 6.28 twice. During the first procedure, there are no time-varying currents. In the second, the dSPACE generates an analog electrical current value using the auxiliary HCS. Figure 6.29 shows the uncalibrated results of the test and the time-varying electrical current in both procedures, respectively, in Figs 6.29(a) and (b). The third subplot, in Fig 6.29(c), depicts the difference between the uncalibrated magnitude measured by the HMC5883L in both cases, similarly to the analysis simulated in Section 6.2.1.

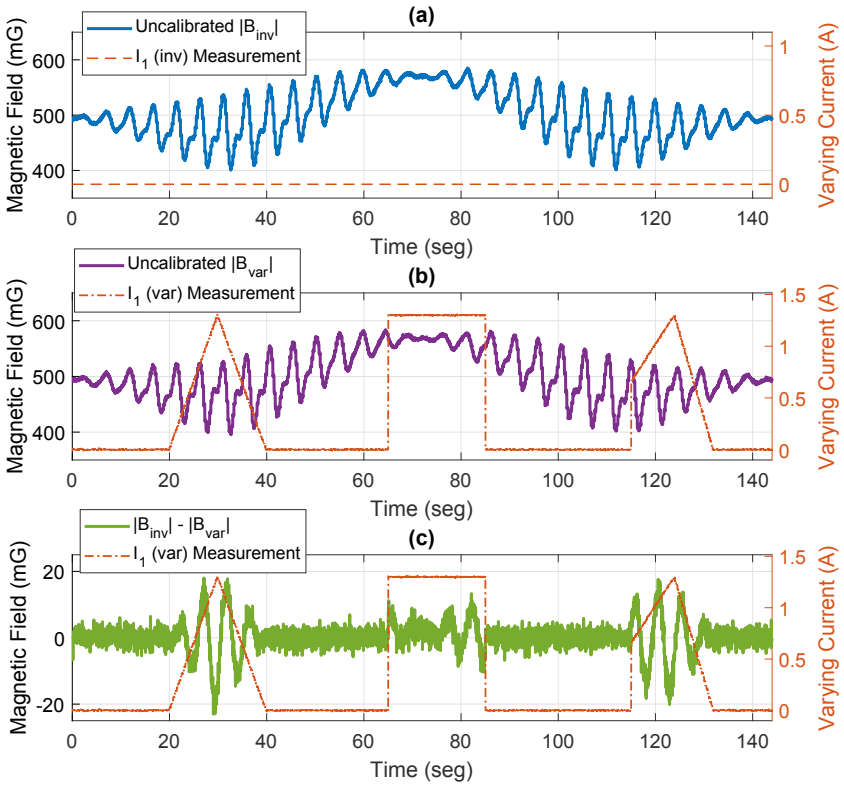

Figure 6.29: Magnitude measurements of the HMC5883L sensor in the first time-varying bias test. (a) Time-invariant sensor model data. (b) Time-varying bias sensor model data. (c) Difference between the time-varying and the time-invariant dataset.

The magnitude results reveal that the HMC5883L data diverges considerably from the expected 500 mG expected value regardless of the time-varying bias. Besides, Fig. 6.29(a) and Fig. 6.29(b) uncalibrated data are almost identical. Nonetheless, Fig. 6.29(c) clearly shows that the magnitude measurements differ during the periods with the time-varying current. In the remainder of the periods, it oscillates around zero, indicating that the difference between both tests is related to the sensor measurement noise. These results also comply with the observations of Section 6.2.1.

Using the first test measurements (without the varying electrical current), we apply the time-invariant NLLS algorithm in the HMC5883L data. Table 6.16 reports the parameters computed and the calibration uncertainties results. Next, we apply the NLLS solution for both models for the HMC5883L data collected during the second procedure. Table 6.17 displays their calibration parameters and their uncertainties.

Table 6.16: Calibration parameters results for the time-invariant data seen in Fig. 6.29(a).

	Invariant Calib. Model			
Param.	**NLLS** $\mathbf{p_0}$	**NLLS** $\mathbf{p}$	**NLLS** $\mathbf{3\sigma}$	**Unit**
a	0.9947	0.9938	3.59E-4	unitless
b	0.8865	0.8859	3.20E-4	unitless
c	1.0607	1.0607	2.31E-4	unitless
x_0	-47.78	-47.77	0.124	mG
y_0	-19.19	-19.20	0.110	mG
z_0	36.68	36.69	0.094	mG
ρ	-	-2.960	0.033	degrees
ϕ	-	-0.627	0.028	degrees
λ	-	-0.331	0.028	degrees

See Table 6.2 for nomenclature.

Table 6.17: Calibration parameters results for the time-varying data seen in Fig. 6.29(b), using the time-invariant NLLS solution and the one with the time-varying bias parameters.

Param.	NLLS $\mathbf{p_0}$	Time-Invariant Calib. Model		Time-Varying Calib. Model		Unit
		NLLS $\mathbf{p}$	NLLS $\mathbf{3\sigma}$	NLLS $\mathbf{p}$	NLLS $\mathbf{3\sigma}$	
a	0.9959	0.9948	9.50E-4	0.9933	3.73E-4	unitless
b	0.8876	0.8869	8.47E-4	0.8855	3.32E-4	unitless
c	1.0589	1.0590	6.08E-4	1.0613	2.99E-4	unitless
x_0	-44.85	-44.90	0.328	-47.65	0.155	mG
y_0	-23.48	-23.28	0.293	-19.25	0.138	mG
z_0	36.34	36.36	0.248	37.08	0.130	mG
ρ	-	-3.034	0.087	-2.958	0.033	degrees
ϕ	-	-0.974	0.075	-0.664	0.031	degrees
λ	-	0.226	0.076	-0.274	0.031	degrees
x_1	-	-	-	8.576	0.299	mG/A
y_1	-	-	-	-12.570	0.263	mG/A
z_1	-	-	-	-1.800	0.214	mG/A

First, we can compare the time-invariant NLLS algorithm applied in both data. The uncertainties obtained using that solution in the second test indicate that the data is far less trustworthy than the first result, as they have increased by approximately 300% for every parameter. Also, there are significant differences in the estimates of the parameters. For example, the y_0 value difference is around 4 mG, and the misalignment angle ϕ estimate went from -0.627 to -0.974 degrees.

On the contrary, the estimates using the sensor model with time-varying bias in the second procedure are much closer to those obtained in the time-invariant test. Moreover, the values of the uncertainties are also in the same order of magnitude, with only slightly worse values, which is expected if we consider that there are errors and noise in the current measurements of $\tilde{I}_1$. Besides, we see that the initial state algorithm estimates of the offsets and scale factors in Table 6.17 are compatible with the time-invariant one in Table 6.16. More importantly, these results are consistent with the simulations performed in Section 6.2.1; thus, they display the efficacy of the experimental procedure.

At last, it is notable that the differences in every parameter for both solutions in Table 6.17 are greater than the computed uncertainties. Therefore, it implies that the 3σ boundaries of the time-invariant solution applied in the time-varying data did not reflect the actual error. Consequently, it confirms that the uncertainties indicate the quality of the estimation; however, if the sensor model is not adequate, it will not reflect the actual error. That was also observed in the simulations and is a reasonable conclusion by inspecting the experimental data.

Next, we proceed with the calibrated magnetic field magnitude analysis, depicted in Fig. 6.29. Subplot (a) shows the results for the time-invariant test, (b) the calibration using the time-invariant sensor model during the time-varying procedure, and (c) the solution with the time-varying bias. In addition, Table 6.18 displays the numerical data analysis of the calibrated magnitude data and its error, calculated using the calibrated data minus the expected value of 500 mG. Table 6.18 also includes the uncalibrated results reported above.

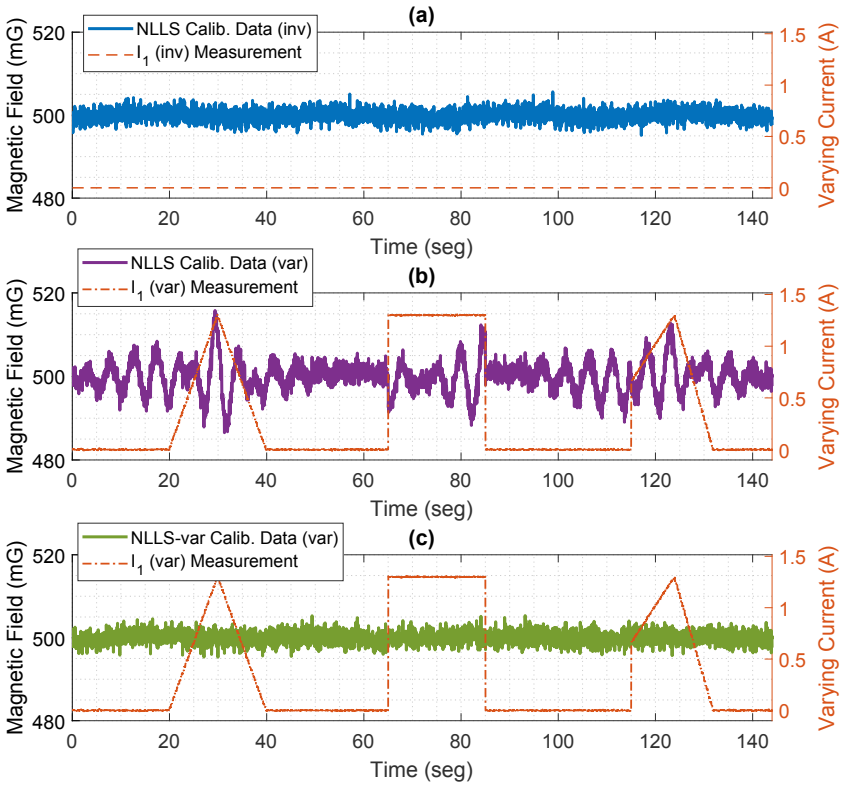

Figure 6.30: Calibrated magnitude measurements of the HMC5883L sensor in the first time-varying test. (a) Time-invariant measurements and sensor model. (b) Time-varying measurements calibrated by the time-invariant model. (c) Time-varying measurements and sensor model.

Table 6.18: Numerical analysis of the results for the first experimental test with time-varying bias.

Sensor Simulated Data Type	Calibration Algorithm	Mean Magnitude (mG)	RMSE (mG)	Absolute Max. Error (mG)	Pk-Pk Error (mG)
Time Invariant	Uncalib.	503.47	44.68	99.50	184.71
	NLLS-Inv	499.99	1.42	5.62	10.49
With Time-Varying bias	Uncalib.	503.21	44.10	104.44	188.39
	NLLS-Inv	499.93	3.75	15.78	29.24
	NLLS-Var	499.99	1.42	5.33	10.03

The graphical data in Fig. 6.30(c) shows that the calibration procedure outcome in the magnetic field magnitude is comparable to those in Fig. 6.30(a). Hence, it confirms that the time-varying calibration in the test corrupted by the varying electrical current is effective and performs similarly to the time-invariant solution in the procedure used as a benchmark. On the contrary, the calibrated magnitude using the time-invariant sensor model while in the presence of the varying current, seen in Fig. 6.30(b), had a much worse result.

The numerical data of Table 6.18 corroborates the graphical examination. In the time-invariant test, the calibrated RMSE value of the HMC5883L measurements was 1.42 mG, the same value obtained in the test with the varying currents using the NLLS time-varying bias algorithm. On the contrary, the invariant solution had an RMSE value of 3.75 mG in the second test. Furthermore, similar outcomes are observed in the absolute maximum and the peak-to-peak error values.

The experimental tests have results consistent with those reported in the simulations in Section 6.2.1. Therefore, they show the effectiveness of the proposed test bench in evaluating time-varying interference

through the magnetic field simulator and the time-varying bias calibration procedure.

6.3.4 Experimental Demonstration of the Calibration for Multiple Sources of Time-Varying Interference

This section seeks to demonstrate the time-varying bias calibration with multiple sources of errors analogously to the simulation reported in Section 6.2.2. During this test, the HiL simulation uses the auxiliary HCS to produce the first varying current signal and a relay to generate a second electrical current with only two states.

Figure 6.31 displays the time-varying signals (the state of I_2 and the current measurement for I_1) and the uncalibrated magnitude data of the HMC5883L sensor. We apply the time-invariant model and the time-varying bias algorithms in the HCM5883L measurements. The calibration parameters calculated using both solutions are seen in Table 6.19, which also includes the offsets and scale factors computed using the initial estimate algorithm.

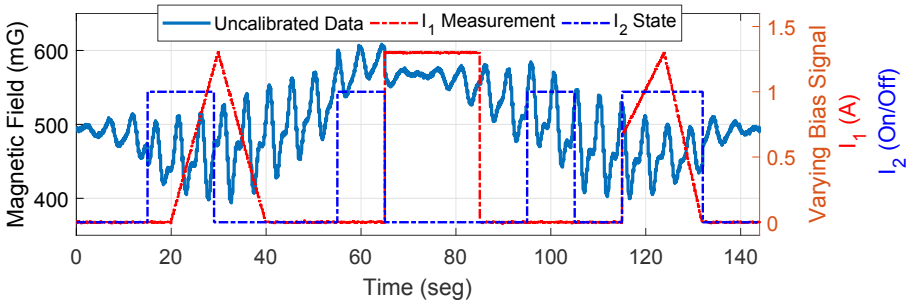

Figure 6.31: Magnitude of the uncalibrated data of the HMC5883L sensor obtained in the test with multiple sources of time-varying bias, the current measurements of $\tilde{I}_1$, and the signal state of I_2.

Table 6.19: Calibration parameters results for the experimental test with multiple sources of time-varying bias whose uncalibrated data is seen in Fig. 6.31.

Param.	NLLS	Time-Invariant NLLS		Time-Varying NLLS		Unit
		NLLS-inv	NLLS-inv	NLLS-inv	NLLS-inv	
	$\mathbf{p_0}$	$\mathbf{p}$	$\mathbf{3\sigma}$	$\mathbf{p}$	$\mathbf{3\sigma}$	
a	0.9902	0.9892	2.27E-3	0.9929	3.78E-4	unitless
b	0.8832	0.8826	2.02E-3	0.8852	3.37E-4	unitless
c	1.0623	1.0623	1.49E-3	1.0615	3.04E-4	unitless
x_0	-46.46	-46.44	0.790	-47.74	0.183	mG
y_0	-19.28	-18.81	0.705	-19.17	0.165	mG
z_0	43.64	43.89	0.609	37.34	0.155	mG
ρ	-	-3.097	0.210	-2.971	0.032	degrees
ϕ	-	-1.130	0.185	-0.654	0.031	degrees
λ	-	0.129	0.186	0.309	0.031	degrees
x_1	-	-	-	8.739	0.300	mG/A
y_1	-	-	-	-12.791	0.263	mG/A
z_1	-	-	-	-2.040	0.221	mG/A
x_2	-	-	-	-3.436	0.265	mG
y_2	-	-	-	10.621	0.236	mG
z_2	-	-	-	26.147	0.220	mG

First, one should note that the estimates of the first varying biases terms and the second have different meanings and units. For instance, for the electrical current generated by the auxiliary HCS, we have a measurement taken by the INA219 integrated circuit. Therefore, x_1, y_1, and z_1 are given in mG/A. However,

the actual value of the I_2 signal is unknown, as the information available is the relay state (dimensionless). Consequently, the varying biases x_2, y_2, and z_2 are given in milligauss.

In addition, although we will not make a detailed analysis of the calibration parameters in Table 6.19, we can compare them to those obtained in Section 6.3.3 and reported in time-invariant data in Table 6.16 and the time-varying results of Table 6.17[2]. By comparing them, it is evident that the scale factors, offsets, misalignment angles estimates, and the first set of time-varying biases (x_1, y_1, and z_1) of the time-varying NLLS in Table 6.19 are consistent among them. Thus it corroborates the effectiveness of the experimental procedure methodology and the parameters estimated in both tests.

Moreover, the uncertainties data of the time-invariant solution indicate how poorly those results are compared to those obtained with the sensor model with the time-varying biases parameters. Nevertheless, the calibrated magnetic field magnitude is more suitable for supporting that statement and comparing both algorithms. Hence, Fig. 6.32 shows the calibrated data of the time-invariant and the varying bias NLLS for the test, and Table 6.20 the numerical data analysis of the results.

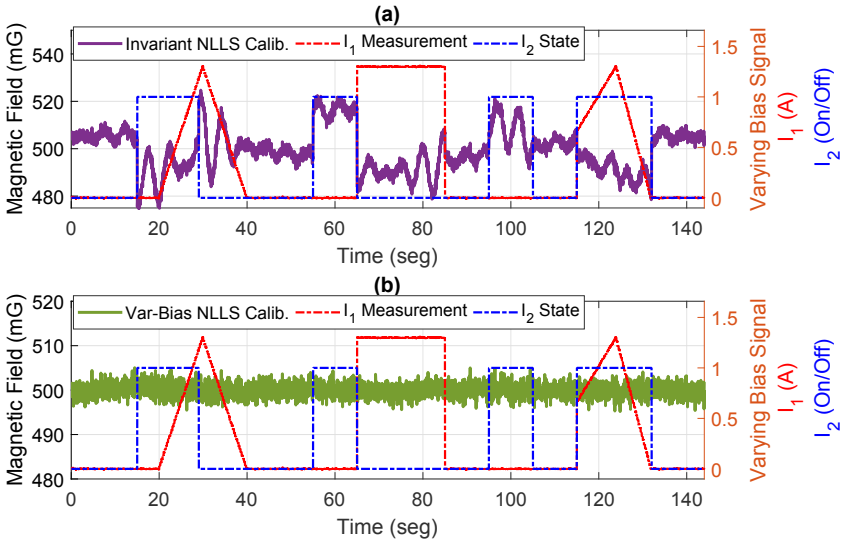

Figure 6.32: Magnitude of the calibrated data of the HMC5883L sensor obtained in the test with multiple sources of time-varying bias. (a) Time-invariant calibration. (b) Varying bias model.

Table 6.20: Numerical analysis of the results for the experimental test with multiple sources of time-varying bias.

Sensor Simulated Data Type	Calibration Algorithm	Mean Magnitude (mG)	RMSE (mG)	Absolute Max. Error (mG)	Pk-Pk Error (mG)
With Time-Varying bias	Uncalib.	502.48	48.92	108.49	214.70
	NLLS-Inv	499.58	9.12	25.19	49.90
	NLLS-Var	499.99	1.40	5.03	9.85

Notably, the calibrated results are comparable to those obtained in the first experimental test with a single time-varying current source, and the calibration outcome worsens when employing the typical time-invariant solution. For instance, we had a magnitude with an RMSE value of 9.12 mG for that scenario compared to 1.40 mG of the calibrated data with the time-varying biases. Also, it is noteworthy that the 1.40 mG is

[2]The tests in Sections 6.3.3 and 6.3.4 were performed right after one another; consequently, it is reasonable to compare them.

better, even if by a minimal margin, than the time-invariant benchmark test of the previous section, which had a numerical RMSE value of 1.42 mG (Table 6.18). Furthermore, Fig. 6.32(a) magnitude data shows that the time-invariant data deviates considerably during the entire test period, not only during the time-varying current moments.

At last, the vector components plots (spatial distribution over the *attitude sphere*) of the uncalibrated and the calibrated data for both algorithms are seen in Fig. 6.33. While the uncalibrated data is away from the 500 milligauss reference sphere, both solutions compensate for most of the errors regardless. Nevertheless, it is visible that the calibrated measurements in Fig. 6.6(c) have a better coincidence with the 500 mG sphere than those in Fig. 6.6(b).

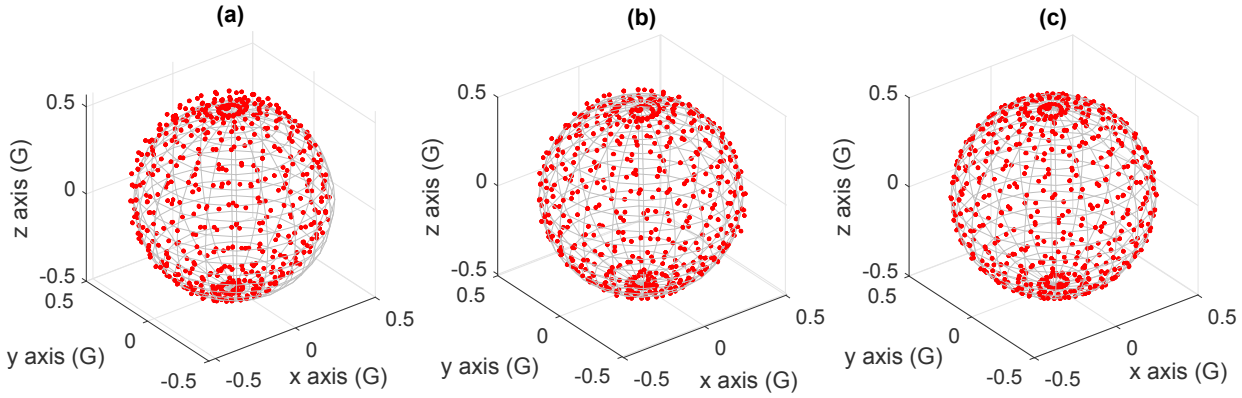

Figure 6.33: Vector components plot in three dimensions obtained in the time-varying bias test with multiple sources of errors. (a) Uncalibrated data. (b) NLLS calibrated data without the varying bias parameters. (c) NLLS calibrated data with the time-varying bias.

6.3.5 Evaluation of the Errors for Distinct Conditions of the Time-Varying Bias

The last experimental test complements the simulations of Section 6.2.6, which assessed many Monte Carlo simulations to put the calibrated magnitude RMSE into perspective for distinct conditions of the time-varying bias. This section performs a similar analysis; however, we display the magnitude errors instead of examining the resultant RMSE value of the runs. Once more, we have two sets of tests, each with six cases.

The first analysis demonstrates the calibration outcome for different values of the time-varying bias magnitude. To experimentally address that, we generate the magnetic field while changing the time-varying electrical current, thus, generating different values of the time-varying bias. To achieve that, we use a rheostat to control the electrical current value generated in the relay output. In each case, we used a square waveform with a duty cycle of 0.5 to define the relay state.

Table 6.21 displays the conditions of each case, where the varying electrical current was progressively increased between tests using the rheostat to tune the value. Table 6.21 also includes the numerical results of the estimated time-varying bias parameters, exhibiting the values computed in each case and the ratio between the magnitude of the estimated time-varying bias and the current value. As observed, the ratio values were close during all procedures, which is the expected outcome as the time-varying bias is directly proportional to the current; consequently, the ratio should be constant regardless of the current value.

Table 6.21: Approximate value of the electrical current, the calculated time-varying bias parameters, and their ratio, for cases 1 to 6.

Case	$\tilde{I}_1$ Value On (A)	Time-Varying Bias (mG)				$\lvert\hat{B}_1\rvert/\tilde{I}_1$ (mG/A)
		$\hat{x}_1$	$\hat{y}_1$	$\hat{z}_1$	$\lvert\hat{B}_1\rvert$	
1	0.125	-0.59	1.75	4.38	4.79	38.03
2	0.250	-1.09	3.65	8.81	9.60	38.40
3	0.500	-2.34	6.91	17.88	19.31	38.62
4	0.750	-3.84	11.03	26.72	29.16	38.88
5	1.000	-4.74	14.64	35.64	38.82	38.82
6	1.250	-5.84	18.34	44.52	48.50	38.80

The graphical results of the procedure are depicted in Fig. 6.34, which displays the calibrated magnitude of the HMC5883L measurements by both algorithms (time-invariant and varying-bias NLLS). Besides, it is noteworthy that the first three subfigures (a)-(c) have a different y-axis scale than (d)-(f). In addition, Table 6.22 exhibits the numerical analysis of the calibrated magnitude of the measurements.

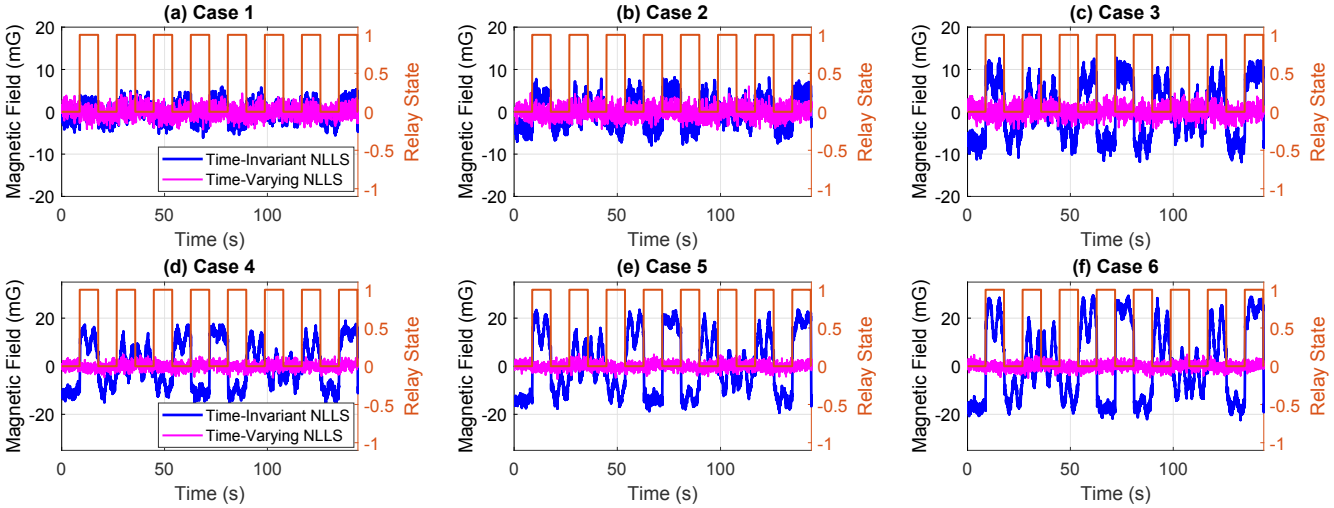

Figure 6.34: Magnitude plot versus time obtained in the experimental test for six distinct values of the time-varying bias magnitude. (a)-(f) Cases 1 to 6 (Table 6.21).

Table 6.22: Error analysis of the magnetic field magnitude results seen in Fig. 6.34.

Case	Time-Invariant NLLS				Time-Varying Bias NLLS			
	Mean Value	RMSE Value (mG)	Abs. Max. Error (mG)	Pk-Pk Error (mG)	Mean Value	RMSE Value (mG)	Abs. Max. Error (mG)	Pk-Pk Error (mG)
1	499.98	2.08	6.05	12.00	499.99	1.40	5.07	9.52
2	499.94	3.45	9.33	17.33	499.99	1.43	5.96	10.99
3	499.70	6.50	13.01	24.87	499.90	1.44	6.34	11.09
4	499.51	9.63	18.96	34.90	499.96	1.43	4.96	9.64
5	499.19	12.77	24.12	43.58	499.99	1.45	5.91	11.20
6	498.75	15.92	31.16	53.54	499.99	1.44	6.71	12.11

These experimental results corroborate the investigation in Section 6.2.6 that the time-varying bias calibration effectiveness is uncorrelated to the varying bias magnitude. In all six cases, the RMSE of the calibrated measurements is around 1.40-1.45 mG, regardless of the amplitude of the electrical current interference.

Oppositely, the typical time-invariant calibration suffers a considerable performance drop due to the varying

hard iron error. Even in the first case, with a bias magnitude of about 5 mG, the RMSE error increases by almost 50% compared to the solution using the varying sensor model. In the last case, we observe a magnitude RMSE of almost 16 mG, over ten times worse than the outcome with the time-varying bias NLLS and with a peak-to-peak error greater than 50 mG. Thus, the procedure conclusions are consistent with those simulated, demonstrating that time-varying electrical currents can significantly impact the time-invariant calibration.

In the last six cases, the electrical current value was constant and set to 0.26 A (equivalent to approximately 10 mG of time-varying bias magnitude); however, between them, the HiL setup progressively increased the duty cycle of the time-varying electrical current. Table 6.23 shows the duty cycle values and the estimated values of the time-varying bias parameters in each condition.

Table 6.23: Duty cycle of the varying electrical current and the calculated time-varying bias parameters for cases 7 to 12.

Case	$\tilde{I}_1$ Duty Cycle	Time-Varying Bias (mG)			
		$\hat{x}_1$	$\hat{y}_1$	$\hat{z}_1$	$\lvert\hat{B}_1\rvert$
7	0.05	-1.29	3.75	9.66	10.44
8	0.10	-1.29	3.84	9.74	10.55
9	0.25	-1.14	3.86	9.51	10.33
10	0.50	-1.16	3.80	9.41	10.22
11	0.75	-1.22	3.71	9.51	10.28
12	0.90	-1.21	3.92	9.55	10.39

Since the varying current was constant throughout the cases, the time-varying bias should remain unchanged between them; thus, the different duty cycle values should not affect the estimation of the parameters. Table 6.23 data reveal that the estimates of x_1, y_1, z_1, and the magnitude of the varying bias were close regardless of the duty cycle; thus, the result was as expected.

Once more, we must inspect the calibrated magnitude of the HMC5883L measurements to draw conclusions about the calibration outcome for both algorithms. Therefore, Fig. 6.35 shows the graphical results of the magnitude error in each case, and Table 6.24 assesses the numerical values of the errors.

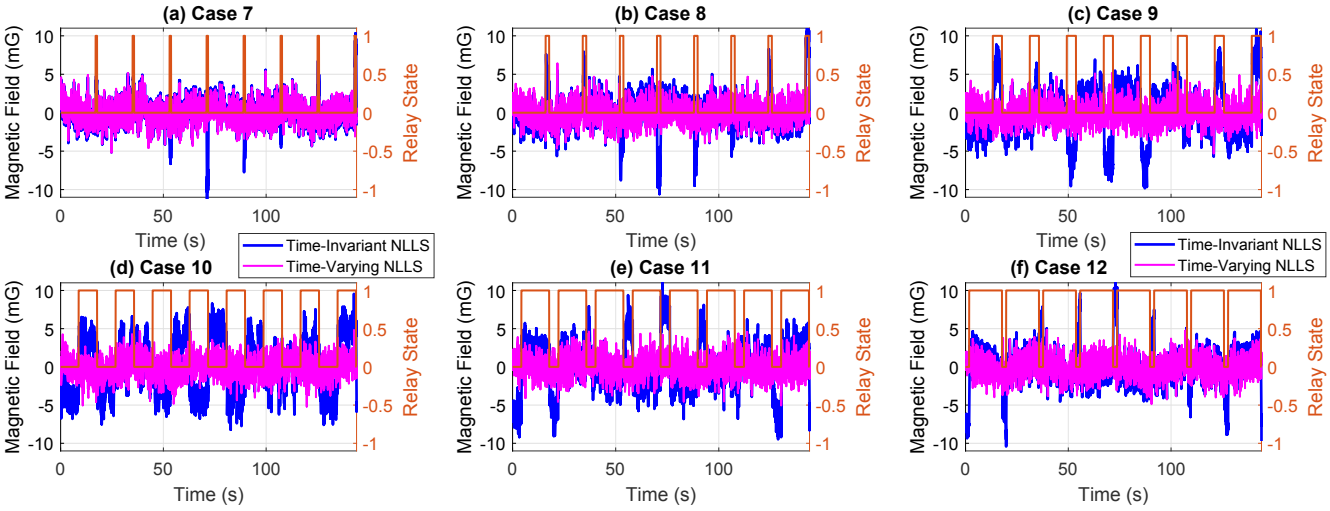

Figure 6.35: Magnitude plot versus time obtained in the experimental test for six distinct values of the duty cycle of the time-varying electrical current. (a)-(f) Cases 7 to 12 (Table 6.23).

Table 6.24: Error analysis of the magnetic field magnitude results seen in Fig. 6.35.

Case	Time-Invariant NLLS				Time-Varying Bias NLLS			
	Mean Value	RMSE Value (mG)	Abs. Max. Error (mG)	Pk-Pk Error (mG)	Mean Value	RMSE Value (mG)	Abs. Max. Error (mG)	Pk-Pk Error (mG)
7	499.98	1.81	11.65	22.98	499.99	1.43	5.38	10.56
8	499.97	2.37	12.11	22.86	499.99	1.39	6.43	12.38
9	499.95	3.26	10.89	21.36	499.99	1.43	5.32	10.59
10	499.94	3.64	9.54	17.76	499.99	1.43	5.19	9.98
11	499.92	3.27	11.22	22.39	499.96	1.45	5.75	10.92
12	499.97	2.52	12.70	24.55	499.99	1.44	5.06	9.94

The conclusions extracted from the data are identical to those reported in the simulation analysis in Section 6.2.6, likewise observed in cases 1 to 6. Again, the RMSE of the calibrated data using the time-varying bias solution has an outcome independent of the duty cycle; oppositely, the time-invariant sensor model results alter depending on that. The data also depicts that the worst case happens when half of the measurements are affected by I_1, equivalent to the duty cycle of 0.5 in case 10. Table 6.24 RMSE data verifies that. Besides, as discussed in Section 6.2.6, the RMSE progressively increases until the duty cycle reaches the worst-case condition (0.5) and decreases in the same proportion beyond that.

Lastly, it is noteworthy that every experimental test had results consistent with the respective simulation investigation in Section 6.2. Therefore, the analysis demonstrates the proposed approach, using the magnetic field simulator as a test bench, is effective in conducting experimental studies on time-varying interference.

6.4 Chapter Conclusions

This chapter has shown the formulation of the Non-Linear Least Squares (NLLS) to estimate the calibration parameters with additional time-varying biases parameters. The matter was thoroughly addressed by simulations showing the sensor model, and the NLLS algorithm is effective in compensating for varying hard-iron errors occasioned by time-varying electrical currents or electronics around the sensor.

In addition to that, we show a hardware-in-the-loop setup explicitly tailored to provide a test bench and a simulation environment for time-varying interference conditions. Therefore, it is possible to use the magnetic field simulator together with the proposed methodology to characterize the effect of time-varying bias on magnetometers. It also presents a successful calibration strategy for low-cost MEMS sensors to illustrate the proposed method. These results also validate the open-loop use of the magnetic field simulator without the closed-loop topology with the fluxgate sensor as the ground truth.

Future works could use other magnetic field simulators to reproduce the approach of testing their systems before a mission. Therefore, CubeSats, small UAVs, and other applications that require the measurements of Earth's magnetic field could benefit from avoiding the effect of time-varying bias by seeking calibration strategies for their respective application.

At last, it is also left for future authors to compare specific conditions of the time-varying bias and its impact on the accuracy of an attitude determination system. Hence, it would be possible to quantify the attitude errors in these systems if the varying bias is not accounted for.

7 Conclusions and Suggestions for Future Work

The main goal of this work was to develop and demonstrate a HiL setup suitable to perform the analysis of magnetic sensors subject to time-varying interference. To achieve that, an extensive part of this thesis was dedicated to improving the magnetic field simulator setup first reported in [26]. Hence, Chapters 2 and 4 focus on the simulator description, experimental validation, and its open-loop use methodology and calibration.

Compared to other magnetic field simulators discussed in the literature, a considerable advantage of the built apparatus is the fast transient time before reaching the steady state of the generated magnetic field. The results reported in Chapter 2 validate that the setup can simulate up to 16 distinct magnetic field points per second when testing a magnetometer with an output data rate of 40 Hz. Besides, higher values are doable with a synchronization mechanism between the HiL simulation and the sensors under test. These values are considerably higher than many existent coils. In addition, the simulator operates with current and voltage levels compatible with those available at power operational amplifiers. Hence, it allowed the application of the Howland Current Source in the design. Nevertheless, compared to other simulators, a disadvantage of the Helmholtz coil design is the volume of the uniformity region of the generated magnetic field.

The current version of the magnetic field simulator with the improvements described in the thesis, verified by Chapters 2 and 4 results, shows it can operate in real-time with sub-milligauss accuracy. Thus, it provides a suitable testing platform for evaluating low-cost magnetometer systems and applications. Moreover, future authors can use the magnetic field simulator to assess the magnetometer calibration for specific problems. More importantly, future upgrades to the system may also include other elements, such as testbeds, sun simulators, and others, to study on-orbit magnetometer calibration and simulate other actual applications' conditions in the controlled environment provided by the simulator.

Nevertheless, in the current stage, the setup has a drawback caused by the analog converters available at the dSPACE HiL solution. The limiting factor of the current setup is the resolution of the analog converters, both the DAC and the ADC, available at the DS2211 HiL board used in the interface with the Howland Current Source and the FGM3D acquisition electronics. Their improvement would allow for further Helmholtz Coil calibration testing and to seek a better accuracy of the open-loop field generation, which could enable the testing of magnetic sensors with better specifications. Therefore, future work may seek these improvements.

The most straightforward solution to the resolution issue is the acquisition of better converters for the dSPACE hardware. However, that would come at a very high cost, which might not be viable. An alternative, left as a suggestion, would be to design custom electronics explicitly tailored to the problem. Hence, the setup would have two dedicated electronics. The first would be responsible for sampling the output voltage of the fluxgate sensor used as the ground truth. For instance, a design with 18 bits would be suitable, and besides,

the analog converter must support simultaneous conversion (sampling) of at least three channels. The second electronic would have a dedicated DAC with at least 16 bits and simultaneous updating of at least three channels; consequently, it would be possible to update all Howland Current Sources channels simultaneously. Finally, one could interface both electronic systems to the current dSPACE processor via a high-speed CAN or UART available at the DS2211 hardware.

Another vital part of this thesis was the analysis and experimental tests of the power Howland Current Source circuit used to drive the simulator. Although the Howland current source is a very accurate, extremely simplistic design, and easily controlled, its use is most reported in biomedical applications. The results in this thesis show that if carefully designed, the HCS can output a very accurate and stable current even in high current and voltage conditions.

Using the HCS allows an easy way to control the electrical current of the magnetic field simulator using any digital-to-analog converter, providing a great alternative to power a magnetic field generation system. Most importantly, it does not require an external loop that could degrade the setup's transient time and accuracy. Furthermore, it is cheaper than a commercially available external controlled current supply and, likely, has a faster response dependent only on the OpAmp power bandwidth. The contribution seen in [32] proposes and describes how to design the HCS into a magnetic simulator, and other authors may develop their electronics to power their simulators. For higher current and voltage conditions, amplifiers from Apex Microtechnology could provide the solution using the HCS circuit. The HCS error analysis in Chapter 3 provides the basis for minimizing non-linear errors.

Regarding the magnetometer calibration topic, we have shown that the non-linear least squares (NLLS) algorithm can estimate the parameters using the non-linear sensor model proposed by Foster and Elkaim in the Extended Two Step (ETS) solution [2]. By employing the NLLS linearized iterative solution, we can avoid rewriting the problem using auxiliary variables. We have verified that the NLLS has an estimation slightly better, although only by a minimal margin, than an analytical solution of the ETS algorithm recently computed by Menezes Filho et al. [36].

Furthermore, the NLLS algorithm has a few advantages over the ETS. It allows for the computation of the parameters' uncertainties, is easily expanded to include additional parameters, such as the time-varying biases, and has an excellent computational effort compared to other solutions. The drawback of the proposed method is its convergence, which is only assured if a reasonable initial estimate of the parameters is available. Nevertheless, this thesis has reported possible solutions and algorithms to circumvent that issue in Chapter 5.

At last, our work has shown that a magnetic field simulator is a valuable tool for conducting experimental analysis of magnetometer calibration. Although this thesis focuses on the time-varying bias calibration problem, the setup can simulate numerous other conditions and replicate the environments of many applications. For example, it is possible to: reproduce the Earth's magnetic field for on-orbit nanosatellite magnetometer calibration, experimentally address low-cost magnetic sensors and compare them, simulating specifically data scattering of sensors (limited spatial distribution), and others. Therefore, future authors may use it as a testbench for numerous scenarios and in evaluating conditions expected in specific missions.

Bibliography

[1] GEBRE-EGZIABHER, D.; ELKAIM, G. H.; POWELL, J. D.; PARKINSON, B. W. Calibration of Strapdown Magnetometers in Magnetic Field Domain. *Journal of Aerospace Engineering*, v. 19, n. 2, p. 87–102, apr 2006.

[2] FOSTER, C.; ELKAIM, G. Extension of a two-step calibration methodology to include nonorthogonal sensor axes. *IEEE Transactions on Aerospace and Electronic Systems*, v. 44, n. 3, p. 1070–1078, jul 2008.

[3] CARUSO, M. J. Applications of magnetic sensors for low cost compass systems. In: *IEEE 2000. Position Location and Navigation Symposium (Cat. No.00CH37062)*. San Diego, CA: IEEE, 2000. p. 177–184. ISBN 0-7803-5872-4.

[4] CAI, J.; ANDERSEN, N. L.; MALUREANU, C. In-Field Practical Calibration of Three-Axis Magnetometers. In: *Proceedings of the 2010 International Technical Meeting of The Institute of Navigation*. San Diego, CA: The Institute of Navigation, 2010. p. 67–73.

[5] WANG, M.; LUO, Q.; IRAVANTCHI, Y.; CHEN, X.; SAMPLE, A.; SHIN, K. G.; TIAN, X.; WANG, X.; CHEN, D. Automatic calibration of magnetic tracking. In: *Proceedings of the 28th Annual International Conference on Mobile Computing And Networking*. New York, NY, USA: ACM, 2022. p. 391–404. ISBN 9781450391818.

[6] BOUWMEESTER, J.; GUO, J. Survey of worldwide pico- and nanosatellite missions, distributions and subsystem technology. *Acta Astronautica*, v. 67, n. 7-8, p. 854–862, oct 2010.

[7] SPRINGMANN, J. C.; CUTLER, J. W. Attitude-independent magnetometer calibration with time-varying bias. *Journal of Guidance, Control, and Dynamics*, v. 35, n. 4, p. 1080–1088, 2012.

[8] HAN, K.; WANG, H.; XIANG, T.; JIN, Z. Magnetometer Compensation Scheme and Experimental Results on ZDPS-1A Pico-satellite. *Chinese Journal of Aeronautics*, v. 25, n. 3, p. 430–436, jun 2012.

[9] SOKEN, H. E. A survey of calibration algorithms for small satellite magnetometers. *Measurement*, v. 122, p. 417–423, jul 2018.

[10] KIM, E.; BANG, H.; LEE, S.-H. Attitude Independent Magnetometer Calibration Considering Magnetic Torquer Coupling Effect. *Journal of Spacecraft and Rockets*, v. 48, n. 4, p. 691–694, jul 2011.

[11] ALLEN, L.; CHEPKO, A.; BEACH, T.; CLAVIER, O. Algorithms for accurate LEO geomagnetic measurements with satellite-mounted magnetometers. *IEEE Transactions on Aerospace and Electronic Systems*, v. 50, n. 4, p. 2736–2745, oct 2014.

[12] FREY, J.; HAWKINS, J.; THORSEN, D. Magnetometer calibration in the presence of hard magnetic torquers. In: *2014 IEEE Aerospace Conference*. Big Sky, MT, USA, 2014: IEEE, 2014. p. 1–6. ISBN 978-1-4799-1622-1.

[13] INAMORI, T.; HAMAGUCHI, R.; OZAWA, K.; SAISUTJARIT, P.; SAKO, N.; NAKASUKA, S. Online Magnetometer Calibration in Consideration of Geomagnetic Anomalies Using Kalman Filters in Nanosatellites and Microsatellites. *Journal of Aerospace Engineering*, v. 29, n. 6, p. 04016046, nov 2016.

[14] KLESH, A.; SEAGRAVES, S.; BENNETT, M.; BOONE, D.; CUTLER, J.; BAHCIVAN, H. Dynamically Driven Helmholtz Cage For Experimental Magnetic Attitude Determination. *Advances in Austronautical Sciences*, v. 135, p. 1–14, 2009.

[15] BERAVS, T.; BEGUš, S.; PODOBNIK, J.; MUNIH, M. Magnetometer calibration using kalman filter covariance matrix for online estimation of magnetic field orientation. *IEEE Transactions on Instrumentation and Measurement*, v. 63, n. 8, p. 2013–2020, aug 2014.

[16] POPPENK, F. M.; AMINI, R.; BROUWER, G. F. Design And Application Of a Helmholtz Cage For Testing Nano-Satellites. In: *6th International Symposium on Environmental Testing for Space Programmes*. Noordwijk: ESA/ESTEC, 2007.

[17] SPRINGMANN, J. C.; Y, J. W. C.; BAHCIVANZ, H. Magnetic sensor calibration and residual dipole characterization for application to nanosatellites. *AIAA/AAS Astrodynamics Specialist Conference 2010*, n. August, 2010.

[18] BREWER, M. R. *CubeSat Attitude Determination and Helmholtz Cage Design*. 92 p. Thesis (Master's Thesis) — Air Force Institude of Technology, 2012.

[19] HADDOX, P. G. The Development of a Hardware-in-the-Loop Attitude Determination and Control Simulator for IlliniSat-2. In: *52nd Aerospace Sciences Meeting*. Reston, Virginia: American Institute of Aeronautics and Astronautics, 2014.

[20] SILVA, R. C. da; ISHIOKA, I. S. K.; CAPPELLETTI, C.; BATTISTINI, S.; BORGES, R. A. Helmholtz Cage Design and Validation for Nanosatellites HWIL Testing. *IEEE Transactions on Aerospace and Electronic Systems*, v. 55, n. 6, p. 3050–3061, dec 2019.

[21] ZIKMUND, A.; JANOSEK, M.; ULVR, M.; KUPEC, J. Precise calibration method for triaxial magnetometers not requiring earth's field compensation. *IEEE Transactions on Instrumentation and Measurement*, v. 64, n. 5, p. 1242–1247, May 2015.

[22] PASTENA, M.; GRASSI, M. Optimum design of a three-axis magnetic field simulator. *IEEE Transactions on Aerospace and Electronic Systems*, v. 38, n. 2, p. 488–501, Apr 2002.

[23] PIERGENTILI, F.; CANDINI, G. P.; ZANNONI, M. Design, Manufacturing, and Test of a Real-Time, Three-Axis Magnetic Field Simulator. *IEEE Transactions on Aerospace and Electronic Systems*, v. 47, n. 2, p. 1369–1379, apr 2011.

[24] OLIVEIRA, D. A. de. *Calibração e Controle de Bobinas de Helmholtz para Aplicação Espacial*. 126 p. Thesis (Mestrado em Engenharia e Tecnologia Espaciais/Mecânica Espacial e Controle)) — Instituto Nacional de Pesquisas Espaciais, 2008.

[25] BATISTA, D. S.; GRANZIERA, F.; TOSIN, M. C.; MELO, L. F. de. Three-axial helmholtz coil design and validation for aerospace applications. *IEEE Transactions on Aerospace and Electronic Systems*, v. 54, n. 1, p. 392–403, 2018.

[26] BATISTA, D. S. *Plataforma de Simulação HiL contendo uma Bobina de Helmholtz e aplicada a Sistemas Aeroespaciais*. 268 p. Thesis (Master's thesis in Electrical Engineering) — State University of Londrina, 2016.

[27] ARNAUDOV, D.; SOKEROV, B. Power Supply for Helmholtz Coil. In: *2018 IX National Conference with International Participation (ELECTRONICA)*. Sofia, Bulgaria: IEEE, 2018. p. 1–4. ISBN 978-1-5386-5801-7.

[28] MAHNAM, A.; YAZDANIAN, H.; Mosayebi Samani, M. Comprehensive study of Howland circuit with non-ideal components to design high performance current pumps. *Measurement*, v. 82, p. 94–104, mar 2016.

[29] TUCKER, A. S.; FOX, R. M.; SADLEIR, R. J. Biocompatible, High Precision, Wideband, Improved Howland Current Source With Lead-Lag Compensation. *IEEE Transactions on Biomedical Circuits and Systems*, v. 7, n. 1, p. 63–70, feb 2013.

[30] BATISTA, D. S.; GRANZIERA JR., F.; TOSIN, M. C.; MELO, L. F. de. Sistema Mecatrônico baseado em Sensores MEMS voltado à Determinação de Atitude em Pequenos Satélites. In: *XX Congresso Brasileiro de Automática*. Belo Horizonte: Associação Brasileira de Engenharia e Ciências Mecânicas, 2014b. p. 3190–3197.

[31] STEELE, J.; GREEN, T. Tame Those Versatile Current-Source Circuits. *Electronic Design*, Apex Microtechnology Corp., p. 61–71, 1992.

[32] BATISTA, D. S.; SILVA, G. B.; GRANZIERA JR, F.; TOSIN, M. C.; GAZZONI FILHO, D. L.; MELO, L. F. Howland current source applied to magnetic field generation in a tri-axial helmholtz coil. *IEEE Access*, v. 7, p. 125649–125661, 2019.

[33] CRASSIDIS, J. L.; JUNKINS, J. L. Optimal Estimation of Dynamic Systems. In: _____. 2nd. ed. [S.l.]: Chapman & Hall/CRC, 2011. p. 24–29. ISBN 1439839859, 9781439839850.

[34] BATISTA, D. S.; GRANZIERA, F.; TOSIN, M. C.; MELO, L. F. de. Analysis and practical implementation of a high-power Howland Current Source. *Measurement: Journal of the International Measurement Confederation*, v. 207, p. 112404, feb 2023.

[35] BATISTA, D. S.; GRANZIERA, F.; TOSIN, M. C.; MELO, L. F. de. Attitude-Independent Magnetometer Calibration using Non-Linear Least Squares. *IEEE Sensors Journal*, In Press, p. 1–14, 2023.

[36] FILHO, R. P. M.; SILVA, F. O.; CARVALHO, G. S. Accurate and computational-efficient analytical solutions for the extended two-step magnetometer calibration. *IEEE Transactions on Aerospace and Electronic Systems*, p. 1–15, 2022.

[37] NOWICKA, J. Z. *Model-based Testing of Real-Time Embedded Systems in the Automotive Domain*. 245 p. Thesis (Doctor of Engineering Science Thesis) — Technical University Berlin, 2009.

[38] HIMMLER, A. Hardware-in-the-Loop Technology Enabling Flexible Testing Processes. In: *51st AIAA Aerospace Sciences Meeting including the New Horizons Forum and Aerospace Exposition*. Reston, Virigina: American Institute of Aeronautics and Astronautics, 2013.

[39] SENSYS GMBH. *SENSYS FGM3D Matrix of Technical Parameters*. Accessed Jan. 27, 2022. 2015. Available online: <https://sensysmagnetometer.com/products/fgm3d/>.

[40] ADAME, S. M.; GALVAN, J. C. O.; LITTLEWOOD, E. C.; PEREZ, R. E.; BRISSET, E. B. Coil Systems to Generate Uniform Magnetic Field Volumes. In: *Excerpt from the proceedings of the COMSOL conference*. Boston, MA: COMSOL, 2010.

[41] GERMANOVIX, G. R. *Projeto e construção de uma bobina de Helmholtz de três eixos aplicada à calibração de magnetômetros*. 112 p. Trabalho de Conclusão de Curso — Universidade Estadual de Londrina, 2014.

[42] CHULLIAT, A.; BROWN, W.; ALKEN, P.; BEGGAN, C.; NAIR, M.; COX, G.; WOODS, A.; MACMILLAN, S.; MEYER, B.; PANICCIA, M. *The US/UK World Magnetic Model for 2020-2025: Technical Report*. 2020.

[43] ADVANCED NAVIGATION. *SPATIAL MEMS GNSS/INS*. Rev. 3.1. 2021. Available online: <https://www.advancednavigation.com/wp-content/uploads/2021/11/Spatial-Datasheet.pdf>.

[44] HONEYWELL. *3-Axis Digital Compass IC HMC5883L*. Rev. E. 2013.

[45] ANALOG DEVICES. *ADIS16448: Compact, Precision Ten Degrees of Freedom Inertial Sensor*. Rev. H. 2019.

[46] APEX MICROTECHNOLOGY. *Bandwidth for Power Amplifiers Crash Course*. Rev A. 2018. (Application Note, 61).

[47] BERTEMES-FILHO, P.; FELIPE, A.; VINCENCE, V. C. High Accurate Howland Current Source: Output Constraints Analysis. *Circuits and Systems*, v. 04, n. 07, p. 451–458, 2013.

[48] BOUCHAALA, D.; KANOUN, O.; DERBEL, N. High accurate and wideband current excitation for bioimpedance health monitoring systems. *Measurement*, v. 79, p. 339–348, feb 2016.

[49] TOUMAZOU, C.; LIDGEY, F.; MAKRIS, C. Extending voltage-mode op amps to current-mode performance. *IEE Proceedings G Circuits, Devices and Systems*, v. 137, n. 2, p. 116, 1990.

[50] WANG, N.; FANG, H.; LEI, H.; YE, D. Dual feedback based bipolar current source with high stability for driving voice coil motors in wide temperature ranges. *Review of Scientific Instruments*, v. 92, n. 5, p. 054708, may 2021.

[51] POLETTO, C.; VAN DOREN, C. A high voltage, constant current stimulator for electrocutaneous stimulation through small electrodes. *IEEE Transactions on Biomedical Engineering*, v. 46, n. 8, p. 929–936, aug 1999.

[52] GHOVANLOO, M.; NAJAFI, K. A Compact Large Voltage-Compliance High Output-Impedance Programmable Current Source for Implantable Microstimulators. *IEEE Transactions on Biomedical Engineering*, v. 52, n. 1, p. 97–105, jan 2005.

[53] SCHUETTLER, M.; FRANKE, M.; KRUEGER, T. B.; STIEGLITZ, T. A voltage-controlled current source with regulated electrode bias-voltage for safe neural stimulation. *Journal of Neuroscience Methods*, v. 171, n. 2, p. 248–252, jun 2008.

[54] ZHAO, D. High output-impedance current source for electrical impedance tomography. In: *2011 4th International Conference on Biomedical Engineering and Informatics (BMEI)*. Shanghai, China: IEEE, 2011. p. 1106–1109. ISBN 978-1-4244-9352-4.

[55] CONSTANTINOU, L.; TRIANTIS, I. F.; BAYFORD, R.; DEMOSTHENOUS, A. High-Power CMOS Current Driver With Accurate Transconductance for Electrical Impedance Tomography. *IEEE Transactions on Biomedical Circuits and Systems*, v. 8, n. 4, p. 575–583, aug 2014.

[56] ZHANG, H.; LI, J. K.-J. Noninvasive Monitoring of Transient Cardiac Changes with Impedance Cardiography. *Cardiovascular Engineering*, v. 8, n. 4, p. 225–231, dec 2008.

[57] MOHAMADOU, Y.; OH, T. I.; WI, H.; SOHAL, H.; FAROOQ, A.; WOO, E. J.; MCEWAN, A. L. Performance evaluation of wideband bio-impedance spectroscopy using constant voltage source and constant current source. *Measurement Science and Technology*, v. 23, n. 10, p. 105703, oct 2012.

[58] KARKI, B.; WI, H.; MCEWAN, A.; KWON, H.; OH, T. I.; WOO, E. J.; SEO, J. K. Evaluation of a multi-electrode bioimpedance spectroscopy tensor probe to detect the anisotropic conductivity spectra of biological tissues. *Measurement Science and Technology*, v. 25, n. 7, p. 075702, jul 2014.

[59] NIKOLOVA, B. M.; NIKOLOV, G. T. Investigation and Design of High Current Sources for B-H Loop Measurements. In: *Proceedings of Electronics-ET 2008*. Sozopol, Bulgaria: Electronics 2008, 2008. p. 97–102.

[60] SRIRAM, N.; SWAMINATHAN, P.; MANIVANNAN, D. Design and Analysis of Current Mode Amplifier as Drive Electronics for Linear Voice Coil Motor. *Indian Journal of Science and Technology*, v. 8, n. 12, jun 2015.

[61] PANDIEV, I. M. Analysis and design of voltage-controlled current sources for a grounded load. *International Journal of Circuit Theory and Applications*, v. 43, n. 6, p. 756–775, jun 2015.

[62] YANG, A. D.; XIA, B. S.; OUYANG, C. L.; HOU, D. W.; GUO, E. L. An ultrahigh performance laser driver based on novel composite topology enhanced Howland current Source. *Review of Scientific Instruments*, v. 93, n. 12, p. 123001, dec 2022.

[63] TEXAS INSTRUMENTS. *A Comprehensive Study of the Howland Current Pump*. 2013. (Application Note, 1515).

[64] DATAFORTH CORPORATION. *AN102 - Errors, What are They and How Bad Can They Be*. n.d. 1–9 p.

[65] PALMER, R. *DC Parameters: Input Offset Voltage*. 2001. 1–24 p.

[66] PALLAS-ARENY, R.; WEBSTER, J. Common mode rejection ratio in differential amplifiers. *IEEE Transactions on Instrumentation and Measurement*, v. 40, n. 4, p. 669–676, 1991.

[67] LOKERE, K.; HUTCHISON, T.; ZIMMER, G. *Precision matched resistors automatically improve differential amplifiers CMRR - Here's How*. 2012. 1–20 p.

[68] DEVICES, A. *Op Amp Common-Mode Rejection Ratio (CMMR)*. 2021. (MT-042 Tutorial).

[69] VISHAY DRALORIC. *Cemented Leaded Wirewound Resistors*. Mar 2017. (AC, AC-AT Series Resistor).

[70] MORCELLES, K. F.; SIRTOLI, V. G.; BERTEMES-FILHO, P.; VINCENCE, V. C. Howland current source for high impedance load applications. *Review of Scientific Instruments*, v. 88, n. 11, p. 114705, nov 2017.

[71] LIU, J.; QIAO, X.; WANG, M.; ZHANG, W.; LI, G.; LIN, L. The differential Howland current source with high signal to noise ratio for bioimpedance measurement system. *Review of Scientific Instruments*, v. 85, n. 5, p. 055111, may 2014.

[72] SIRTOLI, V. G.; VINCENCE, V. C.; BERTEMES-FILHO, P. Mirrored enhanced Howland current source with feedback control. *Review of Scientific Instruments*, v. 90, n. 2, p. 024702, feb 2019.

[73] TEXAS INSTRUMENTS. *LM675 Power Operational Amplifier*. Revised March 2013. May 1999.

[74] BURR-BROWN. *OPA544 High-Voltage, High-Current Operational Amplifier*. 1995.

[75] APEX MICROTECHNOLOGY. *PA09 Power Operational Amplifier*. PA09U Rev S. abr. 2018.

[76] JIANG, N. A Large Current Source with High Accuracy and Fast Settling. *Analog Dialogue 52-10*, Analog Devices, p. 1–4, 2018.

[77] ALONSO, R.; SHUSTER, M. D. Complete Linear Attitude-Independent Magnetometer Calibration. *The Journal of the Astronautical Sciences*, v. 50, n. 4, p. 477–490, dec 2002.

[78] VASCONCELOS, J. F.; ELKAIM, G.; SILVESTRE, C.; OLIVEIRA, P.; CARDEIRA, B. Geometric Approach to Strapdown Magnetometer Calibration in Sensor Frame. *IEEE Transactions on Aerospace and Electronic Systems*, v. 47, n. 2, p. 1293–1306, apr 2011.

[79] CRASSIDIS, J. L.; CHENG, Y. Three-Axis Magnetometer Calibration Using Total Least Squares. *Journal of Guidance, Control, and Dynamics*, v. 44, n. 8, p. 1410–1424, aug 2021.

[80] WU, Z.; WU, Y.; HU, X.; WU, M. Calibration of Three-Axis Magnetometer Using Stretching Particle Swarm Optimization Algorithm. *IEEE Transactions on Instrumentation and Measurement*, v. 62, n. 2, p. 281–292, feb 2013.

[81] WU, Y.; SHI, W. On Calibration of Three-Axis Magnetometer. *IEEE Sensors Journal*, v. 15, n. 11, p. 6424–6431, nov 2015.

[82] PAPAFOTIS, K.; SOTIRIADIS, P. P. MAG.I.C.AL.–A Unified Methodology for Magnetic and Inertial Sensors Calibration and Alignment. *IEEE Sensors Journal*, v. 19, n. 18, p. 8241–8251, sep 2019.

[83] HONG, J. H.; KANG, D.; KIM, I.-J. Robust autocalibration of triaxial magnetometers. *IEEE Transactions on Instrumentation and Measurement*, v. 70, p. 1–12, 2021.

[84] PAPAFOTIS, K.; NIKITAS, D.; SOTIRIADIS, P. P. Magnetic field sensors' calibration: Algorithms' overview and comparison. *Sensors*, v. 21, n. 16, 2021.

[85] CRASSIDIS, J. L.; LAI, K.-L.; HARMAN, R. R. Real-Time Attitude-Independent Three-Axis Magnetometer Calibration. *Journal of Guidance, Control, and Dynamics*, v. 28, n. 1, p. 115–120, jan 2005.

[86] ALONSO, R.; SHUSTER, M. D. TWOSTEP: A Fast Robust Algorithm for Attitude-Independent Magnetometer-Bias Determination. *The Journal of the Astronautical Sciences*, v. 50, n. 4, p. 433–451, dec 2002.

[87] GEBRE-EGZIABHER, D.; ELKAIM, G. H.; POWELL, J. D.; PARKINSON, B. W. A non-linear, two-step estimation algorithm for calibrating solid-state strapdown magnetometers. In: *8th Saint Petersburg International Conference on Integrated Navigation Systems*. Saint Petersburg, Russia: Elektropribor Central Scientific and Research Institute, 2001. p. 28–30.

[88] ALI, A.; SIDDHARTH, S.; SYED, Z.; EL-SHEIMY, N. Swarm Optimization-Based Magnetometer Calibration for Personal Handheld Devices. *Sensors*, v. 12, n. 12, p. 12455–12472, sep 2012.

[89] WU, Z.; WU, Y.; HU, X.; WU, M. Calibration of Three-Axis Magnetometer Using Stretching Particle Swarm Optimization Algorithm. *IEEE Transactions on Instrumentation and Measurement*, v. 62, n. 2, p. 281–292, feb 2013.

[90] SILVA, C. P. da; GRANZIERA Jr., F.; BATISTA, D. S.; TOSIN, M. C. Altoritmo de otimização por enxame de partículas aplicado à calibração de sensores MEMS em tríade. In: *VIII Simpósio Brasileiro de Engenharia Inercial*. São José dos Campos: INPE, 2015.

[91] ZENG, W.; BIAN, Q.; GAO, J.; CHANG, L.; TONG, Y. Attitude-Independent Magnetometer Calibration Based on Adaptive Filtering. *IEEE Sensors Journal*, v. 22, n. 1, p. 195–202, jan 2022. Available online: <https://ieeexplore.ieee.org/document/9541346/>.

[92] XIAOMING, Z.; GUOBIN, C.; JIE, L.; JUN, L. Calibration of triaxial MEMS vector field measurement system. *IET Science, Measurement & Technology*, v. 8, n. 6, p. 601–609, nov 2014.

[93] OUSALOO, H. S.; SHARIFI, G.; MAHDIAN, J.; NODEH, M. T. Complete Calibration of Three-Axis Strapdown Magnetometer in Mounting Frame. *IEEE Sensors Journal*, v. 17, n. 23, p. 7886–7893, dec 2017.

[94] LI, X.; SONG, B.; WANG, Y.; NIU, J.; LI, Z. Calibration and Alignment of Tri-Axial Magnetometers for Attitude Determination. *IEEE Sensors Journal*, v. 18, n. 18, p. 7399–7406, sep 2018.

[95] ALKEN, P.; THÉBAULT, E.; BEGGAN, C. D.; AMIT, H.; AUBERT, J.; BAERENZUNG, J.; BONDAR, T. N.; BROWN, W. J.; CALIFF, S.; CHAMBODUT, A.; CHULLIAT, A.; COX, G. A.; FINLAY, C. C.; FOURNIER, A.; GILLET, N.; GRAYVER, A.; HAMMER, M. D.; HOLSCHNEIDER, M.; HUDER, L.; HULOT, G.; JAGER, T.; KLOSS, C.; KORTE, M.; KUANG, W.; KUVSHINOV, A.; LANGLAIS, B.; LÉGER, J.-M.; LESUR, V.; LIVERMORE, P. W.; LOWES, F. J.; MACMILLAN, S.; MAGNES, W.; MANDEA, M.; MARSAL, S.; MATZKA, J.; METMAN, M. C.; MINAMI, T.; MORSCHHAUSER, A.; MOUND, J. E.; NAIR, M.; NAKANO, S.; OLSEN, N.; PAVÓN-CARRASCO, F. J.; PETROV, V. G.; ROPP, G.; ROTHER, M.; SABAKA, T. J.; SANCHEZ, S.; SATURNINO, D.; SCHNEPF, N. R.; SHEN, X.; STOLLE, C.; TANGBORN, A.; TØFFNER-CLAUSEN, L.; TOH, H.; TORTA, J. M.; VARNER, J.; VERVELIDOU, F.; VIGNERON, P.; WARDINSKI, I.; WICHT, J.; WOODS, A.; YANG, Y.; ZEREN, Z.; ZHOU, B. International Geomagnetic Reference Field: the thirteenth generation. *Earth, Planets and Space*, v. 73, n. 1, p. 49, dec 2021. Available online: <https://earth-planets-space.springeropen.com/articles/10.1186/s40623-020-01288-x>.

[96] LÖTTERS, J.; SCHIPPER, J.; VELTINK, P.; OLTHUIS, W.; BERGVELD, P. Procedure for in-use calibration of triaxial accelerometers in medical applications. *Sensors and Actuators A: Physical*, v. 68, n. 1-3, p. 221–228, jun 1998.

[97] PANG, H.; LI, J.; CHEN, D.; PAN, M.; LUO, S.; ZHANG, Q.; LUO, F. Calibration of three-axis fluxgate magnetometers with nonlinear least square method. *Measurement*, v. 46, n. 4, p. 1600–1606, may 2013.

[98] LIU, J.; YAN, Y.; YAN, S.; LI, X. A Hybrid Calibration Method for a Three-Axis Magnetometer in Limited-Range Attitudes. *IEEE Sensors Journal*, v. 22, n. 1, p. 203–210, jan 2022.

[99] SPRINGMANN, J. C. *Satellite Attitude Determination with Low-Cost Sensors*. Thesis (Doctor of Philosophy in Aerospace Engineering) — University of Michigan, 2013.

[100]KUIPERS, J. B. *Quaternions and rotation sequences: a primer with applications to orbits, aerospace, and virtual reality*. Princeton, NJ: Princeton Univ. Press, 1999.

APPENDIX A – Complementary Analysis of Chapters 5 and 6

This appendix shows complementary analyses of the calibration examinations reported in Chapters 5 and 6. The three sections of the appendix have the following content:

- Appendix A.1 depicts the noise analysis of the HMC5883L low-cost magnetometer and the resulting noise of the sensor model proposed in the NLLS algorithm.
- The second section, Appendix A.2, compares the proposed algorithms in Section 5.4 to estimate the offsets and scale factors to initialize the NLLS solution.
- At last, Appendix A.3 discusses the expansion of the proposed algorithm to estimate offsets and scale factors, reported in Section 5.4.3, to include the time-varying bias parameters, and compares the results with the time-invariant algorithm under different conditions of the parameters.

A.1 Sensor Noise Analysis

This first appendix displays the noise analysis of the HMC5883L low-cost magnetometer and the resulting noise of the sensor model proposed in the NLLS algorithm. The former is presented in the first subsection, whereas the latter is shown in the subsequent one.

A.1.1 The HMC5883L Noise for a Static Magnetic Field Value

The first test assesses the HMC5883L noise in three different conditions:

1. with the magnetic field simulator turned off;
2. while the setup generates a static magnetic field using the open-loop non-compensated topology;
3. with the simulator generating a static magnetic field using the closed-loop topology.

The goal of the test is to confirm the behavior of the HMC5883L measurements and understand if the magnetic field simulator has any impacts on them. Thus, we collected 12000 measurements, during 300 seconds, for each of the conditions above. In the first scenario, the magnetometer measures the Earth's magnetic field within the coil. In the other two, we set the simulator to generate approximately 281 milligauss on each axis. Note that the HMC5883L axes are not necessarily aligned with those of the setup, and besides, the measurements shown are the raw uncalibrated ones.

For each axis and condition, the 12000 measurements are used to calculate the data's mean value and standard deviation. The graphical results include the measurements versus time, the $\pm 3\sigma$ boundaries, and the data histogram, including the Gaussian distribution obtained using the mean and standard deviation values. The results of each condition for all three axes are seen in Figs. A.1, A.2, A.3, respectively.

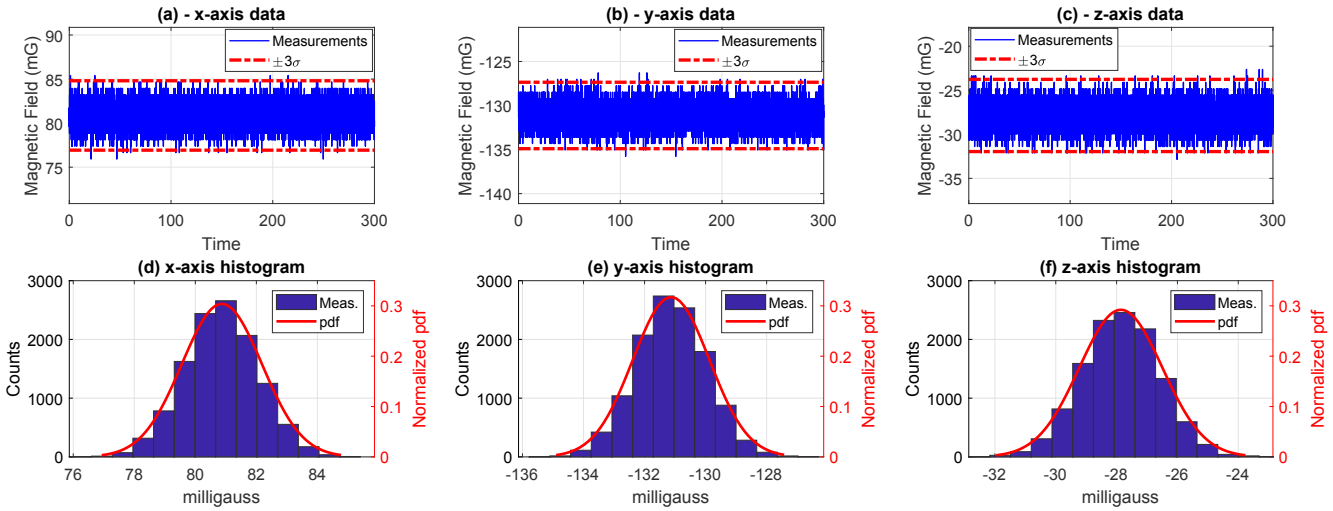

Figure A.1: Measurements taken during 300s by the HMC5883L low-cost magnetometer with the magnetic field simulator turned off.

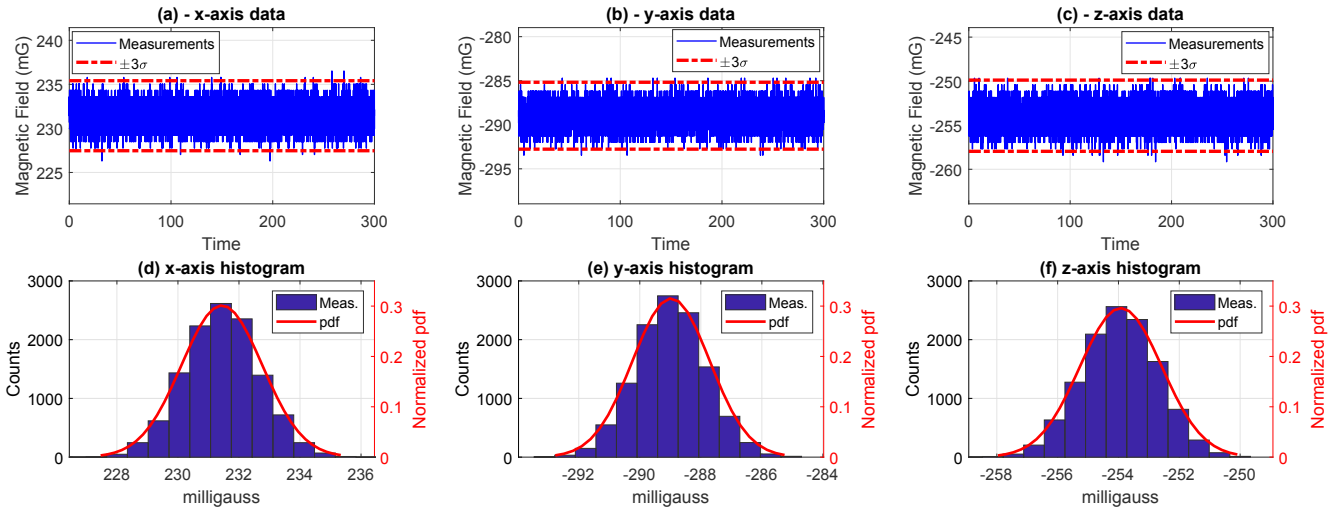

Figure A.2: Measurements taken during 300s by the HMC5883L low-cost magnetometer with the setup generating a constant magnetic field in the open-loop topology.

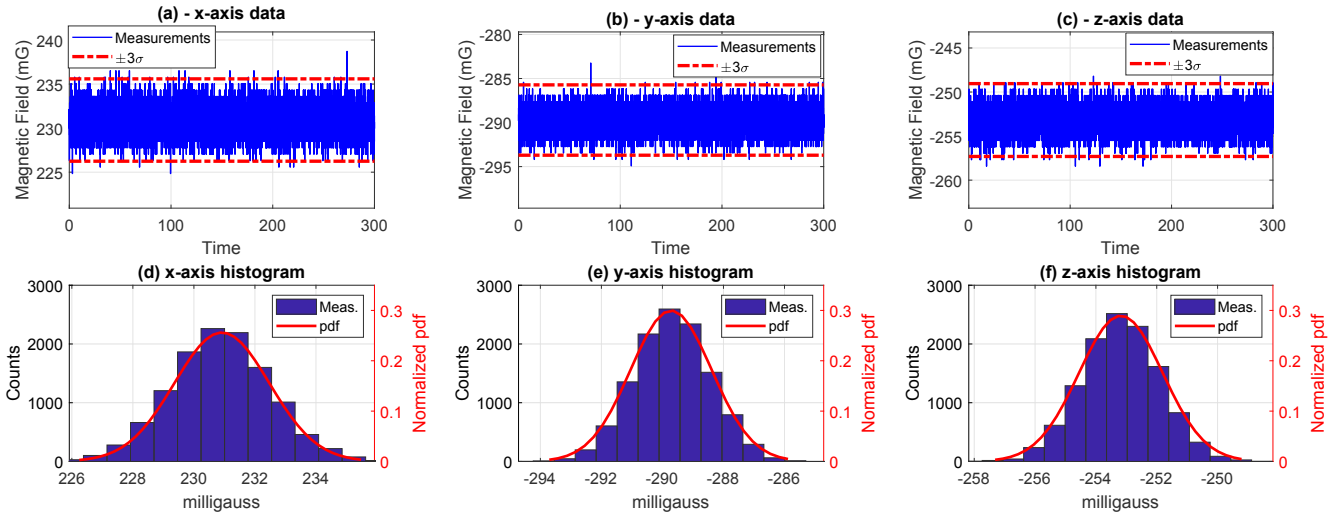

Figure A.3: Measurements taken during 300s by the HMC5883L low-cost magnetometer with the setup generating a constant magnetic field in the closed-loop topology.

By inspecting Figs. A.1-A.3, it is evident that the measurements have a Gaussian distribution in every scenario. Furthermore, every plot showing the measurements versus time, subplots (a)-(c) in each figure, has the same amplitude in the measurement scale. The same is true for the horizontal scales of the histogram plots. Therefore, it is possible to visualize that only the x-axis measurements of the closed-loop measurements (Fig. A.3) have a slightly worse standard deviation (SD) value, which is confirmed by the numerical data of the standard deviation, reported in Table A.1.

Table A.1: Numerical analysis of the SD value of the HMC5883L measurements plotted in Figs. A.1-A.3.

Simulator State	Axis			Unit
	x	y	z	
Turned-Off	1.313	1.257	1.366	mG
Open-Loop	1.324	1.265	1.347	mG
Closed-Loop	1.558	1.331	1.378	mG

The numerical data shows that the HMC5883L has an RMS noise of around 1.25 to 1.40 milligauss, which

is befitting with the values specified in the sensor's datasheet [44]. Hence, we have adopted the 1.5 milligauss in the Monte Carlo simulations throughout this thesis. In addition, although we do not investigate the reason, the x-axis higher standard deviation in the measurements taken during the closed-loop topology is related to any oscillations occasioned by the PID-controller loop. That assumption is plausible since the open-loop operation did not show the same behavior; consequently, the additional noise compared to the measurements taken with the setup turned off is unrelated to the HCS or the remainder of the electronics.

A.1.2 NLLS Model and Calibrated Magnitude Noise

Now that we have established the raw noise of the measurements, we proceed with the analysis of the NLLS model formulation and the calibrated magnitude noise. For the sake of simplicity, we proceed exclusively with the examination using simulated data generated with the approximate standard deviation values computed above. Using the procedure and methodology described in Section 5.5.1, we simulated a corrupted dataset of measurements. The calibration parameters are the same as used in that section, and the only difference is that we use a noise with a standard deviation value of 1.5 mG. The simulation generates eight cycles of that waveform, resulting in a procedure with 288 seconds and 8896 measurements. Then, using precisely the same approach reported in that section, we calibrate the data using the NLLS algorithm.

After the algorithm reaches the convergence, we compute the magnitude of every simulated measurement as well as the value of the residual error $\mathbf{e}$, calculated through (5.13), or $\mathbf{e} = \mathbf{B}_e^2 - \mathbf{f}(\widetilde{\mathbf{B}}, \hat{\mathbf{p}})$. Besides, one should recap that the standard deviation of $\mathbf{e}$, and consequently its variance, calculated after the NLLS reaches convergence, is the information used to compute the uncertainties of the estimation.

We extract the standard deviation and the mean value for both the magnitude and the residual error data. Figure A.4 shows the magnitude data and its $\pm 3\sigma$ boundaries (a), the magnitude histogram plot and the normalized probability distribution function (c), the residual error data and its $\pm 3\sigma$ boundaries (b), and the residual error histogram plot and the normalized probability distribution function (d).

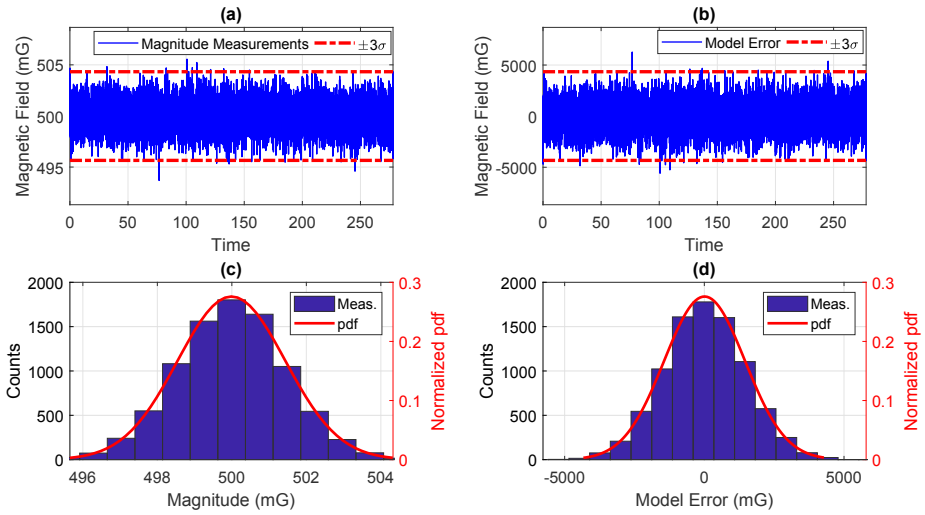

Figure A.4: Simulated data analysis for the calibrated magnitude and the residual error of the NLLS algorithm. (a) Calibrated magnitudes measurements and $\pm 3\sigma$ boundaries. (b) Residual error values and $\pm 3\sigma$ boundaries. (c) Histogram and probability distribution function of the calibrated magnitudes measurements. (d) Histogram and probability distribution function of the residual error.

These results are a clear indication that if the measurements have a Gaussian distribution, so will have the residual error and the magnitude of the calibrated data.

A.2 Comparison of the Initial Estimate Algorithms

Section 5.4 reports three algorithms to estimate an initial state for the scale factors and offsets parameters, which are: 1 - The algorithm proposed by Gebre-Egziabher et al. [1], described in Section 5.4.1, and limited to the premise that every measurement has the same magnetic field magnitude; 2 - the adaptation of the previous method for non-constant magnitude cases, seen in Section 5.4.2, and unsuitable for the constant case; 3 - the proposed alternative simplified formulation, reported in Section 5.4.3, which does not have the magnitude constraints and computes the offsets and scale factors in different steps.

During Chapter 5, the simulations and experimental results have shown that the proposed solution performed satisfactorily in the conditions tested with a good spatial distribution of the data over the attitude sphere. To complement those results, Subsection A.2.1 evaluates and compares the proposed algorithm to the solution of Gebre-Egziabher et al., whereas Subsection A.2.2 assesses and contrasts the proposed method and the adaptation of Gebre-Egziabher et al.'s algorithm for the non-constant magnitude scenario.

The test follows an identical methodology to the Monte Carlo simulations reported in Section 5.5.2. Figure A.5 shows the vector components plot in three dimensions of the three waveforms used in the simulation. Again, the parameters have the same uniform distribution, and the data is corrupted by Gaussian noise with 1.5 mG of standard deviation in each of the sensor's sensing elements.

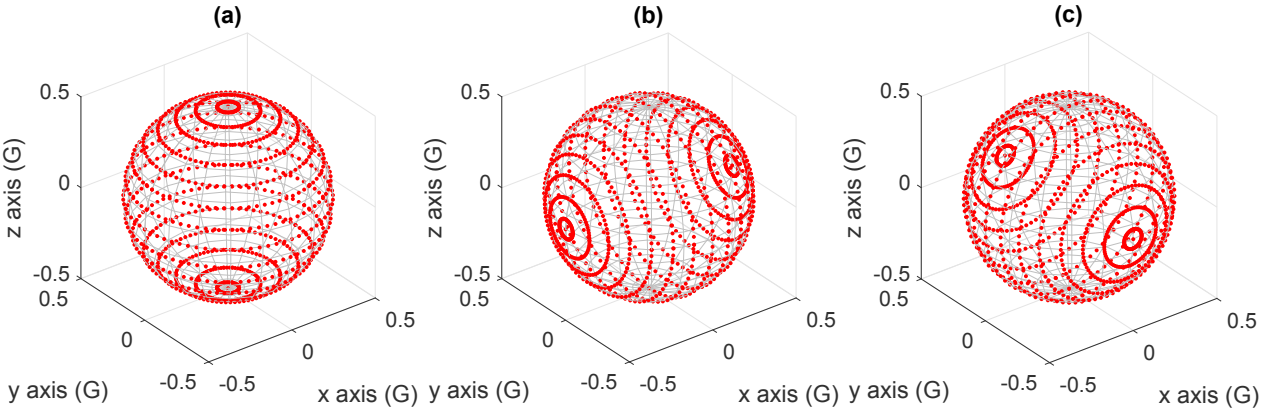

Figure A.5: Theoretical data vector components plot in three dimensions used in the Monte Carlo simulations to compare the proposed algorithms to compute the initial state of offsets and scale factors. (a) first waveform. (b) second waveform. (c) third waveform.

A.2.1 Constant Magnitude Simulation Results

We use all three waveforms to compare the solution Gebre-Egziabher et al. [1] and the proposed algorithm for the constant magnetic field magnitude case. Once more, the Monte Carlo simulation has 5000 runs for each of them. To summarize the results, we display the distribution plot of the parameters' errors for each case. Figures A.6, A.7, and A.8 depict the distribution for the first, the second, and the third waveform, respectively. The G-E nomenclature stands for Gebre-Egziabher et al. solution in the following figures.

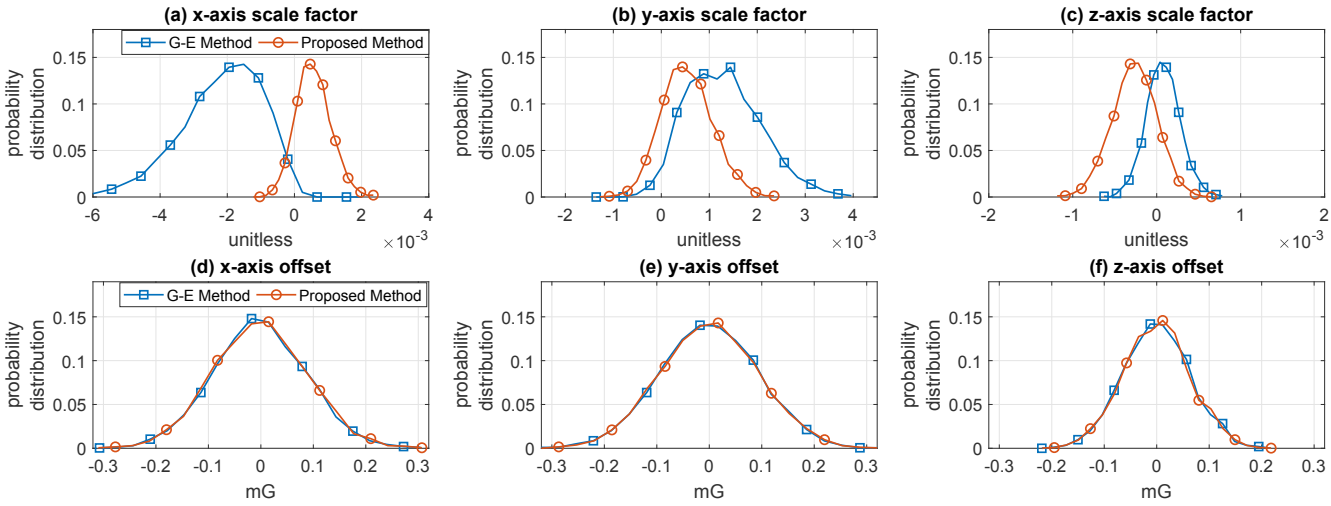

Figure A.6: Comparison of Gebre-Egziabher et al. [1] algorithm (G-E) and the proposed method of Section 5.4.3 for measurements with a constant magnetic field magnitude. Results for the first waveform.

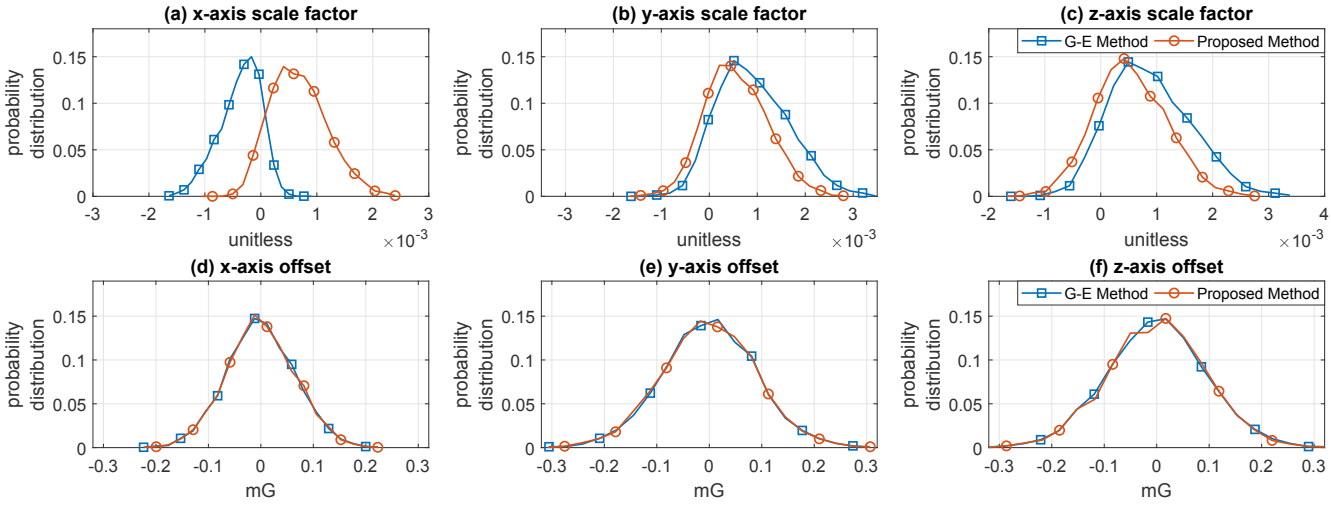

Figure A.7: Comparison of Gebre-Egziabher et al. [1] algorithm (G-E) and the proposed method of Section 5.4.3 for measurements with a constant magnetic field magnitude. Results for the second waveform.

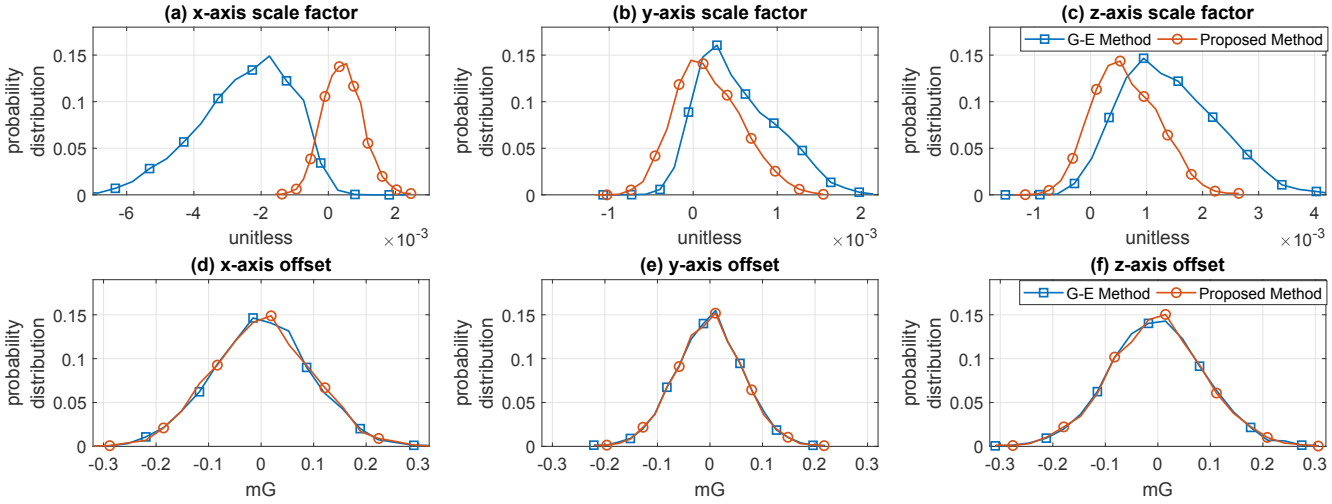

Figure A.8: Comparison of Gebre-Egziabher et al. [1] algorithm (G-E) and the proposed method of Section 5.4.3 for measurements with a constant magnetic field magnitude. Results for the third waveform.

First, the distributions seen in Figs. A.6 to A.8 indicates that the offsets estimations are almost identical for both solutions. On the contrary, the scale factors parameters have a more pronounced difference among the algorithms and between each waveform. Despite the differences, the graphical analysis is sufficient to assess the scale factors estimates.

Overall, the error distribution is closer to having a mean value of zero and a smaller standard deviation compared to Gebre-Egziabher et al.'s algorithm (G-E) [1]. For instance, this is more notable in the x-axis scale factor of the first and the third waveform, respectively seen in Fig. A.6(a) and A.8(a). Therefore, the proposed algorithm performed slightly, although by a minimal margin, better in the simulations.

Nevertheless, we can see that the error margin is minimal in the 10^{-3} order for the scale factors. Thus, these results allow us to conclude that both methods are suitable to provide the initial state of scale factors and offsets for the NLLS algorithm. Finally, as already noted in Chapter 5, we compare the estimations using measurements with optimal good distribution data over the *attitude sphere*. It is recommended that future authors observe the algorithms' accuracy and performance in non-ideal scenarios and for data with a limited spatial range (data scattering of the vector components).

A.2.2 Non-Constant Magnitude Simulation Results

We use the first and the second waveform to compare the proposed method and the adaptation of Gebre-Egziabher et al. [1] algorithm for non-constant magnitudes. The vector components plot seen in Fig. A.5 would be normalized. Again, there are 5000 runs for each waveform, and the parameters' distribution follows every other Monte Carlo simulation range. The magnetic field magnitude varies between 300 and 500 milligauss identically in every run, similar to the test reported in Section 5.5.4.

The distribution plot of the parameters' errors for each case is seen in Figs. A.9 and A.10, respectively, for the first and the second waveform. The G-E NCM nomenclature stands for the algorithm of Gebre-Egziabher et al. tailored for the non-constant magnitude scenario.

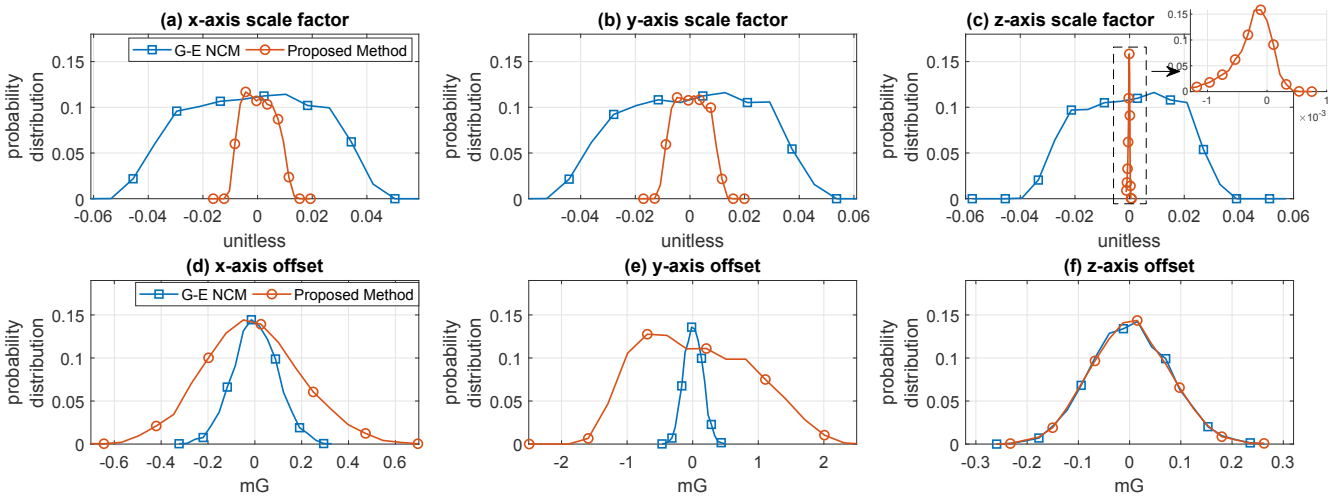

Figure A.9: Comparison of Gebre-Egziabher et al. [1] algorithm (G-E NCM) adapted for measurements with a non-constant magnitude and the proposed method of Section 5.4.3. Results for the first waveform.

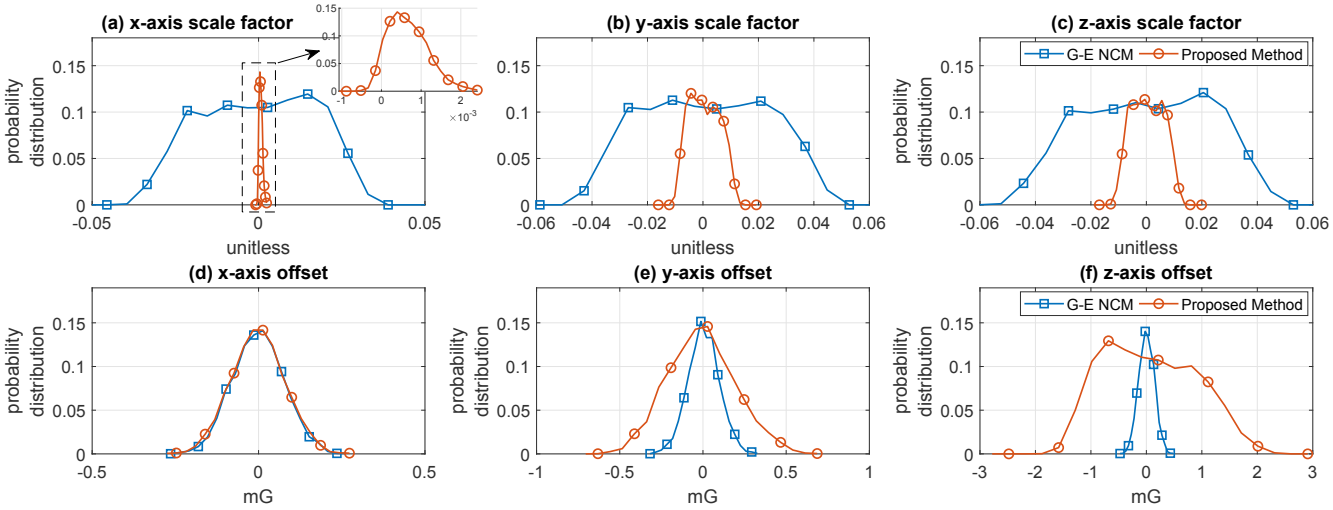

Figure A.10: Comparison of Gebre-Egziabher et al. [1] algorithm (G-E NCM) adapted for measurements with a non-constant magnitude and the proposed method of Section 5.4.3. Results for the second waveform.

These results show much more pronounced differences in the errors among the algorithms and between the waveforms compared to the simulation with the constant magnetic field magnitude. For instance, the offsets and the scale factors distributions are now distinct depending on the case, while the offsets were similar in the previous analysis. Furthermore, although the proposed solution has a consistently better scale factor estimation, it performs worse in the offsets than the other solution.

Comparing the scale factors, we can see that the adaptation of Gebre-Egziabher et al.'s solution has a distribution with a standard deviation value in the same order of magnitude in all axes regardless of the waveform. On the contrary, data scattering affects the outcome of the scale factor estimation in the proposed algorithm described in Section 5.4.3. For instance, Figs. A.9(c) and A.10(a) displays that the z-axis distribution for the first waveform, and the x-axis distribution for the second waveform, have an error with one order of magnitude narrower than the other axes of the respective waveform. Besides, that complies with the findings in Chapter 5, which demonstrated that the first waveform has the best spatial distribution over the z-axis and the second over the x-axis.

A similar observation is seen in the offsets estimated by the proposed algorithm, where it performs better for the z-axis and the x-axis, respectively, for the first and second waveforms. Furthermore, in these axes, the outcome of the error distribution is similar to the adapted algorithm of Gebre-Egziabher et al. However, the proposed algorithm performs slightly worse in the remainder of the axes. Compared to the constant magnitude error, the distribution of the data increased from ± 0.3 milligauss to a couple of milligauss in the worst scenarios, seen in Figs. A.9(b) and A.10(c). The adaptation of Gebre-Egziabher et al.'s solution has a similar error distribution for the offsets regardless of the non-constant magnitude.

Therefore, the results indicate that each algorithm suffers a specific impact when dealing with non-constant magnitude measurements. Nevertheless, despite a worse overall outcome, both algorithms still provide a very reasonable estimate for the offsets and scale factors. However, since the probability distribution of the errors has shown to be more susceptible to the waveform, future works need to bare that in case of a limited spatial distribution of the data.

A.3 Inclusion of the Time-Varying Bias Parameters in the Initial Guess Algorithm

Even though Chapter 6 shows that the NLLS algorithm, including the time-varying bias, performs satisfactorily using the time-invariant initial state algorithm of Section 5.4.3, this appendix discusses the expansions of that to include the time-varying biases.

The simplified sensor model without the misalignment angles is enhanced to include the time-varying biases. Thus, it leads to a measurement model in each axis given by (A.1)-(A.3), respectively.

$$\widetilde{B}_{\mathrm{x}} = aB_{\mathrm{x}} + x_0 + \sum_{i=1}^{n} x_i \tilde{I}_i + \eta_{\mathrm{x}} \tag{A.1}$$

$$\widetilde{B}_{\mathrm{y}} = bB_{\mathrm{x}} + y_0 + \sum_{i=1}^{n} y_i \tilde{I}_i + \eta_{\mathrm{y}} \tag{A.2}$$

$$\widetilde{B}_{\mathrm{z}} = cB_{\mathrm{z}} + z_0 + \sum_{i=1}^{n} z_i \tilde{I}_i + \eta_{\mathrm{z}}. \tag{A.3}$$

Analogously to the NLLS formulation, it is possible to write the expected square magnitude as a function of each axis measurement:

$$B_e^2 = B_x^2 + B_y^2 + B_z^2 = \left(\frac{\tilde{B}_x - x_0 - \sum\limits_{i=1}^{n} x_i \tilde{I}_i}{a} \right)^2 + \left(\frac{\tilde{B}_y - y_0 - \sum\limits_{i=1}^{n} y_i \tilde{I}_i}{b} \right)^2 + \left(\frac{\tilde{B}_z - z_0 - \sum\limits_{i=1}^{n} z_i \tilde{I}_i}{c} \right)^2, \tag{A.4}$$

The offsets and scale factor estimation were performed separately in the proposed initial guess algorithm. Once more, the solution to include the time-varying bias maintains that concept. Hence, it first estimates the offsets and time-varying biases and, in a second procedure, the scale factors.

Therefore, in the first step, the algorithm has to simplify (A.4) further to include only the offsets and time-varying biases parameters, leading to:

$$B_e^2 = B_x^2 + B_y^2 + B_z^2 = \left(\tilde{B}_x - x_0 - \sum_{i=1}^{n} x_i \tilde{I}_i \right)^2 + \left(\tilde{B}_y - y_0 - \sum_{i=1}^{n} y_i \tilde{I}_i \right)^2 + \left(\tilde{B}_z - z_0 - \sum_{i=1}^{n} z_i \tilde{I}_i \right)^2, \tag{A.5}$$

Theoretically, assuming m magnetometer measurements, (A.5) can be expanded and put in the linear form $\mathbf{y} = \mathbf{H}\mathbf{x}$, which allows computing the three offsets parameters plus three time-varying biases for each varying source of error using the batch least square solution. Nevertheless, that leads to an extensive matrix depending on the number of varying sources of errors i. Consequently, we limit the discussion and depict the formulation for a single source of varying bias in the following subsection.

Assuming that these parameters (offsets and time-varying biases) have been estimated, it is possible to compute the scale factor similarly to the time-invariant solution. Therefore, (A.4) can be rewritten as:

$$B_e^2 = \frac{1}{a^2} B_x'^2 + \frac{1}{b^2} B_y'^2 + \frac{1}{c^2} B_z'^2 ., \tag{A.6}$$

where B_x', B_y', and B_z' can be calculated for each measurement by means of (A.7)-(A.9) using the estimated

offsets and time-varying biases ($\hat{x}_0$, $\hat{y}_0$, $\hat{z}_0$, $\hat{x}_i$, $\hat{y}_i$, $\hat{z}_i$).

$$B'_x = \tilde{B}_x - \hat{x}_0 - \sum_{i=1}^{n} \hat{x}_i \tilde{I}_i \tag{A.7}$$

$$B'_y = \tilde{B}_y - \hat{y}_0 - \sum_{i=1}^{n} \hat{y}_i \tilde{I}_i \tag{A.8}$$

$$B'_z = \tilde{B}_z - \hat{z}_0 - \sum_{i=1}^{n} \hat{z}_i \tilde{I}_i \tag{A.9}$$

Finally, it is possible to put (A.6) in the linear form $\mathbf{y} = \mathbf{H}\mathbf{x}$, assuming m measurements, solve it using the batch least squares, and extract the scale factors similar to the procedure including only the time-invariant parameters.

A.3.1 Solution for a Single Source of Time-Varying Error

For a single time-varying source of error, mapped to the varying bias x_1, y_1, and z_1 through the measurement of I_1, (A.5) can be rewritten as (A.10).

$$B_e^2 = B_x^2 + B_y^2 + B_z^2 = \left(\tilde{B}_x - x_0 - x_1\tilde{I}_1\right)^2 + \left(\tilde{B}_y - y_0 - y_1\tilde{I}_1\right)^2 + \left(\tilde{B}_z - z_0 - z_1\tilde{I}_1\right)^2. \tag{A.10}$$

Expanding (A.10), and defining the correct intermediate variables, it is possible to rewrite it as:

$$\xi = -2\tilde{B}_x x_0 - 2\tilde{B}_y y_0 - 2\tilde{B}_z z_0 + \beta_0 - 2\tilde{B}_x\tilde{I}_1 x_1 - 2\tilde{B}_y\tilde{I}_1 y_1 - 2\tilde{B}_z\tilde{I}_1 z_1 + 2\tilde{I}_1\beta_{1a} + \tilde{I}_1^2\beta_{1b}, \tag{A.11}$$

where $\xi = B_e^2 - \tilde{B}_x^2 - \tilde{B}_y^2 - \tilde{B}_z^2$ and $\beta_0 = x_0^2 + y_0^2 + z_0^2$, similarly to the time-invariant solution, and the new intermediate variables, β_{1a} and β_{1a}, are given by (A.12) and (A.13), respectively.

$$\beta_{1a} = x_0 x_1 + y_0 y_1 + z_0 z_1 \tag{A.12}$$

$$\beta_{1b} = x_1^2 + y_1^2 + z_1^2 \tag{A.13}$$

Finally, taking m measurements, (A.11) can be expanded to a matrix form following the linear relationship $\mathbf{y} = \mathbf{H}\mathbf{x}$, which allows computing $\mathbf{x}$ using the batch linear least square. In this solution, $\mathbf{y}$ is a $m \times 1$ vector, $\mathbf{H}$ an $m \times 9$ matrix, and $\mathbf{x}$ a 9×1 vector with the offsets, time-varying biases, and the intermediate variables β_0, β_{1a} and β_{1b}, given by (A.14).

$$\mathbf{x} = \begin{bmatrix} x_0 & y_0 & z_0 & \beta_0 & x_1 & y_1 & z_1 & \beta_{1a} & \beta_{1b} \end{bmatrix}^{\mathrm{T}} \tag{A.14}$$

Once the offsets and the time-varying biases are computed, the scale factors solution will follow the time-invariant procedure described in Section 5.4.3 and using (A.6)-(A.9).

The issue with that formulation is that it performs poorly under scenarios with relatively low values of time-varying bias. Nevertheless, beyond a threshold where the bias values are increased, it provides a reasonable estimate and converges to the actual expected value. The following subsection address that.

A.3.2 Simulation Results for a Single Source of Time-Varying Error

The simulation to demonstrate the initial state solution, including one set of time-varying biases, uses a similar methodology described in Section 6.2.1. However, we now simulate 10 cases where the offsets (time-invariant) and the time-varying parameters are different.

To sum up, there are two values of offsets, whose values are interchangeable during the cases. Every odd case has an offset of 15, 18, and -8 milligauss per axis, and all even cases have a value ten times greater than those. In addition, the time-varying biases are progressively increased every couple of cases. For instance, the first two cases have one value of time-varying bias, cases three and four another value, and in like manner for the remaining cases. The true simulated values of the offsets and the time-varying bias for each case are seen in Table A.2. That table also includes the values estimated using the algorithm described in the previous subsection.

Table A.2: Conditions and results of the simulation to evaluate the expanded initial guess algorithm to include scale factors, offsets, and time-varying bias.

Case	x_0 (mG)		y_0 (mG)		z_0 (mG)		x_1 (mG/A)		y_1 (mG/A)		z_1 (mG/A)	
	True	Est.	True	Est.	True	Est.	True	Est.	True	Est.	True	Est.
1	15	18.92	18	14.41	-8	-3.31	4	-12.58	-10	3.31	20	9.85
2	150	150.46	180	177.75	-80	-73.72	4	-13.15	-10	2.89	20	9.78
3	15	19.04	18	14.26	-8	-3.35	8	-9.01	-20	-6.34	40	29.56
4	150	153.82	180	176.46	-80	-75.27	8	-8.42	-20	-6.47	40	29.39
5	15	18.87	18	14.38	-8	-3.21	16	-0.41	-40	-26.43	80	69.97
6	150	154.27	180	176.41	-80	-75.39	16	-1.23	-40	-26.59	80	69.96
7	15	19.09	18	14.47	-8	-3.39	32	14.90	-80	-66.57	160	150.02
8	150	153.78	180	176.38	-80	-75.29	32	15.87	-80	-66.47	160	150.02
9	15	18.87	18	14.33	-8	-3.39	80	63.25	-120	-106.90	175	165.35
10	150	153.98	180	176.35	-80	-75.35	80	63.12	-120	-106.09	175	164.92

Table A.2 data provides some interesting results. First, it is notable that the absolute values of the simulated offsets (x_0, y_0, and z_0) have a minor impact on the time-varying bias estimates. For example, comparing cases 1 and 2, cases 3 and 4, and in like manner for the remainder of cases, the outcome of the estimated values of x_1, y_1, and z_1 are very close in each pair. In addition, for higher values of offsets (even cases), these parameter estimates are accurate, regardless of the time-varying biases values. For lower values (odd cases), the estimate is slightly worse. Nevertheless, it still tends to converge to the true value.

Finally, we should assess the results of the time-varying biases estimates. It is evident that for low values of x_1, y_1, and z_1, seen in the first two cases, the estimated values are inferior, mainly for the x_1 and y_1 parameters, whose values are smaller than the z-axis one. For instance, the estimate of x_1 in the first two cases was around -13 mG, while the simulated value was 4 mG. Although results were less poor for z_1, the approximate estimate of 10 mG is relatively far from the true value of 20 mG.

When increasing the time-varying biases values, we can see that the estimated error is much lower, proportionally, when compared to the simulated value. For example, for the z-axis, we can see that beyond case 3, the estimated value of z_1 is already significantly better. However, for the x-axis, the estimates are extremely poor for cases 1-6, where the true values vary from 4 to 16 mG. Only in the last two cases that

the x_1 estimate are reasonable compared to the true value. To support these statements and facilitate the analysis, Table A.3 displays the percentage error of the estimated offsets and time-varying bias for each case.

Table A.3: Percentage errors of the offsets and the time-varying biases results in Table A.2.

Case	x_0 (mG)		y_0 (mG)		z_0 (mG)		x_1 (mG/A)		y_1 (mG/A)		z_1 (mG/A)	
	Value	Error (%)	Value	Error (%)	Value	Error (%)	Value	Error (%)	Value	Error (%)	Value	Error (%)
1	15	26.13	18	19.94	-8	58.63	4	414.50	-10	133.10	20	50.75
2	150	0.31	180	1.25	-80	7.85	4	428.75	-10	128.90	20	51.10
3	15	26.93	18	20.78	-8	58.13	8	212.63	-20	68.30	40	26.10
4	150	2.55	180	1.97	-80	5.91	8	205.25	-20	67.65	40	26.53
5	15	25.80	18	20.11	-8	59.88	16	102.56	-40	33.93	80	12.54
6	150	2.85	180	1.99	-80	5.76	16	107.69	-40	33.53	80	12.55
7	15	27.26	18	19.61	-8	57.63	32	53.44	-80	16.79	160	6.24
8	150	2.52	180	2.01	-80	5.89	32	50.41	-80	16.91	160	6.24
9	15	25.80	18	20.39	-8	57.63	80	20.94	-120	10.92	175	5.51
10	150	2.65	180	2.03	-80	5.81	80	21.10	-120	11.59	175	5.76

Such results reveal that the algorithm performs poorly for relatively low values of time-varying bias. Generally speaking, the threshold of providing an adequate result is around $40 - 50$ milligauss. Nevertheless, the results reported in Section 6.2.5 (see Table 6.13) demonstrated that the NLLS solution, using the initial estimate without the time-varying biases, only had convergence problems for time-varying bias with a magnitude greater than 200 milligauss. For reference, the simulated cases 7 and 8 have a time-varying bias magnitude of approximately 182 mG, and the last two cases are around 226 mG. Note that these values are much higher than those reported in works related to time-varying bias [7, 8, 10, 13].

Therefore, these results demonstrate why Chapter 6 analysis maintained the initial state algorithm of offsets and scale factors reported in Section 5.3.4.

APPENDIX B – Initial pages of the paper published in the journal *IEEE Transactions on Aerospace and Electronic Systems*

Title: Three-Axial Helmholtz Coil Design and Validation for Aerospace Applications.

Authors: Daniel Strufaldi Batista, Francisco Granziera Jr., Marcelo Carvalho Tosin and Leonimer Flávio de Melo.

Journal: IEEE Transactions on Aerospace and Electronic Systems (ISSN 0018-9251). Volume 54, Issue 1, Pages 392-403.

Classification (Qualis-CAPES): A1 / IF$= 3.491$ (Engenharias IV).

Publication Date: Feb 2018.

Three-Axial Helmholtz Coil Design and Validation for Aerospace Applications

DANIEL STRUFALDI BATISTA, Member, IEEE
FRANCISCO GRANZIERA JR., Member, IEEE
MARCELO CARVALHO TOSIN
LEONIMER FLÁVIO DE MELO
Department of Electrical Engineering,
State University of Londrina, Londrina, Brazil

This paper presents the detailed design, construction, and validation of a three-axis square Helmholtz coil. It also describes the methodology used to drive each pair of coils as well as the setup to operate it in a closed-loop system using a digital PID controller. The coil will be mainly used for aerospace applications, especially to aid the development and testing of attitude determination and control systems that use the earth's magnetic field as a reference vector. Most of the system was built using commercial components, reducing cost, and complexity compared to similar commercial systems. The assembled Helmholtz coil has approximately one cubic meter and can generate magnetic fields up to 2 G/ axis, keeping a uniformity of 0.04% around 11 cm of the center, in each axis. A custom-designed voltage-controlled current source, based on the Howland current pump, was employed, requiring no complex electronic circuits. The coil was designed to be part of a hardware-in-the-loop (HiL) system, which is controlled by a dSPACE modular simulation hardware and uses a commercial fluxgate magnetometer as the reference. This setup reduces the complexity of the proposed system when compared to similar ones. This paper presents two distinct results: first, there is the validation and results of the uniformity regarding the generated field around the system's center; second, results of the setup with the closed-loop HiL simulation are shown, which includes tests of the coil when generating a dynamic magnetic field.

Manuscript received July 14, 2016; revised April 26, 2017 and August 16, 2017; released for publication September 7, 2017. Date of publication October 9, 2017; date of current version February 7, 2018.

DOI. No. 10.1109/TAES.2017.2760560

Refereeing of this contribution was handled by M. R. Akella.

This work was supported in part by the Brazilian Space Agency (AEB) through the UNIESPAÇO program, and in part by the Department of Electrical Engineering of the State University of Londrina, Londrina, Brazil, and in part by the Brazilian Space Agency (AEB) through the UNIESPACO program.

Authors' addresses: D. S. Batista, F. Granziera Jr., M. C. Tosin, and L. F. de Melo are with the Department of Electrical Engineering, State University of Londrina, Londrina PR 445 KM 380, Londrina, Brazil, E-mail: (daniel.strufaldi@gmail.com; granziera@uel.br; mctosin@uel.br; leonimer@uel.br). *(Corresponding author: Daniel Strufaldi Batista).*

I. INTRODUCTION

The development of magnetic field simulators has been a subject of study for many decades. Several areas of study use magnetic fields for different purposes, from biomedical to aerospace engineering systems. In terms of the latter, geomagnetic field measurements contain information used by attitude determination systems for airplanes and satellites [1], for example.

The most commonly implemented magnetic field simulators found in the literature are the Helmholtz, Merritt, and Ruben coil systems, which are all discussed in [2]. The Helmholtz coil is the simplest and used in several works because it has only two windings per axis. It basically consists of two parallel coaxial coils. Due to the symmetry of its structure and the proximity between both coils, it is possible to generate a uniform magnetic field in one direction on a certain region around the center of the set. In order to generate a field in any direction, one uses three orthogonal Helmholtz coils aligned to each of the x-, y-, z-axes of a rectangular coordinate system.

Though the theory behind the Helmholtz coil is relatively well known, the design and construction of a triaxial coil is not trivial and commercial devices are quite expensive. Moreover, the specifications of a magnetic field simulator, such as the total field intensity and its uniformity within a volume, the transient response time, the coil's inductance, among others, can vary significantly depending on the application. For instance, [3] shows a system capable of generating magnetic fields greater than 20 G in a small volume for bioelectromagnetics application, while [1] describes a very complex system that can produce a homogeneous field in a large volume for nanosatellite validation.

This paper presents the design, implementation, and validation of a triaxial Helmholtz coil of which the main applications will be the validation of attitude determination systems and the calibration and testing of low-cost magnetic sensors. Two recent examples of design and manufacturing of triaxial systems for similar applications are given in [4] and [5]. Both were developed for geomagnetic field simulation for earth orbit. In turn, the works in [6]–[8] show similar uses of the Helmholtz system but do not present a detailed discussion about the coils itself.

The detailed requirements of the proposed system and how they were defined are discussed in Section II. At this point, it is emphasized that the uniformity of the field within the desired volume inside the system is a crucial design parameter. Sections III-B and III-C discuss the square Helmholtz coil's uniformity and further information is found in [9]–[11]. Also, as discussed in [12], the frequency response to variable currents is essential if the goal is to simulate aerospace applications in real time, which is also the aim of this paper. Tests under these conditions are presented.

There is also a discussion on the current source used to drive the Helmholtz coil as well as the setup to operate it with a digital closed-loop control system. Most works

in the literature do not show how the current drive is implemented and controlled. The proposed voltage-controlled current driver is shown in Section VII-A and consists of a Howland current pump (HCP) [13]. The electronic system employed is very simple and capable of driving the current using linear circuits. Therefore, disadvantages typical of nonlinear or *H bridge* drivers, such as the zero-crossing problem, are avoided. Also, implementing a closed-loop system becomes much simpler.

With respect to the closed-loop control, it is usually performed by means of an electronic system consisting of a PID controller. Although the theory is simple, its implementation and tuning might prove challenging, as in the prototype presented in [4]. To overcome this problem, this paper uses a hardware-in-the-loop simulation based on dSPACE modular hardware. This system is fully compatible with MATLAB/Simulink model design, which greatly simplifies electronic circuits, thus reducing time needed for testing and validation. Basically, the only electronics needed is the Howland current driver that is controlled by the digital-to-analog converter on the dSPACE hardware. This setup allows fast evaluation and modifications on the Helmholtz coil controller and the complete integration with Simulink software develop to test both nanosatellite attitude control and magnetic sensors. Furthermore, it is possible to implement the control system as a low-cost embedded electronic system, using the automatic code generation available in the Simulink/dSPACE tools.

A. Contributions of This Paper

The original contribution of this paper is the unveiling of the design details of a low cost three-dimensional (3-D) Helmholtz coil that has enough performance to be applied as a tool for aerospace applications, specifically for the development and testing of nanosatellite attitude determination and control systems based on low-cost magnetic sensors.

To accomplish this, the paper shows a simple and inexpensive construction methodology and materials to build the windings and to assemble them as a 3-D Helmholtz coil, following its design calculations. This paper also reports the successful use of a much simpler electronic circuit to drive the current through the coils, when compared to the solutions found elsewhere.

The topology used is the modified HCP, which retains a linear response during zero crossing of the current signal. This paper presents a control system for the magnetic field produced by the coil based on the PID strategy. It was implemented in the digital domain using a Simulink-dSPACE dedicated system, which enormously simplified its development. This methodology is readily suitable to be applied in the development of a low cost embedded control system.

At last, a dynamic analysis is presented by submitting the Helmholtz coil to both step and sinusoidal inputs, considering the system in the closed-loop setup. Such tests are important to evaluate the system response and whether it meets the requirements for the desired applications.

B. How this paper is organized

Section II presents the main aspects and requirements of the project to meet the needs of the proposed applications, followed in Section III by the theoretical study and basis for a square Helmholtz coil system. Section IV brings a very comprehensive description of the structural and electrical design chosen for the constructed coil as well as the prototype results. The remaining sections present the results, which are divided in two parts. First, the uniformity was tested by a specific setup and then the final prototype system was tested with dSPACE hardware running the HiL simulation.

II. COIL DESIGN MAIN REQUIREMENTS

A decision was made to build a Helmholtz coil with square shape and rounded corners, rather than a circular one, due to the simplicity of the construction and assembly procedure. Although circular coils simplify the winding process, its manufacturing and fastening structures between pairs are far more complex, resulting in higher cost and less design flexibility [9]. It was also implied that the square structure could be simply built using straight commercial aluminum profiles, that are commonly used as structural elements for various applications. This concept greatly reduces the effort and cost for building a relatively large structure and also adds flexibility to the system. In addition to the mechanical advantages, the square system also produces a slightly better uniformity region than a circular coil of same size [11].

Other important requirements are the maximum field strength and the uniformity percentage needed. Since the applications mainly consist of the validation and testing of navigation equipment that uses magnetic sensors and the geomagnetic field simulation for aerospace missions, the field generation capacity was decided to be at least enough to compensate the earth's field (creating a field in the opposite direction in order to *cancel* it) and subsequent generation of a new field of strength up to 1.2 G in either direction (coordinate). Thus, it was established that each pair of coils must generate a field strength of 2.0 G.

The uniformity region must be large enough to allocate the magnetic sensor that will be used as reference for the closed-loop control and further equipment or sensors that will be evaluated. The low-cost attitude determination system described in [14], which seeks to use low-cost sensors for nanosatellite applications, places its sensors in a volume of approximate 8 cm $\times$ 8 cm $\times$ 8 cm. An 11 cm-sized cube is necessary to place this equipment and the fluxgate magnetometer used as reference inside the coil. The magnetic field must be uniform enough so that the resolution of the sensors under test are not capable of detecting such variation, regardless of the position within the delimited volume. Assuming a full scale of 1.2 G and 0.02% uniformity per axis, this means 240 μG of variation in each axis. Such value is sufficiently small not to be detected by most of the low-cost magnetic sensors.

APPENDIX C – Full paper published in the journal *IEEE Access*

Title: Howland Current Source Applied to Magnetic Field Generation in a Tri-Axial Helmholtz Coil.

Authors: Daniel Strufaldi Batista, Guilherme Brandão da Silva, Francisco Granziera Jr., Marcelo Carvalho Tosin, Décio L. Gazzoni Filho and Leonimer Flávio de Melo

Journal: IEEE Access (ISSN 2169-3536). Volume 7, Pages 125649 - 125661.

Classification (Qualis-CAPES): A2 / IF$= 3.476$ (Engenharias IV).

Publication Date: Sep 2019.

IEEE Access
Multidisciplinary ⋮ Rapid Review ⋮ Open Access Journal

Received July 9, 2019, accepted August 19, 2019, date of publication September 2, 2019, date of current version September 17, 2019.

Digital Object Identifier 10.1109/ACCESS.2019.2939117

Howland Current Source Applied to Magnetic Field Generation in a Tri-Axial Helmholtz Coil

DANIEL S. BATISTA, (Member, IEEE), GUILHERME B. SILVA, FRANCISCO GRANZIERA, JR., (Member, IEEE), MARCELO C. TOSIN, DÉCIO L. GAZZONI FILHO, AND LEONIMER F. MELO

Department of Electrical Engineering (DEEL), State University of Londrina (UEL), Londrina 86057-970, Brazil

Corresponding author: Daniel S. Batista (daniel.s.batista@ieee.org)

This work was supported in part by the Brazilian Space Agency (AEB), through the Uniespaço Program, and in part by the Coordenação de Aperfeiçoamento de Pessoal de Nível Superior - Brasil (CAPES).

ABSTRACT This work describes the design and testing of a power Voltage-Controlled Current Source (VCCS) based on the Howland Current Source (HCS) topology. This source is part of a system that contains a three-axial Helmholtz coil and is used to generate a controlled magnetic field environment for aerospace applications. Initially, the paper presents the HCS theory and practical limitations on the premise that the system must be built using low-cost off-the-shelf components. The paper also carefully address on how to design and plan the VCCS matching physical and electrical parameters/limitations of a specific Helmholtz coil. All project details as well as the built VCCS electronics and its results are shown. These include linearity and a first order calibration test, stability and low-frequency error measurement, step response and a frequency limitation analysis. The built source is capable of sourcing up to ± 1.5 A at ± 25 V, maintaining its linearity and achieving an error smaller than 0.5% with a first order calibration. The final HCS prototype together with the Helmholtz coil allows an excellent capability regarding magnetic field generation for both open and closed-loop applications.

INDEX TERMS Helmholtz coil, Howland current source, magnetic field generator, power operational amplifier, voltage-controlled current source.

I. INTRODUCTION

The Helmholtz coil is a valuable tool to obtain constant and controllable magnetic fields. There are several applications from distinct areas as aerospace, medicine, physics, chemistry, pharmacy, biology, robotics, and others, where its use can be extremely relevant.

Though the Helmholtz coil theory [1] is not the main topic in this paper, its working principle is simple: it transforms a constant current, flowing through a pair of concentric coils, into a constant magnetic field in a central volume of the system, acting as a magnetic lens. By combining three-pairs of such coils, or three lenses, a three-dimensional system can be built [2], [3]. By controlling the current in each lens, this system can be used to synthesize a controllable time-varying magnetic field, allowing a number of studies for the aforementioned areas.

The associate editor coordinating the review of this manuscript and approving it for publication was Bora Onat.

The tri-axial Helmholtz coil described in [4] was designed to perform Hardware-in-the-Loop (HIL) simulation for aerospace systems development, including the testing of attitude determination and control systems and the calibration of low-cost magnetic sensors. That paper delineates the design guidelines of such a coil, as well as a closed-loop HIL simulation capable of controlling the magnetic field within the coil's volume. That and other papers present different perspectives of the design of the Helmholtz coil considering bounds of a specific application [2], [3], [5]–[7]. Their contribution focuses on design guidelines and performance analysis of their described system, and do not pay attention to the design of the current source that powers the coil's lenses.

The current source is an essential part of the Helmholtz coil. Its characteristics are greatly influenced by the coil's construction and electrical parameters [8]. Hence, the power supply and its design parameters must be addressed during the entire system design process.

To properly supply the coil's lenses of [4] the source has to: provide current from positive to negative values, which in turn, is a necessary feature so that the magnetic field is generated in any sense; output currents up to a couple of amperes to coils with tens of ohms of impedance; have a precision so that a resolution on the hundreds of micro-ampere can be achieved; and have low-noise. Furthermore, the output current transfer function must be accurate, preferably linear and have repeatability (so that it can be calibrated). Moreover, efficiency is not an issue since the system is used in a laboratory to test and validate the mentioned aerospace applications using HIL simulation. It is also desired that the source does not have filters or compensators that could end up compromising the HIL setup due to delays in the magnetic field response.

In this direction, this paper outlines the design of a voltage controlled current source (VCCS) tailored specifically to power that Helmholtz coil. This article and [4] were written aiming to fill a literature gap, providing a didactic and comprehensive set of guidelines regarding the Helmholtz coil whole design process.

The VCCS built is classified as an improved Howland Current Source (HCS) [9], [10]. The HCS is a linear VCCS and widely used for biomedical applications [10]–[14] due to its construction simplicity, resolution and temperature stability. If carefully designed, the HCS can output a very accurate, precise and symmetric current signal that is independent of the load impedance. Most biomedical applications are in the micro- or tens of milli-amperes range. On the other hand, our Helmholtz coil requires each VCCS to handle tens of watts in a much lower impedance and frequency compared to the typical HCS designs found in the above works. Therefore, the HCS must be built using power components and, tough efficiency is not a concern, the system must guarantee that the power losses and the generated heat do not compromise accuracy and precision.

The power HCS allows a linear solution to the problem and have a few advantages over its alternatives. It can easily handle both negative and positive currents, and, specifically, the zero current transitions (crossover) with low errors. Furthermore, it allowed a low-cost and simple electronic design using commercial off-the-shelf components only, where the essential one is the LM675 power operational amplifier (OpAmp). Also, comparing to switching sources, it has a less complex design, has few noise problems, and does not require an external control loop.

It is also worth mentioning that most of similar Helmholtz coil works in the literature either do not discuss the current source [5], or uses custom-built solutions based on switching inverting topologies [3], [15], or end up using commercial sources [6], which can also be expensive and might not strictly comply with the system's requirements. Additionally, most of these works do not present or discuss their current sources capabilities, performance, or limitations in detail.

One of the contributions of this paper is the design methodology of a VCCS based on the improved HCS to power the magnetic lenses of a tri-dimensional Helmholtz coil. Another contribution is the construction and characterization of the referred HCS for a high current situation, which is absent in the literature. Its performance data shows that it can successfully generate symmetric currents from milli up to a couple of amperes.

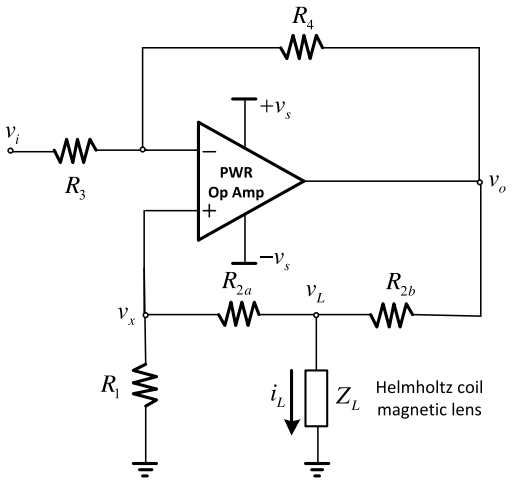

FIGURE 1. Basic Howland Current Source circuit.

At last, it should be noted that the power HCS shown can be adapted to a number of scenarios, as long as the load characteristics, the output frequency signal and the components limitations are known. Based on that, the methodology presented here can be used, regardless of the application, to parameterize the HCS to match the specific needs of any system.

II. HOWLAND CURRENT SOURCE

The basic circuit of a Howland Current Source [9], [10] can be seen in Fig. 1. The output current is controlled by the applied input voltage v_i to the OpAmp's negative feedback loop. The load Z_L is one of the Helmholtz coil's magnetic lens, where its two set of windings are connected in series. The magnetic lens can be modeled by a series resistor-inductor circuit.

The modeling of the above circuit, also discussed in [16], is reproduced here for didactic reasons and, more importantly, to describe the design constraints of a power HCS able to output a load-independent current proportional to the input voltage. Subsection II-A deduces both the output current i_L as a function of the input voltage v_i and the conditions necessary to maintain this relationship true regardless of the load.

A typical power OpAmp is not rail-to-rail, meaning its output voltage swing is lower than its supply voltage. Additionally, most of the current that flows through the magnetic lens impedance Z_L also flows through R_{2b}, so the voltage on the lens v_L is lower than the OpAmp output voltage v_0. This can be seen by inspecting the schematic diagram in Fig. 1. Therefore, the maximum output voltage, Z_L, R_{2b}, and the maximum current ($i_{L\,\max}$) are concurrent parameters in an HCS design. Subsection II-B equates $i_{L\,\max}$ of the HCS as a function of the other parameters.

A. CURRENT IN THE LOAD

The relationship between the output and the input voltages can be found by equating the negative feedback loop. Since the currents through R_3 and R_4 are the same, then

$$\frac{v_o - v_x}{R_4} = \frac{v_x - v_i}{R_3} \tag{1}$$

Similarly, equating the positive feedback loop we obtain

$$i_L = \frac{v_L}{Z_L} = \frac{v_o - v_L}{R_{2b}} - \frac{v_L}{R_1 + R_{2a}} \tag{2}$$

The current that flows through R_{2a} and R_1 is the same, then an equation that relates the voltage at the non inverse input (v_x) and the voltage on the load (v_L) can be written as

$$v_x = v_L \frac{R_1}{R_1 + R_{2a}} \tag{3}$$

Replacing v_x in (1) from (3) and isolating v_o, we have

$$v_o = v_L \frac{R_1}{(R_1 + R_{2a})} + v_L \frac{R_4 R_1}{R_3(R_1 + R_{2a})} - \frac{R_4}{R_3} v_i \tag{4}$$

Combining (2) with (4) to eliminate v_o and after some algebraic manipulation, i_L is given by

$$i_L = \frac{R_4(R_1 + R_{2a})}{Z_L(R_4R_1 - R_3R_{2a} - R_{2b}R_3) - R_3R_{2b}(R_1 + R_{2a})} v_i \tag{5}$$

The schematic diagram in Fig. 1 behaves as a VCCS if i_L is independent of Z_L. Therefore, the first term in denominator at the right side of (5) must vanish, so

$$Z_L(R_4R_1 - R_3R_{2a} - R_{2b}R_3) = 0 \tag{6}$$

This condition requires the following relationship to be maintained

$$R_4R_1 = R_3(R_{2a} + R_{2b}) \tag{7}$$

Accounting that (7) is satisfied, (5) can be rewritten as (8), which describes the output current of the HCS as a function of its input voltage.

$$i_L = -\frac{R_4}{R_3R_{2b}} v_i \tag{8}$$

B. MAXIMUM OUTPUT CURRENT

The maximum possible output current depends on the OpAmp output voltage swing, which can be considerably lower than the supply voltage. Furthermore, the current is also limited by the voltage drop in R_{2b}. We can write v_o as a function of v_L by rearranging (2), hence

$$v_o = v_L \left(1 + \frac{R_{2b}}{Z_L} + \frac{R_{2b}}{R_1 + R_{2a}}\right) \tag{9}$$

Replacing v_L by the product $i_L Z_L$, isolating the output current i_L, and finally accounting for the OpAmp maximum output voltage $v_{o\max}$, we can rewrite (9) as

$$i_{L\max} = \frac{v_{o\max}}{R_{2b} + Z_L\left(1 + \frac{R_{2b}}{R_1 + R_{2a}}\right)} \tag{10}$$

Since the load is modeled as a RL series equivalent circuit, Z_L impedance can be expressed by

$$Z_L = \sqrt{(R_s)^2 + (\omega L_s)^2} \tag{11}$$

Substituting (11) into (10) we obtain the maximum output current in (12).

$$i_{L\max} = \frac{v_{o\max}}{R_{2b} + \left(\sqrt{R_s^2 + \omega^2 L_s^2}\right)\left(1 + \frac{R_{2b}}{R_1 + R_{2a}}\right)} \tag{12}$$

Equation (12) relates the maximum HCS output current given the voltage swing limits, the feedback resistor R_{2b}, the load, i.e., a Helmholtz coil lens resistance R_s and inductance L_s, and the applied current frequency ω.

Given the HCS is a VCCS, variations in the frequency causes the output voltage v_o to change in order to maintain load current constant. Despite being obvious that with a limited output voltage swing the maximum working current will decrease with frequency, this restraint must be considered both in the Howland current source and in the magnetic lenses design.

III. PRACTICAL ASPECTS AND LIMITATIONS

Three main aspects are important when designing the system: the Power OpAmp characteristics; the stability and issues around the temperature variation of R_{2b}; overall power dissipation and its effects on the design. Each one is covered in the following subsections, respectively.

A. LM675 POWER OPAMP LIMITS

The Texas Instruments LM675 is a typical low-cost power OpAmp and was selected as the main component of the HCS described in this article.

According to the LM675 technical specifications, its input voltage is limited to ±30 V and the output current can swing up to ±3 A. Additionally, the output voltage must be limited in the range of ±26 V to guarantee its linear operation when supplied with ±30 V. Another limitation is that the LM675 has a stable operation only if its negative feedback gain is greater than 10.

Those constrains are very important in the subsequently discussion on how to dimension the Helmholtz Coil and the HCS physical and electrical characteristics to guarantee the correct system operation within its design requirements.

B. HCS STABILITY DUE TO R_{2B} TEMPERATURE

An important aspect in the HCS design is the electrical characteristics deviation of the passive components used in its construction, specially the thermal drift.

The resistors R_1, R_3, R_{2a} and R_4 in Fig. 1 have values in the kilo-ohms range. They are subjected to low currents in the order of mili-ampere. On the other hand, R_{2b} is around one ohm and is subjected to almost the same current i_L as the load, which makes heating expected in this component.

This component must be a power resistor, which can dissipate the heat to the ambient keeping temperature within

its operating limits. Quality commercial power resistors will have its thermal parameters, such as the its heat resistance to the air and the temperature coefficient of resistance (TCR) characterized within its operating temperature range and made available by its manufacturer. This component should have the smallest variation of its resistance as possible within the operating temperature range. Additionally, it is desirable that the temperature of this component be as stable as possible within the operating range of current applied by the HCS's OpAmp. Having said that, the dissipated power over this resistor may causes significantly temperatures variations in it, which will cause proportional resistance variation accordingly to the resistor's TCR.

Owing to the described, the modeling of the generated current variation as a function of the R_{2b} resistance variation and the input voltage variation for the HCS is justified. A resistor's resistance variation with temperature can be expressed as

$$\Delta R_i = \alpha R_i \Delta T, \tag{13}$$

where ΔT is the temperature variation in the interval $(T_f - T_i)$, α is the resistor TCR in ΔT, R_i is the resistor value at t_i and ΔR is the resistance variation in ΔT.

Taking the current total differential of (8) as a function of the variations in each of the elements, we have

$$\Delta i_L = \frac{\partial i_L}{\partial R_4}\Delta R_4 + \frac{\partial i_L}{\partial R_3}\Delta R_3 + \frac{\partial i_L}{\partial R_{2b}}\Delta R_{2b} + \frac{\partial i_L}{\partial v_i}\Delta v_i \tag{14}$$

Evaluating the first two partial derivatives ($\partial R4$ and $\partial R3$) and replacing the ΔR_i with (13), the relationship shown in (15) holds if an identical temperature variation occurs in both resistors and assuming their TCR is the same.

$$-\frac{1}{R_3 R_{2b}}\alpha R_4 \Delta T + \frac{R_4}{R_3^2 R_{2b}}\alpha R_3 \Delta T = 0 \tag{15}$$

As variations in R_4 and R_3 compensates each other, (14) can be rewritten as

$$\Delta i_L = \left(\frac{R_4}{R_3 R_{2b}^2}\Delta R_{2b}\right) v_i - \frac{R_4}{R_3 R_{2b}}\Delta v_i \tag{16}$$

Combining (8) with (16) and after some algebraic manipulation, (17) describes the relationship between the relative rate of change of the current load as function of the resistor's TCR and the relative rate of change of the input voltage, within a specified temperature range.

$$\frac{\Delta i_L}{i_L} = -\frac{\Delta R_{2b}}{R_{2b}} + \frac{\Delta v_i}{v_i} \tag{17}$$

Equation (17) shows that a variation of R_{2b} will cause a proportional variation on i_L. This relationship is deduced from (8), which is based on the premise that (7) holds. As explained above, the resistance value chosen for R_{2b} is around one ohm and the other resistors have values 10^3 times greater, at least. Since R_{2b} must dissipate heat, considering a temperature rise not greater than 100 °C above ambient temperature and also considering the use of a common wirewound power resistor with TCR of ±100 ppm/°C [17], from (13), its resistance variation will be on the order of ±0.01 ohm. From (7), this small variation on R_{2b} is negligible if compared to the kilo-ohms range of the other resistor. Since the relation stated by (7) is fullfilled, (8) will hold and the circuit in Fig. 1 will behave as a VCCS.

However, as it is also seen in (8), a variation of R_{2b} will affect the VCCS' transconductance gain and (17) dictates that. Using the same TCR parameters that guided the discussion in the above paragraph and considering an applied current of 1 A, a current variation in the order of ±0.01 A may be caused by R_{2b} temperature variation. Thus, the linearity of the HCS built must be addressed experimentally.

C. POWER DISSIPATION EFFECTS ON THE VCCS

According to the circuit in Fig. 1 and assuming $i_L \approx i_{R_{2b}}$, the instantaneous dissipated power is the sum of those dissipated at the load (P_L), at R_{2b} ($P_{R_{2b}}$), and internally by the OpAmp (P_D), thus

$$P_T \approx P_L + P_{R_{2b}} + P_D \approx i_L v_L + i_L(v_o - v_L) + i_L(v_s - v_o) \approx v_s i_L \tag{18}$$

Modeling of power dissipated in R_{2b} was already addressed in the last subsection.

The power applied to the load is dissipated in the coil windings, causing a temperature rise which modifies the resistivity of the winding material, and consequently the load impedance. However, the VCCS compensates for such changes and maintains a constant output current.

The heat generated by the OpAmp due to its internally dissipated power needs to be managed by a thermal dissipation apparatus to keep its temperature within safe limits. Unlike the other power components, P_D does not increase monotonically with the current. Taking the derivative of P_D as a function of i_L or v_o and looking for a zero, it is found that the maximum power dissipated at the OpAmp occurs when

$$i_L = \frac{v_s}{2(R_{2b} + Z_L)} \Leftrightarrow v_o = \frac{v_s}{2} \tag{19}$$

Assuming maximum currents close to 2 A, a supply of ±30 V, and depending on the load impedance, the LM675 might need to dissipate as much as 30 W internally. Thus, generating a considerable amount of heat and, like any class AB or B linear amplifier, having low efficiency.

However, as already stated in the introduction, this is not a concern to our application. The main focus is to achieve good stability, linearity, and low-noise. Therefore, the VCCS design must be as immune as possible so that the heat generated won't cause the components' temperature to go beyond a value where the HCS is impaired.

IV. HOWLAND CURRENT SOURCE DESIGN

This section provides a detailed discussion about the HCS design based on the Helmholtz coil parameters presented in [4].

A. A BRIEF HELMHOLTZ COIL DESCRIPTION

The used Helmholtz coil is a three-dimensional field generator composed by three sets of square magnetic lenses mounted one inside each other. The coils are square shaped with a side length S_L, such as the outer lens has $S_{L\text{ext}} = 1.00$ m, the middle has $S_{L\text{mid}} = 0.94$ m and the inner has $S_{L\text{inn}} = 0.88$ m. The dimensions and the distances between the coils were chosen to produce a constant magnetic field with an uniformity of 0.02 % inside a central squared volume with 11 cm edge. This is the primal requirement of the Helmholtz coil built. The coil and its constructive mechanical details can be found in [4].

B. ESTABLISHING HCS BOUNDARY CONDITIONS

The Helmholtz coil was designed to produce a magnetic field twice the value of Earth's field in each of its lenses. This allows the coil to produce an opposing field to the Earth's magnetic field, which in turn produces a null biased field inside the coil. Then the system can create a field simulating an object moving in any position of the earth's globe, specially the field seen by an object in low orbit showing a complex dynamics.

Referring to the latest version of the world magnetic model, the WMM2015, and to attend the above requisite with a safety margin of about 25 %, each lens should generate at least 180 μT (1.8 gauss).

Considering the optimum design of a square Helmholtz coil [3], [18], the relationship between the magnetic field intensity, given in tesla (T), generated by each lens as a function of the current I applied to it, the number of turns n of enamelled copper wire wrapped in its pair of coils, and its side length S_L is given by (20).

$$B = 1.628733 \cdot 10^{-6} \times \frac{nI}{S_L} \tag{20}$$

From (20), one can obtain the desired maximum field intensity for a given lens with known side length S_L as a function of the product nI. For instance, if we take the outer lens, which has $S_{L\text{inn}} = 1.00$ m, the minimum value of nI so the system can generate at least 180 μT is

$$(nI)_{\min} \geq 110 \text{ ampere-turn.} \tag{21}$$

The relation stated by (21) is essential to the design of both the Helmholtz coil and the HCS. The lens' coils number of turns and the maximum current necessary to achieve the desired field are tightly related.

For example, by increasing the number o turns, a lower current is needed to generate the desired field. There are two consequences within this scenario.

First, the inductance of the lens depends on the square of the number of turns n, so

$$L = k_\alpha n^2, \tag{22}$$

where the multiplicative term k_α is a constant factor of proportionality. Therefore an increase in the lens' coils number of turns will increase its inductance. According to (12) this will reduce the current effectively applied to the lens, reducing also the field generated as the frequency of the current signal applied increases. This has an impact on the VCCS, since it has to generate higher currents to achieve the desired field intensity to compensate the increasing lens' impedance as the current signal frequency increases. Additionally, since the system will operate in closed loop, the plant LR time constant will raise impacting on the system's frequency response. As a consequence, a higher inductance value will limit the scope of field simulations that can be performed with the Helmholtz coil.

Second, the system also must allow the production of controllable small magnetic filed variations, showing enough resolution to the applications which is designed for. Additionally it has to be immune to induced and leaked currents. Such characteristics are difficult to achieve if the maximum current is reduced drastically. For instance, if $B_{\max}$ is produced by a 50 mA current, then to produce 1/1000 of this field the current would be 50 μA. If the current to produce $B_{\max}$ is 1000 mA the fraction 1/1000 thereof would be 1 mA. The latter would have a higher signal-to-noise ratio, i.e., greater immunity to parasitic currents, but the price to pay is the need of a powerful HCS, with higher energy consumption and dissipation.

On the other side, reducing the number of turns may cause problems related to the excessive current necessary to drive the lens and, consequently, the necessity of larger gauge wires. This latter may implicate in issues related to the constructive methods and mechanical design of the lenses. Coiling larger gauge wires requires higher tensions to conform the wire around the lens' structures. The wire, the structures and the machinery required for the winding have to withstand such process. Also, coils with small number of turns are more difficult to produce replicas with the exact same characteristics. Any misalignment in the turns caused by the winding process may impact on its inductance and also on the field generated. In coils with larger number of turns, eventual misaligned turns will be diluted.

If high current levels are needed to drive the system, the HCS electronics will be more complex so the design and construction of dedicated circuits may be necessary due to the lack of commercial-off-the-shelf (COTS) solutions available, such as the power OpAmp (LM675). The maximum voltage that must be provided by the OpAmp mainly depends on the lens impedance, as stated by (10). Thus, the lens' windings resistance should be kept at reasonable values so there are COTS solutions available that are able to produce the maximum voltages to drive the lens. Also, the use of linear topologies may lead to power dissipation problems, so the HCS components must have thermal and physical characteristics to withstand that. Disregarding the limitations described will lead to the use of a non-linear topology, such as a commercial and relatively expensive VCCS.

Based on the above, it is clear that a careful analysis of the Helmholtz coil requirements must guide the choices for the wire gauge, the number of turns and the maximum current necessary to produce the desired magnetic field. Also the

TABLE 1. AWG enameled wire parameters linked with the windings' constructive characteristics.

AWG	D (mm)	S (mm^2)	R/km	R_{292}	$V_{@1.5A}$	$I_{@26V}$
17	1.1500	1.04	16.61	9.70	14.55	2.68
18	1.0240	0.82	20.95	12.24	18.35	2.12
19	0.9116	0.65	26.42	15.43	23.14	1.69
20	0.8118	0.52	33.31	19.45	29.18	1.34
21	0.7230	0.41	42.00	24.53	36.79	1.06

analysis shown must guide the design and component selection for the HCS.

C. PLANNING AND DESIGNING THE COIL'S WINDING

The HCS load resistance can be found from the coil number of turns multiplied by the resistance per meter of the chosen gauge. Also, since the coil dimension L and the necessary magnetic field intensity B were already defined by the coil's application requirements, the factor of $nI = 110$ ampere-turn was obtained as described before. With these information, it is necessary to check the necessary voltage and current ranges so that they match the wire gauge selected. Now, the outer coil has the highest resistance and it is used as the reference calculation.

Considering the power OpAmp LM675 already explained, the output swing has to be within ±26 V / ±3 A. The chosen wire must withstand the project's maximum current and have a winding total resistance bellow the threshold where its voltage drop won't swing over ±26 V, calculated by means of (12).

Based on the above and aiming to avoid OpAmp working close to its limits, we assumed a starting point of 1.5 A as the absolute maximum current to the project, and then calculating and checking if the remaining values both fit the requirements and are viable. In this case the number of turns is defined as $n = 110.6/1.5 \approx 73$. This amount of turns results in almost 292 meters of enamelled wire to the outer coil.

Looking at a typical AWG table data of enameled wire we assembled Table 1, which contains the following information: R_{292} - the resistance of the lens (two windings connected in series with 292 meters of wire each), $V_{@1.5A}$ - the necessary voltage to produce 1.5 A thought the lens, $I_{@26V}$ - the maximum current that could be produced with ±26 V applied to the winding.

From Table 1 and aware of the LM675 OpAmp characteristics one can choose the most suitable gauge wire. Another fact to be considered is that AWG 17 to 21 wires are malleable enough and can withstand enough tensile strength during coiling. Also, lenses produced with wires from AWG 17 to 19 require less than 26 V to produce the desired current necessary to the maximum magnetic field.

For the middle and inner lenses, the nI product is lower than the one for the outer lenses, as shown in (21). Applying the same current constrain of 1.5 A and knowing that the number of turns and the lenses principal dimension are smaller than those for the outer lens, the middle and inner lenses winding resistances will be also lower than the outer lens resistance. Consequently, the chosen wire gauge for the outer lens is suitable for the middle and inner lenses.

TABLE 2. Electrical parameters obtained on the Helmholtz coil prototype.

Coil	Length (m)	Turns (n)	Resistance (Ω)		Inductance (mH)	
			A	B	A	B
inn	221.8	63	5.89	5.89	8.90	11.1
med	270.7	72	7.13	7.13	15.0	13.6
ext	292.0	73	7.60	7.61	15.8	16.3

Based on facts above, it was decided to employ the AWG 19 on the Helmholtz coil. After building a lens, each of its windings had its resistance and impedance measured. These are presented in Table 2. The resistance and inductance were measured using a 4263B RLC meter from Keysight Technologies. The wire length for each winding were calculated based on the coil side length and the number of turns. Again, all other details of the project can be found in [4].

D. DESIGNING THE HCS CIRCUIT

According to the manufacturer, the LM675 OpAmp must have a minimum closed-loop gain of 10 to be stable. The HCS circuit (Fig. 1) was configured with a 10.1 gain, so the following relation based on (7) must obey (23).

$$\frac{R_4}{R_3} = \frac{R_{2a} + R_{2b}}{R_1} = 10.1 \tag{23}$$

The R_{2b} resistance value must be carefully chosen. It must be much smaller than the remaining HCS resistors, as stated on the discussion presented in section III-B.

Additionally, R_{2b} should be as low as possible to minimize the ohmic loss, as can be seen on Fig. 1, and to minimizie the power losses in the form of heat that must be dissipated. Also, the maximum current that can be driven to the load will be limited by R_{2b}, as shown in (10).

On the contrary, diminishing R_{2b} in excess can increase the transconductance gain to an undesired point, as can be seen in (8). This will impact on the current resolution that can be achieved by the HCS and also on its immunity to noise, as exemplified in section IV-B.

Having said that, to define R_{2b} we first rewrite (12) isolating R_{2b} and knowing that $R_{2b}/(R_1 + R_{2a}) \ll 1$, so

$$R_{2b\,\max} \approx \frac{v_{o\,\max}}{I_{L\,\max}} - \sqrt{R_s^2 + (\omega L_s)^2} \tag{24}$$

Equation (24) establishes a relation between R_{2b} maximum resistance value and the signal frequency that can be applied to the lens.

Using the fact the OpAmp maximum output voltage is 26 V, we can plot curves of R_{2b} as a function of the input signal frequency for various maximum currents applied to the lens. Given that signals up to 25 Hz are sufficient for the aerospace applications aforementioned, we considered a frequency range from 0 to 50 Hz for the analysis. Using the outer lens impedance (see Table 2) and different maximum current values, the boundary curves of R_{2b} were plotted on Fig. 2.

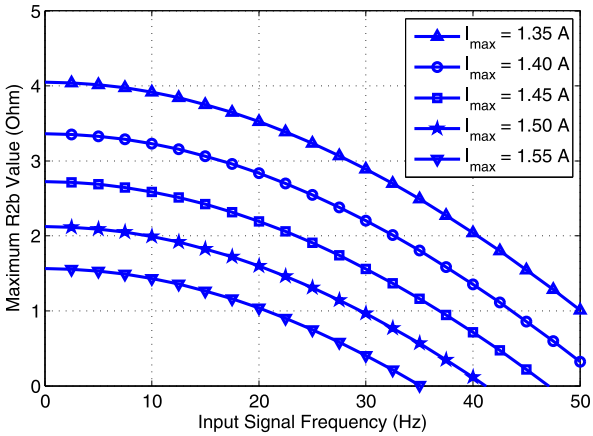

FIGURE 2. Maximum allowed shunt resistor (R_{2b}) based on the input signal frequency and peak current.

Considering a current limit of 1.5 A and input signals close to 25 Hz at most, we can infer that $R_{2b} < 1.5\ \Omega$. From that, a 1.2 Ω resistor was chosen. Flowing 1.5 A through R_{2b} will dissipate 2.7 W, making it possible to employ a typical 5 or 10 W power resistor, so:

$$R_{2b} = 1.2\ \Omega \tag{25}$$

In practice, the curve for the limit of 1.35 A in Fig. 2 should be realistic. In the beginning we established some boundary conditions to dimension the lenses and the HCS constructive parameters. The maximum magnetic field magnitude were overestimated to 180 μT as an initial design precaution. The Earth's magnetic field were the Helmholtz coil is operational have a magnitude lower than 40 μT and the fields to be synthesized by the coil should not have a magnitude greater than 80 μT. But we should account for the fact that as the input signal frequency increases the lens impedance seen by the OpAmp output also increases. Also it was difficult to estimate the lens impedance due to its winding length/cross-sectional area ratio. That justified the initial field magnitude value.

Additionally from Table 1, the AWG 19 wire chosen allow for the outer lens a total winding resistance of 15.43 Ω, which permits 12 % more current than the initial parameter of 1.5 A at the OpAmp maximum voltage (26 V). In the same way this happens to the other two lenses. Also the lenses measured ohmic resistance were sightly lower than the initial estimated values. These facts allow for a higher maximum current and consequently a higher field could be generated.

Again from the 1.35 A curve in Fig. 2 and for $R_{2b} = 1.2\Omega$, one can see that the system could generate magnetic fields with frequencies reaching almost 50 Hz. Obviously, for lower currents and consequently for lower field magnitudes the system frequency bandwidth will increase accordingly.

From (23) and (25), the value of R_{2a} was calculated as 10099 Ω. In practice, R_{2a} is obtained by a series and parallel combination of three resistors: [10000 + (100 // 8200)] = 10099 Ω.

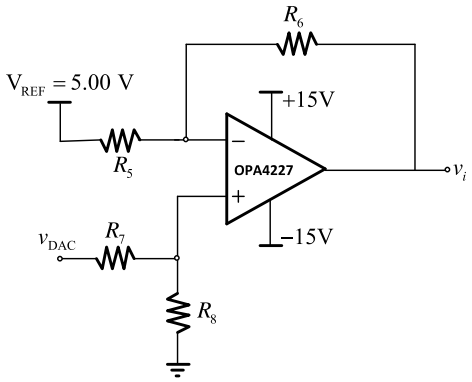

FIGURE 3. Signal conditioning circuit to adequate the dSPACE DAC output voltage range to the HCS input voltage v_i.

Now with the system parameters dimensioned and all resistance values determined, we can obtain the trasconductance gain value and rewrite (8) as

$$i_L = -\frac{R_4}{R_3 R_{2b}} v_i = -8.416667 v_i \tag{26}$$

E. HCS INPUT SIGNAL CONDITIONING

From (26), one can see that for a control voltage varying in the interval ±163.960 mV, the ouput current will vary between the maximum current limit of ±1.38 A.

In this project, the Helmholtz coil is controlled by a dSPACE modular Hardware described in [4]. The modular hardware has a digital to analog converter (DAC) board which generates control signals varying asymmetrically from 0 to 10 V from its outputs. Each output controls its correspondent lens HCS through a signal conditioning circuit that convert the DAC asymmetrical voltage interval output to a voltage interval of ±163.960 mV. This conditioning circuit is presented in Fig. 3.

In the circuit in Fig. 3, the OpAmp is configured as a differential amplifier. If $R_5 = R_7 = 100$ kΩ and $R_6 = R_8 = 3.3$ kΩ, the output voltage (v_i) is given by (27).

$$v_i = \frac{R_6}{R_5}(v_{\text{DAC}} - V_{\text{REF}}) = 0.033 \times (v_{\text{DAC}} - 5) \tag{27}$$

Replacing v_i of (27) in (26), the HCS output current as a function of the DAC output is shown in (28).

$$i_L = -0.27775 \times v_{\text{DAC}} + 1.38875 \tag{28}$$

F. DESCRIPTION OF THE BUILT VCCS

The entire schematic of one VCCS channel is depicted in Fig. 4. There are three channels in the system, each one supplying its respective Helmholtz coil lens. The control input voltage is represented by v^i_{DAC} and the output current is represented by i^i_L, supplied to the Z^i_L lens. The superscript i indicates one of the three channels labeled x, y or z. The first stage of this circuit is the input signal conditioning stage (see Fig. 3) and the second stage is the HCS (see Fig. 1). In the VCCS schematic there are also two linear regulators with

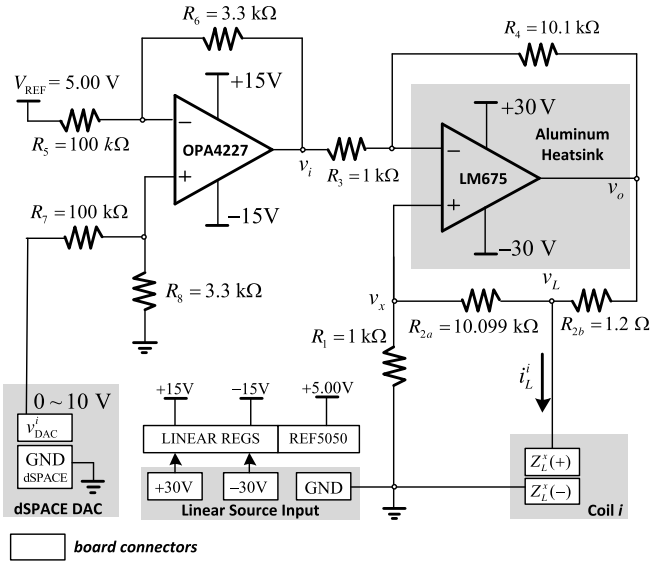

FIGURE 4. Schematic diagram showing one of the VCCS' channels.

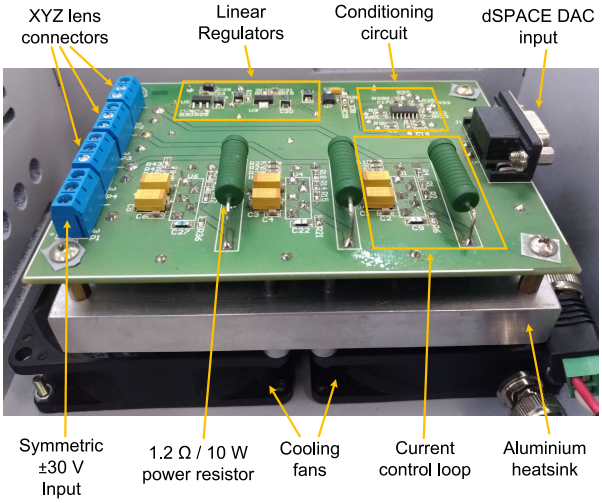

FIGURE 5. Assembled electronic system showing all three VCCS' channels. Each LM675 is mounted directly into the aluminum heatsink.

outputs regulated to +15 V and −15 V, respectively. These supply the OPA4227. At last, there is a precision voltage reference, REF5050, connected to the first stage inverting input. The OPA4227 and the REF5050 have low noise and low drift to improve the system performance. They are manufactured by Texas Instruments. The VCCS is powered by two Agilent E6334A power supplies, operating as a symmetric ±30 V / 5 A voltage sources.

Fig. 5 shows the assembled VCCS mounted together with the heatsink and the two fans used to cool the system by forced convection. The figure also indicates the relevant components and subsystems. The printed circuit board assembly reveals the simplicity of the proposed VCCS.

V. VCCS MEASUREMENTS AND ANALYSIS

The VCCS results were similar across all channels. Therefore, the results shown in the following three

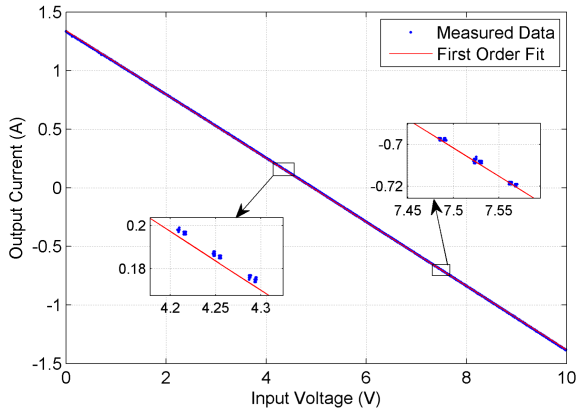

FIGURE 6. HCS channel one current response versus v_{DAC}^i during a 5 hour testing and 18 similar cycles.

subsections refers to the channel that powers the outer lens. The first shows a linearity test, aiming to calibrate the VCCS transfer function and to infer about its statistics. This section also presents a test to investigate the effects of power resistor temperature variation. The next subsection focus on evaluating the VCCS low-frequency noise and stability in a long period. The last one describes both the step response and the maximum current versus signal frequency analysis.

A. HCS LINEARITY AND CALIBRATION TEST

Equation (28) is the VCCS transfer function. To verify that equation and the system linearity an experimental procedure was performed. Also it was possible to infer about the system temperature immunity.

The dSPACE modular hardware was configured to generate continuously 18 voltage cycles by varying the outer lens DAC output. The cycles were generated starting at 5 V, which in practice will drive the VCCS to produce a current close to zero ampere through the lens. The voltage is gradually increased to 10 V, producing close to −1.38 A. Then the voltage is swung back to 0 V, producing near 1.38 A. Finally the voltage is swung forward to 5V, ending the cycle. Every cycle has 512 steps of 39.0625 mV each and the voltage is kept constant for 2 s between steps. During the procedure the DAC input voltage, the VCCS output current and the R_{2b} temperature were measured and acquired by an acquisition system. The procedure had a total elapsed time of 5:08:28 h. The output current and input voltage points collected in each one of the 18 cycles are plotted as different curves in Fig. 6 and they appear superimposed.

A third order polynomial fit was made for each of the 18 curves. The fitting results are summarized in Table 3. The zero and first order coefficients A and B are close to the bias and scale factor found in (28), respectively. The standard deviations of these coefficients show that the VCCS has an acceptable linearity. Also, to corroborate this, the second and third order coefficients are 10^3 and 10^4 smaller than the first order one, respectively.

Since the behaviour of the VCCS is essentially linear, a first order fit was calculated for each of the 18 performed cycles,

TABLE 3. Third order polynomial fit coefficients of $i_L \times v^i_{DAC}$ for all 18 cycles completed in the test.

Cycle	Coef. A	Coef. B	Coef. C	Coef. D
1	1.333576	−0.266970	−7.74E-04	2.57E-05
2	1.333518	−0.266900	−7.92E-04	2.70E-05
3	1.333580	−0.267250	−6.92E-04	2.02E-05
4	1.333600	−0.266929	−7.85E-04	2.63E-05
5	1.333445	−0.266872	−7.91E-04	2.64E-05
6	1.333521	−0.266948	−7.72E-04	2.52E-05
7	1.333599	−0.266953	−7.80E-04	2.61E-05
8	1.333666	−0.266959	−7.80E-04	2.62E-05
9	1.333587	−0.267008	−7.63E-04	2.49E-05
10	1.333465	−0.266888	−7.87E-04	2.62E-05
11	1.333576	−0.266998	−7.67E-04	2.52E-05
12	1.333472	−0.266928	−7.86E-04	2.65E-05
13	1.333491	−0.266900	−7.93E-04	2.68E-05
14	1.333536	−0.266866	−7.98E-04	2.70E-05
15	1.333638	−0.266921	−7.79E-04	2.59E-05
16	1.333662	−0.266917	−7.78E-04	2.59E-05
17	1.333690	−0.266934	−7.71E-04	2.54E-05
18	1.333521	−0.266866	−7.79E-04	2.56E-05
average	1.333562	−0.266953	−7.74E-04	2.56E-05
std. dev.	±0.0000724	±0.0000867	±0.23E-04	±0.15E-05

TABLE 4. First order polynomial fit coefficients of $i_L \times v^i_{DAC}$ for each performed cycle during the test.

Cycle	Coef. A	Coef. B
1	1.341292	−0.272393
2	1.341250	−0.272378
3	1.340846	−0.272336
4	1.341317	−0.272397
5	1.341242	−0.272389
6	1.341285	−0.272394
7	1.341286	−0.272393
8	1.341338	−0.272393
9	1.341258	−0.272391
10	1.341283	−0.272394
11	1.341218	−0.272384
12	1.341181	−0.272394
13	1.341254	−0.272406
14	1.341336	−0.272405
15	1.341354	−0.272372
16	1.341390	−0.272362
17	1.341363	−0.272344
18	1.341283	−0.272340
average	1.341251	−0.272380
std. dev.	±0.0001175	±0.0000218

whose coefficients are presented in Table 4. The calibrated VCCS transfer function is given by the mean value of these coefficients and is given by (29). The calibrated curve is also shown by the red line in Fig. 6.

$$i_{Lcal} = -0.27238 \times v_{\mathrm{DAC}} + 1.34125 \tag{29}$$

Comparing (29) with the calculated transfer function in (28), one can see their parameters are very close. To evaluate this first order calibration, each one of the measurements shown in Fig. 6 was subtracted from the expected current value given each v_{DAC} point. This result is shown in Fig. 7, which also includes the average error curve.

Inspecting Fig. 7 one can see that the maximum positive error was ≈ 4 mA, while the maximum negative error was ≈ 7.5 mA. Therefore, the first order calibration equation

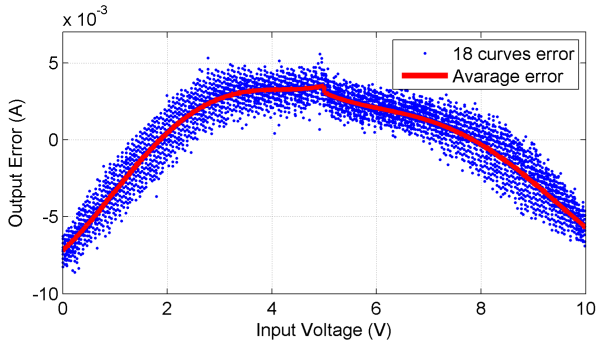

FIGURE 7. Difference between the first order calibrated curve and all measured data during the 18 cycles and its average curve.

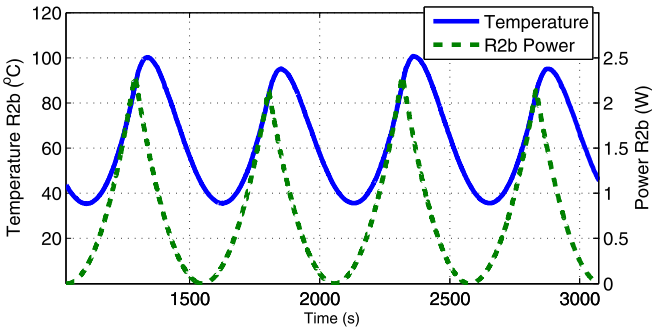

FIGURE 8. Temperature and power over R_{2b} resistor measured during 2 out of the 18 cycles.

results in an error with peak to peak of 11.5 mA given the full input range. As the output swings from ≈ ±1.38 A, the maximum percentage error is: 100 × (0.0115/2.76) ≈ 0.42%.

The R_{2b} temperature and also the calculated power dissipated at this resistor can be seen in Fig. 8, which shows only two cycles for a better viewing. During the most critical cycle, the resistor temperature went from 35 °C up to a maximum of 105 °C.

The analysis in section III-B showed that the temperature variation of R_{2b} is a critical source of errors in the HCS. As the temperature variation was ≈ 70°C, one can suspect that the equivalent current error might be caused by R_{2b} temperature span. By rearranging (17), given (13) and (25), assuming a TCR(R_{2b}) = −80 ppm/°C [17], ΔT = 70 °C, $I_{\max}$ = 1.38 A and considering that the input voltage is constant, thus

$$|\Delta i_{L\,\mathrm{calc}}| = \left|\frac{\Delta R_{2b}}{R_{2b}} i_L\right| \approx 7.7 \text{ mA} \tag{30}$$

This result indicates that R_{2b} variation might be one of main sources of the error observed in Fig. 7. In order to evaluate if that was indeed the case, a new test procedure was planned aiming to keep R_{2b} temperature as constant as possible. The procedure discussed in the next paragraph does not seek to provide a practical solution to cool the system in daily usage.

The apparatus used to maintain R_{2b} constant is depicted in Fig. 9. The resistor was placed inside a PVC pipe immersed in a water reservoir. Ice cubes were constantly fed to the reservoir to maintain the water temperature constant. A pump

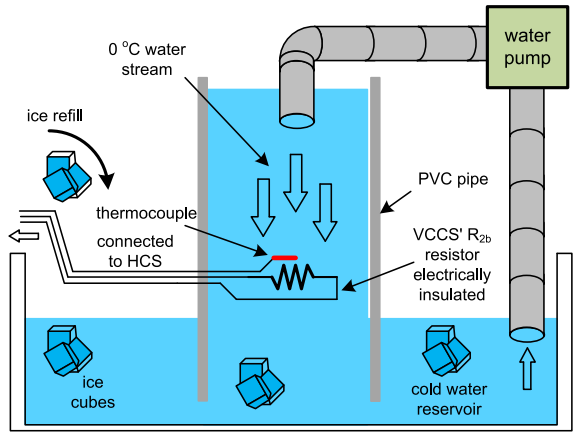

FIGURE 9. Description of the procedure used to minimize R_{2b} temperature variation during the HCS cycling test.

TABLE 5. Third order polynomial fit coefficients obtained in HCS channel one $i_L \times v_{DAC}^i$ to the constant temperature test.

Cycle	Coef. A	Coef. B	Coef. C	Coef. D
1	1.316989	−0.264072	−6.05E-04	3.53E-05
2	1.317538	−0.264310	−5.59E-04	3.22E-05
3	1.317855	−0.264126	−6.24E-04	3.55E-05
4	1.317538	−0.263523	−7.95E-04	4.70E-05
5	1.316509	−0.263342	−7.71E-04	4.42E-05
6	1.316726	−0.264082	−5.74E-04	3.31E-05
7	1.316436	−0.264062	−5.62E-04	3.19E-05
8	1.316720	−0.264228	−5.26E-04	3.01E-05
9	1.317194	−0.264249	−5.53E-04	3.18E-05
10	1.317370	−0.264349	−5.34E-04	3.05E-05
11	1.317495	−0.264291	−5.58E-04	3.21E-05
12	1.317754	−0.264420	−5.38E-04	3.07E-05
13	1.317929	−0.264425	−5.47E-04	3.14E-05
average	1.317233	−0.264112	−5.96E-04	3.43E-05
std. dev.	±0.000513	±0.000329	±0.87E-04	±0.53E-05

produces a water stream inside the tube, directly around the resistor R_{2b}, and a thermocouple measured R_{2b} temperature. Data were acquired similarly as in the non-constant temperature test. 512 points were taken per cycle with the same sample interval and input voltage steps.

During the second experiment, it was possible to complete 13 cycles while the observed thermocouple temperature were between 0 and 1°C. A third order fit was taken for each cycle data, which is shown in Table 5. The coefficients are of a similar order of magnitude as those of Table 3, which showcases the HCS's linearity. However, the first order coefficient is reduced compared to the first test. This shows that the system transconductance has changed when R_{2b} was kept at a lower temperature. Since this resistor's TCR is negative, its resistance raises as the temperature drops. Consequently, the transconductance gain seen in (8) was reduced.

Once again, a first order calibration fit was taken given the HCS linearity. These coefficients are summarized in Table 6 and the calibrated function is seen in (31). Now, for each v_{DAC} measurement across all cycles, the difference (i.e. the error) was computed between the measured current value and that predicted by the calibrated equation. This result, similar to

TABLE 6. First order polynomial fit coefficients obtained in HCS channel one $i_L \times v_{DAC}^i$ to the constant temperature test.

Cycle	Coef. A	Coef. B
1	1.319965	−0.266936
2	1.320377	−0.266998
3	1.321108	−0.267165
4	1.321336	−0.267238
5	1.320462	−0.267067
6	1.319623	−0.266835
7	1.319381	−0.266806
8	1.319421	−0.266772
9	1.320010	−0.266913
10	1.320147	−0.266944
11	1.320341	−0.266980
12	1.320530	−0.267026
13	1.320735	−0.267065
average	1.320264	−0.266980
std. dev.	±0.0005972	±0.0001354

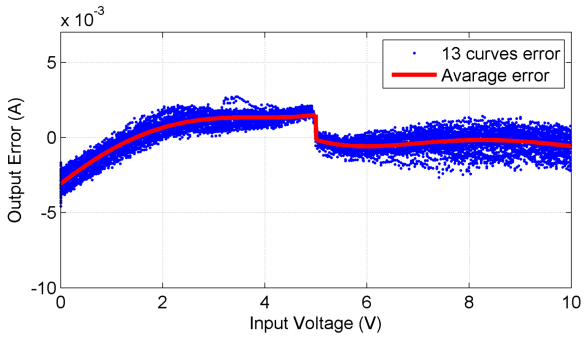

FIGURE 10. Difference between the first order fit curve and all measured data during the 13 cycles and the average curve obtained during the constant temperature test.

the one of Fig. 7, is shown in Fig. 10.

$$i_{L0deg} = -0.26698 \times v_{DAC} + 1.32026 \quad (31)$$

The first order calibration error for the zero degree environment test, seen in Fig. 10, is clearly asymmetric with respect to the positive and the negative cycle. For negative output currents ($5 < v_{DAC} < 10$ V) the error exhibits a very small variation. For positive output currents ($0 < v_{DAC} < 5$ V) it is kept almost constant for currents up to 0.70 A ($v_{DAC} = 2.5$ V), but above that it varies considerably. Furthermore, there is a crossover error of $\approx$ 2 mA in the neighborhood of null output current ($v_{DAC} = 5$ V).

Moreover, given that R_{2b}'s temperature was stable during the test, we can conclude that the error seen in Fig. 10 is unrelated to R_{2b} temperature variation and that it has a non-linear behaviour over the full output current range. By comparing Figs. 7 and 10 we can infer that the error caused by R_{2b} temperature swing has the same magnitude of the one caused by others reasons.

Though the errors of Fig. 10 were not carefully investigated, those non-linearities occurred within the power HCS stage, and, therefore, are related to the LM675 circuit. Owing to these results and that both the power resistor and the OpAmp used were low cost components, it is likely that improving both would result in an improved linearity and,

thus, an even better result considering a first order calibration. In this direction, a chassis-mounted power resistor, with lower TCR and higher power rating, as well as a power OpAmp with better specifications would be recommended.

Despite the discussion about errors, the first order result obtained under normal operation is considerably good. The output current has no compensation as the system is operating in an open-loop design, and, still, the error was smaller than 0.5% throughout the operating range. It must be noted that the VCCS designed is to be used to drive current through the magnetic lenses to generate magnetic field in a closed-loop system, which is discussed in [4]. The results seen in that paper show that the VCCS errors presented here (among others related to the triaxial coil assembly) are compensated by the controller, and that the magnetic field response is not influenced by the open-loop error of the HCS.

B. HCS LONG-TERM STABILITY

The HCS current output has to be as quiet as possible to a constant input signal. To evaluate the output noise and stability over a long time, the dSPACE DAC output was programmed to a constant value while the current through the coil was measured using a precision ammeter. For this test, a 3458A 8-1/2 digit multimeter was used to acquire four current samples per second.

The dSPACE output was set at a random value, which in this case was close to $v_{\text{DAC}} = 3.40$ V. The data was acquired during 4200 seconds, and all the samples were used to generate a Gaussian fit distribution.

This result is seen in Fig. 11. The first plot (a) shows the measured current data bounded by the standard deviation limits from the mean value, represented by the dashed lines. The outer continuous lines represent the limits of a resolution equivalent to $\pm 1/2$ LSB considering the dSPACE DAC converter. The second plot (b) displays the data histogram as well as the Gaussian fit, which yielded a mean value of 465.093 mA and a standard deviation of ± 41.58 μA.

Using the 12 bits dSPACE DAC results in a resolution of ≈ 660 μA/LSB. That is, the source stability seen is considerably better than the output resolution. Therefore, this last could be improved using a better equipment to generate v_{DAC}, without missing effective bits due to the VCCS's noise.

C. STEP RESPONSE AND MAXIMUM CURRENT VERSUS SIGNAL FREQUENCY

The step response allows to identify the load inductance effect and also the delay coefficient in the coil's transfer function $H(s) = 1/(\tau s + 1)$. The maximum current versus frequency aims to verify the VCCS capacity to drive the lens as a function of the input signal frequency. This topic was discussed in section II-B.

The step response of the VCCS was measured by applying a signal that abruptly varies from 5 to 0 V at the input v^i_{DAC}, resulting in a current step from 0 A to the maximum in the HCS. The voltage across R_{2b} was sampled using a KEYSIGHT MSOX3054A oscilloscope and the equivalent

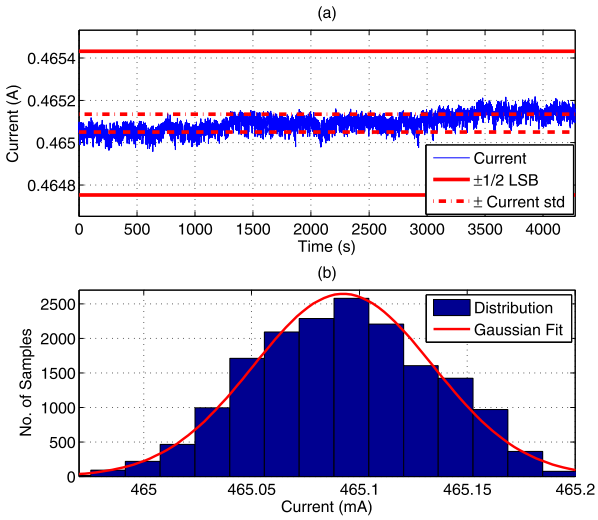

FIGURE 11. Low-frequency stability test result versus time (a) and the current distribution and normal fitting (b).

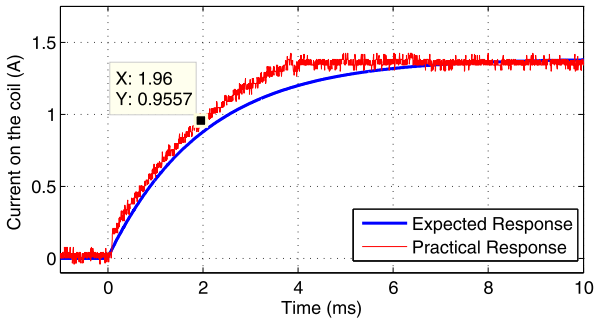

FIGURE 12. Expected step response and measured one to the outer coil.

current was calculated. The expected theoretical result can be described by

$$i_L = i_{L0}\left[1 - e^{-t/(L/R)}\right]u(t), \tag{32}$$

where the outer coil's L and R parameters were given in Tab 2. The relation L/R is the time constant τ of this coil lens.

Fig. 12 shows both the theoretical response and the measured one. Small differences in both graphs are caused by the the error in inductance measurements. The coil's inductance is very sensitive to magnetic field variations caused by the proximity of magnetic materials and electrical equipment. The measurement of the coil time constant is important to the design of any external control loop that can be employed. In this case, the closed-loop control is described in [4].

Section II-B addressed how the power resistor value, the load's impedance, the maximum output voltage swing, the current and the signal frequency are conflicting parameters in the VCCS. This is summarized by (12). Therefore, it is important to verify if the system practical frequency response, $i_{L\,\max}$ versus ω, matches the design.

The analytical relationship between $i_{L\,\max}$ and ω is obtained by replacing the known parameters in (12). The practical curve can be estimated by establishing a fixed output

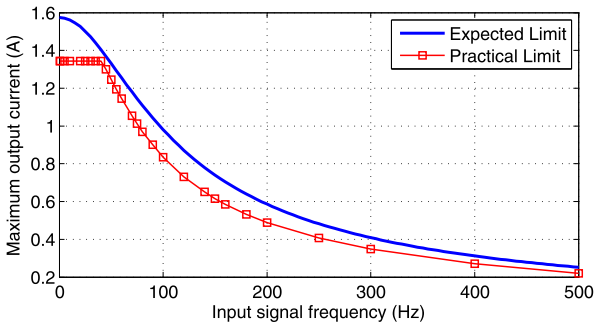

FIGURE 13. Maximal current i_L dependent on the input signal frequency.

current in the HCS and progressively increasing the input signal frequency until the output voltage v_o of the OpAmp reaches its saturation value, or up to the point where non-linearities are seen in the output current. The input signal is a sinusoidal one generated by the dSPACE, while the current value is calculated similarly to the step response, based on the oscilloscopes voltage measurement made over R_{2b}.

Fig. 13 shows both the expected and the practical curves. During the test, the current output had considerable non-linearities when swinging above 25 V, instead of the 26 V expected. That factor resulted in a practical limit slightly lower than the theoretical one.

This result is compatible with the system design and the discussion related to Fig. 2. The HCS design allows signals of up to $\approx$ 40 Hz within the full output current scale (1.38 A). Above this frequency, the load impedance will limit the output current that can be sourced or sinked from the LM675 without swinging above 25 V. For instance, if a 200 Hz input signal has to be considered, the maximum current to prevent non-linearities is $\approx$ 0.50 A. Therefore, from (20), for higher input frequencies the maximum generated magnetic field intensity will be limited.

VI. CONCLUSION

This paper thoroughly addresses the main constrains and limitations involved in matching a Helmholtz coil project and its current source. The steps and decisions necessary to plan the system were carefully discussed, and the technical benefits and issues related to the each aspect of the system were highlighted.

The decisions made in this work are recursive, meaning that after each decision such as R_{2b}, the coil's wire gauge, the maximum current, among others, all other elements must be checked. If small adjustments are made, the hole system has to be re-calculated. Only that way, a final system compatible with the coil's applications can be achieved.

Also, if a time-varying magnetic field is required, more cautious the design has to be. In this scenario, we bring the reader the main limitations and one possible way to plan each Helmholtz coil lenses and the voltage-controlled-current-source.

The system built was planned so that it could be fed using a simple linear solution (the HCS source) based on a power OpAmp. This way, it was avoided the use of commercial sources or inverting switching converters. The first can be quite expensive if we consider that the source must be controlled and have symmetric current. The latter would require a far more complex electronics and control design than a linear one.

The HCS electronic system was built using low-cost and COTS components, making it easy to reproduce. The source had an excellent result regarding its linearity and achieved considerable low errors in open-loop using a first order calibration. It also had an excellent low-frequency stability, which would allow the use of a higher resolution input signal to command the VCCS. The most critical aspects of the built VCCS are the OpAmp, its heatsink, and the choice of the feedback power resistor.

At last, the VCCS design could be improved by using both a power OpAmp and power resistor with better characteristics. The power resistor could be changed by a chassis mount one with a better power and TCR ratings. Such changes would probably improve the open-loop linearity. But as the VCCS is used as part of a closed-loop magnetic field system controlled by a hardware-in-the-loop simulation, a low-cost, simple and fast development design was prioritized.

REFERENCES

[1] S. R. Trout, "Use of Helmholtz coils for magnetic measurements," *IEEE Trans. Magn.*, vol. MAG-24, no. 4, pp. 2108–2111, Jul. 1988.
[2] M. Pastena and M. Grassi, "Optimum design of a three-axis magnetic field simulator," *IEEE Trans. Aerosp. Electron. Syst.*, vol. 38, no. 2, pp. 488–501, Apr. 2002.
[3] F. Piergentili, G. P. Candini, and M. Zannoni, "Design, manufacturing, and test of a real-time, three-axis magnetic field simulator," *IEEE Trans. Aerosp. Electron. Syst.*, vol. 47, no. 2, pp. 1369–1379, Apr. 2011.
[4] D. S. Batista, F. Granziera, M. C. Tosin, and L. F. de Melo, "Three-axial helmholtz coil design and validation for aerospace applications," *IEEE Trans. Aerosp. Electron. Syst.*, vol. 54, no. 1, pp. 392–403, Feb. 2018.
[5] F. M. Poppenk, R. Amini, and G. F. Brouwer, "Design and application of a Helmholtz cage for testing nano-satellites," in *Proc. 6th Int. Symp. Environ. Test. Space Programmes*, Noordwijk, The Netherlands, 2007, p. 14.
[6] A. Klesh, S. Seagraves, M. Bennett, D. Boone, J. Cutler, and H. Bahcivan, "Dynamically driven helmholtz cage for experimental magnetic attitude determination," *Adv. Astron. Sci.*, vol. 135, no. 1, pp. 1–14, 2009.
[7] Q. Cao, X. Han, B. Zhang, and L. Li, "Analysis and optimal design of magnetic navigation system using Helmholtz and Maxwell coils," *IEEE Trans. Appl. Supercond.*, vol. 22, no. 3, Jun. 2012, Art. no. 4401504.
[8] D. Arnaudov and B. Sokerov, "Power supply for Helmholtz coil," in *Proc. 9th Nat. Conf. Int. Participation (ELECTRONICA)*, May 2018, pp. 1–4.
[9] *A Comprehensive Study of the Howland Current Pump*, Texas Instrum., Dallas, TX, USA, 2013.
[10] A. Mahnam, H. Yazdanian, and M. M. Samani, "Comprehensive study of Howland circuit with non-ideal components to design high performance current pumps," *Measurement*, vol. 82, pp. 94–104, Mar. 2016.
[11] C. J. Poletto and C. L. Van Doren, "A high voltage, constant current stimulator for electrocutaneous stimulation through small electrodes," *IEEE Trans. Biomed. Eng.*, vol. 46, no. 8, pp. 929–936, Aug. 1999.
[12] P. Bertemes-Filho, A. Felipe, and V. C. Vincence, "High accurate Howland current source: Output constraints analysis," *Circuits Syst.*, vol. 4, no. 7, pp. 451–458, 2013.
[13] J. Anudev and I. J. Raglend, "Analytical study of Howland current source model," in *Proc. Int. Conf. Comput., Electron. Elect. Technol. (ICCEET)*, Mar. 2012, pp. 314–318.
[14] M. A. Schaning and K. A. Kaczmarek, "A high-voltage bipolar transconductance amplifier for electrotactile stimulation," *IEEE Trans. Biomed. Eng.*, vol. 55, no. 10, pp. 2433–2443, Oct. 2008.

[15] B. P. Sokerov and D. D. Arnaudov, "Modeling and research of magnetic flux generator," in *Proc. IEEE 28th Int. Sci. Conf. Electron. (ET)*, Sep. 2018, pp. 1–4.
[16] I. M. Pandiev, "Analysis and design of voltage-controlled current sources for a grounded load," *Int. J. Circuit Theory Appl.*, vol. 43, no. 6, pp. 756–775, Jun. 2015.
[17] V. Draloric, *Cemented Leaded Wirewound Resistors*, document 28730, Vishay Intertechnology, Malvern, PA, USA, Jul. 2018. [Online]. Available: https://www.vishay.com/docs/28730/acac-at.pdf
[18] J. Spencer and R. Davis, "Helmholtz coils for MIL-STD-462D RS101 testing," in *Proc. IEEE Int. Symp. Electromagn. Compatability Symp. Rec.*, vol. 2, Aug. 1999, pp. 940–942.

DANIEL S. BATISTA (M'12) received the bachelor's and master's degrees from the State University of Londrina, Brazil, in 2014 and 2016, respectively, where he is currently pursuing the Ph.D. degree, all in electrical engineering.

He has been a Researcher and a Collaborator with the Inertial Measurements and Aerospace Instrumentation Laboratory, State University of Londrina, since 2012. His current research interests include electronics systems, embedded systems, instrumentation, sensor calibration, and attitude determination systems.

GUILHERME B. SILVA received the bachelor's degree in electrical engineering from the State University of Londrina, in 2019, where he is currently pursuing the master's degree.

He has been a Researcher with the Inertial Measurements and Aerospace Instrumentation Laboratory, since 2017. His current research interests include electronics systems, embedded systems, instrumentation, and real-time embedded operational systems.

FRANCISCO GRANZIERA, JR. (M'14) received the bachelor's and master's degrees in electrical engineering from the State University of Londrina, Brazil, in 2003 and 2006, respectively, and the Ph.D. degree in space engineering and technology from the National Institute of Space Research, in 2015.

Since 2012, he has been a Researcher with the Inertial Measurements and Aerospace Instrumentation Laboratory, and a Professor with the State University of Londrina. His current research interests include electronics systems involving instrumentation, embedded systems, attitude determination, and Kalman filter.

MARCELO C. TOSIN received the bachelor's degree in physics from the University of São Paulo, in 1994, and the master's and Ph.D. degrees in electrical engineering from the University of Campinas, Campinas, Brazil, in 1998 and 2001, respectively.

Since 2000, he has been the Head of the Inertial Measurements and Aerospace Instrumentation Laboratory and a Professor with the State University of Londrina. His current research interests include embedded systems, inertial sensors, sensor calibration, and attitude determination.

DÉCIO L. GAZZONI FILHO received the bachelor's degree in electrical engineering from the State University of Londrina, Brazil, in 2005, and the master's degree in electrical engineering from the University of São Paulo, Brazil, in 2008.

Since 2012, he has been a Researcher with the Inertial Measurements and Aerospace Instrumentation Laboratory and a Professor with the State University of Londrina, Brazil. His current research interests include electronics systems and real-time embedded systems.

LEONIMER F. MELO received the bachelor's and master's degrees in electrical engineering and the Ph.D. degree in mechanical engineering from the University of Campinas, Campinas, Brazil, in 1985, 2002, and 2007, respectively.

He is currently a Professor of Ph.D. Program with the State University of Londrina, Brazil, where he is also a Collaborator with the Inertial Measurements and Aerospace Instrumentation Laboratory.

APPENDIX D – Initial pages of the paper published in the journal *Measurement*

Title: Analysis and Practical implementation of a high-power Howland Current Source.

Authors: Daniel Strufaldi Batista, Francisco Granziera Jr., Marcelo Carvalho Tosin and Leonimer Flávio de Melo.

Journal: Measurement (ISSN: 0263-2241). Volume 207, Page 112404.

Classification (Qualis-CAPES): A1 / IF$= 5.131$ (Engenharias IV).

Publication Date: Feb 2023.

Measurement 207 (2023) 112404

Contents lists available at ScienceDirect

Measurement

journal homepage: www.elsevier.com/locate/measurement

Analysis and practical implementation of a high-power Howland Current Source

Daniel Strufaldi Batista *, Francisco Granziera Jr., Marcelo Carvalho Tosin, Leonimer Flávio de Melo

State University of Londrina (UEL), Department of Electrical Engineering, Rod. Celso Garcia Cid – PR445, 86057-970, Londrina, PR, Brazil

ARTICLE INFO

Keywords:
Howland Current Source
Voltage-controlled-current-source
Analogue electronics
Operational amplifier
Power amplifier

ABSTRACT

This work presents the theoretical and error analysis, implementation, and validation measurements of a high-power grounded-load voltage-controlled-current-source (VCCS) based on the Howland Current Source (HCS) topology. The VCCS theoretical design can output up to ±2.5 A with ±27.5 V compliance. Typically, biomedical applications use the HCS in the micro and milli-amperes range, and accuracy characterization and error analysis are unseen in the proposed high-current/voltage conditions. Commercially available high-voltage/current operational amplifiers have poor precision specifications compared to precision ones, which makes it a non-trivial problem. The work discusses the HCS theory and presents a thorough analysis of the non-linear errors in the circuit. Practical implementations using different conditions and amplifiers display the effect of those errors in the output current accuracy and linearity. The final design using an OPA544 amplifier yields an accuracy superior to 0.075% after a first-order calibration when driving up to a ±2.10 A current.

1. Introduction

The Howland Current Source (HCS) is a grounded-load linear operational amplifier (OpAmp) based voltage-controlled-current-source (VCCS). The electronic design of an HCS is exceptionally simplistic, requiring a single OpAmp and a bunch of resistors in its improved topology [1,2]. It can provide a very accurate symmetric output and can be built using a typical precision OpAmp. Therefore, the HCS is a high-performance symmetric VCCS that can provide a much simpler solution than other alternatives [3–5].

The HCS is widely used for biomedical applications, such as neural and electrocutaneous stimulation [6–8] and bio-impedance measurement system [1,2]. This latter includes electrical impedance tomography [9,10], impedance cardiograph [11], and others [12,13]. In such applications, if carefully designed, it is possible to combine the construction simplicity with outstanding output impedance, bandwidth, and stability. Therefore, many authors employ the HCS solution in their biomedical systems. In most of these works, the HCS has to output currents in the micro- or tens of milli-amperes range using low-voltage precision OpAmps.

Although the majority of HCS works are on small current ranges, a few authors have shown the possibility of using the HCS on higher current applications [14–18]. The power HCS solution allows a linear solution to the controlled-current source problem and might have a few advantages over other alternatives. It can easily handle negative and positive currents and zero current transitions (crossover) with low errors. It allows simple electronics and a relatively low-cost design using commercial off-the-shelf components. Compared to switching sources, it has a simple design, has few noise problems, and does not require an external control loop. However, power OpAmps have poor precision compared to typical precision amplifiers. Despite being a powerful low-cost alternative, there is a gap in the literature regarding a detailed analysis of the errors, accuracy, and, more importantly, the non-linear errors of the power HCS circuit. The latter is critical in the power design and can severely impact the source's accuracy [18].

The analysis of the power HCS seen in [14] shows the HCS transconductance gain but limits the error discussion to the problems of resistor mismatch impacting the output impedance, which degrades accuracy. Refs. [15,16] follow a similar theoretical examination of the output impedance problems due to mismatch and focus more on detailing their application of the HCS. None of these works quantified their accuracy in their practical implementations. Ref. [17] shows a detailed analysis of the HCS stability and output impedance, and its primary goal is the proposal of a design procedure methodology for the power HCS. It uses as an example a VCCS capable of outputting up to 1 A and ±10 V. The practical implementation uses an OPA564, which can drive up to 1.5 A with a power-supply range of 24 V or ± 12 V. At last, it reports a maximum relative error of around 5%.

* Corresponding author.
E-mail addresses: daniel.strufaldi@uel.br (D.S. Batista), granziera@uel.br (F. Granziera Jr.), mctosin@uel.br (M.C. Tosin), leonimer@uel.br (L.F. de Melo).

https://doi.org/10.1016/j.measurement.2022.112404
Received 30 August 2022; Received in revised form 14 December 2022; Accepted 23 December 2022
Available online 28 December 2022
0263-2241/

In [18], the power HCS is used on a higher current and voltage scenario to drive a magnetic field simulator. Theoretically, that design can drive up to 3 A on a ±27.5 voltage span using an LM675 OpAmp. A first-order calibration improved that circuit accuracy, but the results showed that the power VCCS built using the LM675 amplifier had considerable non-linearities. A practical procedure proved that the power OpAmp and the HCS power resistor influenced the circuit's linearity, and the output current had ±1% of non-linearities when driving up to ±1.35 A for low-frequency currents. This result was adequate to power the magnetic field simulator of [19] because the setup worked in a closed-loop magnetic field topology, compensating for any non-linearities of the current source. As a result, addressing these non-linear errors was not necessary. However, new applications of that system require that the generated magnetic field operates in an open-loop topology. In such circumstances, those HCS errors and that absolute accuracy of 1% translates to a significant inaccuracy in the induced magnetic field. Therefore, an improved design was built and required a thoroughgoing study of the HCS errors. This error analysis and practical investigations are reported here.

Our paper contributes by providing insight into the HCS design using power OpAmps and its characterization, including a detailed analysis of the circuit errors for low-frequency currents. These include the resistor mismatch and variations in the transconductance gain, the R_{2b} resistor influence (see R_{2b} in Fig. 1), offset voltage and bias current, and non-linear errors. Although previous works [1,17,18] observed part of these errors, the characterization was not in detail or the focus. Another novelty shown is the non-linear effects in the circuit owing to heating effects on the OpAmp drifting and the sense resistor R_{2b}. These errors translate to non-linearities in the output for a direct current (DC) or a low-frequency operation, affecting the accuracy and linearity of the circuit. Simulations and practical testing of the VCCS are shown to different amplifiers and distinct circuit conditions to evaluate the mentioned errors. Although the simulations show that heating has a significant impact on the output performance of the power HCS, a SPICE simulation is unlikely to cover and display an exact model of the non-linearities, and practical implementations are necessary to address the power HCS behavior in a particular condition.

The proposed VCCS requires driving a maximum current of 1.35 A (with a theoretical limit of 2.5 A) at 27.5 V (using a ±30 V supply) at a DC or low-frequency output (<100 Hz). The practical implementation uses three amplifiers from Texas Instruments (LM675/OPA544 / OPA548). The study of the HCS operation, accuracy, and errors around those ranges are absent in the literature. Higher voltage and current are possible using other OpAmps options, such as the OPA541 from the same manufacturer or the PA series amplifiers from Apex Microtechnology, but at a considerably higher cost. The calibrated final HCS design had an accuracy and linearities superior to 0.1% when outputting 2.10 A. Such a result is better than those reported in the literature, even if compared to lower voltage and current conditions.

The implementation proves that a low-cost HCS design, built using commercial off-the-shelf components, can achieve outstanding DC and low-frequency performance, as long as the design properly addresses the thermal effects and non-linearities of the circuit. Such conditions and needs for a very accurate and precise power VCCS may arise in other applications, such as component testing, torque control for motors [14], magnetic circuits [15,18], V–I control for valves [17], and others [16]. It is important to note that it is possible to replicate all the analyses conducted to a VCCS in any other current/voltage range.

The remainder of the paper is organized as follows. Section 2 shows the theoretical analysis and constraints of the HCS. The errors and non-ideal study of the HCS circuit are shown in Section 3. Section 4 displays the power HCS requirements, available and possible commercial components, and presents an error budget simulation that evaluates the order of magnitude of all errors discussed in Section 3 for a power HCS. At last, Section 5 shows the practical circuit, the test methodology, and the practical results of the HSC implementation.

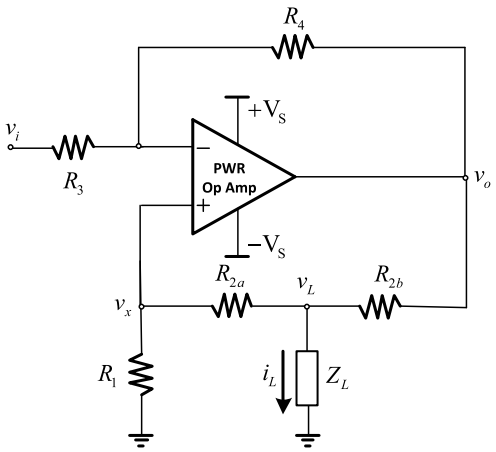

Fig. 1. Electrical circuit of the improved Howland Current Source [21].

2. Howland current source theory

Fig. 1 shows the basic circuit of the improved [1,20] Howland Current Source (or Pump). The HCS seeks to output a current independent of the load and controlled by the applied input voltage v_i to the OpAmp's negative feedback loop. The first step in that circuit is to establish the necessary conditions to ensure it operates as the intended VCCS regardless of the load [17,18], seen in Section 2.1, which also deduce the equations used in the resistor mismatch error analysis. An important aspect of our analysis is that it considers input voltage only in the inverting loop of the circuit. The HCS has different transconductance gains for the positive and negative feedback and driving only one input while grounding the other may avoid unnecessary distortion [21].

The maximum output current value ($i_{L\max}$) and bandwidth are important circuit design constraints. They depend on the OpAmp maximum output voltage (power OpAmps are not rail-to-rail), the voltage drop at the R_{2b} resistor, and the load's impedance Z_L (for non-resistive ones). Therefore, the maximum output current, the maximum output voltage, Z_L, and R_{2b} are interdependent parameters. Also, the maximum current value will depend on the desired output frequency for inductive or capacitive loads. Section 2.2 equates $i_{L\max}$ as a function of the other parameters and discusses these constraints.

2.1. Equating the load's current

The load's current deduction can start by equating the negative feedback loop of the HCS circuit seen in Fig. 1. Since the currents through R_3 and R_4 are the same, then

$$\frac{v_o - v_x}{R_4} = \frac{v_x - v_i}{R_3}. \tag{1}$$

Now, on the positive feedback loop, the current that flows through R_{2a} and R_1 is the same. Thus, it is possible to relate the voltage at the non-inverse input (v_x) and the voltage on the load (v_L), resulting in

$$v_x = v_L \frac{R_1}{R_1 + R_{2a}}. \tag{2}$$

Replacing v_x in (1) from (2) and isolating v_o, we have

$$v_o = v_L \frac{R_1}{(R_1 + R_{2a})} + v_L \frac{R_4 R_1}{R_3(R_1 + R_{2a})} - \frac{R_4}{R_3} v_i. \tag{3}$$

Additionally, the positive feedback loop can be equated as

$$i_L = \frac{v_L}{Z_L} = \frac{v_o - v_L}{R_{2b}} - \frac{v_L}{R_1 + R_{2a}}, \tag{4}$$

APPENDIX E – Initial pages of the paper accepted for publication in the journal *IEEE Sensors*

Title: Attitude-Independent Magnetometer Calibration using Nonlinear Least Squares

Authors: Daniel Strufaldi Batista, Francisco Granziera Jr., Marcelo Carvalho Tosin and Leonimer Flávio de Melo.

Journal: IEEE Sensors (1530-437X). Early access.

Classification (Qualis-CAPES): A1 / IF$= 4.325$ (Engenharias IV).

Publication Date: Available online May 2023.

IEEE Sensors Council IEEE SENSORS JOURNAL, VOL. XX, NO. XX, XXXX 2023 1

Attitude-Independent Magnetometer Calibration using Non-Linear Least Squares

Daniel S. Batista, *Member, IEEE*, Francisco Granziera Jr., Marcelo C. Tosin and Leonimer F. Melo

***Abstract*— This paper presents a new formulation for attitude-independent calibration of three-axis magnetometers. The proposed solution employs a Non-Linear Least Squares (NLLS) estimator that uses the non-linear sensor model proposed by Foster and Elkaim in the well-known Extended Two-Step (ETS) algorithm. Our solution has several advantages over ETS and is more straightforward to implement than many subsequent algorithms. It enables the calculation of the calibration parameters' uncertainties and does not require the assumption that all magnetometer measurements have a constant magnetic field magnitude. The former is essential for evaluating calibration quality, while the latter may be required for on-orbit magnetometer calibration. However, the NLLS has the drawback of requiring an initial parameter estimation to ensure convergence. Therefore, our work presents a new technique to calculate the scale factors and offsets for initializing the NLLS. Simulations and practical implementations demonstrate that our method performs similarly to a recently computed analytical solution of the ETS. Furthermore, a Monte Carlo simulation shows that the NLLS algorithm provides a slightly better estimation of the scale factors than the ETS, in addition to the abovementioned advantages.**

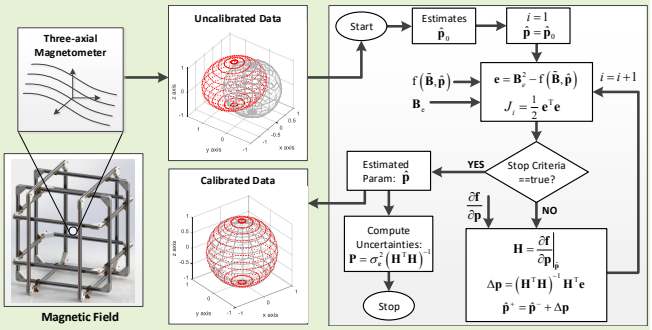

***Index Terms*— Magnetic Field, Magnetometer, Non-Linear Least Squares, Sensor Calibration.**

I. Introduction

THREE-axial magnetic sensors have been used to tackle specific problems in aerospace, defense, military, industry, and others, mainly in navigation applications. However, with technological advances, magnetometers became available as a commercial-off-the-shelf component, opening a new field of low-cost and mass-production applications. These include personal devices or gadgets, healthcare products, drones, and attitude and heading reference systems for low-end avionics and general applications. Furthermore, these sensors are now part of many micro and nanosatellite missions.

Magnetic sensors are subject to many sources of errors, and with low-cost sensors, these problems are worse. Those errors in magnetic sensors are inherently caused by the transductor type and technology used and their fabrication method and tolerances. Magnetometers are also greatly affected by hard- and soft-iron interference caused by the surrounding environment. Furthermore, MEMS technology allowed for highly integrated sensor applications, such as smart devices and nanosatellites, which produce even worse interference for magnetic sensors. All those errors must be dealt with to allow for the proper operation of the sensor application. In most of these, the sensor's measurements are used to determine attitude or provide a reference based on Earth's magnetic field; consequently, a vital topic regarding magnetometers is the attitude-independent calibration problem and its solutions.

The first approach for the attitude-independent problem resulted in the calibration algorithm known as TWOSTEP, which Alonso and Shuster described in [1] and [2]. The former calibrates offset only, and the latter includes scale factors and misalignment between the sensor's axis. Another algorithm, which relies on the premise that the magnetic field magnitude is constant during the calibration process, was proposed by [3] to calibrate scale factors and offsets using a non-linear least squares. Foster and Elkaim [4] proposed an extension of that work to include misalignment angles. This well-known solution, called Extended Two-Step (ETS), rewrites the problem into auxiliary variables and applies a batch least squares next.

Many solutions came afterward, such as the Maximum Likelihood (ML) Estimator of [5] and the optimal ML of [6], the total least-squares solutions of [7], [8], artificial intelligence or adaptive algorithms [9]–[11], among others [12]–[14]. Recently, the works of [15] and [16] compared a few of the previous algorithms.

We also note that many other attitude-independent formulations came to include additional parameters [14], [17]–[20].

Accepted paper Sensors-56200-2023.R1 to the IEEE Sensors Journal. 04 may 2023. "This work was financed in part by the Coordenação de Aperfeiçoamento de Pessoal de Nível Superior - Brasil (CAPES) - Finance Code 001".

All authors are with the Department of Electrical Engineering, State University of Londrina, Paraná, Brazil. (e-mails: daniel.strufaldi@uel.br, granziera@uel.br, mctosin@uel.br, leonimer@uel.br).

For instance, these include the calibration of the magnetometer to a vehicle's or another's sensors frame, unified calibration with inertial sensors, and applications with time-varying bias. However, these go beyond our algorithm's scope and contribution.

We contribute to the attitude-independent calibration problem, including scale factors, offsets, and misalignment angles, similar to the works of [2], [4]. Our paper's novelty is to present the direct application of a Non-Linear Least Squares (NLLS) estimator [21] to the well-known sensor model proposed by Foster and Elkaim [4]. Based on the loss function of the NLLS, it is possible to apply the generalization of Newton's root-solving method using the linearized problem model to find the calibration parameters. Hence, the problem does not need to be rewritten using intermediate variables required by the ETS algorithm. Despite a few differences in the formulation, our method can be related as expansions of the works of [3] and [22], where the authors applied a similar concept to calibrated scale factors and offsets, respectively, for three-axial magnetometers and accelerometers.

Theoretically, the attitude-independent calibration work of Springmann and Cutler [20], which includes time-varying bias parameters, uses a similar minimization technique to estimate the parameters. However, the authors do not explicitly show their solution (their article focuses on the on-orbit nanosatellite calibration, including time-varying bias interference, not on the estimator itself) and indicate that the algorithm's convergence does not depend on the initial parameters. On the contrary, the convergence of the proposed NLLS formulation is not ensured and depends on the parameters' starting value. Appendix I shows evidence of this issue and that, in general, if the NLLS is started with a reasonable estimate of scale factors and offsets, convergence problems are overcome. In this direction, we also present a simplified new formulation to compute the offsets and scale factors, which avoids convergence problems and provides the initial state estimation for the NLLS.

There are a few notable advantages of using the direct NLLS estimator with the non-linear sensor model of the ETS solution. First, it enables the estimation of the Cramér-Rao Inequality lower bounds, which quantify the parameters' uncertainties [21]. Second, it does not require a constant magnetic field magnitude for all measurements; thus, making it suitable for applications such as on-orbit magnetometer calibration, where the field magnitude varies with the spacecraft's position. Third, it is a more straightforward solution than other methods and does not require computing the Hessian matrix, as some algorithms do. Finally, expanding it to include other calibration parameters, such as the time-varying bias proposed in [20], is straightforward.

We compare our algorithm to the analytical solution of the extended two-step (ETS-A) of [4], which was recently computed and shown by [16]. The latter provides a step-by-step solution of the ETS-A algorithm, which allows the exact reproduction. Furthermore, the authors also compare the ETS-A to other algorithms [2], [5]–[7], [14], providing a small survey among their contributions and also comparing their results to other works observations [15], [23]. As a result, it is possible to compare the proposed algorithm and the ETS-A implementation and infer our algorithm performance compared to these other results. Despite the results exhibiting that the proposed algorithm performs very similarly to the ETS-A of [16], the NLLS has a better computational effort and provides a slightly better estimation of the scale factors parameters. Hence, combined with the aforementioned characteristics, it is a simple yet powerful solution to the attitude-independent magnetometer calibration, including offsets, scale factors, and misalignment angles.

The remainder of the paper is organized as follows. Section II briefly recaps the magnetometer errors and presents the sensor model. Sections III and IV show the non-linear least squares (NLLS) solution to the problem and the initial guess algorithm, respectively. Sections V and VI present the algorithm analysis. The former has the simulations, and the latter has the real data analysis.

II. Magnetometer Errors and the Sensor Model

Many authors have discussed the magnetometer errors and model. Our work considers the sensor model of Foster and Elkaim [4]; hence, we redirect readers unfamiliar with the magnetometer errors to that work for a deeper discussion. Additionally, the works of [3], [16], [20] also thoroughly discuss the magnetometer errors. In short, magnetometers are subject to errors either inherent to the sensor or a consequence of elements in their surroundings. The former includes scale factors, null-shift (offset), non-orthogonality, and stochastic sensor noise. The latter includes hard and soft iron distortions, such as those caused by ferromagnetic materials and electronics.

Most calibration authors assume models that compensate for those errors. However, we must note that only time-invariant hard and soft iron errors are compensated. In other words, the model accounts only for sources of errors attached to the same body frame as the magnetometer; thus, the field interference due to hard and soft iron does not depend on the device's or vehicle's attitude. Another consideration is that electronic systems (electrical currents) attached to the device and closed to magnetometers may cause time-varying interference [20]. Again, most models [1]–[4], [16] consider only time-invariant errors. We note here that the time-invariant model and the NLLS solution are expandable to include time-varying bias [24], using the sensor model seen in [20]. The non-linear least squares solution is similar to both conditions.

The time-invariant sensor model of [4] assumes that a nine-parameters model compensates for all previous errors. That is possible because some errors are not distinguished mathematically from one another. For example, hard iron effects and the sensor's null shift error are mathematically identical. The same is true for soft iron interference, which results in a mathematical error similar to scale factors and misalignment inherent to the sensor. Therefore, separating soft iron from null shift (bias) and separating the effects of hard iron from scale factors and non-orthogonality is unfeasible. Thus, the mathematical sensor model is reduced to nine parameters.

The resulting sensor model has nine parameters, including offset and scale factor in each axis and three misalignment

ANNEX I – Specification Sheets of the Magnetic Sensors

This annex includes the mains specification sheets of the magnetometers available at the magnetic field simulator and discussed in Chapter 2. The subsequent pages display:

1. The fluxgate sensor FGM3D/250 [39] specification sheet, in Fig. A.I.
2. The low-cost magneto-resistive HMC5883L [44] magnetometer specification sheet, in Fig. A.II.
3. The magnetometer and the inertial sensors specification sheet of the compact and precision ADIS16448 [45] inertial sensor, in Fig. A.III.
4. The magnetometer and the inertial sensors specification sheet of the Spatial AHRS [43], in Fig. A.IV.

SENSYS®
Magnetometers & Survey Solutions

FGM3D TECHNICAL SPECIFICATION

	FGM3D/4	FGM3D/75	FGM3D/100	FGM3D/125	FGM3D/250	FGM3D/500	FGM3D/1000
Measurement range [µT]	±4	±75	±100	±125	±250	±500	±1,000
Sensor point of reference	See housings types next page						
Declination between axes	≤ ±0.5° (Standard) / ≤ ±0.1° (Option)					≤ ±0.5°	
Declination total	≤ ±1° (Standard) / ≤ ±0.12° (Option)					≤ ±1°	
Resolution	< 150 pT						
Noise [0.1 ... 10 Hz]	>10...≤ 20 pT (Standard) / >7...≤ 10 pT (Dual-use)					> 10...≤ 20 pT	
Cut off frequency (bandwidth)	2 kHz	4 kHz		3 kHz	2 kHz		
Temperature drift	≤ ± 0.3 nT/K						
Zero error	≤ ±5 nT						
Relative error of measurement	±0.1 %					±0.5 %	
Stability	< 5 nT						
Linearity	< 20 ppm						
Sensitivity	2.5 V/µT	0.13 V/µT	0.1 V/µT	0.08V/ µT	0.04V/ µT	0.02V/ µT	0.01V/ µT
Supply voltage	±12 V ... ±15 V						
Current consumption	±26 mA						
Output	±10 V @FS						
Output impedance	< 1 Ω						
Operating temperature	-20 °C to +75 °C						
Storage temperature	-40 °C to +80 °C						
Dimensions	See housings types next page						
Weight w/o cable / Volume	See housings types next page						
Ingress protection	See housings types next page						
Vibration stability	BV044 (partly)						

+49 33631 59 650
info@sensys.de
www.sensys.de

Figure A.I: FGM3D/250 fluxgate magnetometer specification sheet [39].

HMC5883L

SPECIFICATIONS (* Tested at 25°C except stated otherwise.)

Characteristics	Conditions*	Min	Typ	Max	Units
Power Supply					
Supply Voltage	VDD Referenced to AGND VDDIO Referenced to DGND	2.16 1.71	2.5 1.8	3.6 VDD+0.1	Volts Volts
Average Current Draw	Idle Mode Measurement Mode (7.5 Hz ODR; No measurement average, MA1:MA0 = 00) VDD = 2.5V, VDDIO = 1.8V (Dual Supply) VDD = VDDIO = 2.5V (Single Supply)	- -	2 100	- -	µA µA
Performance					
Field Range	Full scale (FS)	-8		+8	gauss
Mag Dynamic Range	3-bit gain control	±1		±8	gauss
Sensitivity (Gain)	VDD=3.0V, GN=0 to 7, 12-bit ADC	230		1370	LSb/gauss
Digital Resolution	VDD=3.0V, GN=0 to 7, 1-LSb, 12-bit ADC	0.73		4.35	milli-gauss
Noise Floor (Field Resolution)	VDD=3.0V, GN=0, No measurement average, Standard Deviation 100 samples (See typical performance graphs below)		2		milli-gauss
Linearity	±2.0 gauss input range			0.1	±% FS
Hysteresis	±2.0 gauss input range		±25		ppm
Cross-Axis Sensitivity	Test Conditions: Cross field = 0.5 gauss, Happlied = ±3 gauss		±0.2%		%FS/gauss
Output Rate (ODR)	Continuous Measurment Mode Single Measurement Mode	0.75		75 160	Hz Hz
Measurement Period	From receiving command to data ready		6		ms
Turn-on Time	Ready for I2C commands Analog Circuit Ready for Measurements		200 50		µs ms
Gain Tolerance	All gain/dynamic range settings		±5		%
I^2C Address	8-bit read address 8-bit write address		0x3D 0x3C		hex hex
I^2C Rate	Controlled by I^2C Master			400	kHz
I^2C Hysteresis	Hysteresis of Schmitt trigger inputs on SCL and SDA - Fall (VDDIO=1.8V) Rise (VDDIO=1.8V)		0.2*VDDIO 0.8*VDDIO		Volts Volts
Self Test	X & Y Axes Z Axis		±1.16 ±1.08		gauss
	X & Y & Z Axes (GN=5) Positive Bias X & Y & Z Axes (GN=5) Negative Bias	243 -575		575 -243	LSb
Sensitivity Tempco	T_A = -40 to 125°C, Uncompensated Output		-0.3		%/°C
General					
ESD Voltage	Human Body Model (all pins) Charged Device Model (all pins)			2000 750	Volts
Operating Temperature	Ambient	-30		85	°C
Storage Temperature	Ambient, unbiased	-40		125	°C

Figure A.II: HMC5883L low-cost magneto-resistive magnetometer specification sheet [44].

SPECIFICATIONS

T_A = 25°C, VDD = 3.3 V, angular rate = 0°/sec, dynamic range = ±1000°/sec ± 1 *g*, unless otherwise noted.

Table 1.

Parameter	Test Conditions/Comments	Min	Typ	Max	Unit
GYROSCOPES					
Dynamic Range		±1000	±1200		°/sec
Initial Sensitivity	±1000°/sec, see Table 12		0.04		°/sec/LSB
	±500°/sec, see Table 12		0.02		°/sec/LSB
	±250°/sec, see Table 12		0.01		°/sec/LSB
Repeatability[1]	−40°C ≤ T_A ≤ +85°C			1	%
Sensitivity Temperature Coefficient	−40°C ≤ T_A ≤ +85°C		±40		ppm/°C
Misalignment	Axis to axis		±0.05		Degrees
	Axis to frame (package)		±0.5		Degrees
Nonlinearity	Best fit straight line		±0.1		% of FS
Bias Repeatability[1, 2]	−40°C ≤ T_A ≤ +85°C, 1 σ		0.5		°/sec
In-Run Bias Stability	1 σ, SMPL_PRD = 0x0001		14.5		°/hr
Angular Random Walk	1 σ, SMPL_PRD = 0x0001		0.66		°/√hr
Bias Temperature Coefficient	−40°C ≤ T_A ≤ +85°C		0.005		°/sec/°C
Linear Acceleration Effect on Bias	Any axis, 1 σ		0.015		°/sec/*g*
Bias Supply Sensitivity	−40°C ≤ T_A ≤ +85°C		0.2		°/sec/V
Output Noise	±1000°/sec range, no filtering		0.27		°/sec rms
Rate Noise Density	f = 25 Hz, ±1000°/sec range, no filtering		0.0135		°/sec/√Hz rms
−3 dB Bandwidth			330		Hz
Sensor Resonant Frequency			17.5		kHz
ACCELEROMETERS	Each axis				
Dynamic Range		±18			*g*
Sensitivity	See Table 16 for data format		0.833		m*g*/LSB
Repeatability[1]	−40°C ≤ T_A ≤ +85°C			1	%
Sensitivity Temperature Coefficient	−40°C ≤ T_A ≤ +85°C		±40		ppm/°C
Misalignment	Axis to axis		0.2		Degrees
	Axis to frame (package)		±0.5		Degrees
Nonlinearity	Best fit straight line		0.2		% of FS
Bias Repeatability[1, 2, 3]	−40°C ≤ T_A ≤ +85°C, 1 σ		20		m*g*
In-Run Bias Stability	1 σ, SMPL_PRD = 0x0001		0.25		m*g*
Velocity Random Walk	1 σ, SMPL_PRD = 0x0001		0.11		m/sec/√hr
Bias Temperature Coefficient	−40°C ≤ T_A ≤ +85°C		±0.15		m*g*/°C
Bias Supply Sensitivity	−40°C ≤ T_A ≤ +85°C		5		mg/V
Output Noise	No filtering		5.1		m*g* rms
Noise Density	No filtering		0.23		m*g*/√Hz rms
−3 dB Bandwidth			330		Hz
Sensor Resonant Frequency			5.5		kHz
MAGNETOMETERS					
Dynamic Range		±1.9			gauss
Initial Sensitivity	25°C, see Table 20 for data format	140.04	142.9	145.76	µgauss/LSB
Sensitivity Temperature Coefficient	Relative to 25°C, 1 σ		800		ppm/°C
Misalignment	Axis to axis		0.25		Degrees
	Axis to frame (package)		0.5		Degrees
Nonlinearity	Best fit straight line		0.1		% of FS
Initial Bias Error	25°C, 0 gauss stimulus		±4		mgauss
Bias Temperature Coefficient	−40°C ≤ T_A ≤ +85°C		0.11		mgauss/°C
Output Noise	25°C, no filtering, rms		2.4		mgauss
Noise Density	25°C, no filtering, rms		0.4		mgauss/√Hz
Bandwidth	−3 dB		25		Hz

Figure A.III: ADIS16448 inertial sensor specification sheet [45].

5.2 Navigation Specifications

Parameter	Value
Horizontal Position Accuracy	2.0 m
Vertical Position Accuracy	3.0 m
Horizontal Position Accuracy (with DGNSS)	0.6 m
Vertical Position Accuracy (with DGNSS)	1.0 m
Velocity Accuracy	0.05 m/s
Roll & Pitch Accuracy (Static)	0.1 °
Heading Accuracy (Static)	0.5 °
Roll & Pitch Accuracy (Dynamic)	0.2 °
Heading Accuracy (Dynamic with GNSS)	0.2 °
Heading Accuracy (Dynamic, magnetic only)	0.8 °
Heave Accuracy	5 % or 0.05 m
Orientation Range	Unlimited
Hot Start Time	500 ms
Internal Filter Rate	1000 Hz
Output Data Rate	Up to 1000 Hz

Table 1: Navigation specifications

5.3 Sensor Specifications

Parameter	Accelerometers	Gyroscopes	Magnetometers	Pressure
Range (dynamic)	2 g 4 g 16 g	250 °/s 500 °/s 2000 °/s	2 G 4 G 8 G	10 to 120 KPa
Noise Density	150 ug/√Hz	0.008 °/s/√Hz	210 uG/√Hz	0.56 Pa/√Hz
Non-linearity	< 0.05 %	< 0.05 %	< 0.05 %	-
Bias Stability	60 ug	3 °/hr	-	100 Pa/yr
Scale Factor Stability	< 0.05 %	< 0.05 %	< 0.05 %	-
Cross-axis Alignment Error	< 0.05 °	< 0.05 °	0.05 °	-
Bandwidth	400 Hz	400 Hz	110 Hz	50 Hz

Table 2: Sensor specifications

Figure A.IV: Spatial AHRS main specification sheet [43].